UNIVERSITÀ DEGLI STUDI DI TRENTO

DEPARTMENT OF MATHEMATICS

Doctoral Programme in Mathematics - Cycle XXXVIII

$\sim \cdot \sim$

Doctoral Thesis

Modelling cardiopulmonary interactions. Towards anatomically detailed and physiologically accurate cardiorespiratory models

Supervisors:
Prof. Lucas Omar Müller
Dr. Sc. Pablo Javier Blanco
Prof. Annunziato Siviglia

Candidate:
Caterina Dalmaso

Academic Year 2025-2026

Abstract

In the last decades, there has been a growing interest in understanding the complex physiological mechanisms that regulate the cardiovascular and respiratory systems and their interactions, due to the increasing healthcare burden related to cardiorespiratory diseases. To this end, physiologically accurate mathematical and computational models can provide an effective tool for the analysis of several physiopathological states and therapeutic strategies through in-silico experiments. Most existing cardiorespiratory models rely on lumped parameter (0D) descriptions not only for the respiratory system and the heart, but also for systemic and pulmonary circulatory districts. This work introduces a novel geometrically multiscale 1D-0D model that couples the fine description of blood flow in 1D domains obtained through the closed-loop Anatomically-Detailed Arterial-Venous Network (ADAVN) model with a PDE model for passive scalar transport and ODE models describing lung and peripheral gas exchange, lung mechanics and local autoregulation.

After a brief literature review, the first part of this thesis presents the methodological framework, detailing the different components of our model and the numerical methods necessary for an accurate solution of the coupled 1D blood flow-transport system. We describe the vascular networks employed for simulations, including a reduced arterial-venous network (ADAVN86) model developed to accelerate the model building and parameter tuning process, and 0D models of the heart (accounting both for a linear and nonlinear end diastolic pressure volume relationship), pulmonary circulation, lungs, peripheral terminals and gas exchange. We propose a first and a second order numerical method for the solution of the 1D coupled blood flow-transport problem, examining the numerical challenges posed by the need to guarantee mass conservation at a discrete level. Finally, we introduce a well-balanced high-order numerical method for the solution of non-conservative hyperbolic PDEs with source terms, able to accurately describe steady-state solutions in the presence of algebraic and/or geometric source terms.

The second part of this thesis focuses on the verification, validation and application of increasingly comprehensive physiological models, transitioning from a purely cardiovascular setting (the original ADAVN model), to anatomically and physiologically accurate descriptions of cardiopulmonary interactions. We first assess the impact of cardiopulmonary mechanical interactions on system haemodynamics, validating our results against patient data published in the literature, and assessing their robustness by means of a local sensi-

tivity analysis. These tests, performed with a cardiac model with a linear end-diastolic PV relationship, required substantial reparametrization of chamber elastances to guarantee physiological results in the presence of respiration. This motivated the adoption of a non-linear end-diastolic model for subsequent studies, introducing a more realistic constraint on chamber volume changes. We then extend our model to include a description of tracer/-gas transport and gas exchange. The transport module is validated through a bolus test against patient data and simulation results obtained through physiology-based pharmacokinetic models. The gas exchange model, parametrized to exploit the anatomical detail provided by our vascular networks, is validated under baseline physiological conditions against literature data and 0D model predictions. Finally, we examine three cerebral local autoregulation models: a purely myogenic one, its combination with a carbon dioxide reactivity model, and a purely metabolic autoregulation model which responds to oxygen and carbon dioxide perturbations. All reproduce the expected physiological responses across multiple test scenarios. The myogenic model, with modified parameters, is further applied to study foot perfusion in the presence of stenoses and occlusions during a cuff-induced ischaemia test.

By combining methodological advances with the development of a comprehensive and extensible framework for the multiscale modelling of cardiorespiratory physiology, which was extensively verified and validated against clinical data, this work establishes a robust foundation for future in-silico investigations of complex cardiopulmonary interactions. The resulting framework is designed to support both fundamental physiological research and the development of patient-specific simulations, ultimately contributing to the improvement of our understanding, diagnosis, and treatment of cardiorespiratory diseases.

Contents

List of Figures

List of Tables

Acknowledgements

First and foremost, I would like to express my sincere gratitude to my supervisors, Prof Lucas Omar Müller, Dr. Sc. Pablo Javier Blanco and Prof. Annunziato Siviglia for their invaluable guidance, advice and support at every stage of my doctoral journey. Their thoughtful feedback, stimulating discussions, and constant encouragement have shaped this work in profound ways. I am deeply grateful for the trust they placed in me as I developed my research and for the many opportunities they provided to grow as a scientist and as a person.

I would also like to extend my thanks to the Department of Mathematics of the University of Trento for providing the financial and academic support that made this PhD project possible. The PhD scholarship, together with the resources that enabled me to participate in conferences, workshops, and advanced courses, played a crucial role in broadening my knowledge and strengthening my research.

Lastly, I am profoundly grateful to my family, who have always supported and encouraged me during this journey, allowing me to focus on my research to the fullest.

1

Introduction

The cardiovascular and respiratory systems act together to deliver oxygen and other nutrients required for cellular metabolism, and to remove carbon dioxide and other metabolic by-products. As illustrated in Herring and Paterson (2018), the distribution of blood flow is regulated by local and global control mechanisms that adjust heart rate, cardiac contractility, and vasomotor tone to meet the metabolic demands of tissues. These adjustments affect the blood flow, and therefore the transport of gases within the vasculature and help shape chemoreflex and ventilatory responses. Indeed, blood concentrations of oxygen and carbon dioxide modulate the depth and frequency of respiration via chemoreceptor activity and influence vascular tone through local metabolic control. Mechanical interactions further reinforce this coupling: respiratory-induced variations in intrathoracic and intra-abdominal pressures affect venous return, ventricular filling, the efficiency of the cardiac pump and the propagation of pressure and flow waves. The result is an integrated system in which mechanical interactions, autonomic reflexes, and metabolic regulation continuously influence one another, with an even stronger interplay during conditions such as exercise, hypoxia (reduced partial pressure of oxygen in the bloodstream), hypercapnia (an increase of partial pressure of carbon dioxide in the bloodstream), sleep-disordered breathing, or mechanical ventilation. Capturing these complex interrelations is therefore essential for understanding cardiorespiratory dynamics and for developing predictive tools to support clinical decision making.

Depending on the desired level of physiological detail, the cardiovascular and respiratory systems can be represented using different modelling paradigms. Three-dimensional (3D) models have been widely used to study arterial haemodynamics due to their ability to reproduce local features such as wall shear stress, interactions between the arterial wall and medical devices, and particle residence time (see for example Xiao et al. (2014)). Moreover, they have been employed to characterise airflow and aerosol transport and deposition in

the airways (Van Ertbruggen et al., 2005), cardiac electromechanics (Regazzoni et al., 2022), and lung tissue deformation (Roth et al., 2017). However, this class of models is characterised by a very high computational cost, restricting their applicability to spatially localised phenomena of interest.

Lumped parameter (0D) models enable fast simulations of the entire cardiovascular system, since they represent arteries and veins through a limited number of compartments governed by ordinary differential equations, defined according to their anatomical location and physical properties. This makes them particularly suitable for sensitivity analyses, uncertainty quantification, and parameter estimation in the development of patient-specific models. It also allows simulations spanning the longer timescales which are commonly associated with interactions between the cardiovascular and other systems (Albanese et al., 2016; Fernandes et al., 2021). Their main limitation, however, is their inability of providing information on local haemodynamics, which is often interconnected with the development of pathological conditions.

One-dimensional (1D) models recover good physiological detail at a reasonably low computational cost, allowing the description of wave propagation phenomena in spatially distributed networks, and the characterisation of wave characteristics and cross-sectional averaged pressure and flow values in the vasculature (Alastruey et al., 2012; Mynard and Smolich, 2015b; Müller et al., 2023; Formaggia et al., 2003). In addition, they allow us to position central nervous system (CNS) receptors at anatomically correct locations, ensuring a more physiologically accurate sensing of the cardiovascular state. Each approach grants different advantages, and their combination is often necessary to achieve a compromise between physiological fidelity and computational cost. Also, 1D models allow us to represent patient-specific anatomical conditions with a higher degree of detail.

The present chapter reviews the main modelling approaches used to describe cardiorespiratory physiology, with a focus on lumped and one-dimensional formulations (section 1.1). The goal is to outline their key features, highlight their strengths and limitations, and identify the challenges that motivate the development of the 1D-0D integrated cardiorespiratory framework proposed in this thesis (section 1.2). The chapter concludes by presenting the contributions of this work (section 1.3).

1.1 Literature review

In recent decades, the impact of cardiorespiratory diseases has spurred the development of mathematical and computational models capable of reproducing the complex interactions between the cardiovascular and respiratory systems. In what follows, we review the main modelling approaches adopted in this field. Section 1.1.1 examines the main families of lumped parameter cardiopulmonary models, highlighting the mechanisms required to reproduce cardiorespiratory interactions in physiological and pathological conditions.

Section 1.1.2 introduces one-dimensional cardiovascular models, outlining their main features and current fields of application, and examining how their advantages and limitations compare with those of 0D formulations in the context of whole-body simulations.

1.1.1 0D cardiorespiratory models

A large body of work has focused on developing fully integrated 0D models of the cardiopulmonary system that combine cardiovascular dynamics, lung mechanics, gas exchange, and autonomic control. These models vary in scope but share the goal of capturing multisystem interactions within a lumped-parameter framework, providing a computationally efficient tool for studying physiological and pathological conditions, testing hypotheses, and performing in silico experiments spanning different ranges of time scales.

Numerous 0D models of differing complexity have been proposed since the 1950s (Grodins et al., 1954; Grodins, 1959; Guyton et al., 1972). Highly influential are the formulations developed by Ursino, Magosso and collaborators (Ursino, 1998; Ursino and Magosso, 2000; Ursino et al., 2008, 2001; Magosso and Ursino, 2001, 2002), and those introduced by Lu et al. (2001, 2003, 2004) between 1994 and 2004. These models laid the foundations for more recent integrated formulations, such as those by Albanese et al. (2016); Cheng et al. (2016, 2010); Trenhago et al. (2015); Fernandes et al. (2021).

Ursino's group developed increasingly sophisticated models to describe the cardiorespiratory system at rest and during exercise. Their early formulation (Ursino, 1998) is for the cardiovascular system alone and focuses on the interaction between the pulsating heart, arterial pressure pulsatility, and the carotid baroreflex. A subsequent extension (Ursino and Magosso, 2000) incorporated the local vasodilatory effect of oxygen and several reflex mechanisms, including peripheral chemoreceptors, lung stretch receptors, and central nervous system responses to hypoxia, to reproduce the amplitude and timing of cardiovascular responses to isocapnic hypoxia. Later models (Magosso and Ursino, 2001; Ursino and Magosso, 2002) improved the description of baroreceptors and introduced nonlinear interactions between oxygen (O_2) and carbon dioxide (CO_2) at the level of peripheral chemoreceptors, the effect of local CO_2 changes on peripheral resistances, the CNS response to CO_2, and the control of central chemoreceptors on ventilation and tidal volume. Despite their extremely detailed characterisation of control mechanisms, these models remain predominantly cardiovascular-oriented and do not include descriptions of airway and lung mechanics. Consequently, arterial gas partial pressures, which are required for chemoreflex activation, are prescribed as external stimuli.

In parallel, Lu's group developed models centred on the mechanical interactions between the cardiovascular and respiratory systems. Lu et al. (2001) included descriptions of heart mechanics (Chung et al., 1997), systemic and pulmonary circulations (Olansen et al., 2000), airway and lung mechanics (Athanasiades et al., 2000), alveolar–capillary transport of O_2,

CO_2, and N_2 (Liu et al., 1998), and baroreflex control (Wesseling and Settels, 1993). Cardiovascular and respiratory modules interact via the effect of pleural and alveolar pressures on pulmonary vascular pressures, and lung capillary resistance is modelled as a quadratic function of alveolar volume to reflect its increase during lung inflation. Lu et al. (2003) addressed the absence of tissue gas exchange, and a further extension (Lu et al., 2004) incorporated a more detailed description of cerebral haemodynamics, autoregulation of cerebral blood flow, and gas exchange between brain capillaries and the extravascular space. While these models capture heart-lung mechanical interactions in great detail, their representation of control mechanisms is comparatively limited, as they neglect cardiopulmonary baroreceptors, central chemoreceptors, and CNS responses.

More recent models aimed to integrate the strengths of these approaches. The model by Albanese et al. (2016) is a closed-loop model that takes inspiratory gas composition and total blood volume as inputs and includes separate cardiovascular and respiratory submodels, coupled through a gas exchange and transport module and a detailed representation of cardiorespiratory control. The cardiovascular subsystem builds on the work of Ursino and Magosso (Magosso and Ursino, 2001; Ursino and Magosso, 2000), modelling the effects of respiration on venous return and cardiac output by subjecting cardiac chambers, pulmonary circulation, and thoracic veins to pleural pressure. The lung mechanics model is adapted from Snyder and Rideout (1969); Mecklenburgh and Mapleson (1998). Gas exchange occurs in both pulmonary and systemic capillaries, and the control mechanisms are adapted from Magosso and Ursino (2001); Ursino and Magosso (2000, 2002). After validation under resting conditions, the response of the model was further assessed under hypercapnic and hypoxic conditions (Cheng et al., 2016). The model has since been adapted to reproduce features of chronic obstructive pulmonary disease and pulmonary fibrosis (Anjana et al., 2025) and used to generate virtual populations to predict in-hospital indicators from wearable-derived cardiorespiratory signals (Laudenzi et al., 2025b). Similarly, Trenhago et al. (2015) provides a cardiorespiratory formulation lacking control mechanisms, later extended by Fernandes et al. (2021) to include autonomic control. These models share many structural features with Albanese's work but incorporate a more detailed description of gas chemistry: gas concentrations depend not only on partial pressures and haemoglobin binding, but also on explicit representations of blood pH and pK (Siggaard-Andersen et al., 1984; Christensen and Dræby; Chiari et al., 1994). The control mechanisms in Albanese's and Fernandes' models are very similar and derived from Ursino and Magosso (Magosso and Ursino, 2001; Ursino and Magosso, 2000), except for the peripheral chemoreceptor model, which follows Ursino and Magosso (2002) in Albanese et al. (2016) and Magosso and Ursino (2001); Ursino and Magosso (2000) in Fernandes et al. (2021).

A summary of the main features of the models presented above is reported in table 1.1, and an illustrative diagram in figure 1.1.

Beyond general-purpose frameworks, several models have been developed to investigate

	Ursino et al.	Lu et al.	Albanese et al.	Fernandes et al.
Primary focus	Cardiovascular control	Mechanical interactions	Integrated framework	Integrated framework
Heart model	Ursino (1998)	Chung et al. (1997)	Magosso and Ursino (2001); Ursino and Magosso (2000)	Liang et al. (2009)
Circulation	Ursino (1998)	Olansen et al. (2000)	Magosso and Ursino (2001); Ursino and Magosso (2000)	Ursino and Magosso (2000)
Lung mechanics	-	Athanasiades et al. (2000)	Snyder and Rideout (1969); Mecklenburgh and Mapleson (1998)	Christensen and Dræby
Gas exchange	-	Liu et al. (1998)	Spencer et al. (1979)	Siggaard-Andersen et al. (1984); Christensen and Dræby; Chiari et al. (1994)
Cardiopulmonary control	Ursino and Magosso (2000); Magosso and Ursino (2001); Ursino and Magosso (2002)	Wesseling and Settels (1993); Daly (1997)	Magosso and Ursino (2001); Ursino and Magosso (2000, 2002)	Magosso and Ursino (2001); Ursino and Magosso (2000)
Strengths	Rich short-term control mechanisms	Detailed heart-lung mechanical interactions; capillary filtration and lymphatic flow	Integrated framework: heart, systemic and pulmonary circulations, lung mechanics, autonomic control, gas transport and exchange	Integrated framework with very detailed pH-pK model
Limitations	0D circulation, arterial gas partial pressures are external inputs	0D circulation, limited control mechanisms	0D circulation, less detailed gas chemistry	0D circulation

Table 1.1: Overview of the cardiorespiratory models by Ursino et al. (Ursino, 1998; Ursino and Magosso, 2000; Ursino et al., 2008, 2001; Magosso and Ursino, 2001, 2002), Lu et al. (Lu et al., 2001, 2003, 2004), Albanese et al. (Albanese et al., 2016; Cheng et al., 2016) and Fernandes et al. (Trenhago et al., 2015; Fernandes et al., 2021)

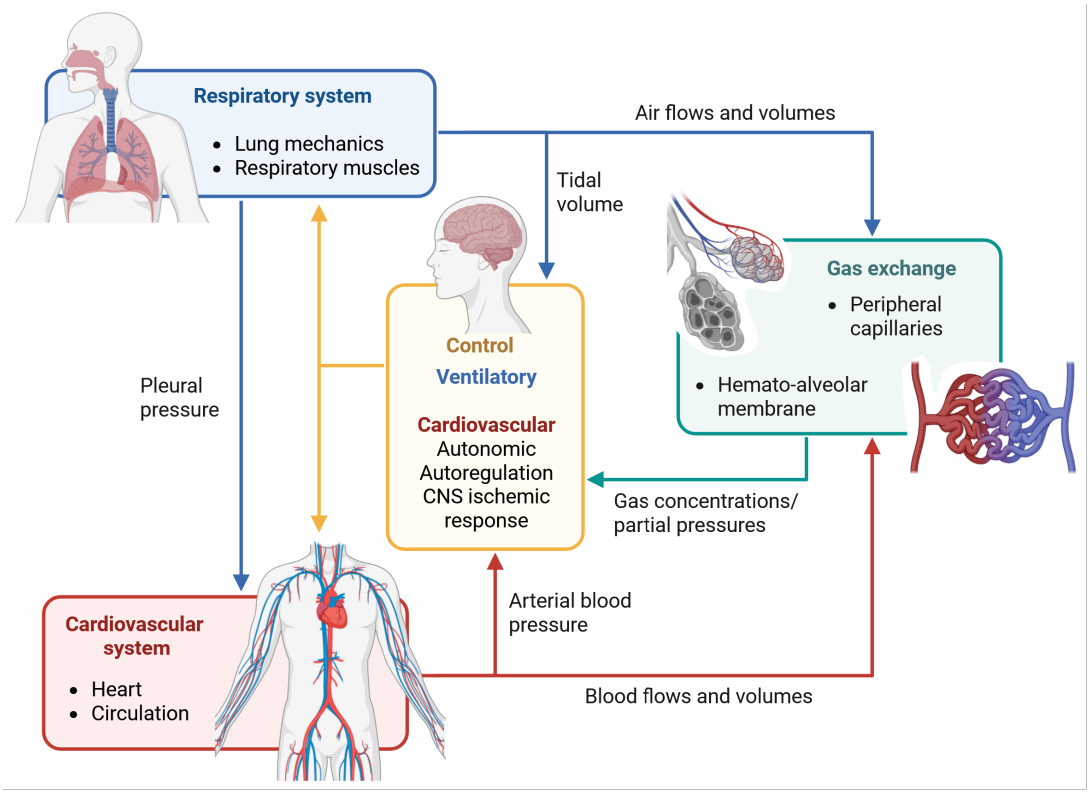

Figure 1.1: Common compartmental structure of cardiorespiratory models

specific physiological or clinical scenarios where cardiorespiratory coupling plays a central role. Cheng et al. (2010) characterised the interactions among the respiratory, cardiovascular and sleep-wake regulation systems observed during sleep-disordered breathing, with Cheng and Khoo (2012) further incorporating the metabolic control of glucose-insulin dynamics. Guerrero et al. (2021) simulated acute obstructive sleep apnea by imposing transient airway occlusions and fitting model parameters to reproduce patient-specific and event-specific desaturation patterns.

Works by Serna et al. (2018); Sarmiento et al. (2021) examined cardiorespiratory adjustments during aerobic exercise, in which metabolic demand strongly modulates ventilation, circulation, and muscle perfusion. Fresiello et al. (2016) analysed how these mechanisms are impaired in heart failure, while Baird et al. (2025) investigated age-related differences in responses to exercise, accounting for changes in lung volumes, metabolic rates, and cardiac function across the lifespan.

Finally, models have been proposed to describe the effects of mechanical ventilation (Das et al., 2015; Karamolegkos et al., 2021), ventilator–patient interaction, and to support ICU decisions (Cushway et al., 2022, 2024). These models typically comprise detailed lung mechanics, recruitment/derecruitment dynamics, and the haemodynamic consequences of positive-pressure ventilation.

1.1.2 1D cardiovascular models

All the models discussed above rely on a 0D representation of the circulatory system, which cannot capture pulse-wave propagation along the vasculature, a phenomenon that is inherently encoded in the one-dimensional equations governing blood flow (Van de Vosse and Stergiopulos, 2011). Indeed, forward and backward travelling waves propagate across the vascular system, generating reflections at every location where system topology and composition change (Westerhof et al., 1972). The superposition of these waves shapes the pressure pulse (Pedley, 1984), and their conformation provides insight into systemic properties such as the wave speed, which is an important indicator of arterial stiffening associated with ageing and cardiovascular disease (Khir et al., 2001; Westerhof and Westerhof, 2013).

One-dimensional equations to describe the flow of an incompressible, homogeneous fluid in deformable vessels are derived by averaging the 3D Navier-Stokes equations over the vessel cross-sectional area. The resulting system of PDEs (for a detailed derivation, we refer to Peiró and Veneziani (2009); Hughes and Lubliner (1973)) enforces the conservation of mass and the balance of momentum in each vascular domain

$$\begin{aligned} &\partial_t A + \partial_x q = 0, \\ &\partial_t q + \partial_x \left(\alpha \frac{q^2}{A} \right) + \frac{A}{\rho} \partial_x p = -R \frac{q}{A}, \end{aligned} \tag{1.1}$$

thereby describing how vessel cross-sectional area $A = A(x,t)$, blood flow rate $q = q(x,t)$ and blood pressure $p = p(x,t)$ vary in space and time. Here α is the so-called momentum correction factor, ρ denotes the blood density and R is a friction coefficient that stands for viscous dissipation. Further assumptions on the velocity profile are required to determine the values of the momentum correction factor and friction coefficient. As an example, considering an axially symmetric, fully developed flow in a cylindrical vessel, the velocity profile can be expressed in radial coordinates as

$$s(r) = \frac{\delta + 2}{\delta}\left(1 - \left(\frac{r}{R}\right)^{\delta}\right), \tag{1.2}$$

with $R = \sqrt{\frac{A}{\pi}}$ vessel radius. In this case,

$$\alpha = \frac{\int_S s^2 d\sigma}{A}, \qquad R = \frac{2(\delta + 2)\pi\mu}{\rho}, \tag{1.3}$$

with S transversal section and μ blood viscosity. In the case of a Poiseuille flow, $\alpha = \frac{4}{3}$ and $R = 8\pi\frac{\mu}{\rho}$.

In the rest of the work, we will assume $\alpha = 1$, due to the considerable mathematical simplifications deriving from this assumption (Spilimbergo et al., 2024).

This system needs to be complemented by a closure condition, called tube law, which characterises the mechanical behaviour of the vessel wall by relating blood pressure and vessel lumen area (Formaggia et al., 2003; Shapiro, 1977; Flaherty et al., 1972; Langewouters et al., 1984; Colombo et al., 2024). A detailed description of the 1D blood flow equations, augmented with a characterisation of the transport of n passive scalars, and the tube laws employed for this work is provided in sections 2.2.1 and 2.2.2, and a description of the numerical methods employed for their solution in sections 2.2.2.1 and 2.2.3.

1D domains can be coupled to form vascular networks of increasing complexity by enforcing mass conservation and total pressure continuity at bifurcations. More complex conditions could be introduced to account for pressure losses caused, for example, by vascular tapering (Stettler et al., 1981) or bifurcation geometry (Formaggia et al., 2003). Additionally, vessels can be coupled with lumped-parameter models representing other components of the circulatory system, such as the heart (section 2.3.1) and peripheral capillaries (section 2.3.3).

Early network models, such as the 55-artery network by Noordergraaf et al. (1963), paved the way for increasingly anatomically realistic representations of the entire systemic circulation. Modellers focused on improving both the anatomical detail of vascular networks and physiological parameters, e.g. by refining the characterisation of wave reflection properties at bifurcations, in peripheral vessels and in relation to vascular tapering (Stergiopulos et al., 1992; Wang and Parker, 2004), and by adjusting vessel geometry and stiffness to

reproduce age-stratified populations (Westerhof et al., 1969). In particular, the development of efficient numerical methods for solving 1D problems over large vascular networks has enabled a progressive increase in the level of detail used to describe vascular anatomy. Avolio (1980) proposed a 128-segment model of the arterial system, thereby extending the model proposed by Noordergraaf et al. (1963) with the goal of improving its topological description and correcting the location of the major reflecting sites in the network. Similarly, Reymond et al. (2009) extended the model by Stergiopulos et al. (1992) to incorporate coronary, cerebral, and extracranial branches. Blanco et al. (2015) presented the ADAN (Anatomically Detailed Arterial Network) model, which includes 2142 arteries outlined in the 3D space pertaining to the vasculatures of the head, trunk, limbs, abdominal organs, brain and heart. This model was calibrated to reproduce a physiological blood flow distribution among 28 organs and 116 vascular territories in the body, and its main applications include the study and characterisation of cardiovascular diseases, organ functioning and tissue microcirculatory perfusion. Additionally, the ADAN vascular network includes the most common collateral connections across vascular districts, thereby enabling characterisation of blood redistribution in pathologies such as peripheral artery disease (PAD). A comparison of results obtained with this model and using a simplified network of 86 vessels (ADAN86) was performed by Blanco et al. (2020), both under physiological conditions and in the case of common carotid artery occlusion to assess the impact of vascular anatomy definition on predicted haemodynamic indices and waveforms. Results showed that, while the two models produced similar results in large vessels under normal conditions, the greater detail of the ADAN model was fundamental for achieving a better characterisation of pathological situations, in which model predictions diverged.

Arterial networks have been coupled with 0D descriptions of the heart and peripheral components, and with 0D (Liang et al., 2009) or 1D (Mynard and Smolich, 2015b; Müller and Toro, 2014) models of the venous circulation, to obtain closed-loop descriptions of the cardiovascular system that allow a characterisation of the global interactions between the heart and vasculature. Notably, Müller et al. (2023) proposed an Anatomically Detailed Arterial Venous Network (ADAVN) model, which combines the ADAN model with a venous network comprising 189 veins that drain blood from 66 vascular regions. Among the considered veins, 14 are coronary, and 58 drain the brain. Except for the cerebral circulation, the anatomical detail by which the venous system is described is inferior to that of the arterial system, meaning that most peripheral veins drain blood from more than one organ/vascular territory of the ADAN model. Connectivity between arterial and venous vessels was established either according to perfusion maps available in the literature or based on the proximity of terminal arteries and terminal veins. Model outputs were validated against clinical reference data for a young, healthy male under resting conditions. We show in Figure 1.2 a comparative view of the ADAN86, ADAN and ADAVN models. Authors envisioned the ADAVN model as a basis for incremental inclusion of physiological features, such as orthostasis and its interplay with the respiratory and lymphatic systems. Additionally, since women and men exhibit both anatomical and functional differences in

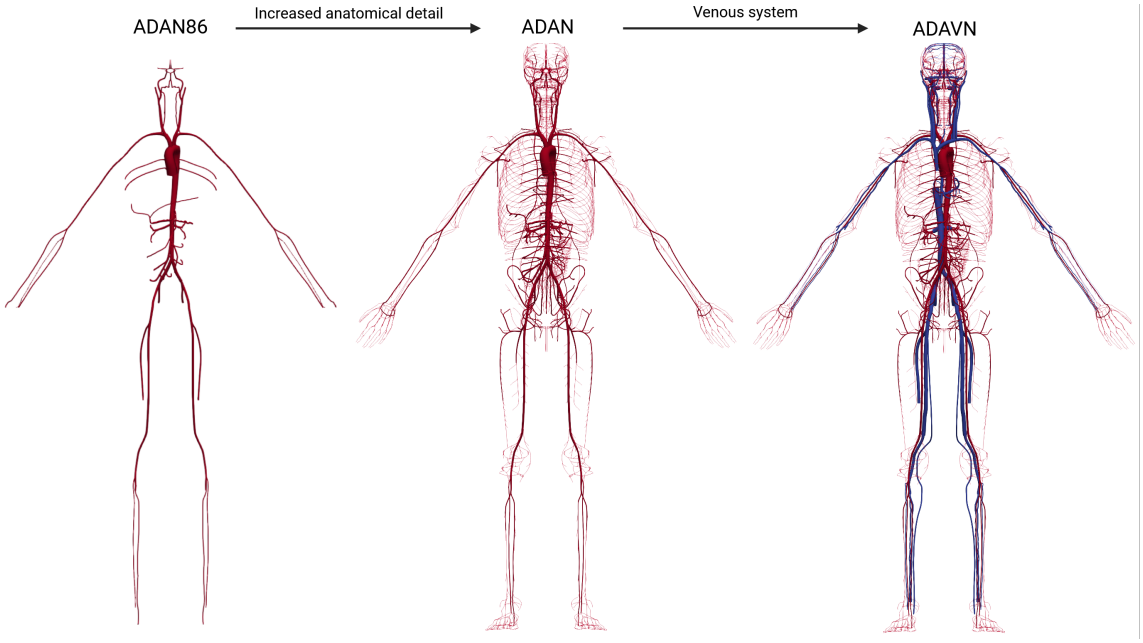

Figure 1.2: Comparative view of the ADAN86, ADAN and ADAVN models

their cardiovascular systems, it is advisable for computational models to incorporate the impact of sex and/or gender. This can be achieved by including female-specific organs (e.g., the uterus) and by adjusting the calibration of key parameters such as ventricular contractility and arterial geometry to reflect sex-specific characteristics in heart rate, systemic pressures, and flow rates (Susin, 2023; Comunale et al., 2020; Corsini et al., 2017; Zaid et al., 2023).

Open and closed-loop 1D vascular networks have been widely used to study pathological conditions such as stenoses (Downing and Ku, 1997; Ge et al., 2020; Carson et al., 2019; Simakov et al., 2016; Dalmaso et al., 2025b; Boileau et al., 2018; Stergiopulos et al., 1992) and hypertension (Li et al., 2017; Celant et al., 2023; Heusinkveld et al., 2019), as well as surgical procedures such as graft implantation (Wan et al., 2002; Steele et al., 2003; Kolachalama et al., 2007; Strocchi et al., 2017), and inter-individual anatomical variability (Fossan et al., 2018; Müller et al., 2021). However, despite the broad applicability of these models, the cardiovascular system has almost always been treated as an isolated subsystem. An important exception comes from literature addressing the dynamics of the cerebrospinal fluid: Kim and Cirovic (2011) proposed a 1D representation of the spinal column coupled to a cranial compartment whose inputs were arterial and venous pressure and flow. Later, Martin et al. (2012) proposed an improved model coupling arterial blood flow and the cerebrospinal fluid system, which accounted for blood supply to the spinal cord. Additionally, in Müller and Toro (2014), a model of the interaction between cere-

bral blood flow (with separate descriptions of arterial, arteriolar, capillary, venular, and venous compartments) and craniospinal dynamics was proposed. Toro et al. (2022) further extended this model to study the effect of strictures in cerebral veins on craniospinal dynamics. As of now, 1D models are being used also to shed light on poorly understood phenomena, such as those involved in brain clearance by the glymphatic circulation (Faghih and Sharp, 2018). Modellers have also started to address the interaction between the cardiovascular system and short-term control mechanisms. As an example, Ryu et al. (2015) and McConnell and Payne (2016) focused on the effects local autoregulation of cerebral blood flow, Blanco et al. (2012) integrated arterial baroreflex control into a 1D model of the arterial network closed by a 0D description of the venous circulation, and Celant et al. (2021, 2023) coupled arterial and cardiopulmonary baroreflex controls to a 1D closed-loop arterio-venous network model, to determine total effective vascular compliance in healthy and hypertensive subjects. Several works are available also to model the effects of gravity. Among the others, Li and Cheng (1993) studied the effects of microgravity in pulmonary circulation, showing the impact of vessel wall stiffness, Zervides et al. (2008) analysed the impact of venous valves in managing high pressure fluctuations such as those experienced during orthostasis. In Zhang et al. (2017), a 1D closed-loop model of the arterio-venous system was employed to investigate the gravitational effects at multiple inclined positions. Finally, Cirovic et al. (2000) studied cerebral perfusion under the effect of strong accelerations, and Mohammadyari et al. (2021) analysed the impact of several conditions, from microgravity to postural changes, on the haemodynamics of vessels in the neck and head.

The characterisation of interactions between the cardiovascular and respiratory systems, which, as we saw in section 1.1.1, has been an active research area for 0D modellers, has instead been mostly overlooked by the 1D modelling community, despite the suitability of 1D-0D models for the description of gas transport by the bloodstream and gas exchange in the alveoli and peripheral circulation. This can be due to several reasons. The main technical difficulty arises from the long time scales required for integrated simulations. Indeed, while the scale of a cardiac cycle is around 1 s, and the scale of respiration is below 10 s, changes in metabolic exchange often occur over thousands of seconds. As a consequence, numerical methods employed to run 1D simulations for such long times should be efficient and preserve conservation properties at a discrete level. Validation also becomes more challenging as model complexity increases, since the large number of parameters and the scarcity of comprehensive in vivo data limit the extent to which predictions can be assessed even for standalone 1D cardiovascular networks. For coupled cardiorespiratory models, this difficulty is amplified by the need to verify interactions among multiple subsystems, with literature data that primarily spans pathological conditions. A few recent studies have begun to explore cardiopulmonary 1D-0D formulations, for example, by prescribing measurement-derived intrathoracic pressure waveforms as external pressures in the tube law (Li et al., 2022, 2023). In addition to imposing a cyclically varying intrathoracic pressure, Cui et al. (2023) also incorporates transport and exchange processes within a 1D arterial network to investigate how venoarterial ECMO support alters haemodynamic

variables and blood-gas indices in severe cardiac or cardiopulmonary failure. Although these contributions illustrate the potential of system integration, they do not yet provide a fully unified cardiorespiratory framework.

To sum up, 1D cardiovascular models provide powerful tools for representing haemodynamics with a level of detail unattainable in lumped formulations. Yet, despite their strengths, existing 1D models do not account for the reciprocal interaction between circulation and respiration, which becomes particularly important for the modelling of physiological or pathological haemodynamic scenarios that go beyond the typical at-rest conditions.

1.2 Motivation and objectives

The cardiovascular and respiratory systems continuously interact via multiple mechanisms in a complex, nonlinear manner. Although purely cardiovascular models can be tuned to reproduce haemodynamics under resting conditions, such parameter adjustments effectively compensate for omitted physiology rather than representing it explicitly. When the system is perturbed, capturing the underlying interrelations, which become even more pronounced under physiological and pathological perturbations such as exercise, hypoxia, hypercapnia, haemorrhage, and mechanical ventilation, is therefore essential for producing physiologically sound predictions. This is particularly relevant when model-predicted variables such as central venous pressure, stroke volume, cardiac output, ejection fractions, and arterial gas partial pressures are interpreted as potential biomarkers to support the diagnosis and monitoring of cardiorespiratory pathologies (Laudenzi et al., 2025a).

As discussed in section 1.1.1, a substantial body of work has focused on 0D integrated cardiopulmonary models, which combine cardiovascular dynamics, lung mechanics, gas exchange, and cardiopulmonary control within a closed-loop framework. These models have a very low computational cost and are able to simulate whole-body responses across a wide range of conditions. However, they cannot capture regional perfusion patterns and wave propagation phenomena, limiting their ability to represent anatomically dependent pathologies such as PAD, aneurysms, COPD, ischaemic stroke and transient ischaemic attacks, aortic coarctation and arteriovenous malformations, as well as the haemodynamic consequences of interventions such as stenting and graft implantation.

Conversely, as illustrated in section 1.1.2, 1D models provide anatomically accurate descriptions of the vasculature, allowing, for example, the investigation of wave propagation dynamics, cardiac-vascular interactions, and the impact of localised disease (stenoses and occlusions) and surgical interventions. The ability of 1D models to resolve wave propagation along the vascular tree also enables a more realistic representation of afferent dynamics at cardiovascular receptors. This is particularly relevant for the baroreflex, whose afferent firing depends not only on mean pressure but also on waveform morphology at the aortic arch and carotid sinuses, where local pressure waveforms may differ because wave

propagation and reflection are influenced by site-specific vascular mechanical properties or the presence of localized pathology such as stenoses or occlusions. Yet, existing 1D models typically neglect the reciprocal interaction between circulation and respiration, even though autonomic reflexes and respiratory-driven changes in intrathoracic and intra-abdominal pressures affect the haemodynamics of the system, influencing cardiac efficiency, wave propagation dynamics, and energy transfer between vessels (see section 4.1). Without these interactions, 1D models fall short in reproducing the integrated cardiorespiratory responses that govern real physiology, especially under non-baseline conditions.

This gap between anatomically detailed haemodynamic and integrated cardiorespiratory physiology modelling motivates the present work. The objective of this thesis is to develop a cardiorespiratory model that integrates respiration phenomena onto a 1D anatomically detailed description of the arterial and venous networks. The proposed formulation combines cardiovascular dynamics, lung mechanics, gas exchange, and local autoregulation, and can reproduce physiologically realistic wave propagation phenomena, regional perfusion, and the effects of localised cardiovascular diseases. The model-building process posed multiple challenges, including the numerical treatment of non-conservative hyperbolic systems of PDEs and the coupling of haemodynamics with gas transport and exchange.

1.3 Contributions

The main contributions of this thesis regard:

(1) A high-order well-balanced finite-volume scheme for non-conservative hyperbolic systems;

(2) A numerical framework for coupled 1D haemodynamics and passive-scalar transport;

(3) A progressively integrated cardiopulmonary model including lung mechanics, gas transport and exchange, and local autoregulation.

(4) An anatomically detailed model of foot perfusion for the study of peripheral artery disease;

They resulted in the following publications:

Peer-reviewed

- Dalmaso, C., Blanco, P.J. Müller, L.O. Cardiopulmonary mechanical interactions. Insights from an anatomically detailed arterial-venous network model. Biomech. Model. Mechanobiol. 24, 1653–1686 (2025). https://doi.org/10.1007/s10237-025-01987-y
  We present a 1D-0D model that couples a 0D description of lung mechanics to the

closed-loop Anatomically-Detailed Arterial-Venous Network (ADAVN) model. We show that our model can satisfactorily reproduce a set of cardiovascular indices of interest observed in healthy young males at rest. Next, we assess the impact of respiration on cardiac performance and on the periodicity and average values of pressure and flow waveforms in different vascular districts. In particular, our results confirm that respiration has a fundamental pumping function, which aids venous return, and that its action affects mainly the average of haemodynamic variables on the arterial side, while on the venous side it has a significant effect on wave periodicity and triggers a complex interplay in terms of waveform conformation. Additionally, we assess the sensitivity of model predictions to variations in model parameters through a local sensitivity analysis, both in the presence and absence of respiration, highlighting a strong relationship between the arterial and venous side of the model.

- Colombo, C., Dalmaso, C., Müller, L. O., Siviglia, A. (2026). Well-balanced high-order method for non-conservative hyperbolic PDEs with source terms: application to one-dimensional blood flow equations with gravity. Journal of Computational Physics, 114975.
  The present work proposes a well-balanced finite volume-type numerical method for the solution of non-conservative hyperbolic partial differential equations (PDEs) with source terms. The method is characterised, first, by the use of a recently introduced high-order spatial reconstruction, based on generalized Riemann problem information from the previous time level. Such reconstruction is well-balanced up to order three, compact, efficient and easy to implement. Second, the method incorporates a well-balanced space-time evolution operator, which allows for well-balanced fully explicit time evolution. The accuracy and efficiency of the method are assessed on both a scalar problem (Burgers' equation) and a nonlinear PDE system (hyperbolized one-dimensional blood flow equations with gravity and friction, and with variable mechanical and geometrical properties). The well-balanced property is verified by showing that numerically-determined stationary solutions are preserved up to machine precision. The order of accuracy in space and time is validated through empirical convergence rate studies. Additionally, the performance of the method is assessed on a network of 86 arteries, under both stationary and transient conditions.
- Bisgaard, M.*, Dalmaso, C.*, Nygaard, J. V., Precht, H., Houlind, K. C., Müller, L. O., Blanco, P. J. (2026). Foot perfusion. Insights from an anatomically detailed arterial network model. Journal of Biomechanics, 113336. (*equal contributors)
  Peripheral artery disease currently affects over 202 million people worldwide. The ankle-brachial index is widely used to assess a reduction in blood flow to the foot, but it cannot characterise tissue perfusion. MRI-based perfusion measurements can provide this information, yet they are time-consuming and can be painful if induction of ischaemia is warranted for the scan. As an alternative, we model foot perfusion during a cuff-induced ischaemia test to characterise how arterial occlusions affect per-

fusion in foot regions. Simulations, not patient-specific at this stage, are conducted on a 1D arterial network model which includes 154 foot and calf arterial segments, providing a realistic description of the topology of the foot vasculature. A baseline model characterises angiosome perfusion under healthy conditions, which is then modified to reflect 42 pathological scenarios by introducing occlusions and different levels of collateral impairment. This approach enables a novel in-silico comparison of angiosome-targeted and best-vessel strategies in a realistic whole-limb geometry, uncovering mechanistic phenomena relevant for revascularisation planning. Results show a marked influence of collateral impairment on angiosome perfusion under the condition of a single-artery occlusion, highlighting the role of blood redistribution. If two feeding arteries are occluded, perfusion markedly decreases at all collateral impairment levels due to the severe reduction in incoming blood flow. These results provide a bridge between the angiosome-targeted and "best-vessel" strategies for revascularisation, showing that both can be correct depending on collateral sufficiency.

Moreover, excerpts of this work were presented at the following conferences:

Upcoming conferences

- WCCM ECCOMAS 2026: An Integrated 1D-0D Model of the Cardiorespiratory System With Short-Term Cardiopulmonary Control Mechanisms. Dalmaso, C., Blanco, P.J., Müller, L.O.

Past conferences and meetings

- Convegno GNCS 2026: Soluzioni Innovative per Sistemi Complessi: Metodi Numerici e Approcci Multiscala.
- SIAM Chapters meeting for Young Researchers: An integrated 1D-0D model of the cardiorespiratory system with local autoregulation
- ECCOMAS YIC 2025 Conference: An integrated 1D-0D model of the cardiorespiratory system with local autoregulation. Dalmaso, C., Blanco, P.J., Müller, L.O.
- ESB 2025 Congress: Foot perfusion. Insights from an anatomically detailed arterial network model. Dalmaso, C., Bisgaard, M., Nygaard, J.V., Precht, H., Houlind, K.C., Müller, L.O., Blanco, P.J.
- COLIBRI Focus Workshop in Computational Medicine: Cardiopulmonary mechanical interactions. Insights from an anatomically detailed arterial-venous network model. Dalmaso, C., Blanco, P.J., Müller, L.O.
- CMBE 2024: Cardiopulmonary mechanical interactions. Insights from an anatomically detailed arterial-venous network model. Dalmaso, C., Blanco, P.J., Müller,

L.O.

- M2P 2023 Emerging Technologies in Computational Science for Industry, Sustainability and Innovation: Uncertainty Quantification and Sensitivity Analysis for Non-invasive Model-based Instantaneous Wave-Free Ratio Prediction. Dalmaso, C., Fossan, F.E., Bråten, A.T., Müller, L.O.

1.4 Structure of the work

The work is organized into five chapters, progressing from the scientific background and methodological developments to the construction, verification, and application of the proposed cardiorespiratory modelling framework.

Chapter 2 presents the numerical methods and modelling components that form the basis of the integrated framework. It describes the vascular networks employed (section 2.1), the governing equations for 1D blood flow and transport (sections 2.2.1 and 2.2.2), and a high-order well-balanced numerical method for non-conservative hyperbolic systems (section 2.2.3). It also illustrates 0D models of the heart (section 2.3.1), pulmonary circulation (section 2.3.2), peripheral terminals (section 2.3.3), lung mechanics (section 2.3.4), gas transport (section 2.3.5) and exchange (section 2.3.6), and control mechanisms (section 2.3.7).

Chapter 3 collects the numerical results obtained for the coupled haemodynamics and transport problem (section 3.1), and reports the numerical tests conducted to evaluate the performance of the proposed well-balanced finite-volume scheme for non-conservative hyperbolic systems (section 3.2).

Chapter 4 focuses on model verification, validation, and applications. We report and discuss the results associated with the incremental development of an integrated cardiopulmonary model, based on the framework proposed by Albanese et al. (2016). In particular, we first assess the impact of respiration on haemodynamic indices and waveforms (section 4.1). We then compare simulations obtained with the ADAVN and ADAVN86 vascular networks (section 4.2.1), as well as with two cardiac models featuring, respectively, linear and non-linear end-diastolic pressure-volume relationships (section 4.2.2). Finally, we validate the transport and exchange modules (section 4.3), together with myogenic and metabolic local autoregulation models (section 4.4). Finally, we show a possible application for an anatomically detailed cardiovascular model with autoregulation by analysing foot perfusion in the presence of arterial occlusions and impaired collateralization (section 4.5). This completes the transition from purely mechanical models to a more physiologically integrated system.

Chapter 5 reports a synthesis of the main contributions of this work, and a discussion of limitations and perspectives for future developments.

2

Model building and numerical methods

This chapter forms the methodological backbone of the thesis and provides a detailed account of the components essential to our model-building effort. We begin in Section 2.1 by describing the three vascular networks considered in this thesis. In Section 4.5, we use the ADAN model to characterise foot perfusion in the presence of pedal arterial occlusions and impaired collateralization. We then adopt the ADAVN model to investigate the impact of respiration on cardiac performance, as well as on the periodicity and average values of pressure and flow waveforms (Section 4.1). Finally, we employ the Reduced Arterial Venous Network (ADAVN86) model to support model verification and validation when longer timescales are required to simulate gas transport, exchange, and control mechanisms (Sections 4.3, 4.4). The name ADAVN86 was chosen because this reduced network was built by including the ADAVN coronary circulation and venous system in the ADAN86 model presented in Blanco et al. (2020), which included the 86 main arteries in our body.

In Section 2.2.1, we introduce the 1D blood flow equations, and in Section 2.2.2 we illustrate several numerical challenges that arise when modelling the advection of a passive scalar within the vasculature, where the advection velocity is space-dependent and obtained from the solution of the 1D haemodynamic problem. In Section 2.2.3, we develop a generic well-balanced high-order method for non-conservative hyperbolic PDEs with source terms, capable of preserving stationary solutions up to machine precision.

Finally, in Section 2.3 we outline the main 0D models required for physiological simulations. We begin by describing the models used to characterise the heart (Section 2.3.1), the pulmonary circulation (Section 2.3.2), and the peripheral terminals (Section 2.3.3). We then present the lung-mechanics model and explain how it is mechanically coupled to the cardiovascular module (Section 2.3.4). Lastly, we describe the models for gas exchange in the lungs and peripheral capillaries (Section 2.3.6), and introduce three local

autoregulation models (Section 2.3.7).

2.1 Vascular networks

We present here the ADAN, ADAN86, ADAVN and ADAVN86 models. The ADAN, ADAN86 and ADAVN models were developed respectively by Blanco et al. (2014, 2015, 2016), Blanco et al. (2020) and Müller et al. (2023). The ADAVN86 model was instead constructed and parametrised specifically for this thesis to support model development and preliminary validation.

2.1.1 Anatomically Detailed Arterial Network (ADAN) model

The ADAN model, proposed by Blanco et al. (2015) and further improved in Blanco et al. (2016), reproduces an average arterial vasculature of a man, outlined in 3D space using a digital dataset of the human skeleton as scaffold. The architecture of this model includes almost every named arterial vessel according to the International Anatomical Terminology (1598 arteries), with a resolution down to the luminal area of perforator arteries (544 vessels that supply blood to peripheral regions). The determination of geometrical parameters of the vasculature, i.e. vessel length, luminal radii, and vessel wall thickness is detailed in Blanco et al. (2015): vessel lengths L were derived from the 3D characterisation of vessels on top of the skeleton, vessel radii R_o were obtained from anatomical and medical literature, and wall thicknesses h were estimated from the radii based on curve-fitting of data published by Avolio (1980)

$$\frac{h}{R_o} = a\exp(bR_o) + c\exp(dR_o), \tag{2.1}$$

with $a = 0.2802, b = -5.053/cm, c = 0.1324$ and $d = -0.1114/cm$. Vessel radii impact also the definition of material properties of the arterial wall. Indeed, large arteries are predominantly elastic, mid-sized ones have more collagen content and smooth muscle than large arteries, and less elastin content, while small arteries are dominantly muscular. For a detailed description of the resulting parametrisation we refer to Blanco et al. (2014).

The model includes blood supply to 28 specific organs (see table 2.1, approximately 64.7% of the cardiac output) and accounts for 116 vascular territories used to distribute flow to the muscles, bones, nerves, fascia and skin (see table 2.2). Peripheral beds are represented through Windkessel models, with resistive elements calibrated in such a way that guarantees the physiologically expected flow fraction to each location. We refer to Blanco et al. (2015) for details regarding the calibration procedure.

Particularly relevant for simulation studies are the collateral circulations present in the model, commonly excluded from less detailed vascular networks, such as the circle of Willis

Organ	Blood flow fraction	Reference	Organ	Blood flow fraction	Reference
Heart	4	Valentin (2002)	Suprarenal (x2)	0.15	Valentin (2002)
Encephalon	12	Valentin (2002)	Stomach	1	Valentin (2002)
Eye (x2)	0.014286	Williamson and Harris (1994)	Pancreas	1	Valentin (2002)
Ear (x2)	0.000014	Prazma et al. (1984)	Spleen	3	Valentin (2002)
Nose	0.000089	Valentin (2002)	Small intestine	10	Valentin (2002)
Tongue	0.3	Valentin (2002)	Large intestine	3.25	Valentin (2002)
Teeth	0.0012	Yoon et al. (2010)	Bladder	0.06	Valentin (2002)
Thyroid	1.5	Valentin (2002)	Penis	0.893140	Halls et al. (2009)
Hypophysis	0.009429	Valentin (2002)	Testicle (x2)	0.028750	Valentin (2002)
Liver	6.5	Valentin (2002)	Rectum	0.75	Valentin (2002)
Gallbladder	0.004286	Valentin (2002)	Diaphragm	1.058718	Loukas et al. (2005)
Kidney (x2)	9.5	Valentin (2002)			

Table 2.1: Blood flow fractions [%] to the 28 organs included in the ADAN model. Total blood flow to these organ is 64.72%.

Region	Side	NT	RVF (%)	TFF (%)
Head and neck	L	10	2.4475	2
	R	10	2.4475	2
Trunk		22	28.9120	7.1915
Upper limb	L	16	5.8828	3.5
	R	16	5.8828	3.5
Lower limb	L	21	27.2137	8.5
	R	21	27.2137	8.5

Table 2.2: Regions of the body which are segmentally subdivided into the 116 territories, each associated to a specific volume fraction and blood flow fraction. NT is the number of territories in each region, RVF is the regional volume fraction, TFF target blood flow fraction.

in the brain, the neck circuits, the mesenteric circuits, the knee, foot and hand vasculatures etc., since they allow us to study blood flow redistribution phenomena occurring in response to pathological conditions, or external stimuli.

A publicly accessible portal for exploring haemodynamic conditions predicted by the ADAN model and reviewing related parameters is available at `http://hemolab.lncc.br/adan-web`. This vascular network was employed for simulations reported in section 4.5.

2.1.2 Reduced Arterial Network (ADAN86) model

The ADAN86 model was developed by Blanco et al. (2020) to evaluate how anatomical detail influences haemodynamic predictions. It is a truncated form of the full ADAN model, which comprises 86 main arteries (Stergiopulos et al., 1992; Alastruey et al., 2014; Wang and Parker, 2004), including the Circle of Willis (Safaei et al., 2016). The anatomical simplification reduces the number of vascular territories and minor organs represented: the encephalon, liver, kidneys, stomach, pancreas, spleen, and intestines are retained, together with extracranial regions, the intercostal space, and the upper and lower limbs. Material parameters of the tube law are identical to those used for the original ADAN network, while terminal resistances were calibrated according to three criteria:

(1) blood supply to major organs is preserved relative to ADAN;

(2) flow to extracranial regions via the external carotid artery and to part of the intercostal space via intercostal vessels matches that of ADAN;

(3) vessels perfusing the upper and lower limbs carry the additional flow required to achieve the target cardiac output.

This parametrisation strategy enables the ADAN86 model to reproduce central haemodynamics of the full ADAN network under baseline "healthy" conditions, with differences in waveforms becoming more evident in peripheral vessels due to a mismatch in the blood supply to the different territories. Under pathological scenarios, such as complete occlusion of the common carotid artery, model predictions diverge substantially because of the reduced number of available collateral pathways.

This vascular network was employed for simulations reported in section 3.2.

2.1.3 Anatomically Detailed Arterial Venous Network (ADAVN) model

The ADAVN model is a cardiovascular model first introduced by Müller et al. (2023), which represents an average male vascular anatomy and couples the ADAN model with a network of 189 veins, 58 of which are cerebral and 14 of which are coronary (see figure 2.9,

left panel). In contrast to the arterial network, the model includes only the cerebral and coronary venous vessels in full, while the remainder of the venous system is represented only through its major vessels. As a result, venous drainage is modelled across 66 vascular regions, with most venous vessels collecting blood from multiple areas among the 28 organs and 116 vascular territories supplied by the arterial network. (Blanco et al., 2015).

Connectivity between arterial and venous networks was established in peripheral territories by means of 0D RCR descriptions of arteriolar, capillary and venular compartments (section 2.3.3), according to existing knowledge regarding brain and heart perfusion, or based on proximity of terminal arteries and terminal veins. The aortic arch, inferior and superior caval veins, and coronary sinus are connected to a 0D model of the heart (section 2.3.1.1), which characterises each chamber as an elastic compartment with a prescribed time-varying elastance. The pulmonary circulation is also described by means of a 0D model which describes pulmonary arteries, capillaries and veins by means of CLR compartments (section 2.3.2). The cardiovascular model includes also 30 venous valves and 53 cerebral Starling resistors, as well as a simple model describing the interaction between cerebral vasculature and intracranial pressure. Table 2.3 shows a summary of the main features of the arterial-venous network.

This vascular network was employed for simulations reported in section 4.1.

Total arterial segments (named)	2142 (1598)
Coronary arteries	23
Cerebral arteries	162
Venous segments	189
Coronary veins	14
Cerebral veins	58
Venous valves	30
Starling resistors in the brain	53

Table 2.3: General features of the ADAVN model.

2.1.4 Reduced Arterial Venous Network (ADAVN86) model

Running long timescale simulations on the ADAVN network is computationally costly and time-consuming, making it less-than-ideal for model building and parameter fine-tuning. As a consequence, in order to reduce computational time and speed up the development of the cardiorespiratory model, we developed a reduced vascular network, which we will call ADAVN86, comprising 86 systemic arteries (the same as in the ADAN86 network presented in section 2.1.2), 23 coronary arteries and the same 189 veins that are present in the full

ADAVN network. We chose to maintain this higher resolution for the venous circulation for further applications of this network, particularly for use in orthostasis simulations, which affect venous more than arterial circulation due to its inherently lower pressure and higher compliance (Colombo et al., 2026). We refer to figure 2.1 for a representation of the network.

Conversely to the ADAVN model, the venous system is more detailed than the arterial one (with the exception of coronary vessels, which are identical). This posed the problem of determining a reasonable arterial-venous connectivity in the various vascular districts and, in particular, in the brain, where 58 cerebral veins drain 6 arteries.

Similarly to the approach followed for the ADAVN model, we operated under the assumption that each terminal artery is connected to an arterial bed which can connect to multiple veins (up to 2 in ADAVN and up to 11 in ADAVN86). Each terminal vein is in turn connected to a venular bed, which can receive blood from multiple arteries. Connectivity was mostly established based on proximity of terminal arteries and terminal veins, trying to reproduce as much as possible the connectivity that was defined for the ADAVN model. Within the brain, we combined this approach with existing literature concerning perfusion of the various brain regions.

Vessels are part of 41 vascular regions (in ADAVN regions are 61 (Müller et al., 2023), see table 2.4 for a comprehensive list), 9 of which contain only veins, and 24 only arteries. Details regarding model parametrisation and verification are provided in section 4.2.1. This network was used for simulations reported in sections 4.3.2.1, 4.3.2.2 and 4.4.

2.1.4.1 Connectivity

We show here the arterial-venous connectivities obtained in the various vascular districts. We do not show coronary vessels, since the connectivity is identical to that in the ADAVN model, and the liver, since only one vein is present.

2.1.4.1.1 Brain and neck

Cerebral connectivity proved to be the most challenging to reconstruct due to the very high number of veins compared to arteries. We traced the pathways in the ADAVN network beginning from the main cerebral artery, also present in the ADAVN86 network, and followed all arteries branching from it, assigning as venous terminals all vessels draining those arterial territories. We then refined these preliminary connections using brain perfusion maps reported in the literature (D'Souza et al.), obtaining the connectivities reported in figure 2.2 (rows 1 and 2). In the neck region, only two arteries (the external carotid arteries) feed all veins. Consequently, we connected arteries and veins depending on their anatomical side (see figure 2.2, row 3).

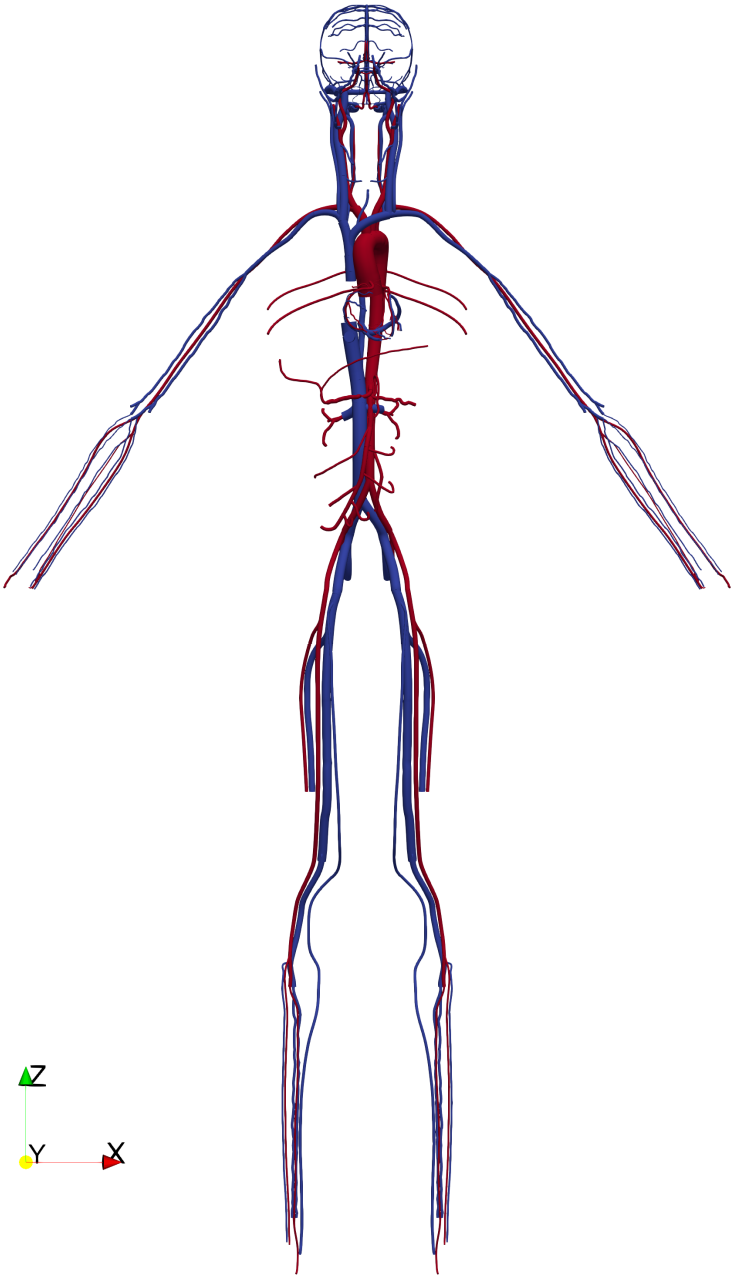

Figure 2.1: ADAVN86 arterial-venous network.

ID	ADAVN	ADAVN86	Name	ID	ADAVN	ADAVN86	Name
1	X	X	head	32	arteries	X	right suprarenal
2	✓	✓	encephalon	33	arteries	X	left suprarenal
3	arteries	arteries	brain	34	arteries	arteries	liver
4	arteries	X	cerebellum	35	arteries	arteries	stomach
5	arteries	X	pons	36	arteries	arteries	spleen
6	veins	veins	dura mater	37	arteries	arteries	pancreas
7	✓	veins	scalp	38	✓	✓	right kidney
8	✓	✓	face	39	✓	✓	left kidney
9	✓	✓	neck	40	arteries	arteries	intestine
10	veins	veins	right upper limb	41	arteries	arteries	dorsum
11	arteries	arteries	right shoulder	42	arteries	X	spinal
12	arteries	arteries	right arm	43	arteries	X	spinal cord
13	arteries	arteries	right forearm	44	arteries	X	cervical spinal cord
14	arteries	X	right hand	45	arteries	X	thoracic spinal cord
15	veins	veins	left upper limb	46	arteries	X	lumbar spinal cord
16	arteries	arteries	left shoulder	47	arteries	X	lumbar
17	arteries	arteries	left arm	48	arteries	X	cauda equina
18	arteries	arteries	left forearm	49	✓	✓	pelvis
19	arteries	X	left hand	50	veins	veins	right lower limb
20	arteries	X	trunk	51	arteries	X	right gluteal region
21	X	X	aorta	52	arteries	arteries	right hip thigh
22	arteries	arteries	aortic arch	53	arteries	arteries	right knee
23	arteries	arteries	thoracic aorta	54	arteries	arteries	right leg
24	arteries	arteries	abdominal aorta	55	arteries	X	right foot
25	✓	veins	chest	56	veins	veins	left lower limb
26	veins	veins	coronaries	57	arteries	X	left gluteal region
27	arteries	arteries	right coronaries	58	arteries	arteries	left hip thigh
28	arteries	arteries	left coronaries	59	arteries	arteries	left knee
29	arteries	X	sternum	60	arteries	arteries	left leg
30	✓	veins	abdomen	61	arteries	X	left foot
31	arteries	X	diaphragm				

Table 2.4: Vascular regions in the ADAVN and ADAVN86 models: for each network, we denote with X regions where no vessels are present, with the check mark regions where both arteries and veins are present, and with ”arteries” or ”veins” regions where only said vessel type is present.

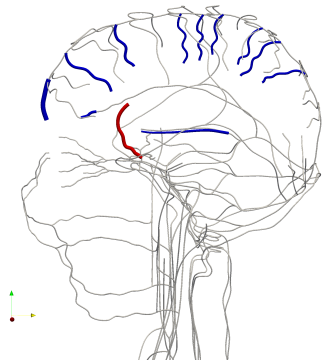

(a) Left anterior cerebral artery.

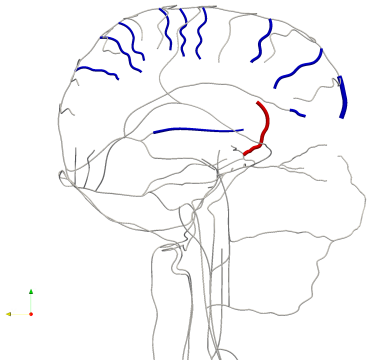

(b) Right anterior cerebral artery.

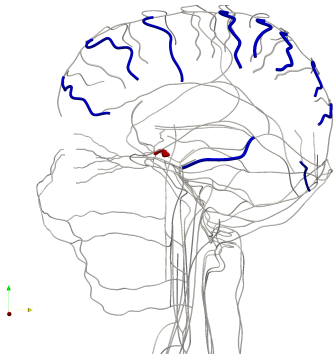

(c) Left middle cerebral artery.

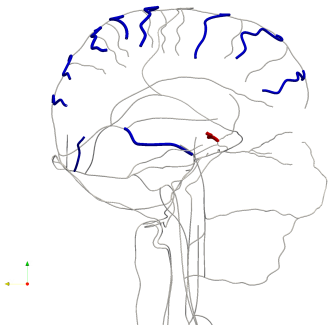

(d) Right middle cerebral artery.

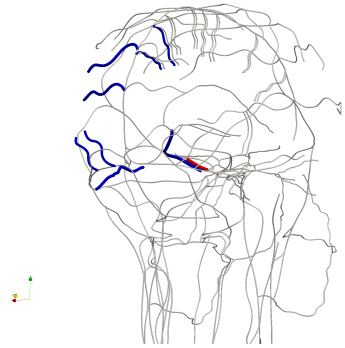

(e) Left posterior cerebral postcommunicating artery.

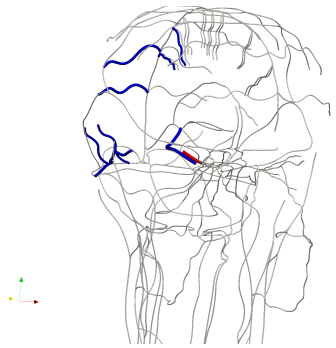

(f) Right posterior cerebral postcommunicating artery.

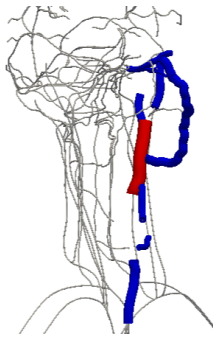

(g) Left external carotid artery.

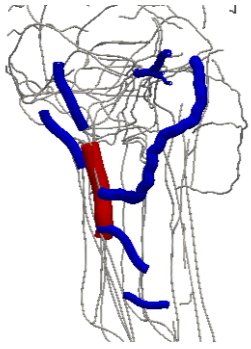

(h) Right external carotid artery.

Figure 2.2: Veins (blue) connected to the cerebral and neck arteries (red) present in the ADAVN86 network.

2.1.4.1.2 Torso and abdomen

In the head and neck we had numerous veins connected to each artery. In this region, we either have a one-to-one connection, or we have multiple arteries connected to a single vein. Connections (reported in figures 2.3, 2.4) were based on those present in ADAVN or performed in terms of proximity.

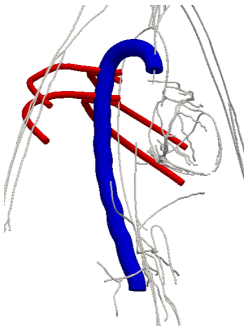

(a) Azygos vein.

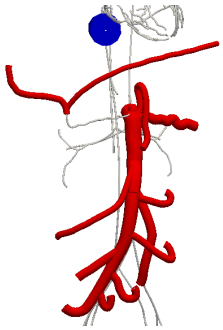

(b) Hepatic vein.

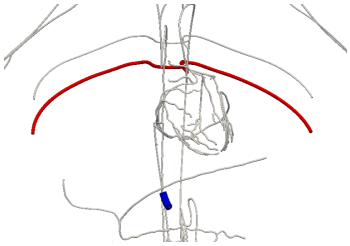

(c) Venous perforator.

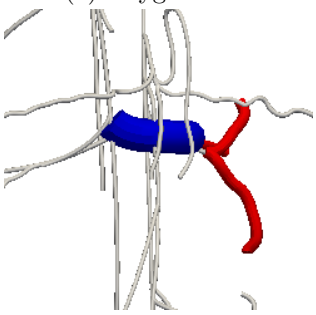

(d) Left renal vein.

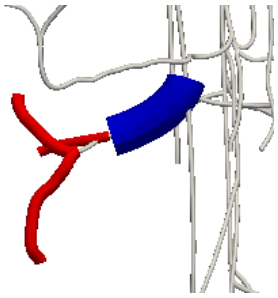

(e) Right renal vein.

Figure 2.3: Arteries (red) connected to veins in the trunk and abdomen (blue) present in the ADAVN86 network.

2.1.4.1.3 Limbs

In the limbs, a maximum of three veins drain each artery. Connectivity was established in terms of proximity, and is shown for the upper limbs in figure 2.5 and for the lower limbs in figure 2.6.

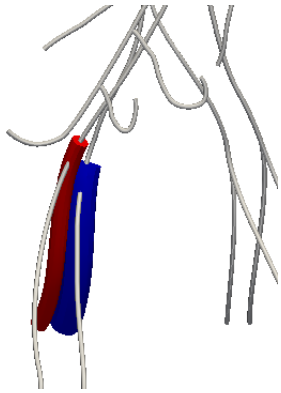

(a) Right internal iliac vein.

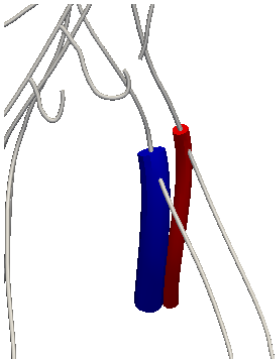

(b) Left internal iliac vein.

Figure 2.4: Iliac arteries (red) and veins (blue).

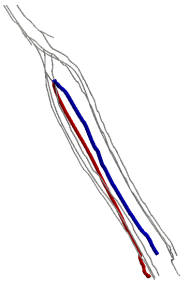

(a) Left posterior interosseous artery.

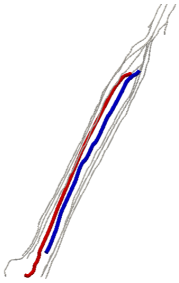

(b) Right posterior interosseous artery.

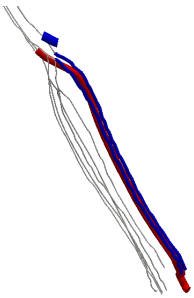

(c) Left radial artery.

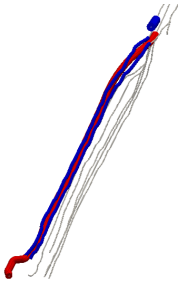

(d) Right radial artery.

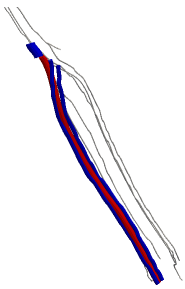

(e) Left ulnar artery.

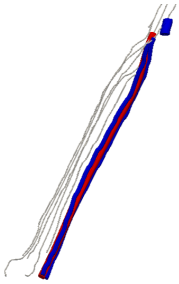

(f) Right ulnar artery.

Figure 2.5: Veins (blue) connected to the arm arteries (red) present in the ADAVN86 network.

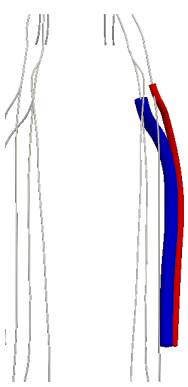

(a) Left profunda femoris artery.

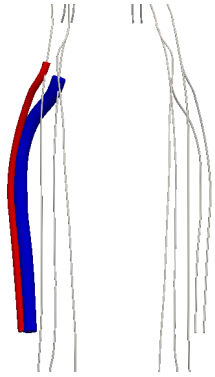

(b) Right profunda femoris artery.

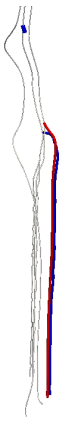

(c) Left anterior tibial artery.

(d) Right anterior tibial artery.

(e) Left posterior tibial artery.

(f) Right posterior tibial artery.

Figure 2.6: Veins (blue) connected to the leg arteries (red) present in the ADAVN86 network.

2.2 1D blood flow models: equations and numerical solution

Blood flow modelling is central to cardiovascular research, offering quantitative insight into the complex dynamics of the circulatory system. In the following, we present an overview of the one-dimensional blood flow and transport equations, introduce a well-balanced finite volume-type numerical scheme for non-conservative hyperbolic systems with source terms, and describe our proposed method for solving the associated transport problem.

2.2.1 1D blood flow equations

Blood flow in 1D vessels can be described through the classical 1D blood flow governing equations

$$\begin{aligned} &\partial_t A + \partial_x q = 0, \\ &\partial_t q + \partial_x\left(\frac{q^2}{A}\right) + \frac{A}{\rho}\partial_x p = -R\frac{q}{A}, \end{aligned} \tag{2.2}$$

where $A = A(x,t)$, $p = p(x,t)$ and $q = q(x,t)$ denote the vessel lumen area, flow rate and blood pressure in time along the vessel axis. For a Poiseuille flow, the friction force coefficient is $R = 8\pi\frac{\mu}{\rho}$, with μ and ρ, respectively, blood viscosity and density.

To close the system, we adopt a viscoelastic tube law of the form

$$p(x,t) = p_{ext}(x,t) + \zeta(x,t) + p_0, \tag{2.3}$$

where $\zeta(x,t)$ accounts for the constitutive law of the vessel tissue, which is different for arteries and veins (Müller et al., 2023), $p_{ext}(x,t)$ accounts for the pressure exerted on the vessels by tissues and extravascular media, and p_0 is the homeostatic equilibrium pressure. In particular, for arteries

$$\zeta^{\text{art}}(x,t) = \frac{\pi R_0 h_0}{A}\left[E_e\varepsilon + E_c\epsilon_r \ln\left(e^{\chi}+1\right) + \frac{K_m^{\text{art}}}{2\sqrt{AA_0}}\frac{\partial A}{\partial t}\right], \tag{2.4}$$

where $R_0 = R_0(x)$, $A_0 = A_0(x)$ and $h_0 = h_0(x)$ are the reference vessel radius, area and wall thickness at the homeostatic equilibrium pressure, $E_e = E_e(x)$ and $E_c = E_c(x)$ are the effective Young moduli of elastin and collagen fibres, and K_m^{art} is the effective viscoelastic parameter. χ was defined as $\chi = \frac{\varepsilon-\varepsilon_0}{\epsilon_r}$, with $\varepsilon = \varepsilon(A, A_0) = \sqrt{\frac{A}{A_0}} - 1$ current fibre strain, $\varepsilon_0 = \varepsilon_0(A_0)$ the strain for which half collagen fibres are recruited, and $\epsilon_r = \epsilon_r(A_0)$ standard deviation of the fibre activation state distribution. The tube law used for veins accounts for vessel collapse and reads as follows (Müller et al., 2023):

$$\zeta^{\text{ven}}(x,t) = K_{\text{eff}}^{\text{ven}}\left[\left(\frac{A}{A_0}\right)^{10} - \left(\frac{A}{A_0}\right)^{-\frac{3}{2}}\right] + \frac{K_m^{\text{ven}}}{A_0\sqrt{A}}\frac{\partial A}{\partial t}, \tag{2.5}$$

where $K_{\text{eff}}^{\text{ven}}$ is the effective vascular stiffness and K_m^{ven} the effective viscoelastic parameter.

The choice of this tube law results in an advection-diffusion-reaction system of PDEs, which can be reformulated, within appropriate parameter and state ranges, in terms of a first-order hyperbolic system with stiff source terms (Montecinos et al., 2014; Müller et al., 2016a,b). In particular, we introduce the auxiliary variable ψ and the relaxation time $T_{\text{rel}} > 0$ such that, as $T_{\text{rel}} \to 0$, $\psi \to \partial_x q$, and define the evolution equation

$$\partial_t \psi = \frac{1}{T_{\text{rel}}}(\partial_x q - \psi). \tag{2.6}$$

This results in the following reformulation of ζ, where $\partial_x q = \psi$

$$\zeta^{\text{art}}(x,t) = \frac{\pi R_0 h_0}{A}\left[E_e\varepsilon + E_c\epsilon_r \ln\left(e^{\chi}+1\right) - \frac{K_m^{\text{art}}}{2\sqrt{AA_0}}\psi\right] \tag{2.7}$$

$$\zeta^{\text{ven}}(x,t) = K_{\text{eff}}^{\text{ven}}\left[\left(\frac{A}{A_0}\right)^{10} - \left(\frac{A}{A_0}\right)^{-\frac{3}{2}}\right] - \frac{K_m^{\text{ven}}}{A_0\sqrt{A}}\psi. \tag{2.8}$$

Spatially variable tube law parameters result in geometric source terms in the momentum balance equation. Following the approach proposed in Toro and Siviglia (2013b), we introduce the trivial evolution equations $\partial_t \alpha = 0$ for $\alpha = A_0, h_0, E_e, E_c, \epsilon_0, \epsilon_r$, and $\partial_t p_{ext} = F(x,t)$ with $F(x,t)$ prescribed.

Since this model cannot be cast in conservative form, its numerical approximation relies on path-conservative formulations and well-balanced techniques. A general framework for the description of inviscid flows (with momentum-correction coefficient equal to one) in compliant vessels with discontinuous material properties, including an advection equation for passive-scalar transport, was developed by Toro and Siviglia (2013b), who derived the exact Riemann solution for subcritical flow regimes. Subsequent work (Spilimbergo et al., 2021) extended this analysis to arbitrary momentum-correction coefficients and more intricate wave interactions.

2.2.2 Modelling transport in 1D domains

We consider here the coupling between the 1D blood flow equations (BFEs) with spatially varying geometrical and mechanical properties and the transport of n passive scalars. We analyse the implications of discretising the transport problem using either a conservative or a path-conservative approach, with particular attention to mass conservation.

The transport of n passive scalars in the vasculature is described by means of a system of n PDEs

$$\partial_t(A\phi_i) + \partial_x\left(\frac{q(A\phi_i)}{A}\right) = 0,\ i = 1\dots n, \tag{2.9}$$

with ϕ_i concentration of the $i-th$ substance transported by blood.

We chose a purely convective transport model since 1D domains comprise only arteries, arterioles and veins, where physiologically convective transport is dominant, while the capillary circulation, where diffusion delivers oxygen from capillary vessels to tissue cells, is described by means of 0D models (Herring and Paterson, 2018). This assumption can be verified by computing the Péclet number (Pe) in the different types of vessels

$$Pe = \frac{\text{Convective transport rate}}{\text{Diffusive transport rate}} = Re \times Sc = \frac{2\pi\rho}{\mu}\frac{q}{R_0} \times \frac{\mu}{\rho D}, \tag{2.10}$$

with Re and Sc Reynolds and Schmidt numbers, respectively, R_0 vessel radius, D diffusivity coefficient, q blood flow rate. μ and ρ denote, respectively, blood viscosity and density. Indeed, $Pe \gg 1$ is associated with a convection-dominated transport, i.e. bulk flow sweeps the tracer along the vessel far faster than molecular diffusion can spread it radially or axially. When Pe approaches or falls below 1, diffusion becomes the primary transport mechanism.

For the computation of Pe, we consider an oxygen diffusivity coefficient of $D \sim 2 \cdot 10^{-5}$ cm^2/s: Goldstick et al. (1976) reports that the average values for D in normal human plasma, at 25 and 37°C, are 1.62 and 2.18·10^{-5} cm^2/s respectively. For normal human blood at 42% haematocrit, the values of D, at 25 and 37°C, are, instead 1.20 and 1.62·10^{-5} cm^2/s respectively. Diffusivity of carbon dioxide in blood was instead reported to be $\sim 5.05 \cdot 10^{-6}$ (Lukitsch et al., 2021). Since $D_{CO_2} < D_{O_2}$, Péclet numbers were computed only for oxygen (see table 2.5). Obtained values confirm that convective transport dominates by far over diffusive effects under physiological conditions in all considered vessels, with the exception of capillaries.

The diffusivity in blood of commonly used contrast agents is similarly of the order of 10^{-6} (Woodall et al., 2018), making also the transport of contrast medium in arteries and veins advection-dominated.

Other mechanisms, such as Taylor dispersion (Taylor, 1953; Azer, 2005), may come into play when assessing bolus transit in the vasculature. However, for this phenomenon to be relevant, transit times in vessels need to be longer than the time required for the solute molecules to diffuse radially, which for a Poiseuille flow can be estimated as

$$t_R \gg \frac{R_0^2}{D}. \tag{2.11}$$

For arterial/venous radii, which typically range from 0.025 to 1.5 cm, 25 s $< t_R <$ 10^4 s, which exceeds typical bolus transit times in those vessels. Taylor dispersion may become relevant for smaller arterioles, venules and capillary vessels, which in our model are described through 0D compartments. In the present model, the dominant mechanism underlying bolus broadening throughout the vasculature is instead geometric dispersion aris-

	Mean Reynolds number	Schmidt number	Péclet number
Ascending aorta	1000	$\sim 2 \cdot 10^3$	$\sim 2 \cdot 10^6$
Abdominal aorta	600	$\sim 2 \cdot 10^3$	$\sim 1.2 \cdot 10^6$
Coronary arteries	250	$\sim 2 \cdot 10^3$	$\sim 5 \cdot 10^5$
Carotid arteries	450	$\sim 2 \cdot 10^3$	$\sim 9 \cdot 10^5$
Arterioles	1	$\sim 2 \cdot 10^3$	$\sim 2 \cdot 10^3$
Capillaries	10^{-3}	$\sim 2 \cdot 10^3$	~ 2
Inferior vena cava	400	$\sim 2 \cdot 10^3$	$\sim 8 \cdot 10^5$

Table 2.5: Reynolds, Schmidt and Péclet numbers computed for oxygen transport in the vasculature assuming $D \sim 2 \cdot 10^{-5}$ cm^2/s.

ing from path-length heterogeneity at network bifurcations (Bassingthwaighle and Warner, 1965).

The combined 1D BFEs and transport system can be reformulated in quasi-linear form, and reads

$$\partial_t \mathbf{Q} + \mathbf{A}(\mathbf{Q})\partial_x \mathbf{Q} = \mathbf{S}(\mathbf{Q}), \tag{2.12}$$

where

$$\mathbf{Q} = \begin{bmatrix} A & q & \psi & A_0 & h_0 & E_e & E_c & p_{ext} & \epsilon_0 & \epsilon_r & A\phi_1 & \dots & A\phi_n \end{bmatrix}^T,$$

$$\mathbf{A}(\mathbf{Q}) = \begin{bmatrix} 0 & 1 & 0 & 0 & 0 & 0 & 0 & 0 & 0 & 0 & 0 & \cdots & 0 \\ c^2-u^2 & 2u & \frac{A}{\rho}\partial_\phi\zeta & \frac{A}{\rho}\partial_{A_0}\zeta & \frac{A}{\rho}\partial_{h_0}\zeta & \frac{A}{\rho}\partial_{E_e}\zeta & \frac{A}{\rho}\partial_{E_c}\zeta & \frac{A}{\rho} & \frac{A}{\rho}\partial_{\epsilon_0}\zeta & \frac{A}{\rho}\partial_{\epsilon_r}\zeta & 0 & \cdots & 0 \\ 0 & -\frac{1}{T_{\text{rel}}} & 0 & 0 & 0 & 0 & 0 & 0 & 0 & 0 & 0 & \cdots & 0 \\ 0 & 0 & 0 & 0 & 0 & 0 & 0 & 0 & 0 & 0 & 0 & \cdots & 0 \\ \vdots & & & & & \cdots & & & & & & & \vdots \\ 0 & 0 & 0 & 0 & 0 & 0 & 0 & 0 & 0 & 0 & 0 & \cdots & 0 \\ -u\phi_1 & \phi_1 & 0 & 0 & 0 & 0 & 0 & 0 & 0 & 0 & u & \cdots & 0 \\ \vdots & \vdots & & & & \cdots & & & & & & \ddots & \\ -u\phi_n & \phi_n & 0 & 0 & 0 & 0 & 0 & 0 & 0 & 0 & 0 & \cdots & u \end{bmatrix},$$

$$\mathbf{S}(\mathbf{Q}) = \begin{bmatrix} 0 & Ru & -\psi/\varepsilon & 0 & 0 & 0 & 0 & 0 & 0 & 0 & 0 & \cdots & 0 \end{bmatrix}^T.$$

Here $c = \sqrt{\frac{A}{\rho}\partial_A\zeta}$, $u = \frac{q}{A}$ is the flow velocity.

The eigenstructure of this system is that of its homogeneous version, and is given by the eigenvalues and associated eigenvectors of the coefficient matrix $\mathbf{A}(\mathbf{Q})$. Eigenvalues are $\lambda_1 = u - c_T, \lambda_2 = \cdots = \lambda_9 = 0, \lambda_{10} = \cdots = \lambda_{10+n-1} = u, \lambda_{10+n} = u + c_T$, with $c_T = \sqrt{c^2 - \frac{A}{\rho}\frac{\partial_\psi \zeta}{T_{\text{rel}}}}$. A possible choice of right eigenvectors $\mathbf{R_j}$ of $\mathbf{A}(\mathbf{Q})$ associated to

eigenvalues $\lambda_1, \ldots, \lambda_{10+n}$ is

$$
\begin{aligned}
\mathbf{R_1} &= \begin{bmatrix} 1 & u - c_T & -\frac{1}{T_{\text{rel}}} & 0 & 0 & 0 & 0 & 0 & 0 & 0 & \phi_1 & \cdots & \phi_n \end{bmatrix}^T \\
\mathbf{R_2} &= \begin{bmatrix} 0 & 0 & 1 & 0 & 0 & 0 & 0 & -\partial_\psi \zeta & 0 & 0 & 0 & \cdots & 0 \end{bmatrix}^T \\
\mathbf{R_3} &= \begin{bmatrix} 0 & 0 & 0 & 1 & 0 & 0 & 0 & -\partial_{A_0} \zeta & 0 & 0 & 0 & \cdots & 0 \end{bmatrix}^T \\
\mathbf{R_4} &= \begin{bmatrix} 0 & 0 & 0 & 0 & 1 & 0 & 0 & -\partial_{h_0} \zeta & 0 & 0 & 0 & \cdots & 0 \end{bmatrix}^T \\
\mathbf{R_5} &= \begin{bmatrix} 0 & 0 & 0 & 0 & 0 & 1 & 0 & -\partial_{E_e} \zeta & 0 & 0 & 0 & \cdots & 0 \end{bmatrix}^T \\
\mathbf{R_6} &= \begin{bmatrix} 0 & 0 & 0 & 0 & 0 & 0 & 1 & -\partial_{E_c} \zeta & 0 & 0 & 0 & \cdots & 0 \end{bmatrix}^T \\
\mathbf{R_7} &= \begin{bmatrix} 1 & 0 & 0 & 0 & 0 & 0 & 0 & \frac{\rho(u^2 - c^2)}{A} & 0 & 0 & \phi_1 & \cdots & \phi_n \end{bmatrix}^T \\
\mathbf{R_8} &= \begin{bmatrix} 0 & 0 & 0 & 0 & 0 & 0 & 0 & -\partial_{\epsilon_0} \zeta & 1 & 0 & 0 & \cdots & 0 \end{bmatrix}^T \\
\mathbf{R_9} &= \begin{bmatrix} 0 & 0 & 0 & 0 & 0 & 0 & 0 & -\partial_{\epsilon_r} \zeta & 0 & 1 & 0 & \cdots & 0 \end{bmatrix}^T \\
\mathbf{R_{10}} &= \begin{bmatrix} 0 & 0 & 0 & 0 & 0 & 0 & 0 & 0 & 0 & 0 & 1 & \cdots & 0 \end{bmatrix}^T \\
\mathbf{R_{10+n-1}} &= \begin{bmatrix} 0 & 0 & 0 & 0 & 0 & 0 & 0 & 0 & 0 & 0 & 0 & \cdots & 1 \end{bmatrix}^T \\
\mathbf{R_{10+n}} &= \begin{bmatrix} 1 & u + c_T & -\frac{1}{T_{\text{rel}}} & 0 & 0 & 0 & 0 & 0 & 0 & 0 & \phi_1 & \cdots & \phi_n \end{bmatrix}^T .
\end{aligned}
$$

System (2.12) is hyperbolic if $\partial_A \zeta - \frac{\partial_\psi \zeta}{T_{\text{rel}}} > 0$. Moreover, it can be shown that the λ_1 and λ_{10+n} characteristic fields are genuinely nonlinear and, consequently, associated with shock and rarefaction waves, while the remaining fields are linearly degenerate and associated with stationary contact discontinuities ($\lambda_2, \ldots, \lambda_9$ characteristic fields) and non-stationary contact discontinuities ($\lambda_{10}, \ldots \lambda_{10+n-1}$ characteristic fields). Riemann invariants for the characteristic field associated with λ_1 are

$$
\begin{aligned}
&u + \int_{\hat{A}}^{A} \frac{\tilde{c}_T(\xi)}{\xi} \mathrm{d}\xi = \text{const}, \quad \psi + \frac{A}{T_{\text{rel}}} = \text{const}, \quad \phi_i = \text{const} \\
&\alpha = \text{const}, \text{ with } \alpha = A_0, h_0, E_e, E_c, p_{ext}, \epsilon_0, \epsilon_r
\end{aligned}
\tag{2.13}
$$

and for the characteristic field associated with λ_{10+n}

$$
\begin{aligned}
&u - \int_{\hat{A}}^{A} \frac{\tilde{c}_T(\xi)}{\xi} \mathrm{d}\xi = \text{const}, \quad \psi + \frac{A}{T_{\text{rel}}} = \text{const}, \quad \phi_i = \text{const} \\
&\alpha = \text{const}, \text{ with } \alpha = A_0, h_0, E_e, E_c, p_{ext}, \epsilon_0, \epsilon_r .
\end{aligned}
\tag{2.14}
$$

Here, $\tilde{c}_T(A) = c_T(A, \tilde{\psi}(A)), \tilde{\psi}(A) = \hat{\psi} + \frac{\hat{A} - A}{T_{\text{rel}}}$, with $\hat{\psi}, \hat{A}$ reference values

The generalised Riemann invariants associated with the stationary contact discontinuities are

$$q = \text{const}, \quad \frac{1}{2}\rho\left(\frac{q}{A}\right)^2 + p = \text{const}, \quad \phi_i = \text{const}. \tag{2.15}$$

If $\lambda_{10}, \dots \lambda_{10+n-1} \neq 0$, Riemann invariant analysis shows that

$$A = \text{const}, \quad q = \text{const}, \quad \alpha = \text{const } (\alpha = A_0, h_0, E_e, E_c, p_{ext}, \epsilon_0, \epsilon_r), \quad \phi_i \neq \text{const} \tag{2.16}$$

For a proof, performed on a simplified system, we refer to Spilimbergo et al. (2021).

2.2.2.1 Numerical solution

In the following, we provide a detailed description of the numerical scheme employed to solve system (2.12), which cannot be cast in conservative form. In particular, we will focus on the numerical solution of the transport problem, while for the solution of the haemodynamic problem we refer to Müller et al. (2016).

We operate in the framework of path-conservative schemes for non-conservative systems (Parés, 2006).

We consider the space-time control volume $V_i^n = \left[x_{i-\frac{1}{2}}, x_{i+\frac{1}{2}}\right] \times \left[t^n, t^{n+1}\right]$ and integrate (2.12) using integration by parts, obtaining

$$\mathbf{Q}_i^{n+1} = \mathbf{Q}_i^n - \frac{\Delta t^n}{\Delta x_i}(\mathbf{D}^-_{i+\frac{1}{2}} + \mathbf{D}^+_{i-\frac{1}{2}}) - \frac{1}{\Delta x_i}\int_{t^n}^{t^{n+1}}\int_{x_{i-\frac{1}{2}}}^{x_{i+\frac{1}{2}}} \mathbf{A}(\mathbf{Q})\partial_x\mathbf{Q}\mathrm{d}x\mathrm{d}t + \Delta t^n \mathbf{S}_i, \tag{2.17}$$

where

$$\mathbf{Q}_i^n \simeq \frac{1}{\Delta x_i}\int_{x_{i-\frac{1}{2}}}^{x_{i+\frac{1}{2}}} \mathbf{Q}(x, t^n)\mathrm{d}x, \tag{2.18}$$

$$\mathbf{S}_i \simeq \frac{1}{\Delta x_i \Delta t^n}\int_{t^n}^{t^{n+1}}\int_{x_{i-\frac{1}{2}}}^{x_{i+\frac{1}{2}}} \mathbf{S}(\mathbf{Q}(x, t^n))\mathrm{d}x\mathrm{d}t \tag{2.19}$$

are, respectively, the approximation of the average of the exact solution at the $i-th$ computational cell at time level t^n and the approximation of the spatial-temporal integral average of the source term at the $i-th$ computational cell. $\mathbf{D}^{\pm}_{i+\frac{1}{2}}$ are obtained as

$$\mathbf{D}^{\pm}_{i+\frac{1}{2}} = \frac{1}{\Delta t^n}\int_{t^n}^{t^{n+1}} \mathcal{D}^{\pm}_{i+\frac{1}{2}}(\mathbf{Q}^-_{i+\frac{1}{2}}(t), \mathbf{Q}^+_{i+\frac{1}{2}}(t), \mathbf{\Psi}(\mathbf{Q}^-_{i+\frac{1}{2}}(t), \mathbf{Q}^+_{i+\frac{1}{2}}(t), s))\mathrm{d}t, \tag{2.20}$$

with $\mathcal{D}^{\pm}_{i+\frac{1}{2}}(\mathbf{Q}^-_{i+\frac{1}{2}}(t), \mathbf{Q}^+_{i+\frac{1}{2}}(t), \mathbf{\Psi}(\mathbf{Q}^-_{i+\frac{1}{2}}(t), \mathbf{Q}^+_{i+\frac{1}{2}}(t), s)$ fluctuations, i.e. the equivalent of numerical fluxes in finite volume schemes for hyperbolic systems written in conservative

form, which arise from the solution of a Riemann problem at the cell interface $x_{i+\frac{1}{2}}$. $\mathbf{\Psi}(\mathbf{Q}^-_{i+\frac{1}{2}}(t), \mathbf{Q}^+_{i+\frac{1}{2}}(t), s))$ is the integration path that links the right and left states in phase space.

Fluctuations are Lipschitz continuous path-dependent functions that have to satisfy

$$\mathcal{D}^{\pm}(\mathbf{Q}, \mathbf{Q}, \mathbf{\Psi}) = 0 \tag{2.21}$$

$$\mathcal{D}^{-}(\mathbf{Q}^-, \mathbf{Q}^+, \mathbf{\Psi}) + \mathcal{D}^{+}(\mathbf{Q}^-, \mathbf{Q}^+, \mathbf{\Psi}) = \int_0^1 \mathbf{A}(\mathbf{\Psi}(\mathbf{Q}^-, \mathbf{Q}^+, s)) \frac{\partial \mathbf{\Psi}}{\partial s} \mathrm{d}s. \tag{2.22}$$

In the case of a first order method, (2.17) reduces to

$$\mathbf{Q}_i^{n+1} = \mathbf{Q}_i^n - \frac{\Delta t^n}{\Delta x_i}(\mathbf{D}^-_{i+\frac{1}{2}} + \mathbf{D}^+_{i-\frac{1}{2}}) + \Delta t^n \mathbf{S}_i, \tag{2.23}$$

2.2.2.1.1 First order numerical scheme

In the following, we report both the path-conservative and conservative approaches for the solution of the transport problem. In Section 3.1, we will then analyse the implications of the two strategies on the numerical results obtained for closed-loop simulations.

Path-conservative approach

In order to develop a first-order path-conservative numerical scheme, we need to compute numerical fluctuations $\mathbf{D}^{\pm}_{i+\frac{1}{2}}$.

For the transport problem, we consider the conservative formulation

$$\partial_t(A\phi_i) + \partial_x\left(\frac{q(A\phi_i)}{A}\right) = 0, \ i = 1 \dots n, \tag{2.24}$$

to guarantee tracer mass conservation, which is fundamental for closed-loop simulations.

Numerical fluctuations are found by solving a classical Riemann Problem for (2.12) with initial condition

$$\mathbf{Q}(x, t^n) = \begin{cases} \mathbf{Q}^-_{i+\frac{1}{2}} = \mathbf{Q}_i^n & \text{if } x < x_{i+\frac{1}{2}}, \\ \mathbf{Q}^+_{i+\frac{1}{2}} = \mathbf{Q}_{i+1}^n & \text{if } x > x_{i+\frac{1}{2}}. \end{cases} \tag{2.25}$$

We chose to solve this Riemann problem through the DOT scheme (Dumbser and Toro, 2011a), computing

$$D^{\pm}_{i+\frac{1}{2}} = \frac{1}{2}\int_0^1 \left[\mathbf{A}(\mathbf{\Psi}) \pm |\mathbf{A}(\mathbf{\Psi})|\right] \frac{\partial \mathbf{\Psi}}{\partial s} \mathrm{d}s, \tag{2.26}$$

with

$$|\mathbf{A}| = \mathbf{R}|\mathbf{\Lambda}|\mathbf{R}^{-1}, \quad |\mathbf{\Lambda}| = \mathrm{diag}(|\lambda_1|, \dots, |\lambda_{10+n}|), \tag{2.27}$$

with $\mathbf{R}$ matrix of right eigenvectors. Consistently with the approach proposed in Müller et al. (2013), when considering space-dependent geometrical parameters, we adopted the segment path for all variables except the cross-sectional area:

$$\mathbf{\Psi}(s) = \left[\underline{\zeta_e}(s)^{-1} \quad \underline{q} \quad \underline{\psi} \quad \underline{A_0} \quad \underline{h_0} \quad \underline{E_e} \quad \underline{E_c} \quad \underline{p_{ext}} \quad \underline{\epsilon_0} \quad \underline{\epsilon_r} \quad \underline{A\phi_1} \quad \dots \quad \underline{A\phi_n}\right]^T, \tag{2.28}$$

with $\underline{V}$ the segment path associated to variable V, i.e. $\underline{V} = V^- + s(V^+ - V^-)$. $\underline{\zeta_e}(s)$ is the segment path for the elastic component of ζ (equations (2.5), (2.4)). Note that $\zeta = \zeta_e$ if $K_m = 0$. Once $\underline{\zeta_e}(s)$ is known, the path $\tilde{A}(s)$ for the area is computed from it through a globally convergent Newton's method.

It can be easily verified for conservative systems that

$$D^-_{\phi_j, i+\frac{1}{2}} = f_{\phi_j, i+\frac{1}{2}} - f_{\phi_j}(\mathbf{Q}^-_{i+\frac{1}{2}}), \qquad D^+_{\phi_j, i-\frac{1}{2}} = f_{\phi_j}(\mathbf{Q}^+_{i-\frac{1}{2}}) - f_{\phi_j, i-\frac{1}{2}}, \tag{2.29}$$

where ϕ_j, $j = 1, \dots, n$ is the considered tracer, $f_{\phi_j}(\mathbf{Q}) = \frac{(A\phi_j)q}{A}$ denotes the physical flux associated to the transport problem and $f_{\phi_j, i\pm\frac{1}{2}}$ are the Osher interface numerical fluxes (Dumbser and Toro, 2011a).

Proof. We show here only the equivalence $D^-_{\phi_j, i+\frac{1}{2}} = f_{\phi_j, i+\frac{1}{2}} - f_{\phi_j}(\mathbf{Q}^-_{i+\frac{1}{2}})$, with

$$\begin{aligned} D^-_{\phi_j, i+\frac{1}{2}} &= \frac{1}{2}\int_0^1 [\mathbf{A}(\mathbf{\Psi})]_6 \frac{\partial \mathbf{\Psi}}{\partial s} \mathrm{d}s - \frac{1}{2}\int_0^1 [|\mathbf{A}(\mathbf{\Psi})|]_6 \frac{\partial \mathbf{\Psi}}{\partial s} \mathrm{d}s \\ f_{\phi_j, i+\frac{1}{2}} &= \frac{1}{2}(f_{\phi_j}(\mathbf{Q}^-_{i+\frac{1}{2}}) + f_{\phi_j}(\mathbf{Q}^+_{i+\frac{1}{2}})) - \frac{1}{2}\int_0^1 [|\mathbf{A}(\mathbf{\Psi})|]_6 \frac{\partial \mathbf{\Psi}}{\partial s} \mathrm{d}s. \end{aligned}$$

Here, $[\mathbf{A}(\mathbf{\Psi})]_6$ denotes the 6^{th} row of coefficient matrix $\mathbf{A}$, evaluated at the integration path $\mathbf{\Psi}$. Without loss of generality, we can consider the simplified problem

$$\partial_t \mathbf{Q} + \mathbf{A}(\mathbf{Q})\partial_x \mathbf{Q} = 0,$$

with

$$\mathbf{Q} = \begin{bmatrix} A(x,t) \\ q(x,t) \\ K(x) \\ A_0(x) \\ p_e(x) \\ A\phi_j(x,t) \end{bmatrix}, \qquad \mathbf{A}(\mathbf{Q}) = \begin{bmatrix} 0 & 1 & 0 & 0 & 0 & 0 \\ c^2 - u^2 & 2u & \frac{A}{\rho}\partial_K \zeta & \frac{A}{\rho}\partial_{A_0}\zeta & \frac{A}{\rho} & 0 \\ 0 & 0 & 0 & 0 & 0 & 0 \\ 0 & 0 & 0 & 0 & 0 & 0 \\ 0 & 0 & 0 & 0 & 0 & 0 \\ -u\phi_j & \phi_j & 0 & 0 & 0 & u \end{bmatrix}.$$

For this proof, we are only interested in the scalar product

$$[\mathbf{A}(\mathbf{\Psi}(s))]_6 \partial_s \mathbf{\Psi}(s) = \left[-\frac{\underline{q}\underline{A\phi_j}}{\tilde{A}^2} \quad \frac{\underline{A\phi_j}}{\tilde{A}} \quad 0 \quad 0 \quad 0 \quad \frac{\underline{q}}{\tilde{A}} \right] \partial_s \mathbf{\Psi}(s),$$

with $\mathbf{\Psi}(s)$ considered integration path (equation (2.28)).

We compute

$$D^-_{\phi_j, i+\frac{1}{2}} = \frac{1}{2} \int_0^1 \left[-\frac{\underline{(A\phi_j)}(\underline{q})}{\tilde{A}^2} \frac{\partial \tilde{A}}{\partial s} + \frac{\underline{A\phi_j}}{\tilde{A}} \frac{\partial \underline{q}}{\partial s} + \frac{\underline{q}}{\tilde{A}} \frac{\partial \underline{A\phi_j}}{\partial s} \right] \mathrm{d}s - \frac{1}{2} \int_0^1 [|\mathbf{A}(\mathbf{\Psi})|]_6 \frac{\partial \mathbf{\Psi}}{\partial s} \mathrm{d}s.$$

Defining

$$F(s) = \frac{\underline{(A\phi_j)}(\underline{q})}{\tilde{A}}$$

and differentiating it with respect to s, we obtain exactly the integrand function. Using the fundamental theorem of calculus we obtain

$$\begin{aligned} D^-_{\phi_j, i+\frac{1}{2}} &= \frac{1}{2}(F(1) - F(0)) - \frac{1}{2} \int_0^1 [|\mathbf{A}(\mathbf{\Psi})|]_6 \frac{\partial \mathbf{\Psi}}{\partial s} \mathrm{d}s \\ &= \frac{1}{2} \left(\frac{(A\phi_j)^+ q^+}{A^+} - \frac{(A\phi_j)^- q^-}{A^-} \right) - \frac{1}{2} \int_0^1 [|\mathbf{A}(\mathbf{\Psi})|]_6 \frac{\partial \mathbf{\Psi}}{\partial s} \mathrm{d}s \end{aligned}$$

for any choice of path.

This implies that

$$D^-_{\phi_j, i+\frac{1}{2}} + f_{\phi_j}(\mathbf{Q}^-_{i+\frac{1}{2}}) = \frac{f_{\phi_j}(\mathbf{Q}^+_{i+\frac{1}{2}}) + f_{\phi_j}(\mathbf{Q}^-_{i+\frac{1}{2}})}{2} - \frac{1}{2} \int_0^1 [|\mathbf{A}(\mathbf{\Psi})|]_6 \frac{\partial \mathbf{\Psi}}{\partial s} \mathrm{d}s.$$

□

Despite this theoretical result, in practice (2.29) depends on the numerical evaluation of

$$D^\pm_{\phi_j, i\mp\frac{1}{2}} = \frac{1}{2} \int_0^1 \left(\mathbf{A}(\mathbf{\Psi}) \pm |\mathbf{A}(\mathbf{\Psi})| \right) \frac{\partial \mathbf{\Psi}}{\partial s} \mathrm{d}s. \tag{2.30}$$

The choice of path (2.28) may render the integrand highly non-linear and poorly approximated by low-degree polynomials. As a consequence, as we will show in chapter 3.1.1, low-order Gaussian quadrature rules can lead to inaccurate approximations of the integral.

Conservative approach

Our choice to consider the conservative formulation of the transport equation reported in equation 2.24 in order to guarantee tracer mass conservation at discrete level allows us to adopt a conservative numerical scheme for solving the transport equation. This scheme relies on the cell-averages of haemodynamic quantities obtained through the path-conservative approach. Here, considering the standard formulation

$$\partial_t \mathbf{Q} + \partial_x \mathbf{f}(\mathbf{Q}) = 0 \tag{2.31}$$

of the conservative problem, $\mathbf{Q} = [A\phi_1, \dots, A\phi_n]^T$ and $\mathbf{f}(\mathbf{Q}) = [\frac{q \cdot A\phi_1}{A}, \dots, \frac{q \cdot A\phi_n}{A}]^T$.

Expression (2.24) can be discretized in the control volume $V_i^n = [x_{i-\frac{1}{2}}, x_{i+\frac{1}{2}}] \times [t^n, t^{n+1}]$ as

$$\mathbf{Q}_i^{n+1} = \mathbf{Q}_i^n - \frac{\Delta t}{\Delta x}(\mathbf{f}_{i+\frac{1}{2}} - \mathbf{f}_{i-\frac{1}{2}}), \tag{2.32}$$

where $\mathbf{Q}_i^n$ is the cell average at time t^n and $\mathbf{f}_{i+\frac{1}{2}}$ is a numerical flux function across interface $x_{i+\frac{1}{2}}$. Several choices of numerical flux functions are available in the literature. Here, we consider the Osher Riemann solver (Dumbser and Toro, 2011b), in which case the numerical flux can be written as

$$\mathbf{f}_{i+\frac{1}{2}} = \frac{1}{2}(\mathbf{f}(\mathbf{Q}^-_{i+\frac{1}{2}}) + \mathbf{f}(\mathbf{Q}^+_{i+\frac{1}{2}})) - \frac{1}{2}\int_0^1 [|\mathbf{A}(\mathbf{\Psi}(\mathbf{Q}^-_{i+\frac{1}{2}}, \mathbf{Q}^+_{i+\frac{1}{2}}, s))|]_{11,\dots,11+n} \frac{\partial \mathbf{\Psi}}{\partial s} \mathrm{d}s, \tag{2.33}$$

where rows $11, \dots, 11+n$ in the coefficient matrix $\mathbf{A}$ are those associated with the transport problem. Here, consistently with the non-conservative approach adopted for the haemodynamic part of the problem, we adopt the segment path for all variables except for the cross-sectional area.

2.2.2.1.2 Second order numerical scheme

The construction of a high-order numerical scheme requires, at each time step, three substeps:

- Piecewise polynomial spatial reconstruction;
- Local space-time prediction;
- Fully explicit data evolution.

In the following, we provide details regarding the spatial reconstruction and local space-time prediction. Data evolution for the transport equations, similarly to the first-order approach, can be performed either through a path-conservative or a conservative approach.

Reconstruction

We perform spatial reconstruction employing the WENO methodology (Liu et al., 1994). At each time level t^n, we reconstruct piecewise polynomials of the type

$$\mathbf{w}_h(x, t^n) = \sum_{i=1}^{M+1} \theta_l \widehat{\mathbf{w}_l}, \tag{2.34}$$

where M is the polynomial degree, θ_l are the corresponding basis functions and $\widehat{\mathbf{w}_l}$ the expansion coefficients. As in Müller et al. (2013), the WENO reconstruction operator is modified to preserve the well-balanced character of the numerical scheme, since the stationary solutions of system (2.12) may not be polynomials. In particular, we employed a spatial reconstruction algorithm whose output, in the presence of a stationary solution, is a polynomial that is equal to the stationary solution at cell interfaces. This is achieved by performing spatial reconstruction on deviations around a hypothetical stationary solution.

Local space-time predictor: Dumbser–Enaux–Toro solver

Once the spatial reconstruction is available, the Generalized Riemann Problem (GRP) for system (2.12) with initial condition

$$\mathbf{Q}(x, t^n) = \begin{cases} \mathbf{w}_{i-1}^n(x), & \text{if } x < x_{i-\frac{1}{2}}, \\ \mathbf{w}_i^n(x), & \text{if } x > x_{i-\frac{1}{2}}, \end{cases} \tag{2.35}$$

is solved at the interface $x = x_{i+\frac{1}{2}}$ in order to obtain a time-dependent solution at the interface, which is then used to compute numerical fluctuations.

Due to the absence of in-cell discontinuities in vessel properties, we consider for the transport equations the equivalent non-conservative formulation

$$\partial_t \phi_i + u(x) \partial_x \phi_i = 0, \ i = 0, \dots, n. \tag{2.36}$$

Consistently with the approach adopted for the haemodynamic part of the coupled system (Müller et al., 2016), to compute the local space-time polynomial $\phi_{i,h} = \phi_{i,h}(x, t)$, we consider a local framework defined by transforming the computational element V^n into the reference element $T_E = [0, 1] \times [0, 1]$, with reference coordinates ξ and τ, defined so that $t = t^n + \tau \Delta t^n$ and $x = x_{i-\frac{1}{2}} + \xi \Delta x$, thus obtaining for $i = 0, \dots, n$

$$\partial_\tau \phi_{i,h} + u^* \partial_\xi \phi_{i,h} = 0, \tag{2.37}$$

with $u^* = \frac{\Delta t}{\Delta x} u_{i,h}$ obtained from the space-time prediction step performed for the blood flow equations.

Multiplying equation (2.36) by a space-time basis function $\theta = \theta(\xi, \tau)$, integrating over the reference element T_E, and using integration by parts for the time derivative term we obtain

$$\int_0^1 \phi_{i,h}\theta \mathrm{d}\xi - \int_0^1 \int_0^1 \phi_{i,h}\partial_\tau\theta \mathrm{d}\xi\mathrm{d}\tau + \int_0^1 \int_0^1 u^*(\xi,\tau)\partial_\xi\phi_{i,h}\theta \mathrm{d}\xi\mathrm{d}\tau = 0. \tag{2.38}$$

Defining the following operators

$$[f,g]^\tau = \int_0^1 f(\xi,\tau)g(\xi,\tau)d\xi, \quad \langle f,g\rangle_{V_h} = \int_0^1\int_0^1 f(\xi,\tau)g(\xi,\tau)d\xi d\tau.$$

we can rewrite equation (2.2.2.1.2) as

$$[\phi_i,\theta]^1 - [\bar{\phi_{i,h}},\theta]^0 - \langle\phi_{i,h},\partial_\tau\theta\rangle_{T_E} + \langle\theta,u^*\partial_\xi\phi_{i,h}\rangle_{T_E} = 0, \tag{2.39}$$

where $\bar{\phi_{i,h}}$ are obtained through the reconstruction procedure.

Analogously to the approach adopted for the haemodynamic portion of the problem, we use the same space-time basis functions θ for $\phi_{i,h}$ and $u^*\partial_\xi\phi_{i,h}$, so that

$$\phi_{i,h}(\xi,\tau) = \sum_{l=1}^{(M+1)^2} \theta_l\widehat{\phi_{i,l}}, \qquad u^*(\xi,\tau)\partial_\xi\phi_{i,h}(\xi,\tau) = \sum_{l=1}^{(M+1)^2} \theta_l\widehat{u^*(\xi,\tau)\partial_\xi}\phi_{i,l}, \tag{2.40}$$

where

$$\langle\theta_k,\theta_l\rangle\widehat{\partial_\xi\phi_{i,l}} = \langle\theta_k,\partial_\xi\theta_l\rangle\widehat{\phi_{i,l}}, \qquad \widehat{u^*\partial_\xi\phi_{i,l}} = \widehat{u_l^*}\widehat{\partial_\xi\phi_{i,l}} = \langle\theta_k,\theta_l\rangle\widehat{u_l^*}\langle\theta_k,\theta_l\rangle^{-1}\langle\theta_k,\partial_\xi\theta_l\rangle\widehat{\phi_{i,l}},$$

with u_l^* obtained by solving the haemodynamic problem. To obtain expansion coefficients $\widehat{\phi_l}$ we need to solve the linear system

$$([\theta_k,\theta_l]^1 - \langle\partial_t\theta_k,\theta_l\rangle_{T_E})\widehat{\phi_{i,l}}^{m+1} = [\theta,\bar{\phi_{i,h}}]^0 - \langle\theta_k,\theta_l\rangle\widehat{u_l^*}^m\langle\theta_k,\theta_l\rangle^{-1}\langle\theta_k,\partial_\xi\theta_l\rangle\widehat{\phi_{i,l}}^m. \tag{2.41}$$

2.2.2.2 Boundary conditions

We couple 1D vessels with each other and with 0D lumped parameter models using a Riemann-problem approach: at each coupling point we define a Riemann problem and solve it through an approximate Riemann solver. The Riemann problem reads

$$\begin{cases} \partial_t\mathbf{Q}^k + \mathbf{A}(\mathbf{Q}^k)\partial_x\mathbf{Q}^k = 0, \ x\in\mathbb{R}, \quad t>0 \\ \mathbf{Q}^k(x,t^n) = \mathbf{Q}_{1D}^k, \quad k = 1,\dots,N_P \end{cases} \tag{2.42}$$

with N_P number of vessels involved in the coupling. The self-similar solution consists of the N_P initial states $\mathbf{Q}_{1D}^k$ provided by the 1D vessels involved in the coupling, together with N_P intermediate states $\mathbf{Q}_k^*$. Intermediate states are connected to the initial states through nonlinear waves and to each other through the linearly degenerate stationary contact discontinuity. The wave relations linking these states in phase space are expressed through the generalized Riemann invariants (2.13), (2.14), (2.15). The Riemann problem is solved through an approximate Riemann solver that only admits the formation of rarefactions (Müller et al., 2016b).

2.2.2.2.1 Fluctuations and numerical fluxes at boundary interfaces

Once the intermediate states $\mathbf{Q}_k^*$ are available, they are used to compute numerical fluctuations in the path-conservative approach and numerical fluxes in the conservative one.

Numerical fluctuations

In order to guarantee mass conservation at coupling sites, we chose to adopt the Godunov method by defining

$$\mathbf{D}_G^-(\mathbf{Q}^-, \mathbf{Q}^+) = \int_0^1 \mathbf{A}(\mathbf{\Psi}(\mathbf{Q}^-, \mathbf{Q}_*, s))\frac{\partial \mathbf{\Psi}}{\partial s}\mathrm{d}s, \tag{2.43}$$

$$\mathbf{D}_G^+(\mathbf{Q}^-, \mathbf{Q}^+) = \int_0^1 \mathbf{A}(\mathbf{\Psi}(\mathbf{Q}_*, \mathbf{Q}^+, s))\frac{\partial \mathbf{\Psi}}{\partial s}\mathrm{d}s, \tag{2.44}$$

$$\tag{2.45}$$

where $\mathbf{Q}_*$ are the states obtained by solving the aforementioned Riemann problem (Parés and Muñoz Ruíz, 2009).

Recalling the Riemann invariants for the problem, the following properties hold:

- Across the characteristic fields associated with eigenvalues $\lambda_1 = u - c_T$ and $\lambda_{11} = u + c_T$, ϕ and the space-dependent geometrical vascular properties are constant.
- Across the stationary contact discontinuity associated with $\lambda_2 = \lambda_3 = \cdots = \lambda_9 = 0$, ϕ, q and total pressure are constant, while geometrical parameters are discontinuous.
- Across the discontinuity associated with $\lambda_{10} = u \neq 0$, all geometrical parameters, q and A are constant, while ϕ is not.
- Across the discontinuity associated with $\lambda_{10} = u = 0$, q and total pressure are constant, while geometrical parameters, A and ϕ not.

Consequently, the choice of this type of numerical fluctuations is convenient for space-dependent geometrical vascular properties, as we connect states across waves that are defined in regions where vascular properties are constant. Consequently, the resulting problem is conservative and the method is well balanced even if we choose $\mathbf{\Psi}$ as the segment path for all considered variables. Moreover, the only discontinuity for ϕ is the contact discontinuity associated with $\lambda_{10} = u$. Consequently, given that the transport equation does not influence the solution of the mass and momentum conservation equations, assuming that the Godunov state A_* for the area has already been computed:

$$\text{if } q > 0 : A_*\phi_* = A_*\phi^-, \qquad \text{if } q < 0 : A_*\phi_* = A_*\phi^+, \qquad \text{if } q = 0 : A_*\phi_* = A_*\phi^-. \tag{2.46}$$

Numerical fluxes

Consistently with the path-conservative approach, if transport is treated through a conservative approach we employ Godunov's method, where the intercell numerical fluxes are computed by using the solutions $\mathbf{Q}_*$ of the local Riemann problems as

$$\mathbf{f}_{i+\frac{1}{2}}^{\mathrm{GOD}} = \mathbf{f}(\mathbf{Q}_*(x_{i+\frac{1}{2}})), \tag{2.47}$$

with $\mathbf{f}(\mathbf{Q})$ physical flux evaluated in state $\mathbf{Q}$.

2.2.2.2.2 Treatment of junctions

In the following, we summarize relations at junctions for the haemodynamic and transport problems.

Haemodynamic problem

The unknown state vectors $\mathbf{Q}_k^*$, with $k = 1, \ldots, N_P$, are obtained by imposing generalized Riemann invariant constancy between $\mathbf{Q}_{1D}^k$ and $\mathbf{Q}_k^*$, and among the $\mathbf{Q}_k^*$ vectors themselves, thereby solving the following system of equations

$$\sum_{k=1}^{N_P} \alpha_P^k q_k^* = 0, \tag{2.48}$$

$$\left(p(A_*^1, \psi_*^1) + \frac{1}{2}\rho\left(\frac{q_*^1}{A_*^1}\right)^2\right) - \left(p(A_*^k, \psi_*^k) + \frac{1}{2}\rho\left(\frac{q_*^k}{A_*^k}\right)^2\right) = 0,\ k = 2, \ldots, N_P, \tag{2.49}$$

$$\frac{q_*^k}{A_*^k} - \frac{q_{1D}^k}{A_{1D}^k} + \alpha_P^k \int_{A_{1D}^k}^{A_*^k} \frac{\tilde{c}_T(\xi)}{\xi} \mathrm{d}\xi = 0,\ k = 1, \ldots, N_P, \tag{2.50}$$

$$\psi_*^k + \frac{A_*^k}{T^k} - \psi_{1D}^k - \frac{A_{1D}^k}{T^k} = 0,\ k = 1, \ldots, N_P, \tag{2.51}$$

with

$$\alpha_P^k = \begin{cases} +1 & \text{if vessel } k \text{ shares its outlet with the junction,} \\ -1 & \text{if vessel } k \text{ shares its inlet with the junction.} \end{cases} \tag{2.52}$$

In the case of second order schemes, in order to employ the WENO reconstruction, we need to define reasonable state variable values at M ghost cells at each side of the 1D domain, with M polynomial degree of the spatial reconstruction. The approach employed to this end is illustrated in Müller et al. (2016), and is based on the definition of a Taylor series expansion around the internal vertex P, shared by the 1D vessel. The spatial derivatives that are needed to compute the Taylor series are computed from a linearized version of the original PDE system.

TRANSPORT PROBLEM

Junctions are modelled as lying along the stationary contact discontinuity (i.e., the characteristic field with zero eigenvalues). The tracer concentration assigned to each vessel whose inlet coincides with a junction j is computed by considering the incoming blood flows to be perfectly mixed before they are redistributed into the outgoing branches.

FIRST ORDER SCHEME Let q_k be the signed flow rate in vessel k, and let $\phi_{i,k}$ be the concentration of tracer ϕ_i in vessel k. Define the set of inflow vessels at junction j as

$$\mathcal{I}_j = \{k : \text{ vessel } k \text{ shares its outlet with the junction and } \frac{q_k}{A_k} > 0\} \cup \tag{2.53}$$

$$\{k : \text{ vessel } k \text{ shares its inlet with the junction and } \frac{q_k}{A_k} < 0\}. \tag{2.54}$$

For each inflow vessel $k \in \mathcal{I}_j$, introduce an orientation factor

$$\sigma_k = \begin{cases} +1 & \text{if vessel } k \text{ shares its outlet with the junction and } \frac{q_k}{A_k} > 0 \\ -1 & \text{if vessel } k \text{ shares its inlet with the junction and } \frac{q_k}{A_k} < 0. \end{cases} \tag{2.55}$$

Then the mass flux of tracer ϕ_i entering junction j is

$$\dot{M}_{\phi_i,j,In} = \sum_{k \in \mathcal{I}_j} \sigma_k q_k \phi_{i,k}. \tag{2.56}$$

Define then the set of outflow vessels at junction j as

$$\mathcal{O}_j = \{k : \text{ vessel } k \text{ shares its outlet with the junction and } \frac{q_k}{A_k} < 0\} \cup \tag{2.57}$$

$$\{k : \text{ vessel } k \text{ shares its inlet with the junction and } \frac{q_k}{A_k} > 0\}. \tag{2.58}$$

Using the orientation factor

$$\gamma_k = \begin{cases} +1 & \text{if vessel } k \text{ shares its outlet with the junction and } \frac{q_k}{A_k} < 0 \\ -1 & \text{if vessel } k \text{ shares its inlet with the junction and } \frac{q_k}{A_k} > 0, \end{cases} \tag{2.59}$$

the total outgoing flow is

$$Q_{j,Out} = \sum_{k \in \mathcal{O}_j} \gamma_k q_k. \tag{2.60}$$

Under these assumptions, $Q_{j,Out} \leq 0$.

Tracer mass conservation at the junction implies that

$$\dot{M}_{\phi_i,j,In} + \sum_{k \in \mathcal{O}_j} \gamma_k q_k \phi_{i,k} = 0. \tag{2.61}$$

Due to uniform mixing, $\phi_{i,j}$ is independent of the considered k. Consequently, recalling (2.60), the common concentration assigned to all outgoing vessels for tracer ϕ_i is

$$\phi_{i,j} = -\frac{\dot{M}_{\phi_i,j,In}}{Q_{j,Out}} \tag{2.62}$$

whenever $Q_{j,Out} \neq 0$.

Note that the unknown transport variable $(A\phi_i)^k_*$ required for the coupling is simply obtained by multiplying the concentration value $\phi_{i,j}$ returned by this procedure to the vessel cross-sectional area A_k.

Second order scheme Following the same approach as in Müller et al. (2016), we compute state variable values in M ghost cells at each side of the 1D domain by using a Taylor series expansion of the solution. Spatial gradients $\partial_x(A\phi)$ required for the expansion are computed by solving a Riemann problem at the junction for a linearized version of the original PDE system

$$\begin{cases} \partial_t(\partial_x \mathbf{Q}^k) + \bar{\mathbf{A}}^k \partial_x(\partial_x \mathbf{Q}^k) = 0, \quad x \in \mathbb{R}, \quad t > 0 \\ \partial_x \mathbf{Q}^k = \partial_x \mathbf{Q}^k_{1D}, \quad k = 1, \dots, N_P, \end{cases} \tag{2.63}$$

with N_P number of vessels involved in the coupling and $\bar{\mathbf{A}}^k = \mathbf{A}(\mathbf{Q}^k_*)$ linearized coefficient matrix of the system evaluated at the solution of Riemann problem (2.42). This corresponds, for the tracer equations, to the enforcement of mass gradients conservation at junctions, under the assumption of a uniform distribution of concentration gradients among vessels sharing their inlet with the junction. For details regarding this procedure, we refer to Müller et al. (2016).

Recalling the definition of the set of inflow vessels at junction j (2.53) and of the orientation factor σ_k (2.55), we define the incoming mass gradient contribution as

$$G_{\phi_i,j,In} = \sum_{k \in \mathcal{I}_j} \left[\sigma_k \phi_{i,k} \partial_x q_k + \sigma_k \frac{q_k}{A_k} (\partial_x (A_k \phi_{i,k}) - \phi_{i,k} \partial_x A_k) \right]. \tag{2.64}$$

For outgoing vessels $k \in \mathcal{O}_j$ (2.57), we impose a uniform concentration gradient, meaning

$$\partial_x \phi_{i,k} = \partial_x \phi_{i,j} \quad \forall k \in \mathcal{O}_j. \tag{2.65}$$

The outgoing mass gradient contribution is therefore

$$G_{\phi_i,j,Out} = \sum_{k \in \mathcal{O}_j} \left[\gamma_k \phi_{i,k} \partial_x q_k + \gamma_k q_k \partial_x \phi_{i,j} \right]. \tag{2.66}$$

Since $\partial_x \phi_{i,j}$ is independent of the considered k,

$$G_{\phi_i,j,Out} = \sum_{k \in \mathcal{O}_j} \gamma_k \phi_{i,k} \partial_x q_k + \partial_x \phi_{i,j} \sum_{k \in \mathcal{O}_j} \gamma_k q_k. \tag{2.67}$$

Using the definition of the total outgoing flow (2.60), this reads

$$G_{\phi_i,j,Out} = Q_{j,Out}\partial_x\phi_{i,j} + \sum_{k\in\mathcal{O}_j} \gamma_k\phi_{i,k}\partial_x q_k, \tag{2.68}$$

with $Q_{j,Out} \leq 0$.

Following the approach illustrated by Müller et al. (2016) for the haemodynamic portion of the problem, by enforcing conservation of mass gradients

$$G_{\phi_i,j,In} + G_{\phi_i,j,Out} = 0 \tag{2.69}$$

we obtain

$$\partial_x\phi_{i,j} = -\frac{\sum_{k\in\mathcal{O}_j} \gamma_k\phi_{i,k}\partial_x q_k + G_{\phi_i,j,In}}{Q_{j,Out}}. \tag{2.70}$$

Finally, the gradient of transported mass assigned to all outgoing vessels is

$$\partial_x(A_k\phi_{i,j}) = A_k\partial_x\phi_{i,j} + \phi_{i,j}\partial_x A_k. \tag{2.71}$$

2.2.3 Well-balanced high-order method for non-conservative hyperbolic PDEs with source terms

This section is adapted from: Colombo, C., Dalmaso, C., Müller, L. O., Siviglia, A. (2026). Well-balanced high-order method for non-conservative hyperbolic PDEs with source terms: application to one-dimensional blood flow equations with gravity. Journal of Computational Physics, 114975.

Several physical phenomena can be modeled through non-conservative hyperbolic PDEs with source terms (Siviglia et al., 2022; Fernández et al., 2022; Gaburro et al., 2018; Bermudez et al., 2016; Müller and Toro, 2013; Toro and Siviglia, 2013a). The solution of such equations in the presence of discontinuities (shock waves) poses several challenges, as the conservative form of the equations no longer holds. One of the main issues is the definition of jump relations across a discontinuity, which has been addressed by Dal Maso et al. (1995) interpreting the jump relations as Borel measures dependent on the path connecting the two sides of the discontinuity.

A second issue is the description of steady-state solutions in the presence of geometric- and/or algebraic-type source terms, which can be discontinuous (Murillo et al., 2019). Such solutions should be accurately captured by the numerical methods used to solve the considered PDEs. Moreover, they should be recovered after small perturbations in the initial data, in order to avoid spurious oscillations that might cause significant deviations from the exact solution (Castro Díaz et al., 2007; Guerrero Fernández et al., 2022).

Numerous methods are available for the solution of blood flow equations (BFEs), tailored to the preservation of some or all stationary solutions of the system (well-balanced and fully well-balanced methods, respectively). Many of these methods were devised to treat space-varying geometrical and physical properties of the vasculature, friction and gravity (Müller and Toro, 2013; Delestre and Lagrée, 2013; Murillo and Garcia-Navarro, 2015; Li et al., 2018; Ghitti et al., 2020; Britton and Xing, 2020; Spilimbergo et al., 2021; Murillo and Garcia-Navarro, 2023).

Recently, Castro and Parés (2020) and Guerrero Fernández et al. (2022) proposed a generic strategy for the development of well-balanced high-order methods in the finite volume and discontinuous Galerkin frameworks, testing them on hyperbolic PDEs with continuous and discontinuous source terms. One of the main obstacles to the development of well-balanced methods is the construction of a well-balanced reconstruction operator (Castro and Parés, 2020), since standard reconstruction operators such as ENO, WENO and MUSCL (Harten, 1989; Liu et al., 1994; Van Leer, 1979) are not usually well-balanced. Indeed, these methods are based on standard interpolation techniques, and there is no guarantee that stationary solutions of the considered PDEs belong to the same class of reconstruction functions. A strategy to modify standard reconstruction operators so that they are well-balanced for all stationary solutions of the considered PDEs has been proposed by Castro et al. (2008). However, this approach requires the solution of a nonlinear system of equations, which might have multiple or no solutions, and might be computationally expensive (Castro and Parés, 2020).

In the following, we present a numerical method that combines the novel centered reconstruction technique by Montecinos et al. (2025) with the well-balancing approach by Castro and Parés (2020) and Guerrero Fernández et al. (2022). The method is developed within the path-conservative framework, using the high-order solver of Müller et al. (2016a) and the well-balancing strategy of Guerrero Fernández et al. (2022), which relies on the knowledge of families of stationary solutions. The reconstruction technique (Montecinos et al., 2025) requires, at each time step and in every computational cell, the cell average of the solution at the current time level and the solution of a generalized Riemann problem (GRP) at the cell interfaces from the previous time level, evolved at time $t^{n-1} + dt^{n-1}$. Provided that the GRP solver being used is well balanced, this minimal data dependence guarantees the well-balancing of the reconstruction technique by construction up to the third order, while also making the technique highly efficient and easy to implement.

Numerical results are reported in Section 3.2, where we show that the resulting numerical method is well-balanced up to order three, testing it on both a scalar problem represented by the Burgers' equation, and a PDE system given by the hyperbolized one-dimensional BFEs presented in (Montecinos et al., 2014), including variable geometrical and mechanical vessel properties, friction and a spatially variable C^0 gravity term.

We consider the following general system

$$\begin{cases} \partial_t \mathbf{Q} + \mathbf{A}(\mathbf{Q})\partial_x \mathbf{Q} = \mathbf{S}(\mathbf{Q}), \quad x \in \Omega, \quad t \in \mathcal{T}, \\ \mathbf{Q}(x,0) = \mathbf{Q}_0(x), \end{cases} \tag{2.72}$$

where $t \in \mathcal{T}$ and $x \in \Omega$ are time and space independent variables, with $\Omega = [x_A, x_B] \subset \mathbb{R}$ a one-dimensional spatial domain and $\mathcal{T} = [0, t^K] \subset \mathbb{R}_0^+$ a temporal domain. $\mathbf{Q}(x,t) \in \mathcal{B}_Q$ is the state vector, with $\mathcal{B}_Q \subset \mathbb{R}^v$ the space of the admissible states, $\mathbf{Q}_0(x) \in \mathcal{B}_Q$ is the initial condition, $\mathbf{S}(\mathbf{Q}(x,t)) \in \mathbb{R}^v$ is the source vector, and $\mathbf{A}(\mathbf{Q}(x,t)) \in \mathbb{R}^{v \times v}$ is the system matrix with real and distinct eigenvalues. If $\mathbf{A}(\mathbf{Q})$ is the Jacobian of the system, then the previous equation reduces to a classical balance law.

Our goal is to construct a numerical scheme that preserves stationary solutions in the framework of path-conservative numerical methods. We begin by identifying the stationary solutions of problem (2.72) as described below. Let $\mathbf{Q}^*(x) \in \mathcal{B}_Q$, $\forall x \in \Omega$, be the stationary solution of problem (2.72), then it holds

$$\mathbf{A}(\mathbf{Q}^*)\partial_x \mathbf{Q}^* = \mathbf{S}(\mathbf{Q}^*). \tag{2.73}$$

Subtracting eq. (2.73) from eq. (2.72) (Guerrero Fernández et al., 2022), we obtain an equivalent problem given by

$$\begin{cases} \partial_t \mathbf{Q} + \mathbf{A}(\mathbf{Q})\partial_x \mathbf{Q} - \mathbf{A}(\mathbf{Q}^*)\partial_x \mathbf{Q}^* = \mathbf{S}(\mathbf{Q}) - \mathbf{S}(\mathbf{Q}^*), \quad x \in \Omega, \quad t \in \mathcal{T}, \\ \mathbf{Q}(x,0) = \mathbf{Q}_0(x). \end{cases} \tag{2.74}$$

Then, we discretize the spatial domain Ω into N computational cells $S_i = [x_{i-\frac{1}{2}}, x_{i+\frac{1}{2}}]$, with $i = 1, \ldots, N$, and the temporal domain $\mathcal{T}$ into K computational cells $T^n = [t^n, t^{n+1}]$ with $n = 0, \ldots, K-1$. Integrating eq. (2.74) in space and time over the control volume $V_i^n = S_i \times T^n$, we obtain the following numerical scheme

$$\mathbf{Q}_i^{n+1} = \mathbf{Q}_i^n - \frac{1}{\Delta x}(\mathbf{B}_i - \mathbf{B}_i^*) - \frac{\Delta t^n}{\Delta x}(\mathbf{D}^-_{i+\frac{1}{2}} + \mathbf{D}^+_{i-\frac{1}{2}}) + \Delta t^n(\mathbf{S}_i - \mathbf{S}_i^*), \tag{2.75}$$

where

$$\mathbf{Q}_i^n \approx \frac{1}{\Delta x}\int_{x_{i-\frac{1}{2}}}^{x_{i+\frac{1}{2}}} \mathbf{Q}(x, t^n)dx, \tag{2.76}$$

$$\mathbf{B}_i \approx \int_{t^n}^{t^{n+1}} \int_{x_{i-\frac{1}{2}}}^{x_{i+\frac{1}{2}}} \mathbf{A}(\mathbf{Q})\partial_x \mathbf{Q} dxdt, \quad \mathbf{B}_i^* \approx \int_{t^n}^{t^{n+1}} \int_{x_{i-\frac{1}{2}}}^{x_{i+\frac{1}{2}}} \mathbf{A}(\mathbf{Q}^*)\partial_x \mathbf{Q}^* dxdt, \tag{2.77}$$

$$\mathbf{S}_i \approx \frac{1}{\Delta x \Delta t^n}\int_{t^n}^{t^{n+1}} \int_{x_{i-\frac{1}{2}}}^{x_{i+\frac{1}{2}}} \mathbf{S}(\mathbf{Q})dxdt, \quad \mathbf{S}_i^* \approx \frac{1}{\Delta x \Delta t^n}\int_{t^n}^{t^{n+1}} \int_{x_{i-\frac{1}{2}}}^{x_{i+\frac{1}{2}}} \mathbf{S}(\mathbf{Q}^*)dxdt, \tag{2.78}$$

and

$$\mathbf{D}^{\pm}_{i+\frac{1}{2}} \approx \frac{1}{\Delta t^n}\int_{t^n}^{t^{n+1}} D^{\pm}_{i+\frac{1}{2}}\left(\mathbf{Q}^{-}_{i+\frac{1}{2}}(t),\mathbf{Q}^{+}_{i+\frac{1}{2}}(t),\mathbf{\Psi}\left(\mathbf{Q}^{-}_{i+\frac{1}{2}}(t),\mathbf{Q}^{+}_{i+\frac{1}{2}}(t),s\right)\right)dt. \tag{2.79}$$

$\Delta x = x_{i+\frac{1}{2}} - x_{i-\frac{1}{2}}$ is the mesh spacing, and $\Delta t^n = t^{n+1} - t^n$ is the n-th time step. $\mathbf{Q}^n_i$ denotes the i-th cell average at time t^n, $\mathbf{B}_i$ and $\mathbf{B}^*_i$ are the non-conservative products of the i-th cell, $\mathbf{S}_i$ and $\mathbf{S}^*_i$ are the numerical source terms of the i-th cell, while $\mathbf{D}^{\pm}_{i+\frac{1}{2}}$ are the numerical fluctuations across the interface $x_{i+\frac{1}{2}}$. $D^{\pm}_{i+\frac{1}{2}}(\mathbf{Q}^{-}_{i+\frac{1}{2}},\mathbf{Q}^{+}_{i+\frac{1}{2}},\mathbf{\Psi})$ are the jump terms on the cells boundaries, also called fluctuations, that arise from the solution of a Riemann problem (RP) at the cell interface $x_{i+\frac{1}{2}}$. They depend on the left and right states at the cell interface $\mathbf{Q}^{\pm}_{i+\frac{1}{2}}(t)$, and on the integration path $\mathbf{\Psi}(\mathbf{Q}^{-}_{i+\frac{1}{2}},\mathbf{Q}^{+}_{i+\frac{1}{2}},s)$. Here, we compute them as described in (Müller and Toro, 2013). The integration path $\mathbf{\Psi}$ is a parametric arc in the parameter $s \in [0,1]$ that is used to connect the left and right states $\mathbf{Q}^{\pm}_{i+\frac{1}{2}}(t)$. Multiple path choices are possible. Theoretical details on the choice of paths are given in (Parés, 2006). Here, we adopt the segment path for the Burgers' equation, and a modification of it for the BFEs (Müller and Toro, 2013). The left and right states $\mathbf{Q}^{\pm}_{i+\frac{1}{2}}(t)$ are space-time reconstructed data that are extrapolated to both sides of the cell interface $x_{i+\frac{1}{2}}$. These space-time reconstructed data are space-time predictions of the sought solution $\mathbf{Q}(x,t)$, computed with a local implicit discontinuous Galerkin scheme. Here, we adopt a modified version of the Dumbser-Enoux-Toro GRP solver (Dumbser et al., 2008) that uses spatial reconstruction polynomials as initial data. These polynomials are computed through a reconstruction procedure that exploits GRP-based predictions from the previous time step to construct the reconstructions at the current step. Together, the GRP solver and the spatial reconstruction technique, described in detail below, provide the quantities required for evaluating the integrals in (2.75), thereby yielding a high-order numerical scheme in both space and time.

In order to have a fully explicit evolution of the data $\mathbf{Q}^{n+1}_i$ at each time step, we have to approximate integrals appearing in eq. (2.75) with the desired order of accuracy. The numerical fluctuations $\mathbf{D}^{\pm}_{i+\frac{1}{2}}$ (2.79) are computed as follows. For each quadrature node $t^n + \tau\Delta t^n$, with $\tau \in [0,1]$, employed in the time integration, we solve a classical RP for system (2.74) with initial condition given by the boundary states $\mathbf{Q}^{\pm}_{i+\frac{1}{2}}(t)$ evaluated at the $i+\frac{1}{2}$ interface and at each time quadrature node $t^n + \tau\Delta t^n$, (see section 2.2.3.3 for the computation of $\mathbf{Q}^{\pm}_{i+\frac{1}{2}}(t)$), namely

$$\mathbf{Q}(x, t^n + \tau\Delta t^n) = \begin{cases} \mathbf{Q}^{-}_{i+\frac{1}{2}}(t^n + \tau\Delta t^n) & \text{if } x < x_{i+\frac{1}{2}}, \\ \mathbf{Q}^{+}_{i+\frac{1}{2}}(t^n + \tau\Delta t^n) & \text{if } x > x_{i+\frac{1}{2}}. \end{cases} \tag{2.80}$$

In particular, the classical RP (2.74)-(2.80) is solved approximately by computing jump

terms $D^{\pm}_{i+\frac{1}{2}}$ as described in (Müller and Toro, 2013), namely

$$D^{\pm}_{i+\frac{1}{2}} \approx \frac{1}{2}\int_0^1 \left[\mathbf{A}\Big(\mathbf{\Psi}(\mathbf{Q}^-_{i+\frac{1}{2}}, \mathbf{Q}^+_{i+\frac{1}{2}}, s)\Big) \pm \left|\mathbf{A}\Big(\mathbf{\Psi}(\mathbf{Q}^-_{i+\frac{1}{2}}, \mathbf{Q}^+_{i+\frac{1}{2}}, s)\Big)\right|\right] \frac{\partial \mathbf{\Psi}}{\partial s} ds, \tag{2.81}$$

where $\Psi(\mathbf{Q}^-_{i+\frac{1}{2}}, \mathbf{Q}^+_{i+\frac{1}{2}}, s)$ is the integration path, and where the absolute value operator of a matrix is defined as

$$|\mathbf{A}| = \mathbf{R}|\mathbf{\Lambda}|\mathbf{R}^{-1}, \quad |\mathbf{\Lambda}| = diag(|\lambda_1|, \ldots, |\lambda_v|), \tag{2.82}$$

with $\lambda_i, i = 1, \ldots, v$ eigenvalues of matrix $\mathbf{A}$, $\mathbf{R}$ the matrix of right eigenvectors of $\mathbf{A}$ and $\mathbf{R}^{-1}$ its inverse. The integral in phase space in (2.81) and the time integral in (2.79) are approximated using second- or third-order quadrature rules with Gaussian quadrature nodes and Lagrange interpolation polynomials defined on these nodes. In analogous manner, the numerical sources $\mathbf{S}_i$ and $\mathbf{S}^*_i$ in (2.78), and the two non-conservative products $\mathbf{B}_i$ and $\mathbf{B}^*_i$ in (2.77) are approximated with the same quadrature rule in both space and time.

2.2.3.1 Summary of the method

Consider a non-conservative hyperbolic PDE system with source terms written as in (2.72). The following list summarizes how to compute its numerical solution with the proposed methodology:

1) Discretize the spatial domain Ω into N computational cells S_i, and the temporal domain $\mathcal{T}$ into K temporal cells T^n.
2) At each time step t^n and for each cell S_i, compute the steady-state solution of problem (2.72) using eq. (2.83) and eq. (2.84) described in section 2.2.3.2
3) At each time step t^n and for each cell S_i, compute the spatial reconstruction polynomials using eq. (2.98) or eq. (2.99) described in section 2.2.3.4
4) At each time step t^n and for each cell S_i, compute the space-time predictions using information from points 2) and 3), and the GRP solver presented in section 2.2.3.3.
5) At each time step t^n and for each cell S_i, use information from points 2) and 4) to approximate integrals (2.76), (2.77), (2.78), and (2.79).
6) At each time step t^n and for each cell S_i, update the solution using eq. (2.75).
7) Repeat points 2)-6) till the final simulation time is reached.

2.2.3.2 Stationary solution identification

In this section, we describe the procedure that, at each time step t^n, and for each computational cell S_i, we use to identify a suitable stationary solution $\mathbf{Q}^*(x)$ of problem (2.72) defined in each of the $P(=2,3)$ quadrature points x_p, $p=0,\dots,P-1$ used in the numerical scheme. To this end, we discretize each computational cell S_i into $P-1$ intervals $[x_{p-1}, x_p]$ of length h. Then, we identify a succession of P values $\{\mathbf{Q}^*_{i,p}\}_{p=0}^{P-1}$ representing the approximated stationary solution in each node x_p. Specifically, this succession is obtained by applying the Runge-Kutta method (RK) of order P and with P stages to eq. (2.73). In this work, we consider the second-order RK with 2 stages, and the third-order RK with 3 stages. In both cases, the standard Butcher tableau with coefficients a_{jk}, b_j, and c_j is employed. Therefore, we compute $\mathbf{Q}^*(x_p) \approx \mathbf{Q}^*_{i,p}$ for $p>0$ as

$$\begin{cases} \mathbf{Q}^*_{i,p+1} = \mathbf{Q}^*_{i,p} + h\sum_{j=0}^{P-1} b_j K_j, \\ K_j = \tilde{f}(x_p + c_j h, \mathbf{Q}^*_{i,p} + h\sum_{k=0}^{P-1} a_{jk} K_k). \end{cases} \tag{2.83}$$

Additionally, in order to identify $\mathbf{Q}^*_{i,0}$, we require that the average stationary solution in S_i coincides with the cell average $\mathbf{Q}^n_i$ (Guerrero Fernández et al., 2022). Particularly, we apply a Gaussian quadrature rule of order P, with nodes x_p and weights w_p, to the average stationary solution integral and we enforce the equivalence at the discrete level. As a result, we compute $\mathbf{Q}^*_{i,0}$ by solving the following non-linear system of equations

$$w_0 \mathbf{Q}^*_{i,0} + \sum_{p=1}^{P-1} w_p \mathbf{Q}^*_{i,p}(\mathbf{Q}^*_{i,0}) = \mathbf{Q}^n_i. \tag{2.84}$$

Here, the solution to this system was found by applying the standard Newton method.

2.2.3.3 The well-balanced DET solver

In this section, we present the procedure for constructing a space-time polynomial $\mathbf{Q}^{ST,n}_i(x,t)$ that approximates the solution $\mathbf{Q}(x,t)$ within V^n_i and is employed in the evaluation of the integrals in eq. (2.75). Particularly, we apply a modified version of the Dumbser-Enaux-Toro (DET) GRP solver (Dumbser et al., 2008) that is based on the calculation of the so-called deviations. Before proceeding with the description of the calculation of $\mathbf{Q}^{ST,n}_i(x,t)$, we note that this will constitute the data needed for the computation of jump terms (2.81), in fact, we have that:

$$\mathbf{Q}^-_{i+\frac{1}{2}}(t) = \mathbf{Q}^{ST,n}_i(x_{i+\frac{1}{1}}, t)\,, \mathbf{Q}^+_{i+\frac{1}{2}}(t) = \mathbf{Q}^{ST,n}_{i+1}(x_{i+\frac{1}{1}}, t) \tag{2.85}$$

We define deviation $\mathbf{d}^n_i(x,t)$ is defined as the difference between the space-time polynomial $\mathbf{Q}^{ST,n}_i(x,t)$ and the stationary solution $\mathbf{Q}^*_i(x)$, namely

$$\mathbf{d}^n_i(x,t) = \mathbf{Q}^{ST,n}_i(x,t) - \mathbf{Q}^*_i(x), \quad \forall (x,t) \in V^n_i. \tag{2.86}$$

In order to compute integrands in eq. (2.75) at the desired time levels, we need to know the solution of the GRP for system in (2.74) with initial condition defined as

$$\mathbf{Q}(x,t^n) = \begin{cases} \mathbf{w}_{i-1}^n(x), & \text{if } x < x_{i-\frac{1}{2}}, \\ \mathbf{w}_i^n(x), & \text{if } x > x_{i-\frac{1}{2}}, \end{cases} \tag{2.87}$$

where $\mathbf{w}_i^n(x)$ is the reconstruction polynomial of order $P-1$ in S_i at time t^n. The computation of $\mathbf{w}_i^n(x)$ is described in section 2.2.3.4 The DET solver (Dumbser et al., 2008) finds the solution to this GRP at the desired time points by first performing a space-time evolution procedure, and then solving classical RPs at those time points using the space-time predictions as initial conditions. In particular, locally evolved data in space and time, the space-time predictions $\mathbf{Q}_i^{ST,n}$, are computed through a local space-time discontinuous Galerkin finite element scheme of order P. Given the structure of the adopted numerical scheme, these predictions $\mathbf{Q}_i^{ST,n}$ are space-time polynomials $\mathbf{Q}_i^{ST,n}(x,t)$ evaluated at spatial and temporal quadrature nodes, i.e. $x_{i-\frac{1}{2}}, x_{i+\frac{1}{2}}$ and t^n, t^{n+1} for a second-order method, and $x_{i-\frac{1}{2}}, x_i, x_{i+\frac{1}{2}}$ and $t^n, t^{n+\frac{1}{2}}, t^{n+1}$ for a third-order method. The classical Riemann solver instead provides the solution of the GRP at the time points along interfaces where such solution is required for the computation of the numerical fluctuations $\mathbf{D}^{\pm}_{i\pm\frac{1}{2}}$ (2.79) and the reconstruction polynomials, by solving classical RPs and using space-time predictions at the previous time level on the left and on the right of the same interface as initial data. Before proceeding with the description of the DET solver, we underline that whenever we refer to a local quantity, we drop both the temporal superscript n and the spatial subscript i, keeping only the subscript h to recall that we are in the local framework, for example $\mathbf{Q}_h^{ST} = \mathbf{Q}_i^{ST,n}$.

The local framework is defined by the transformation of the computational volume V_i^n into the reference space-time element $V_h = [0,1] \times [0,1]$ with the reference coordinate ξ and τ as $x = x_{i-\frac{1}{2}} + \Delta x \xi$, and $t = t^n + \Delta t^n \tau$. Hence, problem (2.74) becomes

$$\begin{cases} \partial_\tau \mathbf{Q}_h^{ST} + \dfrac{\Delta t^n}{\Delta x}\mathbf{A}(\mathbf{Q}_h^{ST})\partial_\xi \mathbf{Q}_h^{ST} - \dfrac{\Delta t^n}{\Delta x}\mathbf{A}(\mathbf{Q}_h^{*})\partial_\xi \mathbf{Q}_h^{*} = \\ \qquad\qquad\qquad\qquad\qquad\qquad \Delta t^n \mathbf{S}(\mathbf{Q}_h^{ST}) - \Delta t^n \mathbf{S}(\mathbf{Q}_h^{*}), \\ \mathbf{Q}_h^{ST}(\xi,0) = \mathbf{w}_h(\xi). \end{cases} \tag{2.88}$$

We note that this change of coordinate does not affect the mesh spacing Δx or the time step Δt^n, as both are constant quantities. Since $\partial_\tau \mathbf{Q}_h^{*} = 0$, using relation (2.86), we replace the term $\partial_\tau \mathbf{Q}_h^{ST}$ with $\partial_\tau \mathbf{d}_h$. Additionally, we write the space-time predictor in terms of deviations as $\mathbf{Q}_h^{ST}(\xi,\tau) = \mathbf{d}_h(\xi,\tau) + \mathbf{Q}_h^{*}(\xi)$. As a result, we transform the unknown of our problem from $\mathbf{Q}_h^{ST}(\xi,\tau)$ to $\mathbf{d}_h(\xi,\tau)$. We also note that if both the non-conservative product $\mathbf{A}(\mathbf{Q})\partial_\xi \mathbf{Q}$ and the source term $\mathbf{S}(\mathbf{Q})$ are linear operators, then eq. (2.88) can be written only in terms of deviations $\mathbf{d}_h(\xi,\tau)$, without the stationary solution $\mathbf{Q}_h^{*}(\xi)$ explicitly appearing in the formulation.

Then, we multiply eq. (2.88) by a space-time basis function $\theta(\xi,\tau) \in \mathbb{P}_{m,m}$ with m the degree of the polynomial, and we integrate it over V_h. After applying integration by parts only in time, we obtain

$$\begin{aligned}[\theta,\mathbf{d}_h]^1 - \langle\partial_\tau\theta,\mathbf{d}_h\rangle_{V_h} - [\theta,\mathbf{d}_h]^0 + \frac{\Delta t^n}{\Delta x}\langle\theta,\mathbf{A}(\mathbf{Q}_h^{ST})\partial_\xi\mathbf{Q}_h^{ST}\rangle_{V_h} \\ - \frac{\Delta t^n}{\Delta x}\langle\theta,\mathbf{A}(\mathbf{Q}_h^{*})\partial_\xi\mathbf{Q}_h^{*}\rangle_{V_h} = \Delta t^n\langle\theta,\mathbf{S}(\mathbf{Q}_h^{ST})\rangle_{Vh} - \Delta t^n\langle\theta,\mathbf{S}(\mathbf{Q}_h^{*})\rangle_{Vh},\end{aligned} \tag{2.89}$$

where we have used the following notation for the two scalar products of two functions $f(\xi,\tau)$ and $g(\xi,\tau)$

$$[f,g]^\tau = \int_0^1 f(\xi,\tau)g(\xi,\tau)d\xi, \quad \langle f,g\rangle_{V_h} = \int_0^1\int_0^1 f(\xi,\tau)g(\xi,\tau)d\xi d\tau. \tag{2.90}$$

We now take the element $[\theta,\mathbf{d}_h]^0$ of eq. (2.89) at reference time $\tau = 0$ and we observe that it is completely defined by the initial condition. The initial condition (Dumbser et al., 2008) is

$$\mathbf{d}_{h,0}(\xi) = \mathbf{d}_h(\xi,0) = \mathbf{w}_h(\xi) - \mathbf{Q}_h^*(\xi), \tag{2.91}$$

where the stationary term $\mathbf{Q}_h^*(\xi)$ is known from previous computations.

Later, using the same basis function $\theta(\xi,\tau)$, we approximate the different quantities in (2.89) expanding them as

$$\mathbf{d}_h(\xi,\tau) = \sum_{l=1}^{P^2}\theta_l\widehat{\mathbf{d}}_l, \quad \mathbf{Q}_h^*(\xi) = \sum_{l=1}^{P^2}\theta_l\widehat{\mathbf{Q}^*}_l, \tag{2.92}$$

$$\mathbf{A}(\mathbf{Q}_h^{ST})\partial_\xi\mathbf{Q}_h^{ST}(\xi,\tau) = \sum_{l=1}^{P^2}\theta_l\widehat{\mathbf{A}\partial_\xi\mathbf{Q}}_l, \quad \mathbf{A}(\mathbf{Q}_h^{*})\partial_\xi\mathbf{Q}_h^{*}(\xi) = \sum_{l=1}^{P^2}\theta_l\widehat{\mathbf{A}^*\partial_\xi\mathbf{Q}^*}_l, \tag{2.93}$$

$$\mathbf{S}(\mathbf{Q}_h^{ST})(\xi,\tau) = \sum_{l=1}^{P^2}\theta_l\widehat{\mathbf{S}}_l = \sum_{l=1}^{P^2}\theta_l\mathbf{S}(\widehat{\mathbf{Q}}_l) = \sum_{l=1}^{P^2}\theta_l\mathbf{S}(\widehat{\mathbf{d}}_l + \widehat{\mathbf{Q}^*}_l), \tag{2.94}$$

$$\mathbf{S}(\mathbf{Q}_h^{*})(\xi) = \sum_{l=1}^{P^2}\theta_l\widehat{\mathbf{S}^*}_l = \sum_{l=1}^{P^2}\theta_l\mathbf{S}(\widehat{\mathbf{Q}^*}_l). \tag{2.95}$$

We observe that the term $\widehat{\mathbf{A}\partial_\xi\mathbf{Q}}_l$ is obtained by assuming that $\widehat{\mathbf{A}\partial_\xi\mathbf{Q}}_l = \mathbf{A}(\widehat{\mathbf{Q}}_l)\widehat{\partial_\xi\mathbf{Q}}_l$, and by computing the expansion coefficients of the spatial derivative as $\langle\theta_k,\theta_l\rangle_{V_h}\widehat{\partial_\xi\mathbf{Q}}_l = \langle\theta_k,\partial_\xi\theta_l\rangle_{V_h}\widehat{\mathbf{Q}}_l$ for $k = 1,\dots,P^2$ (Müller et al., 2016a). Similarly, $\widehat{\mathbf{A}^*\partial_\xi\mathbf{Q}^*}_l = \mathbf{A}(\widehat{\mathbf{Q}^*}_l)\widehat{\partial_\xi\mathbf{Q}^*}_l$, and the spatial derivative is computed as $\langle\theta_k,\theta_l\rangle_{V_h}\widehat{\partial_\xi\mathbf{Q}^*}_l = \langle\theta_k,\partial_\xi\theta_l\rangle_{V_h}\widehat{\mathbf{Q}^*}_l$ for $k = 1,\dots,P^2$. In general, $\forall l = 1,\dots,P^2$, the expansion coefficients $\widehat{\mathbf{Q}^*}_l$, $\widehat{\mathbf{A}^*\partial_\xi\mathbf{Q}^*}_l$, and $\widehat{\mathbf{S}^*}_l$, , are known because of the knowledge of the stationary solution. The expansion coefficients

$\widehat{\mathbf{Q}}_l$ instead can be written in terms of deviations as $\widehat{\mathbf{Q}}_l = \widehat{\mathbf{d}}_l + \widehat{\mathbf{Q}^*}_l$. Finally, the expansions coefficients related to the deviations $\widehat{\mathbf{d}}_l$, $\forall l = 1, \dots, P^2$, which are the resulting unknown of system (2.89), are found applying a fixed-point iteration procedure to the following system

$$\begin{aligned}
&\{[\theta_k, \theta_l]^1 - \langle \partial_\tau \theta_k, \theta_l \rangle_{V_h}\} \widehat{\mathbf{d}}_l^{m+1} - \Delta t^n \langle \theta_k, \theta_l \rangle_{Vh} \mathbf{S}(\widehat{\mathbf{d}}_l^{m+1} + \widehat{\mathbf{Q}^*}_l) = \\
&[\theta_k, \psi_l]^0 \widehat{\mathbf{d}_{0l}} - \frac{\Delta t^n}{\Delta x} \langle \theta_k, \theta_l \rangle_{V_h} \mathbf{A}(\widehat{\mathbf{d}}_l^m + \widehat{\mathbf{Q}^*}_l) \{\langle \theta_k, \theta_l \rangle_{V_h}\}^{-1} \langle \theta_k, \partial_\xi \theta_l \rangle_{V_h} (\widehat{\mathbf{d}}_l^m + \widehat{\mathbf{Q}^*}_l) \\
&+ \frac{\Delta t^n}{\Delta x} \langle \theta_k, \theta_l \rangle_{V_h} \mathbf{A}(\widehat{\mathbf{Q}^*}_l) \{\langle \theta_k, \theta_l \rangle_{V_h}\}^{-1} \langle \theta_k, \partial_\xi \theta_l \rangle_{V_h} \widehat{\mathbf{Q}^*}_l - \Delta t^n \langle \theta_k, \theta_l \rangle_{Vh} \mathbf{S}(\widehat{\mathbf{Q}^*}_l),
\end{aligned} \tag{2.96}$$

for $k = 1, \dots, P^2$, where we have expanded the initial condition as $\mathbf{d}_{h,0}(\xi) = \sum_{l=1}^{P^2} \psi_l \widehat{\mathbf{d}_{0l}} = \sum_{l=1}^{P^2} \psi_l (\widehat{\mathbf{w}}_l - \widehat{\mathbf{Q}^*}_l)$, and where m represents the current iteration step. We underline that due to the non-linearity of the system we decided to evaluate the second term of the right-hand side at the known expansion coefficients $\widehat{\mathbf{d}}_l^m$ of the current iteration. Once the expansion coefficients are known, we finally retrieve the space-time predictions $\mathbf{Q}_i^{ST,n}$ in V_i^n. We remark that the modified version of the DET solver here described is equivalent to the original version of the DET solver if we assume that the stationary solution $\mathbf{Q}_i^*(x)$ is always zero.

2.2.3.4 Spatial reconstruction

In this section, we provide a brief overview of the GRP-based reconstruction procedure used to derive second- and third-order accurate spatial reconstruction polynomials $\mathbf{w}_i^n(x)$ (Montecinos et al., 2025). These polynomials serve as local reconstructed data that provide the initial condition for the GRP solver, which in turns computes high-order space-time predictions of the solution $\mathbf{Q}(x,t)$. As a result, they enable the construction of a high-order scheme in both space and time.

They are piecewise functions of degree $P-1$, with P being the order of the numerical method, defined on each computational cell S_i at time t^n. They are expressed in terms of the cell average of the solution at the current time step $\mathbf{Q}_i^n$, and in terms of left and right boundary states at the previous time step $\mathbf{Q}_{i-\frac{1}{2}}^{+,n-1}$ and $\mathbf{Q}_{i+\frac{1}{2}}^{-,n-1}$. These states arise from the solution of a classical RP at time $t^{n-1} + \Delta t^{n-1}$ at the interfaces $x_{i\pm\frac{1}{2}}$ between two neighboring cells, and are also used to compute the integrand in the time integral of the fluctuations (2.79). For the first time step, these states are obtained directly from the prescribed initial condition, evaluated at time $t = 0$ and at the cell interfaces $x_{i\pm\frac{1}{2}}$. For the left interface $x_{i-\frac{1}{2}}$, the classical RP reads

$$\begin{cases}
\partial_t \mathbf{Q} + \mathbf{A}(\mathbf{Q}) \partial_x \mathbf{Q} = 0, \quad x \in \mathbb{R}, t > t^{n-1}, \\
\mathbf{Q}(x, t^{n-1} + \Delta t^{n-1}) = \begin{cases} \mathbf{Q}_{i-1}^{ST,n-1}(x_{i-\frac{1}{2}}, t^{n-1} + \Delta t^{n-1}) & \text{if } x < x_{i-\frac{1}{2}}, \\ \mathbf{Q}_i^{ST,n-1}(x_{i-\frac{1}{2}}, t^{n-1} + \Delta t^{n-1}) & \text{if } x > x_{i-\frac{1}{2}}, \end{cases}
\end{cases} \tag{2.97}$$

where $\mathbf{Q}_{i-1}^{ST,n-1}$ and $\mathbf{Q}_{i}^{ST,n-1}$ are space-time predictions at time $t^{n-1}+\Delta t^{n-1}$ and related to cells S_{i-1} and S_i, respectively. Their computation is described in the previous section. The solution to RP (2.97) can be obtained using various methods (Toro, 2009). Here we applied the exact Riemann solver for the Burgers' equation, and a two-rarefaction approximate Riemann solver for the BFEs, which yielded a non-linear system in the left boundary states unknowns $\mathbf{Q}_{i-\frac{1}{2}}^{\pm,n-1}$. The $-$ and $+$ superscripts on the left boundary states denote, respectively, values taken from the left and right of the interface. This distinction is essential, since at cell interfaces the solution of the considered RP can exhibit discontinuities. The solution to this problem internal to cell S_i, namely $\mathbf{Q}_{i-\frac{1}{2}}^{+,n-1}$, is then used to find the reconstruction polynomial $\mathbf{w}_i^n(x)$. We emphasize that the use of boundary states computed at time $t^{n-1}+\Delta t^{n-1}$ is essential for stability. If instead interface information evaluated solely at the current time level t^n were employed, the resulting numerical scheme would lead to an unstable method.

Due to the structure of our numerical method, the reconstruction polynomials $\mathbf{w}_i^n(x)$ need to be evaluated only in the quadrature nodes, i.e $x_{i-\frac{1}{2}}$ and $x_{i+\frac{1}{2}}$ for a second-order method, and $x_{i-\frac{1}{2}}, x_i$ and $x_{i+\frac{1}{2}}$ for a third-order method. In particular, for a second-order method, a first degree polynomial evaluated in the 2 quadrature nodes $x_{i\pm\frac{1}{2}}$ of the computational cell S_i at time t^n reads

$$\mathbf{w}_i^n(x_{i\pm\frac{1}{2}}) = \mathbf{Q}_i^n \pm \frac{1}{2}(\mathbf{Q}_{i+\frac{1}{2}}^{-,n-1} - \mathbf{Q}_{i-\frac{1}{2}}^{+,n-1}). \tag{2.98}$$

Similarly, for a third-order method, a second degree polynomial evaluated in the 3 quadrature nodes $x_p \in \{x_{i\pm\frac{1}{2}}, x_i\}$ of the computational cell S_i at time t^n reads

$$\mathbf{w}_i^n(x_p) = a + bx_p + cx_p^2, \tag{2.99}$$

where

$$a = \mathbf{Q}_{i-\frac{1}{2}}^{+,n-1}, \tag{2.100}$$

$$b = \frac{2}{\Delta x}(-2\mathbf{Q}_{i-\frac{1}{2}}^{+,n-1} - \mathbf{Q}_{i+\frac{1}{2}}^{-,n-1} + 3\mathbf{Q}_i^n), \tag{2.101}$$

and

$$c = \frac{3}{(\Delta x)^2}(\mathbf{Q}_{i-\frac{1}{2}}^{+,n-1} + \mathbf{Q}_{i+\frac{1}{2}}^{-,n-1} - 2\mathbf{Q}_i^n). \tag{2.102}$$

Both reconstruction polynomials are fully determined by either computing a slope for a second-order method or interpolating them through the boundary states $\mathbf{Q}_{i\pm\frac{1}{2}}^{\mp,n-1}$ for a third-order method associated with cell S_i, and by enforcing the conservation property, which ensures that the cell average of cell S_i at time t^n is $\mathbf{Q}_i^n$. Consequently, if the cell average is that of the steady-state solution on the same computational cell, and the boundary states lie on the same steady-state solution, then the resulting reconstruction polynomials evaluated in the quadrature nodes x_p coincide with the steady-state solution. We underline

that this feature of the GRP-based reconstruction procedure applies only to first and second degree polynomials. Higher degree polynomials require additional information coming from neighboring cells $S_{i\pm1}$ for their complete identification (Montecinos et al., 2025). Thus, they may fail to coincide with the steady-state solution.

2.3 0D models

Haemodynamic simulations require that appropriate boundary conditions are prescribed at the inlets and outlets of vascular networks. This is commonly done by either prescribing haemodynamic waveforms, or by coupling them to 0D models. This class of models, moreover, can be employed also to represent other systems interacting with the circulatory one. Simulations performed through the ADAN network are open loop: at the inlet of the network, which corresponds to the aortic root, we prescribe the same flow curve as in Blanco et al. (2014), with a cardiac period of 1 s, while we couple its outlets with 3-element Windkessel models, presented in section 2.3.3.1. When considering the ADAVN and ADAVN86 models, instead, we couple the aortic inlet and the outlets of the venae cavae and of the coronary sinus to 0D models of the heart (section 2.3.1), and enforce arterio-venous connectivity through a series of standard RCR lumped parameter models (section 2.3.3.2). Moreover, we couple the cardiovascular model with the 0D lung mechanics model introduced in section 2.3.4. Gas exchange is described in both the lungs and peripheral capillaries as illustrated in sections 2.3.6.1 and 2.3.6.2. 0D models are also used to describe short-term control mechanisms (section 2.3.7), in particular the myogenic autoregulation model presented in section 2.3.7.1 and the metabolic autoregulation models presented in section 2.3.7.2.

2.3.1 Heart

In the following chapters, we consider two heart models that differ in their characterisation of the end-diastolic pressure volume relationship. The first model (section 2.3.1.1), which we use to generate the results presented in section 4.1, is based on a linear end-diastolic pressure-volume relationship, while the second one (section 2.3.1.2), which we verify in section 4.2.2 and use for the simulations illustrated in section 4.3, includes an exponential end-diastolic pressure volume relationship for all chambers, which is closer to the physiological behaviour of the heart.

2.3.1.1 Linear heart model

The heart and its valves are modelled as proposed by Mynard et al. (2012a); Müller et al. (2023). The heart, in particular, is functionally divided into chamber free walls and septal walls, and chamber pressure is described as a function of a chamber-specific time-varying elastance and of multiple interactions between chambers

$$p_\alpha = p_{pc} + E_{\mathrm{nat},\alpha}(V_\alpha - V_{0,\alpha}) - R_{S,\alpha} q_{out,\alpha} + \frac{E_{\mathrm{nat},\alpha}}{E_{\mathrm{sep},\alpha}} p_{CL,\alpha} + p_{ext,\alpha}, \tag{2.103}$$

where $\alpha = \{\mathrm{RA}, \mathrm{RV}, \mathrm{LA}, \mathrm{LV}\}$ denotes the considered chamber, V_α and $V_{0,\alpha}$ are, respectively its current volume and reference volume, $p_{CL,\alpha}$ is the pressure in the contralateral chamber, and $E_{\mathrm{nat},\alpha}$ and $E_{\mathrm{sep},\alpha}$ are, respectively, the native chamber elastance and the septal elastance. The native chamber elastance, which represents the pressure-generating capability of the septal and free walls of the myocardium, is defined as

$$E_{\mathrm{nat},\alpha} = \frac{E_{\mathrm{fw},\alpha} E_{\mathrm{sep},\alpha}}{E_{\mathrm{fw},\alpha} + E_{\mathrm{sep},\alpha}} - \mu_{\mathrm{AV},\alpha} q_{\mathrm{V},\alpha}, \tag{2.104}$$

where $\mu_{\mathrm{AV},\alpha}$ is a constant which, together with ventricular flow $q_{\mathrm{V},\alpha}$, accounts for changes in effective atrial elastance caused by the movement of the atrio-ventricular plane, and $E_{\mathrm{sep},\alpha}$ is the septal elastance

$$E_{\mathrm{sep},\alpha} = \mathcal{K}_C E_{\mathrm{fw},L} + \mathcal{K}_C E_{\mathrm{fw},R}, \tag{2.105}$$

with $\mathcal{K}_C$ the septal elastance constant. Pairs (L, R) are related to atria (LA, RA) or ventricles (LV, RV). $E_{\mathrm{fw},\alpha}$ is the chamber free-wall elastance, described by the following "two-Hill" function

$$E_{\mathrm{fw},\alpha} = k_\alpha \left(\frac{g_{1,\alpha}}{1 + g_{1,\alpha}} \right) \left(\frac{g_{2,\alpha}}{1 + g_{2,\alpha}} \right) + E^{\min}_{\mathrm{fw},\alpha}, \tag{2.106}$$

with

$$g_{i,\alpha} = \left(\frac{t - t_{\mathrm{onset},\alpha}}{\tau_{i,\alpha}} \right)^{m_{i,\alpha}}, \; i = 1, 2 \tag{2.107}$$

$$k_\alpha = \frac{E^{\max}_{\mathrm{fw},\alpha} - E^{\min}_{\mathrm{fw},\alpha}}{\max_{t \in [0,T_H]} \left[\left(\frac{g_{1,\alpha}}{1+g_{1,\alpha}} \right) \left(\frac{g_{2,\alpha}}{1+g_{2,\alpha}} \right) \right]}. \tag{2.108}$$

Here, $\tau_{1,\alpha}/\tau_{2,\alpha}$ and $m_{1,\alpha}/m_{2,\alpha}$ denote, respectively the contraction/relaxation time offsets and rate constants, $t_{\mathrm{onset},\alpha}$ is the onset of the contraction/relaxation, and $E^{\max}_{\mathrm{fw},\alpha}$ and $E^{\min}_{\mathrm{fw},\alpha}$ are the maximum and minimum free-wall elastances which govern, respectively, systolic contractility and diastolic passive stiffness. Also, $R_{S,\alpha}$ is a source resistance defined as

$$R_{S,\alpha} = K_{S,\alpha} E_{\mathrm{nat},\alpha} (V_\alpha - V_{0,\alpha}), \tag{2.109}$$

with $K_{S,\alpha}$ constant. p_{pc} is pericardial pressure, which affects the heart as well as epicardial coronary arteries and veins and is computed as

$$p_{pc} = K_{pc} \exp\left(\frac{V_{pc} - V_{0,pc}}{\Phi_{pc}} \right). \tag{2.110}$$

K_{pc} and Φ_{pc} are empirically determined constants, $V_{0,pc}$ is a volume offset, and V_{pc} is the pericardium volume, computed as

$$V_{pc} = V_{\mathrm{mio}} + V_{\mathrm{pcf}} + \sum_\alpha V_\alpha, \tag{2.111}$$

where V_{mio} and V_{pcf} are, respectively, the volumes of the myocardium and the pericardial fluid.

2.3.1.2 Nonlinear heart model

The heart chamber model proposed here extends the time-varying volume-elastance model by Mynard and Smolich (2015b), by incorporating the non-linear end-diastolic pressure-volume relationship proposed by Santamore and Burkhoff (1991). We outline in the following paragraphs its main features.

2.3.1.2.1 Non-dimensional time-varying elastance

The non-dimensional time-varying free-wall elastance is defined as proposed by Mynard and Smolich (2015b)

$$E^{\mathrm{nd}}_{\mathrm{fw},\alpha} = \frac{k_\alpha}{E^{\mathrm{max}}_{\mathrm{fw},\alpha} - E^{\mathrm{min}}_{\mathrm{fw},\alpha}} \left(\frac{g_{1,\alpha}}{1 + g_{1,\alpha}} \right) \left(\frac{1}{1 + g_{2,\alpha}} \right), \tag{2.112}$$

with α denoting the considered cardiac chamber and $E^{\mathrm{max}}_{\mathrm{fw},\alpha}, E^{\mathrm{min}}_{\mathrm{fw},\alpha}$ maximum and minimum chamber free-wall elastances. Here, $g_{i,\alpha}$ and k_α are defined as in equations (2.107), (2.108).

2.3.1.2.2 Basic end-systolic and end-diastolic pressure-volume relationships

We employ linear end-systolic and exponential end-diastolic pressure-volume relationships of the form introduced by Santamore and Burkhoff (1991)

$$P_{\mathrm{es},\alpha}(V_{\mathrm{es},\alpha}) = E_{\mathrm{es},\alpha}(V_{\mathrm{es},\alpha} - V_{0,\alpha}), \tag{2.113}$$

$$P_{\mathrm{ed},\alpha}(V_{\mathrm{ed},\alpha}) = \beta_\alpha[\exp\left(A_\alpha(V_{\mathrm{ed},\alpha} - V_{0,\alpha})\right) - 1], \tag{2.114}$$

where $\alpha = \{\mathrm{RA}, \mathrm{RV}, \mathrm{LA}, \mathrm{LV}\}$ denotes the considered chamber, $P_{\mathrm{es},\alpha}, P_{\mathrm{ed},\alpha}$ and $V_{\mathrm{es},\alpha}, V_{\mathrm{ed},\alpha}$ are, respectively, the end-systolic and end-diastolic chamber pressures and volumes, $V_{0,\alpha}$ are their unstressed volumes, and the choice of $E_{\mathrm{es},\alpha}, \beta_\alpha, A_\alpha$ depends on the type of chamber interactions that one wants to include in the model. If no chamber interactions are present, these quantities are constant, and the end-diastolic and end-systolic pressure-volume relationships can be combined to obtain the instantaneous relationship between pressure and volume as

$$P_\alpha = E^{\mathrm{nd}}_{\mathrm{fw},\alpha}[P_{\mathrm{es},\alpha}(V_{\mathrm{es},\alpha}) - P_{\mathrm{ed},\alpha}(V_{\mathrm{ed},\alpha})] + P_{\mathrm{ed},\alpha}(V_{\mathrm{ed},\alpha}), \tag{2.115}$$

where we omit the time dependence to improve readability.

2.3.1.2.3 Chamber interactions and other relationships

As proposed by Santamore and Burkhoff (1991), we include both diastolic and systolic chamber interdependence. Additionally, as proposed by Mynard and Smolich (2015b), we

account for changes in effective atrial elastance resulting from the movement of the atrio-ventricular plane, and for the presence of viscous interactions. Furthermore, we include the action of external pressures, which in our case correspond to pericardial pressure p_{pc} (equation (2.110)) and a generic external pressure $p_{ext,\alpha}$. In particular, we consider the following relationships

$$P_{\mathrm{ed},\alpha} = \beta_\alpha[\exp\left(A_\alpha(V_{\mathrm{ed},\alpha} - V_{0,\alpha})\right) - 1], \text{ with } A_\alpha = A_{0,\alpha} + n_\alpha V_{\mathrm{ed},\alpha_{\mathrm{cl}}}, \quad \text{Diastolic interact.} \tag{2.116}$$

$$P_{\mathrm{es},\alpha} = E_{\mathrm{nat},\alpha}(V_{\mathrm{es},\alpha} - V_{0,\alpha}) + \frac{E_{\mathrm{nat},\alpha}}{E_{\mathrm{sep},\alpha}} p_{\mathrm{es},\alpha_{\mathrm{cl}}}, \quad \text{Systolic interact.} \tag{2.117}$$

$$P_\alpha = p_{pc} + P_{\mathrm{es},\alpha} + P_{\mathrm{ed},\alpha}[1 - E^{\mathrm{nd}}_{\mathrm{fw},\alpha}] - R_{S,\alpha} q_{out,\alpha} + p_{ext,\alpha}, \quad \text{Instantaneous rel.} \tag{2.118}$$

Here, α_{cl} denotes the contralateral chamber, and the native elastance $E_{\mathrm{nat},\alpha}$ is defined as in equation (2.104). This definition of $E_{\mathrm{nat},\alpha}$ is analogous to that provided by Santamore and Burkhoff (1991), with the addition of the atrio-ventricular plane piston model. In the definition of A_α, $A_{0,\alpha}$ denotes the exponential coefficient at zero volume, and n_α is the sensitivity of A_α to changes in the contralateral chamber volume. The source resistance $R_{S,\alpha}$ is defined as in equation (2.109).

2.3.2 Pulmonary circulation

The pulmonary circulation is described through a 0D model originally proposed by Sun et al. (1997), which includes three compliance-inertance-resistance (CLR) compartments describing pulmonary arteries (PA), capillaries (PC) and veins (PV). The pressure of each compartment was modelled as an exponential function of its volume

$$p_\xi = E_{0,\xi} V_{0,\xi} \exp\left(\frac{V_\xi}{V_{0,\xi}}\right) + \Omega_\xi \dot{V}_\xi + p_{ext,\xi}, \tag{2.119}$$

where $\xi = \{PA, PC, PV\}$, and $V_{0,\xi}$, $E_{0,\xi}$ and Ω_ξ are the reference volume, elastance and viscoelastance of the compartment ξ. $p_{ext,\xi}$ denotes the external pressure acting on each compartment. The time evolution of volume is described as

$$\dot{V}_\xi = q_{in,\xi} - q_\xi, \tag{2.120}$$

where $q_{in,\xi}$ is the inlet flow for each compartment. The rate of change of flow in each compartment is computed as

$$\dot{q}_\xi = \frac{1}{L_\xi}(p_\xi - p_{down,\xi} - R_\xi q_\xi), \tag{2.121}$$

where $p_{down,\xi}$ is the downstream pressure to compartment ξ.

2.3.3 Peripheral terminals

The choice of terminal models depends on the considered vascular network. Indeed, for a purely arterial system such as the ADAN model, 0D terminal models need to encode the effects of both the microcirculation and venous circulation. Conversely, in closed-loop models (ADAVN, ADAVN86), 0D terminal models describe the connectivity between arterial and venous regions, working as surrogates of arteriolar and venular beds.

2.3.3.1 ADAN model

Peripheral boundary conditions are modelled using 3-element Windkessel models, that is

$$R_a^o R_{av}^o C_a^o \frac{dQ_o}{dt} = R_{av}^o C_a^o \frac{d}{dt}(P_o - P_T) + (P_o - P_T) - (R_a^o + R_{av}^o)Q_o, \tag{2.122}$$

where P_T is the reference terminal pressure, and R_a^o, R_{av}^o, and C_a^o are the parameters that represent peripheral resistances and compliance downstream of each terminal vessel. The resistance of a peripheral bed is $R_{tot}^o = R_a^o + R_{av}^o$, with $R_a^o = 0.2R_{tot,o}$, $R_{av}^o = 0.8R_{tot,o}$. Total peripheral compliance is computed as the 10% of arterial tree compliance, and is distributed among terminals according to the blood flow fraction through them (Blanco et al., 2014). R_{av}^o combines resistances that are downstream the arterial compartment.

2.3.3.2 ADAVN and ADAVN86 models

In these closed-loop models, peripheral circulation consists of two compartments: a proximal compartment, corresponding to arterioles and capillaries, and a distal compartment, corresponding to venules and small veins. With this structure, each terminal artery feeds a proximal compartment with compliance C_a, which is then connected to N_{ven} distal compartments, each with compliance C_v. Conversely, each terminal vein originates from a distal compartment that is linked to N_{art} proximal compartments. The proximal compartment is connected to a 1D artery through a proximal resistance R_a, the distal one drains to a 1D vein through a distal resistance R_v, and the two compartments are coupled through a resistance R_{av}. A diagram of a peripheral terminal with $N_{art} = 2, N_{ven} = 2$ is shown in figure 2.7.

Each terminal is modelled as a series of standard RCR lumped parameter models, under the assumption that arterial and venous pressures p_a and p_v are linear functions of the corresponding volumes V_a, V_v,

$$p_\zeta = \frac{V_\zeta}{C_\zeta} + p_{ext,\zeta}, \tag{2.123}$$

where $\zeta = \{a, v\}$ denotes the arterial/venous compartment, C_ζ denotes the corresponding compliance, and $p_{ext,\zeta}$ denotes any external pressure acting on it. Compartment volume

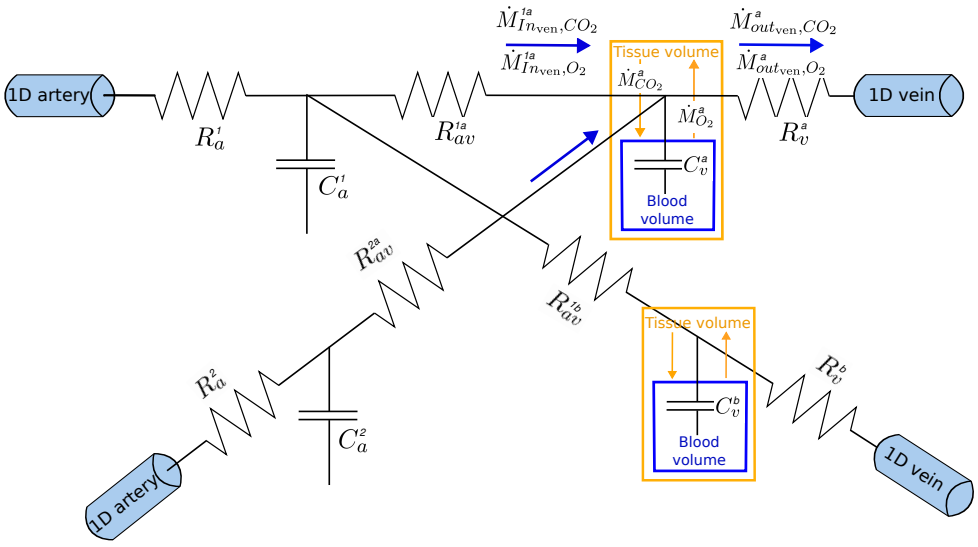

Figure 2.7: Structure of a peripheral terminal comprising two arteries and two veins, analogous to those employed in the ADAVN and ADAVN86 models.

changes according to the mass conservation principle

$$\frac{dV_\zeta}{dt} = q_{\text{in},\zeta} - q_{\text{out},\zeta} \tag{2.124}$$

where $q_{\text{in},\zeta}, q_{\text{out},\zeta}$ are the flow rates entering and exiting the compartments. For proximal compartments, $q_{\text{in},A}$ is computed by enforcing mass conservation and total pressure continuity at the interface with the 1D artery to which the arterial part of the terminal is connected. Analogously, for distal compartments $q_{\text{out},V}$ is computed by imposing mass conservation and total pressure continuity at the interface with the 1D vein to which the venous part of the terminal is connected. Moreover, specific relations were used to account for the peculiarities of blood flow dynamics in the coronary circulation (Mynard et al., 2014; Müller et al., 2023).

2.3.4 Lung mechanics and cardiopulmonary mechanical coupling

We model pulmonary mechanics using the 0D lungs model introduced by Albanese et al. (2016). The system is composed of four elastic compartments arranged in series, representing the larynx, trachea, bronchi, and alveoli, each characterised by a linear resistance (R_{ml}, R_{lt}, R_{tb}, R_{bA}), a compliance (C_l, C_t, C_b, C_A), and an unstressed volume ($V_{u,l}$, $V_{u,t}$, $V_{u,b}$, $V_{u,A}$) (see figure 2.8). Breathing is driven by a muscular pressure source P_{mus}, which acts on the thoracic cavity to mimic the action of the diaphragm (Albanese et al., 2016). P_{mus} is a piecewise function that encodes a parabolic inspiratory profile and an expo-

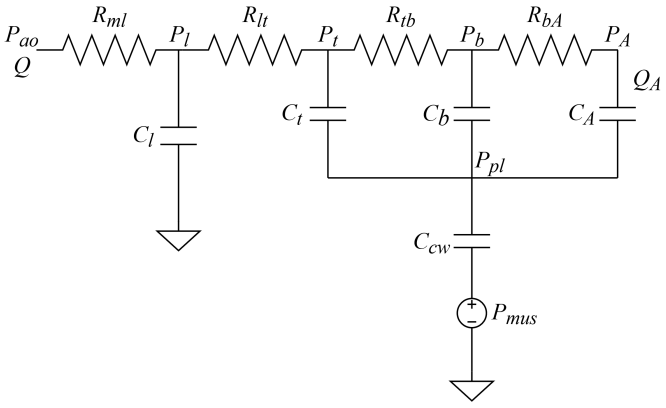

Figure 2.8: Lung mechanics model. Q and Q_A are the total incoming and alveolar airflows; P_{mus} is the pressure exerted by the respiratory muscles and P_{pl} the pleural pressure; R_{ml}, R_{lt}, R_{tb}, and R_{bA} are airway resistances; C_l, C_t, C_b, C_A, and C_{cw} are the compliances associated to airways and chest wall. This figure is taken from Dalmaso et al. (2025a).

nential expiratory one. During inspiration, it decreases from 0 $\mathrm{cmH_2O}$ to its minimum value $P_{mus}^{\min} = -5$ $\mathrm{cmH_2O}$, and then gradually returns to 0 $\mathrm{cmH_2O}$ during expiration. In particular,

$$P_{mus} = \begin{cases} \frac{-P_{mus}^{\min}}{T_I^L \cdot T_E^L} t^2 + \frac{P_{mus}^{\min} \cdot T^L}{T_I^L \cdot T_E^L} t, & t \in [0, T_I^L] \\ \frac{P_{mus}^{\min}}{1 - e^{-T_E^L/\tau}} \left(e^{\frac{t - T_I^L}{\tau}} - e^{-\frac{T_E^L}{\tau}} \right), & t \in (T_I^L, T^L], \end{cases} \tag{2.125}$$

where the inspiratory and expiratory periods T_I^L and T_E^L are fixed fractions of the respiratory period T^L, with $T_I^L / T_E^L = 0.6$, and $\tau = \frac{T_E^L}{5}$ is the time constant of the expiratory profile (Albanese et al., 2016).

Chest-wall deformation during quiet respiration is represented by a constant compliance C_{cw} relating pleural pressure to changes in intrathoracic volume. Applying mass and momentum conservation to the four interconnected 0D compartments, we derive a system of ODEs of the form

$$\frac{dV_j}{dt} = Q_{in,j} - Q_{out,j}, \text{ with } j = l, t, b, A, pl, \tag{2.126}$$

together with algebraic relations describing compartment pressures:

$$P_l = \frac{V_l - V_{u,l}}{C_l}, \tag{2.127}$$

$$P_j = \frac{V_j - V_{u,j}}{C_j} + P_{pl}, \text{ with } j = t, b, A \tag{2.128}$$

$$P_{pl} = \frac{V_{pl}}{C_{cw}} + P_{mus} + P_{pl,ee}, \tag{2.129}$$

where $P_{pl,ee}$ denotes the end-expiratory pleural pressure. To complete the model, we include an equation for intra-abdominal pressure P_{abd}, assuming that the muscular generator acts

in opposite directions on the thorax and abdomen, and that the variation in abdominal volume is opposite to that in pleural volume:

$$P_{abd} = -\frac{V_{pl}}{C_{abd}} - P_{mus} + P_{abd,ee}, \tag{2.130}$$

where C_{abd} is the compliance of the abdominal wall, and $P_{abd,ee}$ the end-expiratory intra-abdominal pressure. Variations in the amplitudes of pleural and abdominal pressures allow different breathing patterns to be represented.

2.3.4.1 Cardiorespiratory mechanical coupling

We couple the lung mechanics model presented in section 2.3.4 with the cardiovascular model by incorporating the contribution of pleural pressure P_{pl} (2.129) and intra-abdominal pressure P_{abd} (2.130) into the external pressure terms $p_{ext}(x,t)$ and $p_{ext,\zeta}$ (see equations (2.3) and (2.123)). These pressure waveforms are applied to all thoracic vessels and peripheral beds (Figure 2.9, mid-top panel) and to all abdominal vessels and beds (Figure 2.9, mid-bottom panel).

Furthermore, since the pulmonary circulation and the heart are within the thorax, their mechanical interaction with the respiratory system is modelled by prescribing the pleural pressure waveform P_{pl} (2.129) as the external sources $p_{ext,\xi}$ and $p_{ext,\alpha}$ in expressions (2.119) and (2.103).

Details regarding the numerical aspects of the coupling are provided in section 4.1.1.2.

2.3.5 Transport in 0D compartments

Equations to describe gas transport in lumped parameter models enforce mass conservation

$$\frac{dM}{dt} = (q\phi)_{in} - (q\phi)_{out}, \tag{2.131}$$

where the values of ϕ employed to define $(q\phi)_{in}$ and $(q\phi)_{out}$ depends on the sign of the flow entering/exiting the considered compartment. Once mass and volume are available at time t^{n+1}, concentration can be computed simply as their ratio. Several works, instead, directly consider the time evolution of concentrations, often under the assumption of a positive flow rate. However, in order to ensure that mass is conserved, this approach requires an additional compatibility equation (e.g. in Albanese et al. (2016) they enforce that the mass entering the thoracic vein compartment is equal to the sum of the masses exiting the other peripheral compartments).

Here, transport is explicitly modelled in peripheral capillaries, coronary capillaries, the heart and in the pulmonary circulation. As we will see in sections 2.3.6.1, 2.3.6.2, in

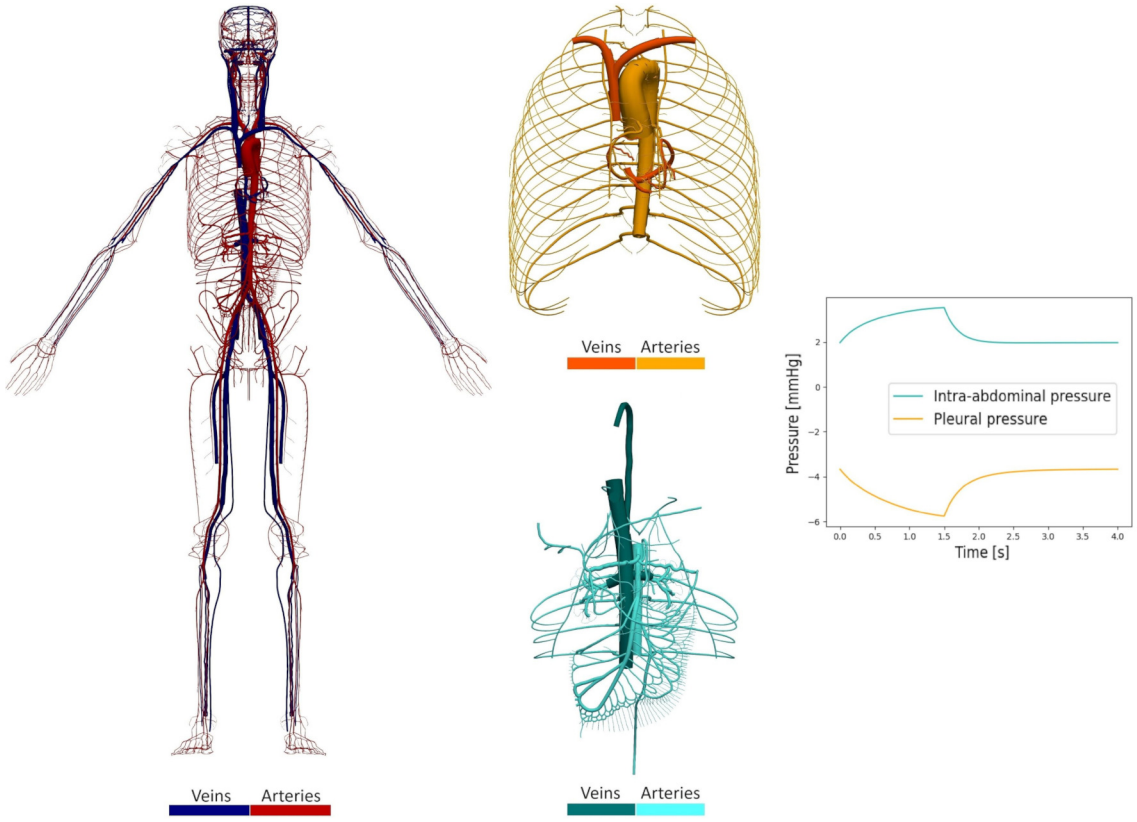

Figure 2.9: From left to right: complete 1D arterial-venous network (arteries in red, veins in blue); a highlight of thoracic (in orange, top panel) and abdominal (in turquoise, bottom panel) vessels; respiratory pressure waveforms, which are prescribed to thoracic (in orange, bottom waveform) and abdominal vessels (in turquoise, top waveform) as an external pressure, and generated through the lung mechanics model illustrated in figure 2.8. This figure is taken from Dalmaso et al. (2025a).

peripheral and coronary capillaries, and in the pulmonary circulation we also need to account for gas exchange.

2.3.6 Gas exchange

Gas exchange occurs when oxygen and carbon dioxide move across thin biological membranes following their partial pressure gradients. In the lungs, this happens across the haemato-alveolar membrane, where inspired oxygen diffuses into the pulmonary capillaries and carbon dioxide diffuses out of the blood to be exhaled. In tissues, the situation reverses: oxygen leaves the systemic capillaries to enter cells for metabolism, while carbon dioxide produced by those cells diffuses into the blood to be transported back to the lungs. We model both mechanisms, without explicitly modelling membrane properties.

2.3.6.1 Gas exchange in the lungs

We base our implementation of gas exchange in the lungs on the approach illustrated by Albanese et al. (2016). The lung gas exchange module includes the anatomical dead space, the alveoli, and the pulmonary capillaries. Moreover, right-to-left pulmonary shunts can be included to model pathological conditions. The pulmonary circulation is described through a 0D model proposed by Sun et al. (1997) and illustrated in section 2.3.2, which includes three CLR compartments describing pulmonary arteries, capillaries and veins. We include the pulmonary shunt ($\xi = PS$) as a parallel compartment to pulmonary capillaries. Here, $E_{0,\xi}, V_{0,\xi}$ and Ω_ξ are the reference elastance, volume and viscoelastance of the compartment ξ, and $p_{ext,\xi}$ is the external pressure acting on each compartment. We compute $R_\xi, L_\xi, E_{0,\xi}, \Omega_\xi, V_{0,\xi}$, with $\xi = \{PC_{new}, PS\}$ as

$$R_{PC_{new}} = R_{PC}\frac{100}{100-sh}; \quad R_{PS} = R_{PC}\frac{100}{sh} \tag{2.132}$$

$$L_{PC_{new}} = L_{PC}\frac{100}{100-sh}; \quad L_{PS} = L_{PC}\frac{100}{sh} \tag{2.133}$$

$$E_{0,PC_{new}} = E_{0,PC}\frac{100}{100-sh}; \quad E_{0,PS} = E_{0,PC}\frac{100}{sh} \tag{2.134}$$

$$\Omega_{PC_{new}} = \Omega_{PC}\frac{100}{100-sh}; \quad \Omega_{PS} = \Omega_{PC}\frac{100}{sh} \tag{2.135}$$

$$V_{0,PC_{new}} = V_{0,PC}\frac{100-sh}{100}; \quad V_{0,PS} = V_{0,PC}\frac{sh}{100}, \tag{2.136}$$

so that the haemodynamic quantities in pulmonary arteries and veins are preserved, and the total flow entering/exiting the combined capillary-shunt compartment is equal to the original flow entering/exiting the pulmonary capillary compartment. Here, sh denotes the percentage of blood flow derived through the shunt.

Equations for the gas exchange model are derived by enforcing mass conservation in each compartment for each considered gas, assuming that compartments are homogeneous and perfectly mixed. The model is built under the assumption that gases are ideal, i.e. gas fractions in the lungs are related to their partial pressures via the ideal gas law. Additionally, empirical dissociation curves employed to relate gas partial pressures to their concentrations in blood account for the Bohr and Haldane effects, i.e. hemoglobin affinity to each gas is a function of the amount of both gases. In contrast to the approach proposed by Albanese et al. (2016), the 1D portion of the model is responsible for the time dynamics associated with gas transport from the lungs to systemic tissues and from the thoracic veins back to the pulmonary capillaries, thereby removing the need for the inclusion of predetermined circulatory transport delays.

Gas fractions $F_{D,\text{gas}}$ in the dead space depend on the fraction of inspired gas $F_{i,\text{gas}}$ and on the flow rate between this compartment, the atmosphere and the alveoli

$$\frac{dF_{D,\text{gas}}}{dt} = \frac{1}{V_D}[u(\dot{V}_{ao,I})\dot{V}_{ao,I}(F_{i,\text{gas}} - F_{D,\text{gas}}) + u(-\dot{V}_{b,A})\dot{V}_{b,A}(F_{D,\text{gas}} - F_{A,\text{gas}})], \quad (2.137)$$

where V_D is dead space volume, $\dot{V_{ao,I}}$ is the airflow entering the model through the airway opening, and $\dot{V_{b,A}}$ is the airflow entering the alveoli from the bronchea. Here, $u(\cdot)$ is the Heaviside step function.

Gas fractions $F_{A,\text{gas}}$ in the alveoli depend on the airflow between this space and the dead space, and on gas exchange with the pulmonary capillaries

$$\frac{dF_{A,\text{gas}}}{dt} = \frac{1}{V_A}[u(\dot{V}_{ao,I})\dot{V}_{b,A}(F_{D,\text{gas}} - F_{A,\text{gas}}) - K\dot{M}_{\text{gas}}], \quad (2.138)$$

where

$$\dot{M}_{\text{gas}} = K_{\text{gas}}(P_{A,\text{gas}} - P_{PC,\text{gas}}), \quad (2.139)$$

where K_{gas} is a constant that summarizes the properties of the respiratory membrane, K is a proportionality constant that allows conversion of volumes from body temperature pressure saturated to standard temperature pressure dry conditions, and

$$P_{A,\text{gas}} = F_{A,\text{gas}}(P_{\text{atm}} - P_{\text{ws}}) \quad (2.140)$$

is gas partial pressure in the alveoli, with $P_{\text{atm}}, P_{\text{ws}}$ atmospheric and water vapor pressures, respectively. $P_{PC,\text{gas}}$ is gas partial pressure in the pulmonary capillaries, computed through the dissociation curves taken from Albanese et al. (2016); Spencer et al. (1979)

$$\phi_{O_2} = \phi_{\text{sat},O_2}\frac{F_{O_2}^{1/h_{O_2}}}{1 + F_{O_2}^{1/h_{O_2}}}, \quad \phi_{CO_2} = \phi_{\text{sat},CO_2}\frac{F_{CO_2}^{1/h_{CO_2}}}{1 + F_{CO_2}^{1/h_{CO_2}}}, \quad (2.141)$$

$$F_{O_2} = P_{O_2}\frac{1 + \beta_{O_2}P_{CO_2}}{k_{O_2}(1 + \alpha_{O_2}P_2)}, \quad F_{CO_2} = P_{CO_2}\frac{1 + \beta_{CO_2}P_{O_2}}{k_{CO_2}(1 + \alpha_{CO_2}P_{O_2})}, \quad (2.142)$$

$$P_{O_2} = r_{O_2} + \sqrt{r_{O_2}^2 - s_{O_2}}, \quad P_{CO_2} = D_{CO_2} \frac{1 + \alpha_{CO_2} P_{O_2}}{1 + \beta_{CO_2} P_{O_2}}, \tag{2.143}$$

$$r_{O_2} = \frac{-(1 + \beta_{O_2} D_{CO_2} - \beta_{CO_2} D_{O_2} - \alpha_{O_2}\alpha_{CO_2} D_{O_2} D_{CO_2})}{2(\beta_{CO_2} + \alpha_{CO_2}\beta_{O_2} D_{CO_2})}, \tag{2.144}$$

$$r_{CO_2} = \frac{-(1 + \beta_{CO_2} D_{O_2} - \beta_{O_2} D_{CO_2} - \alpha_{CO_2}\alpha_{O_2} D_{CO_2} D_{O_2})}{2(\beta_{O_2} + \alpha_{O_2}\beta_{CO_2} D_{O_2})}, \tag{2.145}$$

$$s_{O_2} = \frac{-(D_{O_2} + \alpha_{O_2} D_{O_2} D_2)}{\beta_{CO_2} + \alpha_{CO_2}\beta_{O_2} D_2}, \quad s_{CO_2} = \frac{-(D_{CO_2} + \alpha_{CO_2} D_{CO_2} D_{O_2})}{\beta_{O_2} + \alpha_{O_2}\beta_{CO_2} D_{O_2}}, \tag{2.146}$$

$$D_{O_2} = k_{O_2} \left(\frac{\phi_{O_2}}{\phi_{\text{sat},O_2} - \phi_{O_2}} \right)^{h_{O_2}}, \quad D_{CO_2} = k_{CO_2} \left(\frac{\phi_{CO_2}}{\phi_{\text{sat},CO_2} - \phi_{CO_2}} \right)^{h_{CO_2}}. \tag{2.147}$$

Here $\phi_{\text{sat,gas}}$ is the gas saturation capacity, h_{gas} are Hill coefficients, α_{gas} and β_{gas} are respectively, the slope and intercept of the dissociation curves, and k_{gas} the considered dissociation constants.

Gas concentrations in the pulmonary capillaries $\phi_{PC,\text{gas}}$ are computed as the ratio between the gas mass $M_{PC,\text{gas}}$ in the compartment and the total volume of the compartment, with

$$\frac{dM_{PC,\text{gas}}}{dt} = (q\phi)_{PC_{in},\text{gas}} - (q\phi)_{PC_{out},\text{gas}} + \dot{M}_{\text{gas}}, \tag{2.148}$$

where $(q\phi)_{PC_{in},\text{gas}}$ and $(q\phi)_{PC_{out},\text{gas}}$ denote the gas mass flow rates associated with gas transport in the blood, and $\dot{M}_{\text{gas}}$ is the gas introduced/eliminated from the compartment as a result of lung gas exchange. Here, the subscript PC_{in}, gas refers both to q and ϕ.

Blood oxygen saturation can be computed as

$$S_{a,O_2}\% = \frac{\phi_{a,O_2} - \phi_{a,O_2,\text{diss}}}{1.34 hgb} 100, \tag{2.149}$$

with ϕ_{a,O_2} oxygen concentration in the aortic arch and

$$\phi_{a,O_2,\text{diss}} = \begin{cases} P_{a,O_2} \frac{0.003}{100} & \text{if } \phi_{\text{sat},O_2} - 1.34 hgb - P_{a,O_2} \frac{0.003}{100} \geq 0, \\ \phi_{\text{sat},O_2} - 1.34 hgb & \text{otherwise,} \end{cases} \tag{2.150}$$

with P_{a,O_2} oxygen partial pressure in the aortic arch, and hgb hemoglobin concentration.

2.3.6.2 Gas exchange in peripheral capillaries

Oxygen and carbon dioxide are exchanged in peripheral capillaries. We assume that oxygen consumption and carbon dioxide production occur at constant rates $\dot{M}_{\text{gas}}$ in the distal compartments (venules), where blood and tissues form a combined homogeneous blood-tissue compartment with volume given by the sum of a constant tissue volume V_{tissue} and

the time-dependent blood volume V_{ven}

$$\frac{dM_{\text{ven},O_2}}{dt} = \dot{M}_{in_{\text{ven}},O_2} - \dot{M}_{out_{\text{ven}},O_2} - \dot{M}_{O_2}, \tag{2.151}$$

$$\frac{dM_{\text{ven},CO_2}}{dt} = \dot{M}_{in_{\text{ven}},CO_2} - \dot{M}_{out_{\text{ven}},CO_2} + \dot{M}_{CO_2}, \tag{2.152}$$

$$\phi_{\text{ven,gas}} = \frac{M_{\text{ven,gas}}}{V_{\text{ven}} + V_{\text{tissue}}}. \tag{2.153}$$

Here, $\dot{M}_{in_{\text{ven}},\text{gas}}$ and $\dot{M}_{out_{\text{ven}},\text{gas}}$ are the gas mass flow rates associated with gas transport in the blood compartments. $\dot{M}_{out_{\text{ven}},\text{gas}}$ is computed by imposing coupling conditions that guarantee mass conservation at the interface between the terminal vein inlet and the lumped parameter model.

2.3.6.2.1 Unstressed volumes

In order to correctly reproduce the total mass of gases present in the blood, we need to account for both the stressed and unstressed components of blood volume. A healthy adult male, indeed, generally has a total blood volume of 75–80 mL/kg. Typically, 30–40% of this is the stressed volume, whereas the unstressed volume is the portion of blood that exerts no transmural pressure. Consequently, pressure in 0D terminals can be defined as

$$p_\zeta = p_{ext,\zeta} + \frac{1}{C_\zeta}(V_\zeta - V_{\zeta,0}), \tag{2.154}$$

where $\zeta = \{a, v\}$ denotes the arterial/venous compartment $V_{\zeta,0}$ is the unstressed volume and V_ζ is now the total blood volume in the compartment. Simulations are performed considering 615 mL of arterial unstressed volume, and 2500 mL of venous unstressed blood volume. We refer to Celant et al. (2021) for further details.

2.3.7 Control mechanisms

Several control mechanisms act to maintain homeostasis and to restore equilibrium after physiological challenges. We illustrate in the following the myogenic and metabolic autoregulation models tested and employed in sections 4.5 and 4.4.

2.3.7.1 Myogenic autoregulation

We implement a local myogenic flow regulation model based on Ursino and Lodi (1997), which provides feedback when the flow rate departs from a homeostatic state.

The effect of myogenic autoregulation on peripheral compartments included in region $\mathcal{R}$ is described via a first-order low pass filter

$$\tau \frac{dx_i}{dt} = -x_i + G_{i,\mathcal{R}} \left(\frac{q_i - q_i^{ref}}{q_i^{ref}} \right), \tag{2.155}$$

where τ is the time constant of the dynamics, and $G_{i,\mathcal{R}}$ is its static gain. In the following, q_i and q_i^{ref} will denote, respectively, either the instantaneous or the cardiac cycle-averaged flow rate, and the baseline average flow rate at the midpoint of the 1D vessel coupled to the 0D terminal (see figure 2.7 for an example of a terminal in the ADAVN/ADAVN86 network models). The static gain $G_{i,\mathcal{R}}$ at each terminal i in region $\mathcal{R}$ is computed from the total gain $G_{\mathcal{R}}$ of autoregulation, which is considered proportional to the flow in each region. Once the control action x_i is available, it is used to modify the terminal vascular compliance C_a^i through a sigmoidal relationship as

$$C_a^i = \frac{C_a^{i,ref}((1 - \Delta C_a^i/2) + (1 + \Delta C_a^i/2)\exp(-x_i/k_i))}{1 + \exp(-x_i/k_i)}, \tag{2.156}$$

with $C_a^{i,ref}$ being the baseline terminal compliance,

$$\Delta C_a^i = 2sat_1, \quad k_i = C_a^{i,ref} sat_1 k_{mult,i} \quad \text{if } x_i > 0 \tag{2.157}$$

$$\Delta C_a^i = 2sat_2, \quad k_i = C_a^{i,ref} sat_2 k_{mult,i} \quad \text{otherwise.} \tag{2.158}$$

Here, sat_1, sat_2 are constant parameters that define the upper and lower saturation levels of the sigmoidal curve, respectively $C_{a,max}^i = (1+sat_2)C_a^{i,ref}$ and $C_{a,min}^i = (1-sat_1)C_a^{i,ref}$, and $k_{mult,i}$ is a constant parameter that regulates the steepness of the sigmoid function. Indeed, the slope of the sigmoid is

$$\frac{dC_a^i}{dx}|_{x=0} = C_a^{i,ref} \frac{d}{dx} \frac{C_a^{i,ref}((1 - \Delta C_a^i/2) + (1 + \Delta C_a^i/2)\exp(-x_i/k_i))}{1 + \exp(-x_i/k_i)}\bigg|_{x=0} = -C_a^{i,ref} \frac{\Delta C_a^i}{4k_i}.$$

Hence, $\frac{dC}{dx}|_{x=0} = -\frac{1}{2k_{mult,i}}$. Commonly, $k_{mult,i}$ is chosen equal to 0.5, so that the magnitude of gain G_i corresponds to that of the central gain of autoregulation, i.e. the derivative of the controlled variable with respect to the driving signal, evaluated at the operating point

$$\frac{d\text{Output}}{d\text{Input}}\bigg|_{\text{Baseline}} = \frac{dC_a^i}{d\frac{q_i - q_i^{ref}}{q_i^{ref}}}. \tag{2.159}$$

Here, applying the chain rule, defining $\frac{q_i - q_i^{ref}}{q_i^{ref}} = \xi$ and taking into the account the fact that gain is a steady state parameter which gives no knowledge about the dynamics of the process, we get that

$$\text{central gain} = G_i \frac{-C_a^{i,ref} \Delta C_a^i}{4k_i} = -\frac{G_i}{2k_{mult,i}}. \tag{2.160}$$

Equations (2.155) and (2.156) imply that a decrease in blood flow below its baseline value q_i^{ref} causes vasodilation, which is modelled through an increase in terminal compliance.

Variations in arteriolar resistances R_{av}^i are, instead, modelled as

$$R_{av}^i = R_{av}^{i,ref}\left(\frac{(V_a^i - V_{a,0}^i)^{ref}}{V_a^i - V_{a,0}^i}\right)^2. \tag{2.161}$$

with $R_{av}^{i,ref}$ the baseline terminal resistance, and $(V_a^i - V_{a,0}^i), (V_a^i - V_{a,0}^i)^{ref}$ baseline and current terminal stretched volumes, respectively.

We assume that resistances R_a^i and the venous portion of terminals is not affected by myogenic local autoregulation phenomena (see figure 2.7. We will apply this model to terminals in the brain (section 4.4) and in the leg (section 4.5).

2.3.7.2 Metabolic autoregulation models

The aforementioned myogenic autoregulation model has been integrated by Ursino and Giannessi (2010) with a description of CO_2 reactivity, which accounts for derangements of arterial CO_2 partial pressure from a baseline state. Additionally, a purely metabolic model for local autoregulation has been proposed by Magosso and Ursino (2001), and later used by Albanese et al. (2016). In this section we illustrate the main features of the two models, whose responses will be compared in chapter 4.4.

2.3.7.2.1 CO_2 reactivity model by Ursino and Giannessi (2010)

The effect x_{i,CO_2} of CO_2 reactivity on peripheral compartments included in region $\mathcal{R}$ is described via a first-order low pass dynamics

$$\tau_{CO_2}\frac{dx_{i,CO_2}}{dt} = -x_{i,CO_2} + G_{i,\mathcal{R},CO_2}A_{i,CO_2}\log_{10}\left(\frac{P_{a,CO_2}^i}{P_{a,CO_2}^{i,ref}}\right), \tag{2.162}$$

where τ_{CO_2} is the time constant of the dynamics, $G_{i,\mathcal{R},CO_2}$ the static gain, and P_{a,CO_2}^i and $P_{a,CO_2}^{i,ref}$ are, respectively, the arterial CO_2 partial pressure in perturbed and baseline conditions, computed in the arterial compartment of the 0D terminal. A_{i,CO_2} is a corrective factor employed to describe the steep decrease in $G_{i,\mathcal{R},CO_2}$ during ischaemia, computed as

$$A_{i,CO_2} = \frac{1}{1 + \exp\left(-k_{CO_2}(q_i - q_i^{ref})/q_i^{ref} - b_{CO_2}\right)}. \tag{2.163}$$

The values of parameters k_{CO_2} and b_{CO_2} are defined so that A_{i,CO_2} remains close to 1 until q_i is approximately 50% of q_i^{ref}.

x_{i,CO_2} interacts with the effect of myogenic autoregulation x_i (see equation (2.155)) to modulate terminal compliances:

$$C_a^i = \frac{C_a^{i,ref}((1 - \Delta C_a^i/2) + (1 + \Delta C_a^i/2)\exp((x_{i,CO_2} - x_i)/k_i))}{1 + \exp((x_{i,CO_2} - x_i)/k_i)} \tag{2.164}$$

with C_i^{ref} being the baseline terminal compliance,

$$\Delta C_a^i = 2sat_1, \quad k_i = C_a^{i,ref} sat_1 k_{mult,i} \quad \text{if } x_{i,CO_2} - x_i < 0 \tag{2.165}$$

$$\Delta C_a^i = 2sat_2, \quad k_i = C_a^{i,ref} sat_2 k_{mult,i} \quad \text{otherwise.} \tag{2.166}$$

According to this relationship, a decrease in flow and an increase in P_{a,CO_2}^i cause vasodilation through an increase in vascular compliance. Conversely, an increase in flow and decrease in P_{a,CO_2}^i cause vasoconstriction, which is associated with a reduction in compliance. Resistances are modulated as in equation (2.161).

2.3.7.2.2 Metabolic autoregulation model by Magosso and Ursino (2001)

The metabolic model presented in the previous section neglects the impact of hypoxia, which causes vasodilation in the vascular beds with higher metabolic requirements, such as the coronary, cerebral and skeletal muscle circulations. The model we illustrate in this section accounts for changes in hydraulic peripheral conductances caused by deviations from the baseline of both oxygen and carbon dioxide concentrations, with relations that are specific either to the brain or to the coronary vessels and skeletal muscle. Even though simulations to be performed in chapter 4.4 will only account for cerebral autoregulatory mechanisms, we report below the full set of model equations.

In locally regulated vascular beds, peripheral hydraulic resistance varies linearly with venous O_2 concentration according to a first-order dynamic: when venous O_2 levels drop below their baseline value, the resistance correspondingly decreases according to the following equation

$$\tau_{O_2} \frac{dx_{i,O_2}}{dt} = -x_{i,O_2} - g_{i,\mathcal{R},O_2}(\phi_{v,O_2} - \phi_{v,O_2}^{ref}), \quad \mathcal{R} = \{b, h, m\}. \tag{2.167}$$

Here, τ_{O_2} is the time constant of oxygen reactivity, $g_{i,\mathcal{R},O_2}$ the static gain, x_{i,O_2} the effect of oxygen reactivity on terminal i in region $\mathcal{R}$, and ϕ_{v,O_2} denotes the oxygen concentration in the venous compartments, computed as

$$\phi_{v,O_2} = \frac{\sum_k M_{v,O_2}^{k,\text{blood}}}{\sum_k V_v^k}. \tag{2.168}$$

Here, k denotes the venous compartments connected to the arterial compartment of terminal i, $M_{v,O_2}^{k,\text{blood}}$ is the mass of oxygen dissolved in blood, and V_v^k is total venous blood volume.

Subscripts $\mathcal{R} = \{b, h, m\}$ denote the cerebral, coronary and skeletal muscle territories, respectively.

The effects of CO_2 reactivity are characterised through a region-dependent static non-linear relationship and a first-order, low-pass filter, and describe responses to variations in CO_2 arterial partial pressure. The static relationship used for the cerebral autoregulation reads

$$\Psi_b(Pa^i_{CO_2}) = \frac{A + \frac{B}{1+C\exp(D\log(Pa^i_{CO_2}))}}{A + \frac{B}{1+C\exp(D\log(Pa^{i,ref}_{CO_2}))}} - 1, \tag{2.169}$$

where A, B, C, D are constant parameters. In the coronary and skeletal muscle circulations, instead,

$$\Psi_{h,m}(Pa^i_{CO_2}) = \frac{1 - \exp\left(\frac{Pa^i_{CO_2} - Pa^{i,ref}_{CO_2}}{k_{CO_2}}\right)}{1 + \exp\left(\frac{Pa^i_{CO_2} - Pa^{i,ref}_{CO_2}}{k_{CO_2}}\right)}, \tag{2.170}$$

with k_{CO_2} parameter with the dimension of a pressure related to the slope of the sigmoidal function at the central point. The low pass dynamics is

$$\frac{dx_{i,CO_2}}{dt} = \frac{1}{\tau_{CO_2}}\left(- x_{i,CO_2} + \Psi_{\text{reg}}(Pa^i_{CO_2})\right). \tag{2.171}$$

In the brain, the effects of oxygen and carbon dioxide interact in an additive manner on cerebral hydraulic conductance $G_i = \frac{1}{R^i_{av}}$, with R^i_{av} arteriolar resistance

$$G_i = G^{ref}_i(1 + x_{i,O_2} + x_{i,CO_2}). \tag{2.172}$$

Coronary and skeletal muscular vascular resistances are modulated, instead, according to the following relationship

$$R^i_{av} = R^{i,ref}_{av}\frac{1 + x_{i,CO_2}}{1 + x_{i,O_2}}. \tag{2.173}$$

In this model, terminal compliances remain fixed and are not subject to any regulatory modulation.

2.3.7.3 Summary

We presented three different autoregulation models:

(1) Myogenic autoregulation model (section 2.3.7.1): modulates vascular compliances and resistances in response to variations in blood flow.

(2) CO_2 reactivity model (section 2.3.7.2.1): works in combination with the myogenic mechanism to adjust vascular compliances and resistances in response to changes in arterial CO_2 partial pressure and blood flow.

(3) Purely metabolic autoregulation model (section 2.3.7.2.2): acts independently to modulate vascular resistances in response to deviations in arterial CO_2 partial pressure and venous oxygen concentration.

3

Numerical results

This chapter reports numerical results associated to sections 2.2.2 and 2.2.3. We assess the numerical solution of the transport problem in terms of mass conservation and empirical convergence rates. We then evaluate the performance of the well-balanced high order solver presented in section 2.2.3, both for a scalar case (Burgers' equation) and for the 1D blood flow equations with gravity.

3.1 Modelling transport in 1D domains

In this section we report and discuss a set of tests conducted to assess the performance of the numerical method used for transport simulations.

We start by assessing mass conservation at a discrete level, i.e. verifying that the relative error observed for tracer mass over long timescales (in this case 400 s) is negligible for the purposes of our simulations. To this end, we compare results obtained by solving the transport equation through the conservative and path-conservative approaches described in section 2.2.2.1. Finally, we perform an empirical convergence rate study for the first- and second-order methods that solve the transport equation through a conservative approach, to verify that the expected order of accuracy is attained.

3.1.1 Mass conservation

We assess tracer mass conservation using both a path-conservative and a conservative formulation of the transport problem, considering the first- and second-order numerical schemes illustrated, respectively, in sections 2.2.2.1.1 and 2.2.2.1.2. Simulations are per-

formed on the ADAVN86 vascular network (sections 2.1.4, 4.2.1.1), in the presence of respiration (section 2.3.4), using the nonlinear cardiac model introduced in section 2.3.1.2.

We reproduce the injection of 20 mass units of contrast medium into the antecubital vein at a constant rate over 5 seconds, with the injection starting at $t = 50$ s and the simulation ending at $t = 400$ s.

The injection of a mass $M_{\phi_i,j}$ of tracer i at the level of a vessel junction j is enforced by prescribing

$$\dot{M}^{TOT}_{\phi_i,j,In} = \dot{M}^{BLOOD}_{\phi_i,j,In} + \dot{M}^{INJ}_{\phi_i,j,In}, \tag{3.1}$$

where $\dot{M}^{TOT}_{\phi_i,j,In}$ is the total incoming tracer mass flow ([UM/s], with UM unit of mass), composed of the tracer already present in the blood ($\dot{M}^{BLOOD}_{\phi_i,j,In}$) and by the injected one ($\dot{M}^{INJ}_{\phi_i,j,In}$). The injection term $\dot{M}^{INJ}_{\phi_i,j,In}$ is defined so that the desired mass $M_{\phi_i,j}$ of tracer is delivered over the specified time interval.

Assuming uniform mixing at the junction, the tracer concentration $\phi_{i,j}$ in outlet vessels (in this case the antecubital vein) is computed as

$$\phi_{i,j} = -\frac{\dot{M}^{TOT}_{\phi_i,j,In}}{Q_{j,Out}} \tag{3.2}$$

whenever $Q_{j,Out} \neq 0$.

Figure 3.1 reports the relative errors in total tracer mass obtained using the first order formulation of our numerical scheme (section 2.2.2.1.1) under four configurations

- Space-dependent parameters in tube laws (2.4) and (2.5) ($A_0, h_0, E_e, E_c, \epsilon_0, \epsilon_r$):
  - *Configuration 1* - Conservative transport formulation: DOT numerical fluxes at internal interfaces and Godunov fluxes at boundary interfaces.
  - *Configuration 2* - Path-conservative transport formulation: fluctuations at internal cell interfaces obtained by computing the integral in equation (2.26) through a third-order Gauss-Legendre integral rule.
  - *Configuration 3* - Path-conservative transport formulation: fluctuations at internal cell interfaces obtained by computing the integral in equation (2.26) through a Gauss-Lobatto rule of order 25. In both cases, boundary fluctuations are computed with the third-order Gauss-Legendre integral rule.
- Constant parameters in tube laws (2.4) and (2.5) ($A_0, h_0, E_e, E_c, \epsilon_0, \epsilon_r$):
  - *Configuration 4* - Path-conservative transport formulation: fluctuations at internal cell interfaces obtained by computing the integral in equation (2.26) through a third-order Gauss-Legendre integral rule.

With space-dependent tube law parameters, good mass conservation (relative errors of the order of 10^{-9}) is achieved only when the transport equation is formulated in conservative form, i.e. using DOT fluxes internally and Godunov fluxes at boundaries. In contrast, the path-conservative formulation fails to conserve mass at a discrete level when fluctuations at internal cell interfaces are computed through a third-order Gauss-Legendre integral rule (with this setup, for simulations spanning 24 hours we would lose around 0.06 units of mass out of the 20 injected), and performs worse than the conservative formulation even if an order 25 integral rule is employed.

When constant parameters are considered, instead, the haemodynamic problem becomes conservative, and the numerical method employed for its solution uses the segment path

$$\underline{V} = V^- + s(V^+ - V^-) \tag{3.3}$$

for all considered variables V when computing numerical fluctuations, instead of the variation outlined in equation (2.28). In this setting, tracer mass conservation is satisfactory even with the path-conservative formulation. This suggests that the chosen path may be responsible for the loss of conservation in the variable parameter case. Indeed, numerical fluctuations are computed as

$$D^{\pm}_{\phi_j, i\mp\frac{1}{2}} = \frac{1}{2}\int_0^1 \left(\mathbf{A}(\mathbf{\Psi}) \pm |\mathbf{A}(\mathbf{\Psi})|\right)\frac{\partial \mathbf{\Psi}}{\partial s}\mathrm{d}s, \tag{3.4}$$

and the choice of path (2.28) (see section 2.2.2) may introduce nonlinearities in the fluctuation integral that are not well captured by low-order polynomial approximations. This interpretation is supported by the difference in the mass conservation behaviour observed when solving such integral with an open integral rule of order 3 or with a closed integral rule of order 25: at 400 s, the former produces a $> 0.0012\%$ relative error, while the latter a $\simeq 5 \cdot 10^{-8}\%$ relative error.

Overall, the findings show that tracer mass conservation is strongly influenced by the numerical treatment of the transport equation when vascular parameters vary in space. In this setting, the conservative formulation consistently preserves mass, whereas the path-conservative approach introduces noticeable errors. When parameters are constant, this issue does not arise, and the path-conservative method performs comparably to the conservative one. These observations suggest that, for networks with spatially varying properties, conservative fluxes provide a more reliable option for tracer-transport simulations, while the path-conservative formulation may require a more suitable path choice or higher-order integration to achieve similar accuracy.

For completeness, we report in figure 3.2 a comparison between mass conservation results obtained with the first and second order conservative formulations of our numerical scheme with variable vascular parameters.

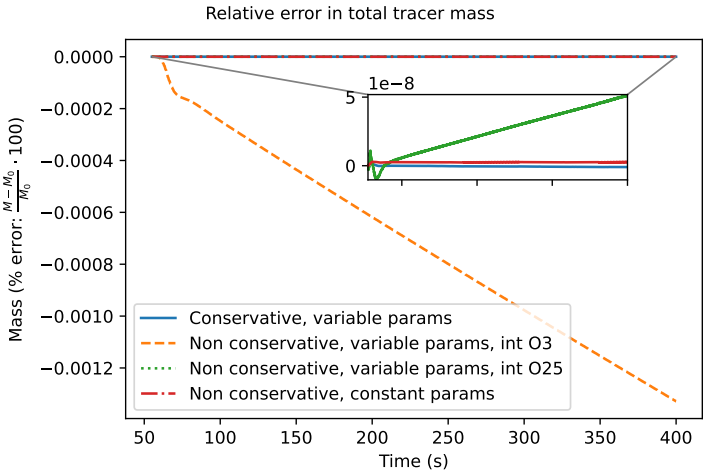

Figure 3.1: Relative errors in total tracer mass obtained using the first order formulation of our numerical scheme with variable vascular parameters: conservative transport description in blue, nonconservative transport descriptions in orange (numerical fluctuations integral solved with a 3rd order open quadrature rule) and green (numerical fluctuations integral solved with a order 25 closed quadrature rule); and with constant vascular parameters: nonconservative transport description in green.

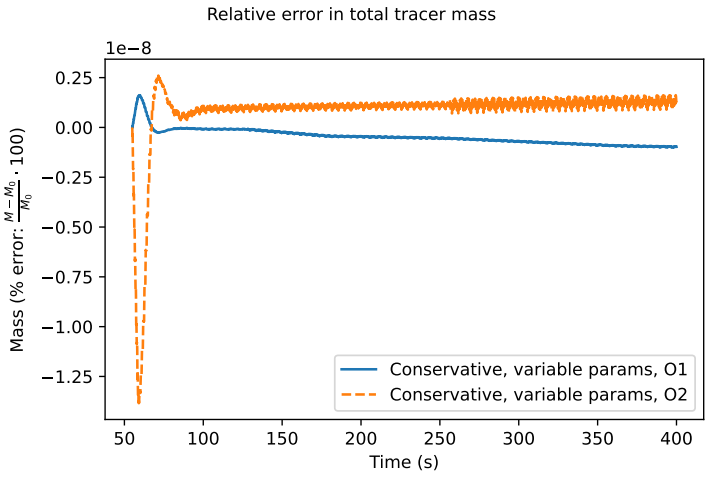

Figure 3.2: Relative errors in total tracer mass obtained using the first and second order conservative formulations of our numerical scheme with variable vascular parameters.

3.1.2 Empirical convergence tests

We assess through the method of manufactured solutions the convergence of the first- and second-order numerical methods that arise from using a conservative treatment of the transport problem (sections 2.2.2.1.1 and 2.2.2.1.2). Namely, we solve a test problem for a modified system of equations obtained as a perturbation of the original coupled system (2.12),

$$\partial_t \mathbf{Q} + \mathbf{A}(\mathbf{Q})\partial_x \mathbf{Q} = \mathbf{S}(\mathbf{Q}) + \hat{\mathbf{S}}(x,t). \tag{3.5}$$

Here, $\hat{\mathbf{S}}(x,t)$ is an analytically constructed source term, built so that a prescribed smooth solution $\hat{\mathbf{Q}}$ becomes an exact solution of the modified problem.

In our case, we are considering two different formulations for the transport equation, a conservative one for the update step

$$\partial_t(A\phi_i) + \partial_x\left(\frac{q(A\phi_i)}{A}\right) = 0,\ i = 1,\dots,n \tag{3.6}$$

and, in the case of the second order numerical method, a non-conservative one for the DET solver

$$\partial_t \phi_i + \frac{q(x)}{A(x)}\partial_x \phi_i = 0,\ i = 1,\dots,n, \tag{3.7}$$

with n the number of tracers.

We consider the following smooth function for the haemodynamic part of the problem (Müller et al., 2016)

$$\hat{\mathbf{Q}}(x,t) = \begin{bmatrix} \hat{A}(x,t) \\ \hat{q}(x,t) \end{bmatrix} = \begin{bmatrix} A^c + \delta_A A^c \sin\left(\frac{2\pi}{L}x\right)\cos\left(\frac{2\pi}{T_0}t\right) \\ q^c - \delta_A A^c \frac{L}{T_0}\cos\left(\frac{2\pi}{L}x\right)\sin\left(\frac{2\pi}{T_0}t\right) \end{bmatrix} \tag{3.8}$$

where quantities with superscript c are average values and terms δ are fluctuations around them.

The transport component $\hat{\phi}_i,\ i = 1,\dots,n$ is defined as

$$\hat{\phi}_i = \Phi^c + \delta_A A^c \sin\left(\frac{2\pi}{L}x\right)\cos\left(\frac{2\pi}{T_0}t\right). \tag{3.9}$$

The source term that results plugging (3.8) and (3.9) in (3.6) is

$$\begin{aligned} \hat{S}_{\phi,c} = &-\frac{2\pi\delta_A A^c}{T_0}\left(A^c + \delta_A A^c \sin\left(\frac{2\pi x}{L}\right)\cos\left(\frac{2\pi t}{T_0}\right)\right)\sin\left(\frac{2\pi x}{L}\right)\sin\left(\frac{2\pi t}{T_0}\right) \\ &+ \frac{2\pi\delta_A A^c}{L}\left(-\frac{L\delta_A A^c}{T_0}\sin\left(\frac{2\pi t}{T_0}\right)\cos\left(\frac{2\pi x}{L}\right) + q^c\right)\cos\left(\frac{2\pi x}{L}\right)\cos\left(\frac{2\pi t}{T_0}\right) \end{aligned} \tag{3.10}$$

and the one that results substituting (3.8) and (3.9) in (3.7) is

$$\begin{aligned}\hat{S}_{\phi,nc} = &-\frac{2\pi\delta_A A^c}{T_0}\sin\left(\frac{2\pi x}{L}\right)\sin\left(\frac{2\pi t}{T_0}\right)\\ &+\frac{2\pi\delta_A A^c\big(-\frac{L\delta_A A^c}{T_0}\sin\left(\frac{2\pi t}{T_0}\right)\cos\left(\frac{2\pi x}{L}\right)+q^c\big)\cos\left(\frac{2\pi x}{L}\right)\cos\left(\frac{2\pi t}{T_0}\right)}{\big(L(A^c+\delta_A A^c\sin\left(\frac{2\pi x}{L}\right)\cos\left(\frac{2\pi t}{T_0}\right))\big)}.\end{aligned} \tag{3.11}$$

The convergence test is performed considering the transport of a single tracer on a network of two vessels connected at both extremities to form a closed loop. Each vessel has a length $L = 100$ cm, and a cross-sectional diameter $R_0 = 1.4$cm.

We perform the test considering the elastic formulation of the problem (which does not require hyperbolization), with tube law characterised by $K_m = 0\text{cm}^{-1}$, $E_c = 0$, $E_e = 3.4 \cdot 10^6$ dyne/cm^2. Moreover, we set $T_0 = 1$ s, $A^c = \pi R_0^2$, $q^c = 100$ mL/s, $\phi^c = 1$ g/mL and $\delta_A = 0.1$. The output time is taken as $t_{\text{end}} = 0.1$ s, and the CFL number used is CFL $= 0.9$. Mesh spacing is defined such that $\Delta x_1 = 2\Delta x_2$, so that the time step ratio between both vessels is roughly 2. Errors are measured in the norms L^1, L^2 and L^∞

$$L^1_{k,err}(t_{\text{end}}, \Delta x_j) = \Delta x_j \sum_{i=1}^{N_j} |Q^{t_{\text{end}}}_{k,i} - Q^{\text{exact}}_{k,i}|, \tag{3.12}$$

$$L^2_{k,err}(t_{\text{end}}, \Delta x_j) = \sqrt{\Delta x_j \sum_{i=1}^{N_j} |Q^{t_{\text{end}}}_{k,i} - Q^{\text{exact}}_{k,i}|^2}, \tag{3.13}$$

$$L^\infty_{k,err}(t_{\text{end}}, \Delta x_j) = \max_{N_j} |Q^{t_{\text{end}}}_{k,i} - Q^{\text{exact}}_{k,i}|, \tag{3.14}$$

with N_j number of cells associated with mesh spacing Δx_j, $Q^{t_{\text{end}}}_{k,i}$ k-th component of the solution vector at the end of the simulation, and $Q^{\text{exact}}_{k,i}$ corresponding exact solution. The order of accuracy at step j is computed as

$$p^n_{k,j} = \frac{\ln\left(\frac{L^n_{k,err}(t_{\text{end}},\Delta x_j)}{L^n_{k,err}(t_{\text{end}},\Delta x_{j-1})}\right)}{\ln\left(\frac{\Delta x_j}{\Delta x_{j-1}}\right)}, \quad n = 1, 2, \infty. \tag{3.15}$$

We consider 5 mesh refinement steps, starting from $N_1 = 32$ computational cells. Table 3.1 displays the empirical convergence rates for the first and second order numerical methods introduced, respectively in sections 2.2.2.1.1 and 2.2.2.1.2, with conservative treatment of the transport problem. The expected convergence rate for all quantities is achieved, and we may notice that errors obtained with the second order method are significantly lower than errors obtained with the first order formulation, especially considering the flow rate.

Variable	Order	Mesh	$L^1_{err}(t_{\text{end}}, \Delta x_j)$	$L^2_{err}(t_{\text{end}}, \Delta x_j)$	$L^\infty_{err}(t_{\text{end}}, \Delta x_j)$	p^1_j	p^2_j	p^∞_j
A	1	32	$6.12{\cdot}10^{-1}$	$7.04{\cdot}10^{-2}$	$1.32{\cdot}10^{-2}$	-	-	-
		64	$3.44{\cdot}10^{-1}$	$3.99{\cdot}10^{-2}$	$7.83{\cdot}10^{-3}$	0.83	0.82	0.76
		128	$1.84{\cdot}10^{-1}$	$2.15{\cdot}10^{-2}$	$4.33{\cdot}10^{-3}$	0.90	0.89	0.85
		256	$9.27{\cdot}10^{-2}$	$1.08{\cdot}10^{-2}$	$2.20{\cdot}10^{-3}$	0.99	0.99	0.98
		512	$4.65{\cdot}10^{-2}$	$5.44{\cdot}10^{-3}$	$1.11{\cdot}10^{-3}$	1.00	0.99	0.99
		1024	$2.33{\cdot}10^{-2}$	$2.73{\cdot}10^{-3}$	$5.58{\cdot}10^{-4}$	1.00	1.00	0.99
	2	32	$3.10{\cdot}10^{-1}$	$3.51{\cdot}10^{-2}$	$6.64{\cdot}10^{-3}$	-	-	-
		64	$6.44{\cdot}10^{-2}$	$7.19{\cdot}10^{-3}$	$1.32{\cdot}10^{-3}$	2.27	2.29	2.33
		128	$5.06{\cdot}10^{-3}$	$5.55{\cdot}10^{-4}$	$9.70{\cdot}10^{-5}$	3.67	3.70	3.77
		256	$1.26{\cdot}10^{-3}$	$1.38{\cdot}10^{-4}$	$2.44{\cdot}10^{-5}$	2.01	2.01	1.99
		512	$3.14{\cdot}10^{-4}$	$3.44{\cdot}10^{-5}$	$6.15{\cdot}10^{-6}$	2.00	2.00	1.99
		1024	$7.84{\cdot}10^{-5}$	$8.62{\cdot}10^{-6}$	$1.58{\cdot}10^{-6}$	2.00	2.00	1.96
q	1	32	$2.81{\cdot}10^{3}$	$3.11{\cdot}10^{2}$	$4.40{\cdot}10^{1}$	-	-	-
		64	$1.48{\cdot}10^{3}$	$1.65{\cdot}10^{2}$	$2.33{\cdot}10^{1}$	0.92	0.92	0.92
		128	$7.55{\cdot}10^{2}$	$8.38{\cdot}10^{1}$	$1.19{\cdot}10^{1}$	0.97	0.97	0.97
		256	$3.80{\cdot}10^{2}$	$4.22{\cdot}10^{1}$	$5.98{\cdot}10^{0}$	0.99	0.99	0.99
		512	$1.91{\cdot}10^{2}$	$2.12{\cdot}10^{1}$	$3.00{\cdot}10^{0}$	0.99	0.99	0.99
		1024	$9.56{\cdot}10^{1}$	$1.06{\cdot}10^{1}$	$1.50{\cdot}10^{0}$	1.00	1.00	1.00
	2	32	$5.44{\cdot}10^{1}$	$7.10{\cdot}10^{0}$	$1.71{\cdot}10^{0}$	-	-	-
		64	$6.32{\cdot}10^{0}$	$1.08{\cdot}10^{0}$	$4.02{\cdot}10^{-1}$	3.11	2.71	2.09
		128	$9.70{\cdot}10^{-1}$	$1.39{\cdot}10^{-1}$	$6.48{\cdot}10^{-2}$	2.70	2.96	2.63
		256	$2.25{\cdot}10^{-1}$	$2.96{\cdot}10^{-2}$	$1.61{\cdot}10^{-2}$	2.11	2.23	2.01
		512	$5.39{\cdot}10^{-2}$	$6.72{\cdot}10^{-3}$	$4.01{\cdot}10^{-3}$	2.06	2.14	2.00
		1024	$1.32{\cdot}10^{-2}$	$1.59{\cdot}10^{-3}$	$1.00{\cdot}10^{-3}$	2.03	2.08	2.00
$A\phi$	1	32	$2.67{\cdot}10^{0}$	$2.95{\cdot}10^{-1}$	$5.20{\cdot}10^{-2}$	-	-	-
		64	$1.15{\cdot}10^{0}$	$1.29{\cdot}10^{-1}$	$2.44{\cdot}10^{-2}$	1.22	1.19	1.09
		128	$4.01{\cdot}10^{-1}$	$4.64{\cdot}10^{-2}$	$9.29{\cdot}10^{-3}$	1.52	1.47	1.39
		256	$2.01{\cdot}10^{-1}$	$2.35{\cdot}10^{-2}$	$4.73{\cdot}10^{-3}$	1.00	0.98	0.97
		512	$1.01{\cdot}10^{-1}$	$1.18{\cdot}10^{-2}$	$2.39{\cdot}10^{-3}$	0.99	0.99	0.99
		1024	$5.05{\cdot}10^{-2}$	$5.95{\cdot}10^{-3}$	$1.20{\cdot}10^{-3}$	1.00	0.99	0.99
	2	32	$4.62{\cdot}10^{-1}$	$7.08{\cdot}10^{-2}$	$2.69{\cdot}10^{-2}$	-	-	-
		64	$8.74{\cdot}10^{-2}$	$1.32{\cdot}10^{-2}$	$5.65{\cdot}10^{-3}$	2.40	2.42	2.25
		128	$1.55{\cdot}10^{-2}$	$2.35{\cdot}10^{-3}$	$1.34{\cdot}10^{-3}$	2.50	2.49	2.07
		256	$3.30{\cdot}10^{-3}$	$4.83{\cdot}10^{-4}$	$3.75{\cdot}10^{-4}$	2.23	2.29	1.84
		512	$7.38{\cdot}10^{-4}$	$1.01{\cdot}10^{-4}$	$9.85{\cdot}10^{-5}$	2.16	2.26	1.93
		1024	$1.73{\cdot}10^{-4}$	$2.22{\cdot}10^{-5}$	$2.45{\cdot}10^{-5}$	2.09	2.19	2.01

Table 3.1: Empirical convergence orders for the first and second order numerical methods introduced in sections 2.2.2.1.1 and 2.2.2.1.2, with conservative treatment of the transport problem.

3.1.3 Computational resources

We assess here the computational resources required to run the following simulations for one cardiac cycle on a workstation equipped with a 12th Gen Intel(R) Core(TM) i9-12900K processor (8 Performance-cores, 8 Efficient-cores, Max Turbo Frequency 5.2 GHz, Performance-core Max Turbo Frequency 5.10 GHz, Efficient-core Max Turbo Frequency 3.90 GHz):

- Purely haemodynamic simulations (H) using the ADAVN and ADAVN86 vascular networks, with first and second order numerical schemes and a characteristic mesh spacing of $\Delta x = 1$ cm;
- Simulations including also tracer transport (H + T) using the ADAVN and ADAVN86 vascular networks, with first and second order numerical schemes and a characteristic mesh spacing of $\Delta x = 1$ cm.

Simulations were executed using a varying number of processes (1, 2, 4, 8). Multithreading did not provide any computational advantage. The numerical method employs local time stepping following a CFL condition, as described in Müller et al. (2016). No additional tests were performed to quantify the impact of gas exchange modelling, as the dominant computational cost is expected to arise from solving the 1D blood-flow equations coupled with transport.

Results are summarised in table 3.2 and figure 3.3. Figures 3.4 and 3.5 illustrate the CPU time scaling behaviour for the ADAVN and ADAVN86 networks, respectively, and figure 3.6 reports the ratios of elapsed times for the two networks. A substantial reduction in computational cost is observed for simulations using the ADAVN86 model, particularly for the second order scheme, with respect to the full model. Profiling indicates that, for this network, a significant slowdown originates from solving the Starling resistor models in the brain. Finally, figure 3.7 reports the ratios between elapsed times obtained with haemodynamics and transport, and with haemodynamic only simulations. The largest impact is observed for second order simulations on the ADAVN86 network, where elapsed times increase by more than 50%. For all other cases, the inclusion of transport leads to an average increase of approximately 25%.

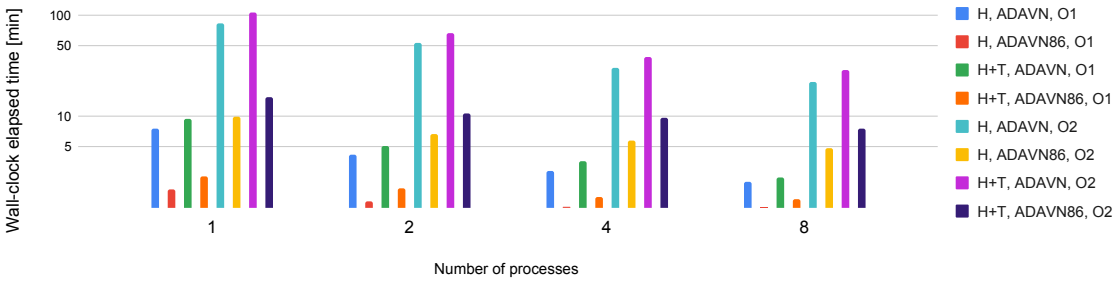

Figure 3.3: Wall clock elapsed time [min]. "pr" denotes the number of processes. Results are expressed using a logarithmic scale.

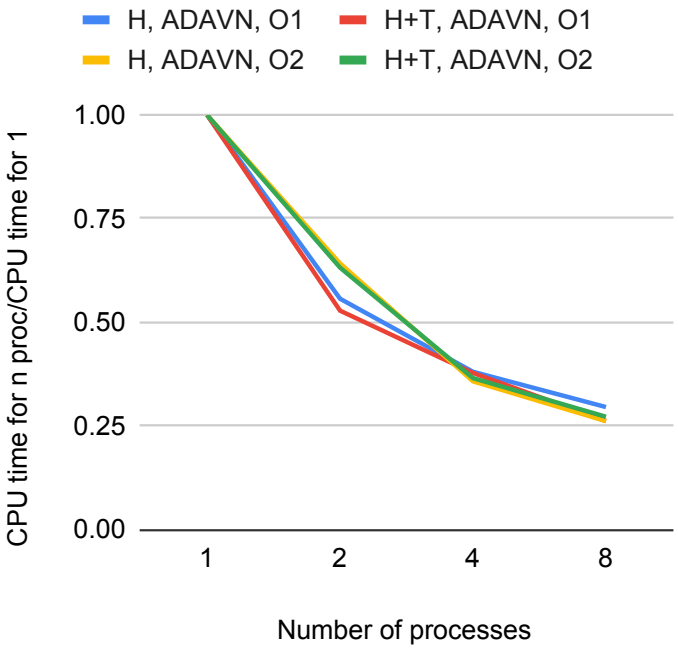

Figure 3.4: Ratio between the elapsed time obtained with *n=1,2,4,8* processes and the elapsed time obtained for 1 process for the ADAVN network.

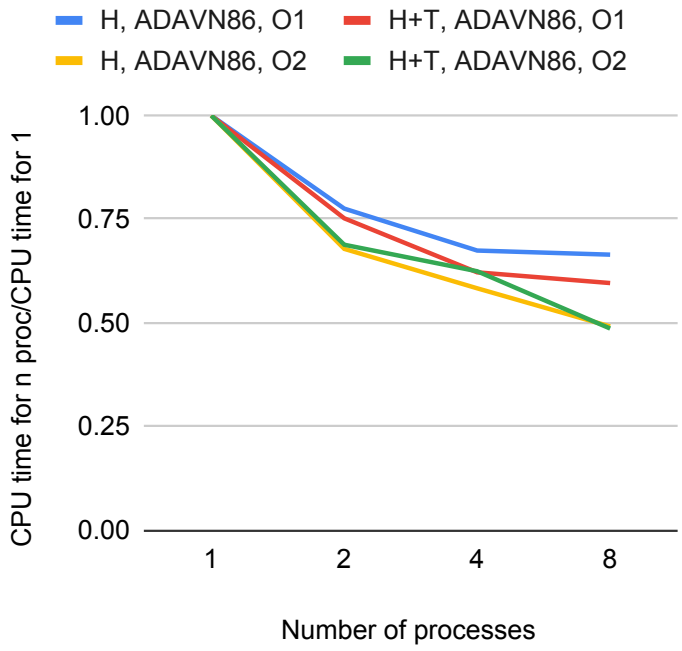

Figure 3.5: Ratio between the elapsed time obtained with *n=1,2,4,8* processes and the elapsed time obtained for 1 process for the ADAVN86 network.

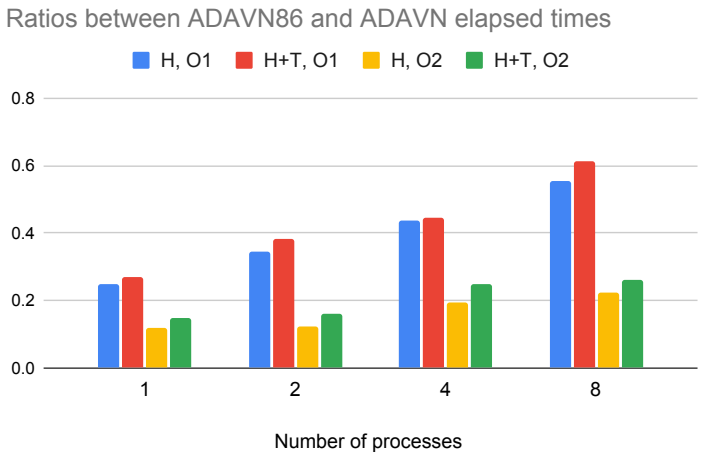

Figure 3.6: Ratio between elapsed times obtained for the ADAVN86 and ADAVN networks.

	Haemodynamics				Haemodynamics + transport			
	ADAVN		ADAVN86		ADAVN		ADAVN86	
	O1	O2	O1	O2	O1	O2	O1	O2
1 pr	457.68	5026.96	112.96	592.88	573.92	6378.8	154.56	932.4
2 pr	254.72	3226.872	87.6	402.16	302.88	4029.12	116.24	641.76
4 pr	174	1795.36	76.16	345.68	216.56	2327.68	96.08	582
8 pr	135.04	1312.16	75.04	291.12	150	1732.48	92.08	453.12

Table 3.2: Wall clock elapsed seconds. "pr" denotes the number of processes.

Figure 3.7: Ratio between elapsed times obtained for simulations with haemodynamics and transport (H + T) and with haemodynamics only (H).

3.2 Well-balanced high-order method for non-conservative hyperbolic PDEs with source terms

This section is adapted from: Colombo, C., Dalmaso, C., Müller, L. O., Siviglia, A. (2026). Well-balanced high-order method for non-conservative hyperbolic PDEs with source terms: application to one-dimensional blood flow equations with gravity. Journal of Computational Physics, 114975.

This section presents the numerical tests conducted to evaluate the performance of the high-order numerical method presented in Section 2.2.3. Two representative test cases are considered: the scalar Burgers' equation and the hyperbolized blood flow equations (BFEs) system with gravity, introduced in section 3.2.2. To carry out these tests, we employ both second- and third-order implementations of four different methods for comparison. The first is our method, which combines the GRP-based reconstruction with the well-balanced DET solver (GRP+DET-WB) Müller et al. (2016). The second method employs the GRP-based reconstruction, coupled with the original, non-well-balanced DET solver (GRP+DET). The third method combines the WENO reconstruction with the well-balanced DET solver (WENO+DET-WB). The fourth method is a reference approach based on the WENO reconstruction combined with the original DET solver (WENO+DET). More details about the WENO reconstruction can be found in (Liu et al., 1994).

3.2.1 Scalar case: Burgers' equation

We replicate the test proposed by Guerrero Fernández et al. (2022), where we consider the following one-dimensional scalar Burgers' equation with algebraic nonlinear source term, expressed in quasi-linear form (2.72) as

$$\partial_t q + q\partial_x q = q^2, \quad x \in \Omega, \quad t \in \mathcal{T}, \tag{3.16}$$

with initial condition (see figure 3.8A) defined as

$$q(x,0) = \exp(x) + 0.3\exp\big(-200(x+0.5)^2\big), \quad x \in \Omega, \tag{3.17}$$

and left boundary condition as

$$q(x_A,t) = \exp(x_A), \quad t \in \mathcal{T}. \tag{3.18}$$

A transparent right boundary condition is also enforced. Stationary solutions of equation (3.16) can be computed either analytically as

$$q(x) = \exp(x), \quad x \in \Omega, \tag{3.19}$$

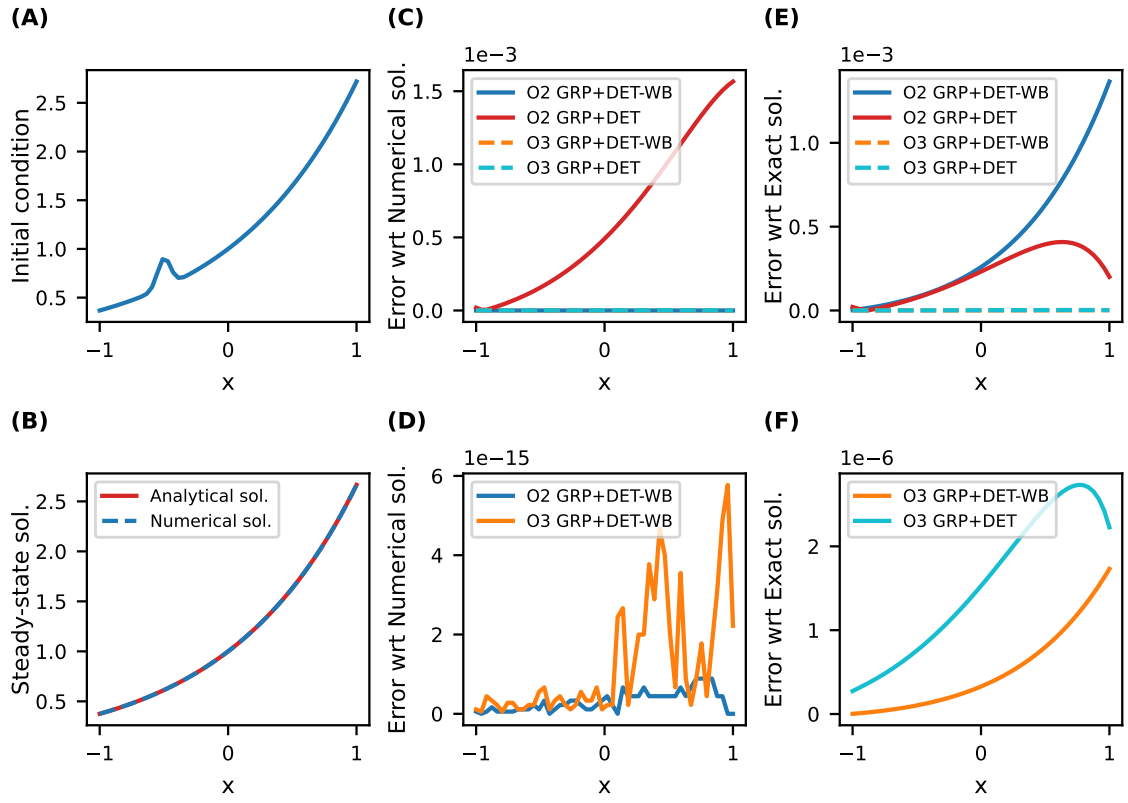

Figure 3.8: Burgers' problem. Initial condition (A), steady-state solution (B), and errors in space between the numerical solution and the steady-state solution obtained either numerically via a Runge Kutta scheme of the same order as the DET solver (Heun's method for O2, RK3 for O3 simulations)
(C and D) or analytically (E and F). Results are shown for both second and third-order implementations of the GRP+DET and the GRP+DET-WB methods.

or numerically by applying the procedure described in section 2.2.3.2.

The goal of this test is to demonstrate the ability of our numerical scheme to recover and preserve the stationary solution of equation (3.16) when the initial condition (3.17) is given by a small spatial perturbation of that stationary solution. We consider a computational domain $\Omega = [-1, 1]$, discretized through a mesh of $N = 50$ computational cells, and we stop our simulations at the final time $t^K = 40\,\mathrm{s}$. We use a CFL number of 0.9 to compute $\Delta t^n = \mathrm{CFL} \cdot \Delta x / \nu$, with

$$\nu = \max(||\mathbf{q}^n||_{L^\infty}, ||\mathcal{V}^n||_{L^\infty}), \tag{3.20}$$

where $\mathbf{q}$ is the vector containing the cell averages q_i^n of the solution in S_i at time t^n, and $\mathcal{V}$ is a vector containing the maximum, on each computational cell, between the left and

N	L^1	L^∞	$O(L^1)$	$O(L^\infty)$	L^1	L^∞	$O(L^1)$	$O(L^\infty)$
	Order 2				Order 3			
32	$1.9{\cdot}10^{-3}$	$3.2{\cdot}10^{-3}$	-	-	$3.8{\cdot}10^{-6}$	$6.4{\cdot}10^{-6}$	-	-
64	$4.9{\cdot}10^{-4}$	$8.4{\cdot}10^{-4}$	2.0	1.9	$4.8{\cdot}10^{-7}$	$8.3{\cdot}10^{-7}$	3.0	2.9
128	$1.2{\cdot}10^{-4}$	$2.2{\cdot}10^{-4}$	2.0	2.0	$6.1{\cdot}10^{-8}$	$1.1{\cdot}10^{-7}$	3.0	3.0
256	$3.1{\cdot}10^{-5}$	$5.5{\cdot}10^{-5}$	2.0	2.0	$7.6{\cdot}10^{-9}$	$1.3{\cdot}10^{-8}$	3.0	3.0
512	$7.8{\cdot}10^{-6}$	$1.4{\cdot}10^{-5}$	2.0	2.0	$9.6{\cdot}10^{-10}$	$1.7{\cdot}10^{-9}$	3.0	3.0

Table 3.3: Burgers' equation: L^1 and L^∞ error norms, and corresponding empirical convergence rates for a second- and third-order implementation of the numerical scheme. N is the number of computational cells.

right states $q^{+,n}_{i-\frac{1}{2}}$ and $q^{-,n}_{i+\frac{1}{2}}$ and their average $\mathcal{M} = 0.5(q^{+,n}_{i-\frac{1}{2}} + q^{-,n}_{i+\frac{1}{2}})$. The time step Δt^n is updated at each iteration of the method and, if necessary, when computing space-time predictions. In this way, we account for the highest wave speed that arises in the presence of shocks and rarefactions. Moreover, we solve equation (2.96) employing a maximum number of iterations equal to the order of accuracy of the method (Dumbser et al., 2008).

In figures 3.8C and 3.8D, we show the absolute errors between the numerical solution of the steady-state problem obtained through an appropriate Runge-Kutta scheme, and the numerical solution of equation (3.16) obtained using the GRP+DET-WB and the GRP+DET methods. Similarly, we display in figures 3.8E and 3.8F the errors between the analytical solution (3.19) and the numerical solution obtained using the GRP+DET-WB and the GRP+DET methods.

We also perform an empirical convergence test to verify whether our method reaches the expected order of accuracy. We report in table 3.3 L^1 and L^∞ error norms between the numerical solution obtained with the GRP+DET-WB method and the analytical solution (3.19), along with the corresponding empirical convergence rates.

3.2.2 System case: hyperbolized blood flow equations

We consider the hyperbolized BFEs system introduced in chapter 2.2.2, where we drop the transport equations, the space dependency of ϵ_0 and ϵ_r, and include a gravity term Ag_x in the source term. This system of PDEs can be written in quasi-linear form as in equation (2.72), where we have

$$\mathbf{Q} = [A, q, \psi, A_0, h_0, E_e, E_c, p_r]^T, \tag{3.21}$$

$$\mathbf{A}(\mathbf{Q}) = \begin{bmatrix} 0 & 1 & 0 & 0 & 0 & 0 & 0 & 0 \\ c^2 - u^2 & 2u & \frac{A}{\rho}\partial_\psi\zeta & \frac{A}{\rho}\partial_{A_0}\zeta & \frac{A}{\rho}\partial_{h_0}\zeta & \frac{A}{\rho}\partial_{E_e}\zeta & \frac{A}{\rho}\partial_{E_c}\zeta & \frac{A}{\rho} \\ 0 & -1/T & 0 & 0 & 0 & 0 & 0 & 0 \\ 0 & 0 & 0 & 0 & 0 & 0 & 0 & 0 \\ \vdots & & & & \cdots & & & \vdots \\ 0 & 0 & 0 & 0 & 0 & 0 & 0 & 0 \end{bmatrix}, \tag{3.22}$$

with $u = q/A$, and $c = \sqrt{\frac{A}{\rho}\partial_A\zeta}$, and where

$$\mathbf{S}(\mathbf{Q}) = \left[0, Rq/A + Ag_x, -\psi/T, 0, 0, 0, 0, 0\right]^T. \tag{3.23}$$

x is the axial coordinate along the vessel, t is the time, $A(x,t)$ represents the cross-sectional area of the vessel lumen, $q(x,t)$ is the flow rate, and $\psi(x,t)$ is an auxiliary variable used in the hyperbolization process (Montecinos et al., 2014) along with the relaxation time $T > 0$. $R(< 0)$ is the coefficient of the friction term, while $g_x(x)$ is the projection of gravity along the vessel's axis defining the gravity term. $\zeta(x,t)$ is the considered constitutive relation that links the cross-sectional area with the blood pressure, thus characterising the vessel's wall mechanics. $\zeta(x,t)$ depends on space-dependent parameters $A_0(x)$, $h_0(x)$, $E_e(x)$, $E_c(x)$, and $p_r(x)$. More details about the spatial parameters, the adopted pressure-area relation, and the system itself along with its eigenstructure can be found in chapter 2.2.1.

The computation of the boundary states for RP (2.97), associated with the hyperbolized BFEs, is carried out as described in section 3.2.2.1, while the adopted path $\mathbf{\Psi}$ is the one reported in equation (2.28), where the transport components are neglected, which ensures that steady states with vanishing velocity ($u = 0$) are exactly preserved, so that the resulting scheme is well-balanced with respect to such equilibria.

To test our method on this PDE system, we considered two geometries. First, we used a single blood vessel to verify the empirical convergence of the method to the desired order of accuracy and to compare its efficiency to that of other numerical schemes. Later, we used an arterial network to assess the well-balanced property of the method over a complex geometry and its performance in transient scenarios. Specifically, we considered the ADAN86 network presented in section 2.1.2. Among all the arteries of ADAN86, we also considered the right internal carotid artery (ICA) as the single blood vessel on which run the first set of tests, due to its tortuous geometry.

The PDE system was solved in each artery of the ADAN86 network using an initial condition given by constant pressure equal to 60 mmHg, and constant zero flow rate. Additionally, three different types of boundary conditions were enforced. At the inlet of the ascending aorta, an inflow boundary condition was set. At the outlet of terminal vessels, either a Dirichlet boundary condition in cross-sectional area or an outflow boundary condition were used. Finally, at the joins between two or three arterial segments, junction

coupling conditions were prescribed. Further details on the treatment of these boundary conditions and their assignment in the context of the proposed numerical scheme are given in (Müller et al., 2016a,b; Müller and Blanco, 2015). We emphasize that boundary and coupling conditions computed as reported in these references are used by the implemented GRP-based reconstruction, thereby discarding the need for more sophisticated techniques, such as ghost cell filling, to achieve high-order accuracy. We also underline that, given the high computational cost of computing (2.79) along junctions, we adopt the local time-stepping algorithm proposed in (Müller et al., 2016a), where, for all tests, the user-defined CFL value is 0.8.

3.2.2.1 Solution to RP (2.97) for the BFEs

Let us consider the following classical RP for the hyperbolized BFEs

$$\begin{cases} \partial_t \mathbf{Q} + \mathbf{A}(\mathbf{Q})\partial_x \mathbf{Q} = \mathbf{0}, \quad x \in \mathbb{R}, t > 0 \\ \mathbf{Q}(x,0) = \begin{cases} \mathbf{Q}_L, & \text{if } x < x_{i+\frac{1}{2}}, \\ \mathbf{Q}_R, & \text{if } x > x_{i+\frac{1}{2}}. \end{cases} \end{cases} \tag{3.24}$$

$\mathbf{Q}_L$ and $\mathbf{Q}_R$ are constant states defined on both sides of the cell interface $x_{i+\frac{1}{2}}$.

Under the assumption of a subcritical flow there is only a possible wave configuration in the $x-t$ half plane given by 4 constant states, namely $\mathbf{Q}_L, \mathbf{Q}_{*L}, \mathbf{Q}_{*R}, \mathbf{Q}_R$ (Spilimbergo et al., 2021). The left and right constant states $\mathbf{Q}_L$ and $\mathbf{Q}_R$ are separated from the unknown states $\mathbf{Q}_{*L}$ and $\mathbf{Q}_{*R}$, respectively, by the left family of waves associated to eigenvalue λ_1, and the right family of waves associated to λ_8. $\mathbf{Q}_{*L}$ and $\mathbf{Q}_{*R}$ are separated from each other by contact discontinuities.

To solve the RP, we assume that the waves associated to λ_1 and λ_8 are rarefactions, and we use the related Riemann invariants to identify the unknowns (Müller et al., 2016a; Spilimbergo et al., 2021). The application of the solver to our problem yields

$$A_{0,L} = A_{0,*L}, \quad h_{0,L} = h_{0,*L}, \quad E_{e,L} = E_{e,*L}, \quad E_{c,L} = E_{c,*L}, \quad p_{r,L} = p_{r,*L}, \tag{3.25}$$

$$A_{0,R} = A_{0,*R}, \quad h_{0,R} = h_{0,*R}, \quad E_{e,R} = E_{e,*R}, \quad E_{c,R} = E_{c,*R}, \quad p_{r,R} = p_{r,*R}, \tag{3.26}$$

and

$$\begin{cases} \psi_L + A_L/T = \psi_{*L} + A_{*L}/T, \\ u_{*L} = u_L - \int_{A_L}^{A_{*L}} \frac{\tilde{c}_T(\xi)}{\xi} d\xi, \\ \psi_R + A_R/T = \psi_{*R} + A_{*R}/T, \\ u_{*R} = u_R + \int_{A_R}^{A_{*R}} \frac{\tilde{c}_T(\xi)}{\xi} d\xi, \\ q_{*L} = q_{*R}, \\ p_{*L} + \frac{1}{2}\rho u_{*L}^2 = p_{*R} + \frac{1}{2}\rho u_{*R}^2. \end{cases} \tag{3.27}$$

The equivalences in equation (3.25) and (3.26) identify the first set of unknowns, while the system in equation (3.27) leads us to the determination of the remaining six variables, namely $A_{*L/R}$, $q_{*L/R}$, and $\psi_{*L/R}$.

In order to solve system (3.27), we first apply the midpoint rule to the two integrals appearing in it. Specifically, we have

$$\int_{\hat{A}}^{A} \frac{\tilde{c}_T(\xi)}{\xi} d\xi \cong (A - \hat{A}) \left[\frac{\tilde{c}_T\left(\frac{A+\hat{A}}{2}\right)}{\frac{A+\hat{A}}{2}} \right], \tag{3.28}$$

with $\hat{A} = \{A_L, A_R\}$, and $A = \{A_{*L}, A_{*R}\}$. Later, we assume that the integrand function between $\hat{A}$ and A is flat enough to write that

$$\frac{\tilde{c}_T\left(\frac{A+\hat{A}}{2}\right)}{\frac{A+\hat{A}}{2}} \approx \frac{\tilde{c}_T(\hat{A})}{\hat{A}}. \tag{3.29}$$

As a result, system (3.27) becomes

$$\begin{cases} \psi_{*L} = \psi_L + A_L/T - A_{*L}/T & = g_1(A_{*L}), \\ u_{*L} = u_L + \tilde{c}_T(A_L) - (A_{*L}/A_L) \cdot \tilde{c}_T(A_L) & = h_1(A_{*R}), \\ \psi_{*R} = \psi_R + A_R/T - A_{*R}/T & = g_2(A_{*R}), \\ u_{*R} = u_R - \tilde{c}_T(A_R) + (A_{*R}/A_R) \cdot \tilde{c}_T(A_R) & = h_2(A_{*L}), \\ q_{*L} = q_{*R}, & \\ p_{*L} + \frac{1}{2}\rho u_{*L}^2 = p_{*R} + \frac{1}{2}\rho u_{*R}^2. & \end{cases} \tag{3.30}$$

We note that $q = Au$, which allows us to write the fifth equation as

$$A_{*L} u_{*L} = A_{*R}, \tag{3.31}$$

and to identify a relation between A_{*L} and A_{*R}, i.e. an ellipse of the form

$$\frac{\tilde{c}_T(A_R)}{A_R} A_{*R}^2 + (u_R - \tilde{c}_T(A_R)) A_{*R} + \frac{\tilde{c}_T(A_L)}{A_L} A_{*L}^2 - (u_L + \tilde{c}_T(A_L)) A_{*L} = 0. \tag{3.32}$$

Writing thus A_{*R} as a function of A_{*L}, i.e. $A_{*R} = f(A_{*L})$, which represents the solution to the ellipse, we can now write all the equations of system (3.30) in terms of the same unknown, obtaining a nonlinear equation

$$p_{*L} + \frac{1}{2}\rho h_1^2(A_{*L}) = p_{*R} + \frac{1}{2}\rho h_2^2(f(A_{*L})), \tag{3.33}$$

which can be solved through a standard Newton method to identify A_{*L}, and a system of

relationships which allow us to retrieve the remaining unknowns.

$$\begin{cases} \psi_{*L} = g_1(A_{*L}), \\ \psi_{*R} = g_2(f(A_{*L})), \\ u_{*L} = h_1(A_{*L}), \\ u_{*R} = h_2(f(A_{*L})), \\ A_{*R} = f(A_{*L}). \end{cases} \tag{3.34}$$

3.2.2.2 Efficiency analysis for a single blood vessel (ICA test)

An efficiency analysis was performed to assess if our method was able to attain a prescribed error at low computational cost. To this end, we considered three different scenarios of increasing complexity, all defined on the same blood vessel, the ICA, and subject to identical boundary conditions. The difference among the scenarios arises solely from the choice of both the gravity term and the spatial parameters, in order to highlight the importance of combining appropriate reconstruction techniques with well-balanced solvers to achieve maximal efficiency.

The first scenario (S1) considers the parameters of the pressure-area relation to be constant along all the vessel axis. Specifically, $A_0 = 0.24$ cm^2, $h_0 = 0.05$ cm, $E_e = 3.4 \cdot 10^6$ dyn/cm^2, and $E_c = 5 \cdot 10^7$ dyn/cm^2. It also assumes the gravity projection g_x to be constant and equal to $981\,\mathrm{cm/s^2}$. For this first scenario, we compared the results obtained using a second-order implementation of the GRP+DET-WB, the GRP+DET, the WENO+DET-WB, and the WENO+DET methods.

The second scenario (S2) considers the parameters of the pressure-area relation to be variable and continuous in space. Additionally, a smooth function of the gravity projection is taken into account

$$g_x(x) = |g|\big[\exp(-x) - \exp(-L)\big], \tag{3.35}$$

where L is the axial length of the ICA, while $|g| = 981\,\mathrm{cm/s^2}$ is the gravitational acceleration modulus. In this second case, we only compared results obtained with the second-order GRP+DET-WB method, to those obtained with the second-order GRP+DET method, to better highlight the differences among the well-balanced and the non-well-balanced solvers.

The third and final scenario (S3) considers a variation to the second case, where the gravity projection is now a polyline. Here, we took into account the real 3D geometry of the ICA and we projected the gravitational acceleration on the vessel axis.

For all the scenarios, we assumed a final simulation time of 10 s, and a minimum number of 4 spatial computational cells that are doubled for each of the 4 considered mesh refinements. Additionally, we assumed a no-flow boundary condition at the inlet of the vessel, and fixed

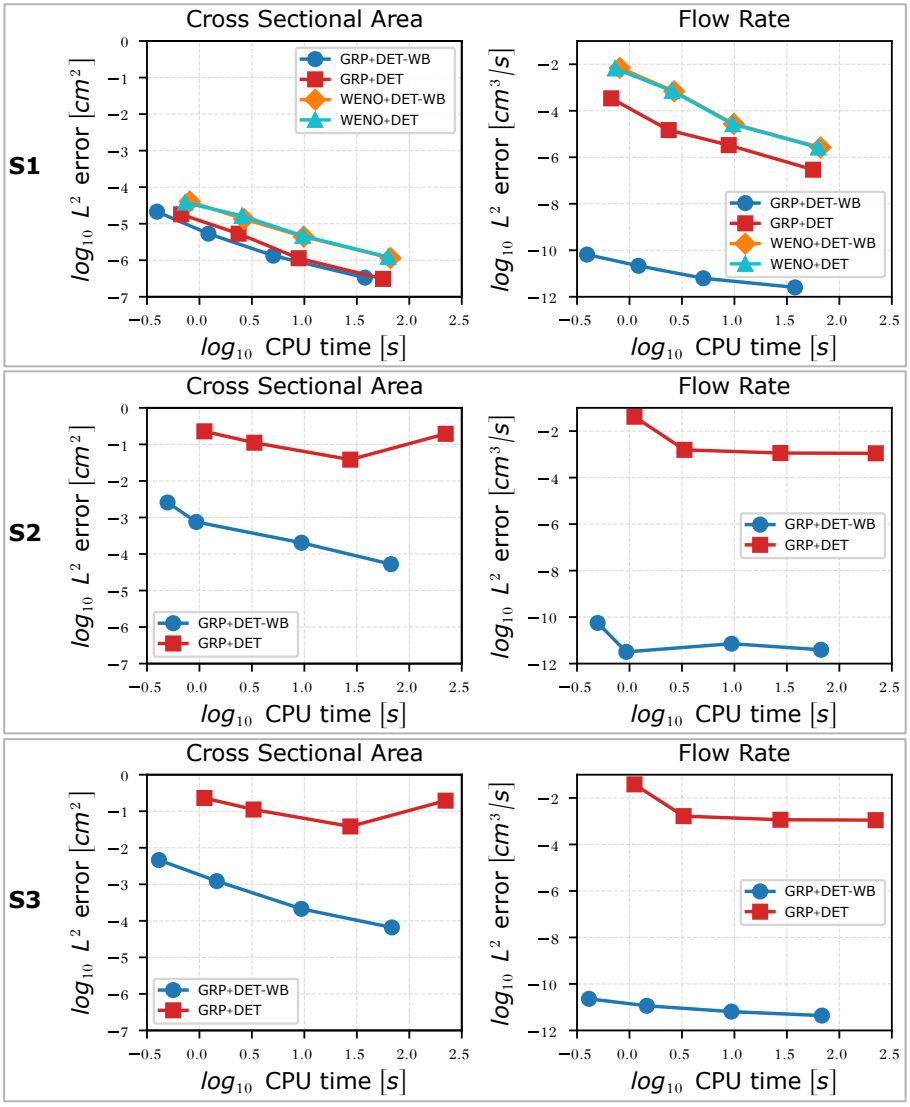

Figure 3.9: Efficiency plots for ICA test. CPU times versus L^2 error norms between the numerical solution and either the exact solution (S1 and S2) or a reference solution (S3), for all the considered scenarios and for 4 consecutive mesh refinements. Each row refers to a different scenario (S1, S2, and S3). Results are shown for both cross-sectional area (left panels) and flow rate (right panels) in logarithmic scale on both axes.

cross-sectional area at the outlet such that the corresponding pressure was 60 mmHg. In all the cases, we run our tests on a workstation that had a Intel Core i9 processor with 16 cores and 24 threads (3.2 GHz clock speed), and 64 GiB of RAM, using 1 thread per test.

Figure 3.9 shows the obtained results at the final simulation time for a second-order implementation of all the considered methods in terms of CPU time and L^2 error norms between the numerical solution and either the exact solution (S1 and S2), or a reference solution (S3) obtained by running a test with 4 times the number of computational cells considered in the final mesh refinement. For all tests, we show results in terms of cross-sectional area and flow rate.

3.2.2.3 Empirical convergence rates for ICA test

An empirical convergence test was carried out to verify whether the proposed method attains its expected theoretical order of accuracy. Convergence rates were computed for the ICA test cases obtained with the GRP+DET-WB method across the three scenarios (S1, S2, and S3). The errors between the computed numerical solutions and either the exact solution (S1 and S2) or a reference solution (S3) were evaluated in both L^1 and L^∞ norms. The results, reported in table 3.4, are given in terms of cross-sectional area. Errors for the flow rate are omitted, as they consistently remained below 10^{-10} cm^3/s.

Variable	N	L^1	L^∞	$O(L^1)$	$O(L^\infty)$	L^1	L^∞	$O(L^1)$	$O(L^\infty)$
Scenario S1		Order 2				Order 3			
A [cm^2]	4	$7.84{\cdot}10^{-5}$	$5.92{\cdot}10^{-6}$	—	—	$8.49{\cdot}10^{-8}$	$6.28{\cdot}10^{-9}$	—	—
	8	$1.96{\cdot}10^{-5}$	$1.48{\cdot}10^{-6}$	2.0	2.0	$1.08{\cdot}10^{-8}$	$1.17{\cdot}10^{-9}$	2.97	2.42
	16	$4.90{\cdot}10^{-6}$	$3.72{\cdot}10^{-7}$	2.0	2.0	$1.36{\cdot}10^{-9}$	$1.68{\cdot}10^{-10}$	2.99	2.80
	32	$1.23{\cdot}10^{-6}$	$9.30{\cdot}10^{-8}$	2.0	2.0	$1.74{\cdot}10^{-10}$	$2.34{\cdot}10^{-11}$	2.97	2.84
Scenario S2		Order 2				Order 3			
A [cm^2]	4	$8.59{\cdot}10^{-3}$	$9.59{\cdot}10^{-4}$	—	—	$5.90{\cdot}10^{-3}$	$4.37{\cdot}10^{-4}$	—	—
	8	$2.49{\cdot}10^{-3}$	$2.85{\cdot}10^{-4}$	1.78	1.75	$9.72{\cdot}10^{-4}$	$1.13{\cdot}10^{-4}$	2.60	1.96
	16	$6.71{\cdot}10^{-4}$	$7.84{\cdot}10^{-5}$	1.89	1.86	$1.36{\cdot}10^{-4}$	$2.03{\cdot}10^{-5}$	2.84	2.47
	32	$1.74{\cdot}10^{-4}$	$2.04{\cdot}10^{-5}$	1.95	1.94	$1.72{\cdot}10^{-5}$	$2.82{\cdot}10^{-6}$	2.99	2.84
Scenario S3		Order 2				Order 3			
A [cm^2]	4	$1.64{\cdot}10^{-2}$	$1.64{\cdot}10^{-3}$	—	—	$9.79{\cdot}10^{-4}$	$1.16{\cdot}10^{-4}$	—	—
	8	$4.04{\cdot}10^{-3}$	$5.15{\cdot}10^{-4}$	2.02	1.67	$8.38{\cdot}10^{-4}$	$8.36{\cdot}10^{-5}$	0.22	0.47
	16	$6.66{\cdot}10^{-4}$	$9.75{\cdot}10^{-5}$	2.60	2.40	$7.48{\cdot}10^{-5}$	$1.36{\cdot}10^{-5}$	3.49	2.62
	32	$2.05{\cdot}10^{-4}$	$3.70{\cdot}10^{-5}$	1.70	1.40	$3.17{\cdot}10^{-5}$	$4.34{\cdot}10^{-6}$	1.24	1.65

Table 3.4: L^1 and L^∞ error norms, and corresponding empirical convergence rates for the cross-sectional area $A(x,t)$ at the final simulation time and for scenarios S1, S2, and S3 for the ICA test, for a second- and a third-order implementation of the numerical scheme. N is the number of computational cells.

3.2.2.4 Well-balance property for the ADAN86 geometry (zero-flow test)

This test is designed to verify if our method can accurately approximate a specific steady-state solution, characterised by zero flow throughout the network and a hydrostatic pressure distribution (i.e. the pressure varies linearly along the vertical axis of the body due to gravity, with higher values in lower regions, such as in the legs, and lower values in elevated regions, such as in the head).

To this end, we considered the ADAN86 network in the upright posture, enabling the simulation of hydrostatic pressure gradients induced by gravity. Then, we assumed the parameters of the pressure-area relation to be variable and continuous in space. In this test, the gravity term $g_x(x)$ was a piecewise polynomial. Specifically, we took into account the real 3D geometry of the different vessels and we projected the gravitational acceleration on the vessels' axes. All blood vessels were discretized using a maximum mesh spacing of 1 cm, and the simulations were performed over 20 s. Finally, we assumed no-flow boundary conditions at both inlet and outlets of the terminal vessels.

Results are shown in figure 3.10 and 3.11 in terms of flow rate (top panel) and pressure (bottom panel). Specifically, the two networks in each panel display the errors at the final simulation time along the ADAN86 network between the zero-flow solution and the numerical solutions obtained with a second (and third) order implementation of the GRP+DET-WB and the GRP+DET methods. A focus on three vessels (left anterior cerebral artery, thoracic aorta, and left femoral artery) is provided in the middle of each panel, where results are reported for the midpoint of the vessels axis and for the last second of simulation. Additionally, figure 3.12 and 3.13 shows the obtained pressure distribution along the network for both the applied methods of order two and three at the final simulation time. A focus on different vessels at different heights of the network is provided in the middle of the panel, where results are displayed for the midpoint of the chosen vessels axis.

3.2.3 Discussion

In this section, we discuss results obtained through the numerical tests outlined above, assessing the accuracy and efficiency of our numerical method, and evidencing its limitations.

Empirical convergence results reported in tables 3.3 and 3.4 demonstrate that the GRP+DET-WB scheme converges with the expected order of accuracy to either the analytical steady-state solution or to a reference solution computed on a sufficiently fine mesh. Additionally, results reported in figure 3.8D confirm that the method is well-balanced when applied to find the steady-state solution of problem (3.16). This proves numerically that, as opposed to the standard WENO reconstruction, the GRP-based reconstruction is well-

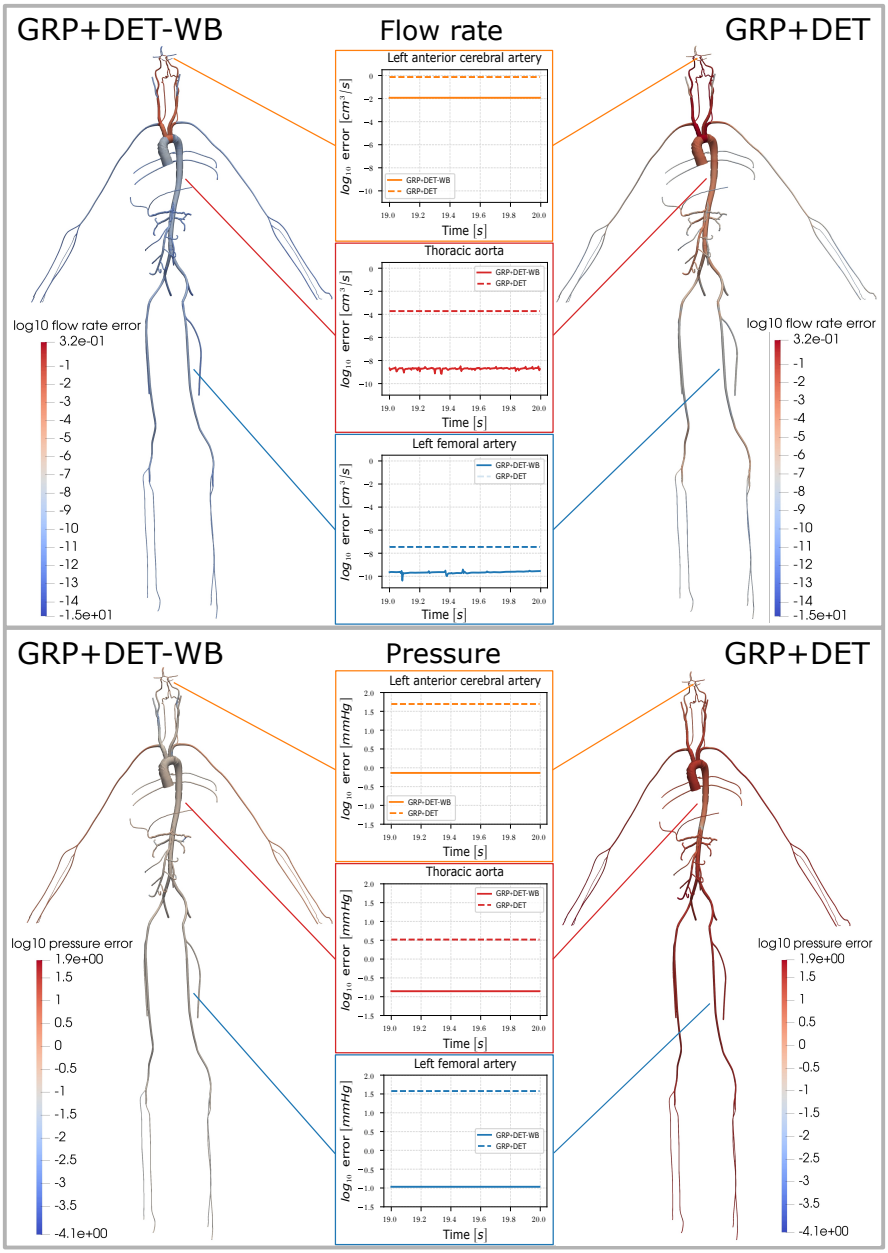

Figure 3.10: zero-flow test. A representation of the ADAN86 network is shown. In the top panel, the colors indicate the errors between zero-flow solution and the second-order numerical solution computed with either the GRP+DET-WB, or the GRP+DET. In the bottom panel, the colors indicate the errors between the reference hydrostatic pressure distribution and the numerical solution computed with either the GRP+DET-WB, or the GRP+DET. A focus on three vessels is provided in the middle of both panels. All the results are shown in logarithmic scale.

balanced up to the third order of accuracy by construction. Indeed, as mentioned in section 2.2.3.4, reconstruction polynomials are computed by enforcing that the boundary states associated with each cell are used either to compute the polynomials slopes or as interpolation points, and that the conservation property holds. Consequently, if the cell average is that of the steady-state solution on the same computational cell, and the boundary states lie on the same steady-state solution, then they are not perturbed by the reconstruction procedure.

This is also confirmed from the efficiency plots reported in figure 3.9. When considering scenario S1 (top row), we can notice that the choice of the spatial reconstruction plays a significant role: results obtained through the GRP+DET method present lower errors, with the same spatial discretization, than results obtained through the WENO+DET method. Moreover, the former are comparable, when considering the cross-sectional area, to results obtained through the GRP+DET-WB scheme. As a consequence, we can conclude that the only well-balancing errors introduced within the GRP+DET framework are those associated with the DET solver.

A comparison between numerical results and either the analytical solution of the problem or the reference solution computed on a sufficiently fine mesh (see figures 3.8E, 3.8F, and 3.9), shows that, while the GRP+DET-WB and GRP+DET methods perform similarly in simple cases such as the Burgers' equation and scenario S1 for the BFEs, there is an evident advantage in choosing a well-balanced scheme for more complex scenarios. When considering scenarios S2 and S3 for the BFEs, numerical errors for the cross-sectional area and the flow rate obtained through the GRP+DET-WB scheme are significantly lower than those obtained in the GRP+DET setup with analogous meshes, highlighting the higher consistency of the well-balanced setup. The similar performance of the GRP+DET-WB and GRP+DET schemes in simple scenarios suggests that the approximation of steady-state solutions (see section 2.2.3.2) has a significant impact on the overall numerical errors introduced by the scheme. This poses the problem of choosing an ordinary differential equation solver of high enough accuracy to avoid the introduction of numerical errors that are comparable or higher than those introduced by the absence of well-balancing.

The ability of our numerical method to preserve stationary solutions is also particularly evident when the method is applied to solve the BFEs over a complex geometry like the ADAN86 network. In fact, observing figure 3.10, top panel, it is evident that the errors in flow rate between the exact solution given by zero-flow and the numerical solution are always higher for the GRP+DET case with respect to the GRP+DET-WB case. A minimum of two orders of magnitude difference between the solutions obtained with the two methods is always detected. Additionally, we observe that the maximum errors for the GRP+DET-WB case are found in the neck and head region, due to its intricate geometry. This region presents multiple vessels junctions, and blood vessels with high geometrical variability, which results in a gravity projection ranging from $-981\,\mathrm{cm/s^2}$ to $981\,\mathrm{cm/s^2}$ along the same vessel axis that can significantly influence the approximation of the solution.

Similarly, observing the bottom panel of figure 3.10, we note that the errors in pressure between the zero-flow solution and the numerical solution are generally larger for the GRP+DET case with respect to the GRP+DET-WB case. These errors strongly affect the representation of the pressure distribution. In particular, we expect to see an hydrostatic pressure distribution along the network when a steady-state is reached, with a maximum pressure in the legs region that gradually decreases towards the cerebral region. This behavior is correctly reproduced in figure 3.12 by the GRP+DET-WB scheme, whereas the GRP-DET scheme completely fails to capture the hydrostatic distribution, leading to an incorrect approximation of the target solution with a maximal error of 100 mmHg.

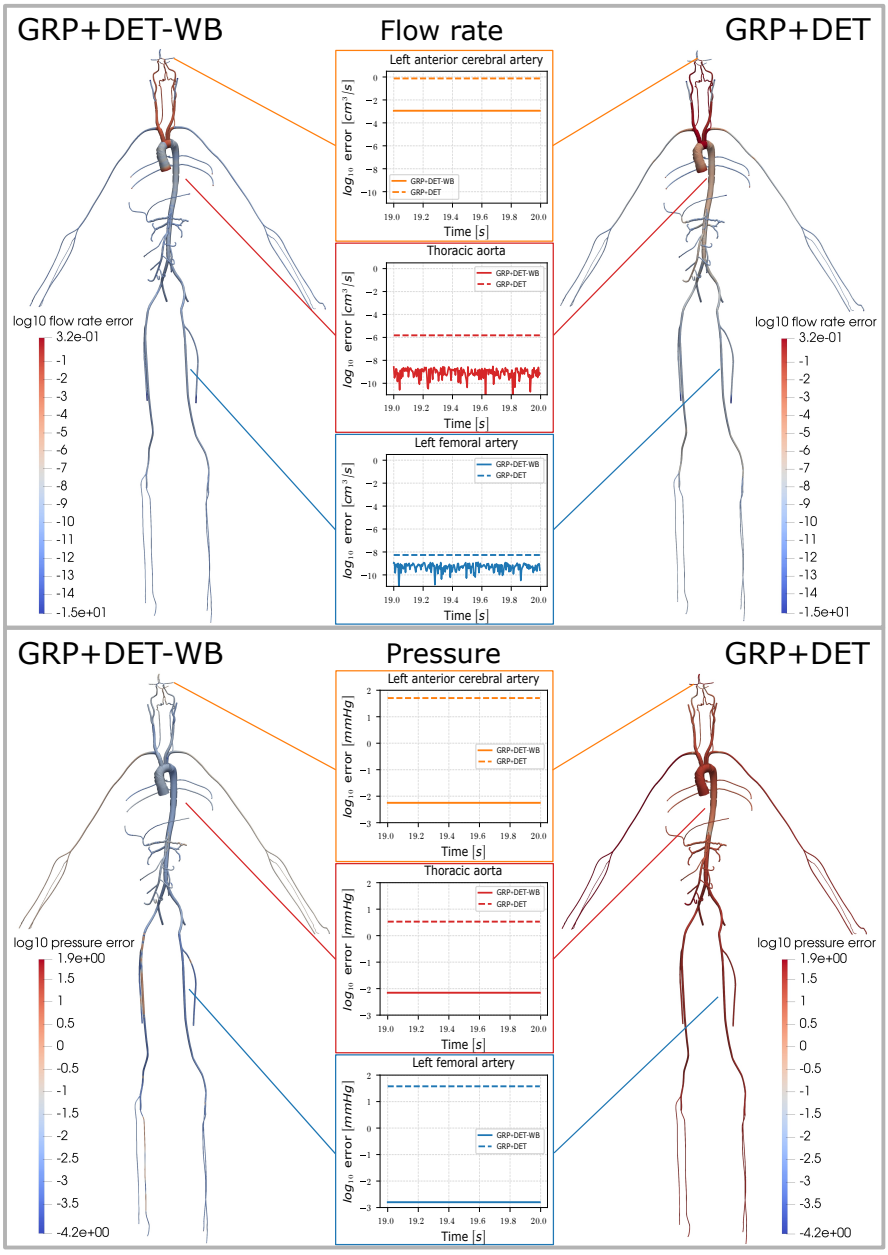

Figure 3.11: Zero-flow test. A representation of the ADAN86 network is shown. In the top panel, the colors indicate the errors between zero-flow solution and the third-order numerical solution computed with either the GRP+DET-WB, or the GRP+DET. In the bottom panel, the colors indicate the errors between the reference hydrostatic pressure distribution and the numerical solution computed with either the GRP+DET-WB, or the GRP+DET. A focus on three vessels is provided in the middle of both panels. All the results are shown in logarithmic scale.

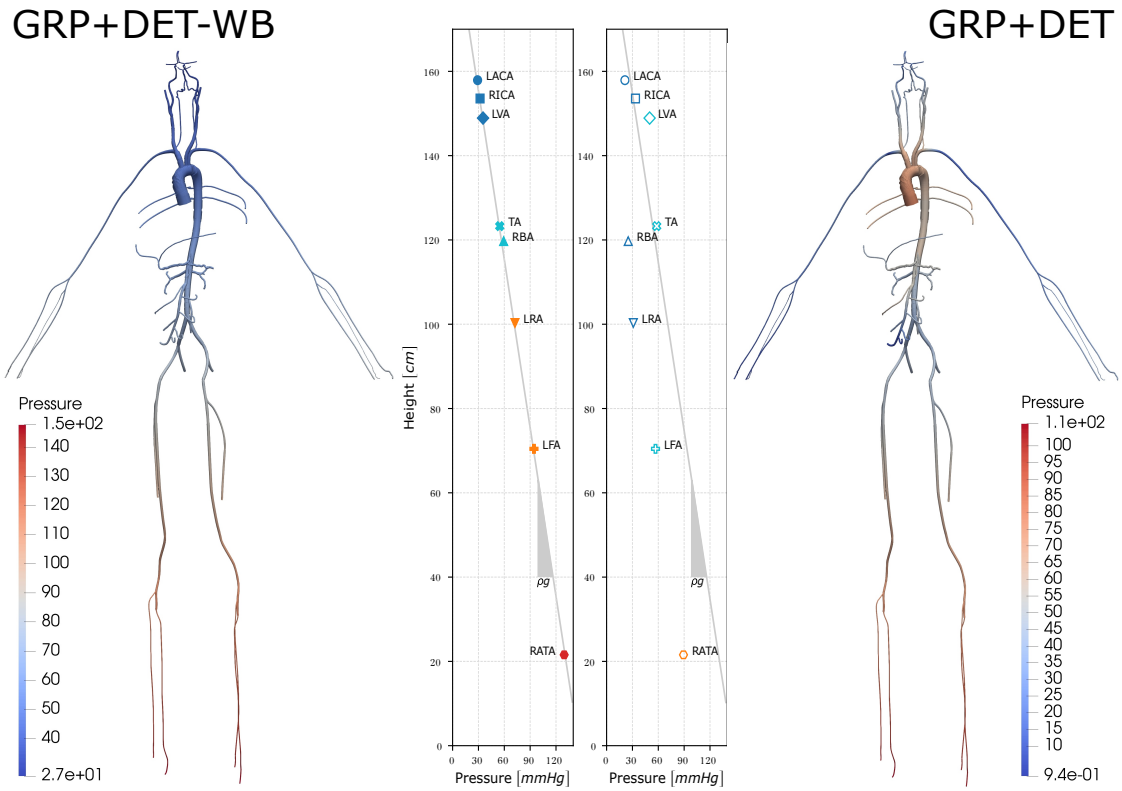

Figure 3.12: Pressure distribution. Pressure distribution at the final simulation time along the ADAN86 network obtained with a second-order implementation of both the GRP+DET-WB method (left) and the GRP+DET method (right). A focus on eight vessels is provided in the middle of the panel, showing how the GRP+DET-WB results respect the expected hydrostatic distribution indicated in light gray. The considered vessels are: LACA: left anterior cerebral artery, RICA: right internal carotid artery, LVA: left vertebral artery, TA: thoracic aorta, RBA: right brachial artery, LRA: left radial artery, LFA: left femoral artery, RATA: right anterior tibial artery.

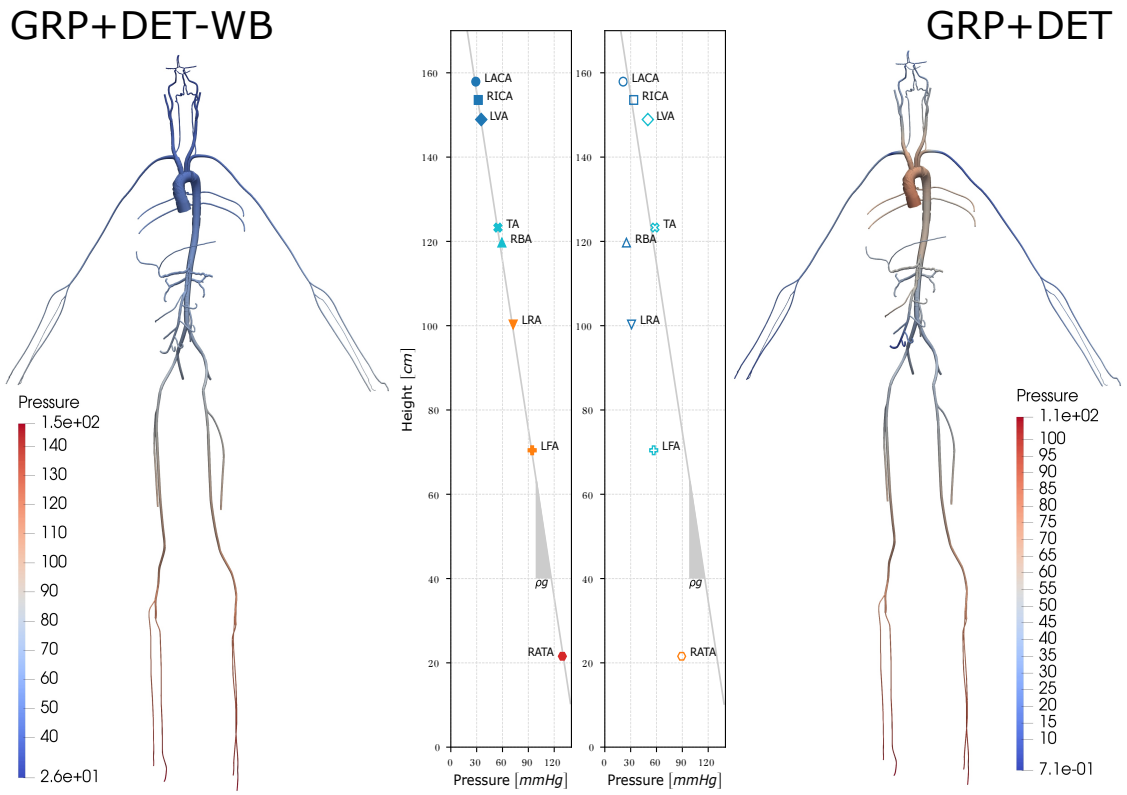

Figure 3.13: Pressure distribution. Pressure distribution at the final simulation time along the ADAN86 network obtained with a third-order implementation of both the GRP+DET-WB method (left) and the GRP+DET method (right). A focus on eight vessels is provided in the middle of the panel, showing how the GRP+DET-WB results respect the expected hydrostatic distribution indicated in light gray. The considered vessels are: LACA: left anterior cerebral artery, RICA: right internal carotid artery, LVA: left vertebral artery, TA: thoracic aorta, RBA: right brachial artery, LRA: left radial artery, LFA: left femoral artery, RATA: right anterior tibial artery.

4

Model verification, validation and applications

This chapter focuses on the verification, validation and application of increasingly complex physiological models, to shift from a purely cardiovascular framework to anatomically and physiologically accurate descriptions of cardiopulmonary interactions. Sections 4.1, 4.2, 4.3 and 4.4 illustrate results obtained through the incremental development of an integrated cardiopulmonary model. Section 4.1 focuses on the computational characterisation of cardiopulmonary mechanical interactions. Section 4.3 extends this framework by incorporating a 1D-0D description of gas transport and exchange. Finally, Section 4.4 introduces local control mechanisms, examining in particular the action of cerebral autoregulation in response to variations in mean arterial pressure and blood gas levels. Section 4.5 presents an application of our model, tailored to the investigation of foot perfusion following a cuff-induced ischaemia test to characterise angiosome perfusion under healthy and pathological conditions.

4.1 Modelling cardiopulmonary mechanical interactions: model validation and physiological insights

This section is adapted from: Dalmaso, C., Blanco, P.J. & Müller, L.O. Cardiopulmonary mechanical interactions. Insights from an anatomically detailed arterial-venous network model. Biomech Model Mechanobiol 24, 1653–1686 (2025). https://doi.org/10.1007/s10237-025-01987-y

The cardiovascular and respiratory systems guarantee optimal organ and tissue perfusion by continuously adjusting their functions in response to internal and external stimuli. In particular, the movement of respiratory muscles during respiration causes cyclic variations

in intrathoracic and intra-abdominal pressures, which in turn affect pressures and flow rate regimes in vessels and organs within the thoracic and abdominal cavities. To model this interplay, we mechanically coupled the ADAVN model (Müller et al., 2023) with the 0D lung mechanics model by Albanese et al. (2016) by prescribing intrathoracic and intra-abdominal pressure waveforms obtained through the latter as external pressures that act on thoracic and abdominal vessels and on the heart.

We verify model predictions with respect to literature data for young healthy males under resting conditions. In addition, we provide a sensitivity analysis of the cardiorespiratory model and compare it with the analysis obtained for the model when respiration is deactivated. The model predictions are discussed in terms of pressure and flow rate waveforms, harmonic analysis, and wave intensity/power analysis.

4.1.1 Simulation setup

In order to assess the impact of respiration on cardiac performance and haemodynamics, we will consider three simulation scenarios throughout sections 4.1.2 and 4.1.3:

- Scenario 1: no respiration, original parametrisation from Müller et al. (2023);
- Scenario 2: respiration, modified parametrisation reported in table 4.2;
- Scenario 3: no respiration, modified parametrisation reported in table 4.2.

To ensure that a periodic state was reached, i.e. that the error in mean arterial pressure and cardiac output obtained for two consecutive respiratory cycles was below 1%, simulations were run for 125 cardiac cycles, each lasting 0.8 s (25 respiratory cycles, each lasting 4 s). Haemodynamic variables were averaged over the last considered respiratory cycle.

4.1.1.1 Parametrisation

Model parameters were assigned, as done by Albanese et al. (2016) and Müller et al. (2023), to reproduce the physiological state of a healthy young male in resting conditions.

4.1.1.1.1 Lung mechanics model

The lung mechanics model presented in section 2.3.4 was parametrised starting from the parameter values reported by Albanese et al. (2016) for simulations in basal conditions. The values of abdominal compliance C_{abd} and end-expiratory abdominal pressure $P_{abd,ee}$ were instead taken from Malbrain et al. (2016); Cobb et al. (2005). In addition, we increased the respiratory rate to $RR = 15$ breaths/min, so that the respiratory cycle duration was a multiple of the cardiac period, which we assumed to be $T_C = 0.8$ s. Respiratory parameters

are reported in table 4.1. Initial conditions were assigned assuming that, at end-expiration, pressures in the lungs equalise with the atmospheric pressure, which is assumed to be equal to zero, pleural pressure has a subatmospheric value of -5 cmH_2O, and intra-abdominal pressure is 2.45 cmH_2O (Cobb et al., 2005).

Compliances [L/cmH_2O]	Unstressed volumes [L]
$C_l = 0.00127$	$V_{u,l} = 0.0344$
$C_t = 0.00238$	$V_{u,t} = 0.00663$
$C_b = 0.0131$	$V_{u,b} = 0.0187$
$C_A = 0.2$	$V_{u,A} = 1.263$
$C_{cw} = 0.2445$	-
$C_{abd} = 0.183$	-
Resistances [cmH_2O s/L]	**Pressures [cmH_2O]**
$R_{ml} = 1.021$	$P_{pl,ee} = -5$
$R_{lt} = 0.3369$	$P_{abd,ee} = 2.45$
$R_{tb} = 0.3063$	
$R_{bA} = 0.0817$	

Table 4.1: Compliances, unstressed volumes, and resistances employed to parametrise the lung mechanics model.

4.1.1.1.2 Cardiovascular model

For the parametrisation of the cardiovascular model, we followed the strategy described in Müller et al. (2023), to which we refer for details.

Total blood volume is composed of stretched and unstretched components. Stretched components include the pressure-generating blood within the 1D systemic circulation, the cardiac chambers, the pulmonary circulation, and the terminal lumped parameter models. In particular, since only stretched blood volume contributes to mean systemic pressure and produces flow, simulations are performed considering only the stretched component, which is set to $V_{\text{set}}^{\text{str}} \simeq 2273 cm^3$.

The application of a negative pressure on the thoracic compartment and of a positive pressure on the abdominal one resulted in increased cardiac output and systemic pressures, and decreased atrial pressures (see table A.1 in appendix A.2). As a consequence, following the local sensitivity analysis reported in (Müller et al., 2023) and noting that physiologically we expect respiration to act as a pump aiding venous return, we empirically modified the free-wall elastances of the cardiac chambers reported by Müller et al. (2023) (equation (2.106)) as reported in table 4.2.

	$E^{\min}_{\mathrm{fw},\alpha}$ RA, LA	$E^{\min}_{\mathrm{fw},\alpha}$ RV, LV	$E^{\max}_{\mathrm{fw},\alpha}$ RA, LA	$E^{\max}_{\mathrm{fw},\alpha}$ RV, LV
Mult. factor	$2.4, 2.4$	$1.7, 1.3$	$2.6, 2.6$	$0.8, 0.8$

Table 4.2: Empirically-determined multiplicative factors affecting the model parameters defined in the original cardiovascular parametrisation (Müller et al., 2023). $E^{\min}_{\mathrm{fw},\alpha}/E^{\max}_{\mathrm{fw},\alpha}$: min/max elastances of chamber α. LA/RA stand for left/right atria, LV/RV for left/right ventricles. All elastances (free-wall, septal and native) are expressed, in the model, in dyn/cm^5.

4.1.1.2 Numerical methods

We provide here a short summary of the methodology employed for the discretisation of the 1D blood flow equations and for the coupling to lumped parameter models, and refer to relevant references for further details. The blood flow equations (2.2), (2.3) constitute an advection-diffusion-reaction system of PDEs, which can be reformulated, within appropriate parameter and state ranges, in terms of a first-order hyperbolic system with stiff source terms (Montecinos et al., 2014; Müller et al., 2016a,b). For baseline simulations, the system was discretised on each 1D domain through the second-order finite volume-type path-conservative numerical scheme presented in Müller et al. (2016a). For the sensitivity analysis, we chose instead to employ a first-order numerical scheme, due to its lower computational cost, after verifying that for a selected subset of parameters the indices obtained through the two methods were comparable. The time step used to conduct the simulations was determined according to the local time step algorithm proposed in Müller et al. (2016a), with a maximum local time step $\Delta t_{\max} = 1ms$ and a Courant-Friedrichs-Lewy number of 0.9. Spatial discretisation was performed considering a characteristic mesh spacing of 1 cm, which guaranteed mesh independence for all considered haemodynamic indices, and all vessels shorter than that were discretised through a single computational cell. Ordinary differential equations for the lung mechanics model were solved through RK4, while those for the remaining lumped parameter models were discretised with the explicit Euler method, with time steps equal to the local time steps of the 1D vessels to which they are coupled (valves, Starling resistors), to the predetermined maximum local time step $\Delta t_{\max}$ (lung mechanics, intracranial pressure), or computed with the same approach used for junctions (heart and pulmonary circulation) (Müller et al., 2016a). In particular, to couple respiratory mechanics to the haemodynamics, we added the pleural pressure P_{pl} (equation (2.129)) and abdominal pressure P_{abd} (equation (2.130)) values generated by the lung mechanics model at each millisecond to the pre-existing external pressures $p_{ext}(x,t)$ (equation (2.3), section 2.2.1), $p_{ext,\zeta}$ (equation (2.123), section 2.3.3), $p_{ext,\alpha}$ (equations (2.103), (2.118), section 2.3.1) and $p_{ext,\xi}$ (equation (2.119), section 2.3.2). Lumped parameter models of the heart, peripheral circulation, and aortic valve were coupled to the 1D vasculature following a standard Riemann problem approach (Müller et al., 2016a).

4.1.2 Results

We assess the performance of our model in terms of cardiac and haemodynamic variables of interest, and show pressure, area and flow rate waveforms, their spectra and intensities at selected locations. Finally, we present local sensitivity analysis results.

4.1.2.1 Waveform analysis

We briefly explain here the methods we employed to analyse the pressure and flow waveforms generated by our cardiorespiratory model, and the motivations underlying their use.

4.1.2.1.1 Spectral analysis

A spectral analysis of pressure and flow waveforms allowed us to identify the main determinants of their oscillatory behaviour. Indeed, while for purely cardiovascular models wave periodicity is only related to cardiac pulsations, in the presence of respiration it is determined by the interaction of a short cardiac component and a longer respiratory component. In particular, the moduli of the harmonics allowed us to assess the effects of respiratory and cardiac pulsatility in veins and arteries located in different parts of the body. Here, the fundamental frequency (first harmonic) of the wave corresponds to the respiratory period, while, since the frequency of the heart rate is assumed to be five times that of the respiratory rate, the fifth harmonic corresponds to the cardiac period. The phase of the first harmonic, moreover, characterises the inspiratory and expiratory behaviors of the considered waves. To perform spectral analysis, we chose to employ the fast Fourier transform algorithm (Cooley and Tukey, 1965) to compute the discrete Fourier transform F_k of a given waveform, characterised by the time points x_n, $n = 0, \dots, N-1$, in order to obtain the amplitude and phases of its harmonics. The single-sided full amplitude of the Fourier transform was computed for the frequency domain indices $k = 1, \dots, N/2 - 1$ as

$$AF_k = 2\left|\frac{1}{N}\sum_{n=0}^{N-1}\left(x_n \exp\left(-i\frac{2\pi}{N}nk\right)\right)\right|. \tag{4.1}$$

Its phase was computed as the anticlockwise angle from the positive real axis on the complex plane, defined between (-180°, 180°]. According to this definition, when considering the first harmonic (fundamental frequency), positive values of the phases are associated with sinusoids that intercept the y-axis during the decreasing portion of their period, while negative values of the phases are associated with sinusoids that intercept it during the increasing portion of their period. As a consequence, we can assert that waveforms whose first harmonics have a positive phase are either decreasing during inspiration or minimal around its beginning, while waveforms whose first harmonics have a negative phase increase during inspiration or are maximal around its beginning.

4.1.2.1.2 Wave intensity analysis (WIA)

Wave intensity analysis (WIA) is a time-domain analysis developed in the field of gas dynamics, which has been employed in the field of cardiovascular physiology to provide mechanistic and prognostic data regarding several pathological conditions such as aortic stenosis, myocardial infarction and left ventricular hypertrophy. This technique is based on the concept that waves travelling along the vasculature can be regarded as the summation of successive wavefronts, which act to either increase or decrease pressure and flow velocity, and can travel forward or backward (Broyd et al., 2017). A positive value of wave intensity indicates that forward-travelling waves predominate, while a negative value indicates that backward-travelling waves predominate.

We performed a nonlinear wave intensity analysis to assess how wave intensities vary over the respiratory cycle, following the procedure described in Mynard and Smolich (2015a); Mynard et al. (2012b); Blanco et al. (2020). We report here only the main equations, and refer to the aforementioned works for details regarding their derivation

$$\mathrm{d}w_{\pm} = \mathrm{d}U \pm \frac{1}{\rho c(P)}\mathrm{d}P, \tag{4.2}$$

$$\mathrm{d}P_{\pm} = \pm\frac{\rho c_{\pm}}{2}\mathrm{d}w_{\pm}, \tag{4.3}$$

$$\mathrm{d}U_{\pm} = \frac{1}{2}\mathrm{d}w_{\pm}, \tag{4.4}$$

$$\mathrm{d}I_{\pm} = \pm\frac{\rho c_{\pm}}{4}\left(\frac{\mathrm{d}w_{\pm}}{\Delta t}\right)^2. \tag{4.5}$$

Here, $w_{\pm}$ denote the Riemann invariants of the mass and momentum conservation equations, U is the cross-sectional averaged flow velocity, $c(P) = \sqrt{\frac{A}{\rho}\frac{\partial P}{\partial A}}$. Furthermore, $c_{\pm} = c(P_{\pm})$, i.e. the wave speed c evaluated at the forward/backward components of pressure, differs from net c if there are either only forward or only backward waves (Mynard et al., 2012b). $\mathrm{d}P_{\pm}$, $\mathrm{d}U_{\pm}$ and $\mathrm{d}I_{\pm}$ are the forward-backward nonlinear decompositions of pressure, flow velocity, and wave intensity. WIA was performed over the five cardiac cycles present in a respiratory cycle to study differences in these waves along the different respiratory phases. We separated wave intensity into forward and backward components, and further distinguished compression and expansion waves. In particular, forward and backward compression waves are characterised by a positive $dP_{\pm}$ and, respectively, a positive dU_{+} and a negative dU_{-}. Forward and backward expansion waves are, instead, characterised by a negative $dP_{\pm}$ and, respectively, a negative dU_{+} and a positive dU_{-}.

4.1.2.1.3 Wave power analysis (WPA)

Wave intensity is not a conserved quantity, so it is not distributed among the vessels in a junction, and it is sensitive to diameter variations. To overcome these limitations, Mynard

and Smolich (2016) proposed to make an analysis in terms of an alternative quantity, the wave power, which is defined in terms of incremental variations of pressure and flow rate. We report here only the main equations used for the analysis and refer to the aforementioned work for details about their derivation

$$\mathrm{d}w_{\pm} = \mathrm{d}Q \pm \frac{1}{Z_c}\mathrm{d}P, \tag{4.6}$$

$$\mathrm{d}P_{\pm} = \pm\frac{Z_{c\pm}}{2}\mathrm{d}w_{\pm}, \tag{4.7}$$

$$\mathrm{d}Q_{\pm} = \frac{1}{2}(1 \mp M)\mathrm{d}w_{\pm} \simeq \frac{1}{2}\mathrm{d}w_{\pm}, \tag{4.8}$$

$$\mathrm{d}\pi_{\pm} = \pm\frac{Z_{c\pm}}{4}\left(\frac{\mathrm{d}w_{\pm}}{\Delta t}\right)^2. \tag{4.9}$$

Here, $Z_c = \frac{\rho c}{A}$ denotes the characteristic impedance, and $Z_{c\pm} = Z_c(A, c_{\pm})$ is its evaluation in the forward/backward components of c. The approximation in the definition of $\mathrm{d}Q_{\pm}$ derives from the assumption that, in physiological settings, flow velocity u is much lower than wave speed c and, as a consequence, the impact of the speed index $M = \frac{u}{c}$ in this equation can be neglected. We chose to adopt, consistently with the approach used for the WIA, a "time-normalized" expression for the wave power, so that the obtained values do not depend on the sampling intervals.

4.1.2.2 Local sensitivity analysis

Local sensitivity indices were computed as

$$\mathcal{S}^{\pm}_{\mathcal{M},\mathcal{P}} = \frac{\hat{\mathcal{M}}^{\pm} - \mathcal{M}}{0.01 \cdot \mathcal{M}}, \tag{4.10}$$

where $\mathcal{M}$ is the baseline value of the cardiac or haemodynamic variable of interest, and $\hat{\mathcal{M}}^{\pm}$ is its value obtained by increasing or decreasing a given parameter $\mathcal{P}$ by 10% of its reference value.

4.1.2.3 Haemodynamic variables

Table 4.3 reports the values of selected cardiac and haemodynamic indices computed with our model for the three aforementioned scenarios, along with reference values from the literature. Figure 4.1 shows how selected haemodynamic indices vary during the respiratory cycle due to the pulsatility of intrathoracic and intra-abdominal pressure, highlighting the role played by the diaphragm as a pump that aids venous return. In addition, figure 4.2 reports ventricular volumes, stroke volume indices, and ejection fractions at end-inspiration and end-expiration, and their averages over the respiratory cycle. We refer to appendix

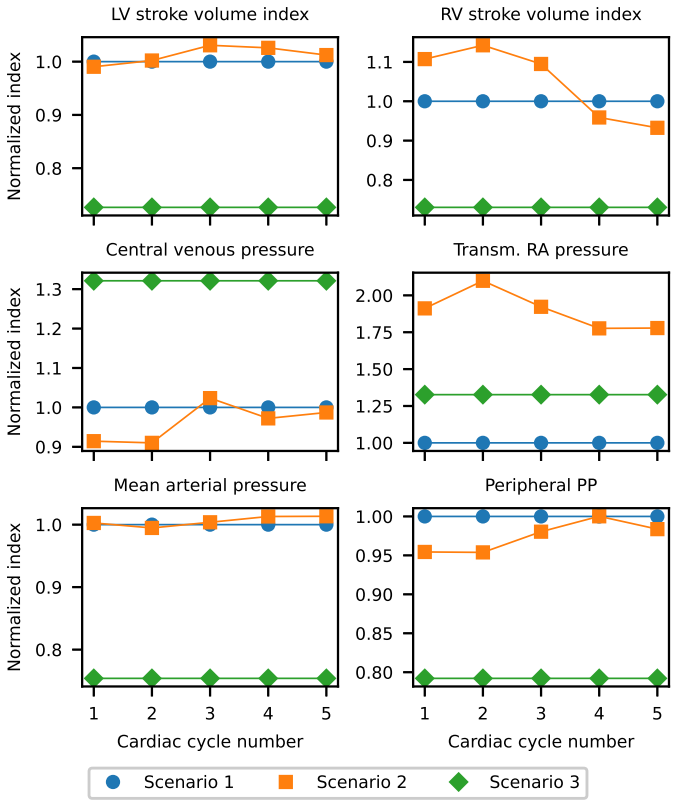

Figure 4.1: Variation of selected haemodynamic indices obtained through scenarios 1-3 (see section 4.1.1) during one respiratory cycle. Indices are normalised with respect to Scenario 1. In blue (round markers) we show Scenario 1, in orange (square markers) Scenario 2, and in green (diamond markers) Scenario 3. The first two markers denote fully/predominantly inspiratory cardiac cycles, while the remaining three markers are associated with purely expiratory cardiac cycles. LV/RV: left/right ventricle; Transm. RA Pressure: transmural right atrial pressure; PP: pulse pressure.

A.1.1 for details regarding the computation of each haemodynamic index and the main features of the population for which the reported reference value was measured.

4.1.2.4 Haemodynamic waveforms

Figures 4.3 and 4.4 show the comparison between waveforms for the heart and pulmonary circulation, which are described through 0D models, obtained for the three considered scenarios (see section 4.1.1). In particular, figure 4.3 shows the pressure/volume waveforms for the four cardiac chambers, while figure 4.4 reports pressure and flow waveforms for pulmonary arteries and veins.

Figures 4.5, 4.6 and 4.7 show haemodynamic waveforms and spectra for selected arteries and veins located in the head, thorax, abdomen and lower limb, to assess how the impact of the external pressures generated by respiration changes across the different regions of the vascular system.

Finally, in figures 4.8, 4.10 and 4.12 we collect results obtained through wave intensity analysis, and in figures 4.9, 4.11 and 4.13 results obtained through wave power analysis.

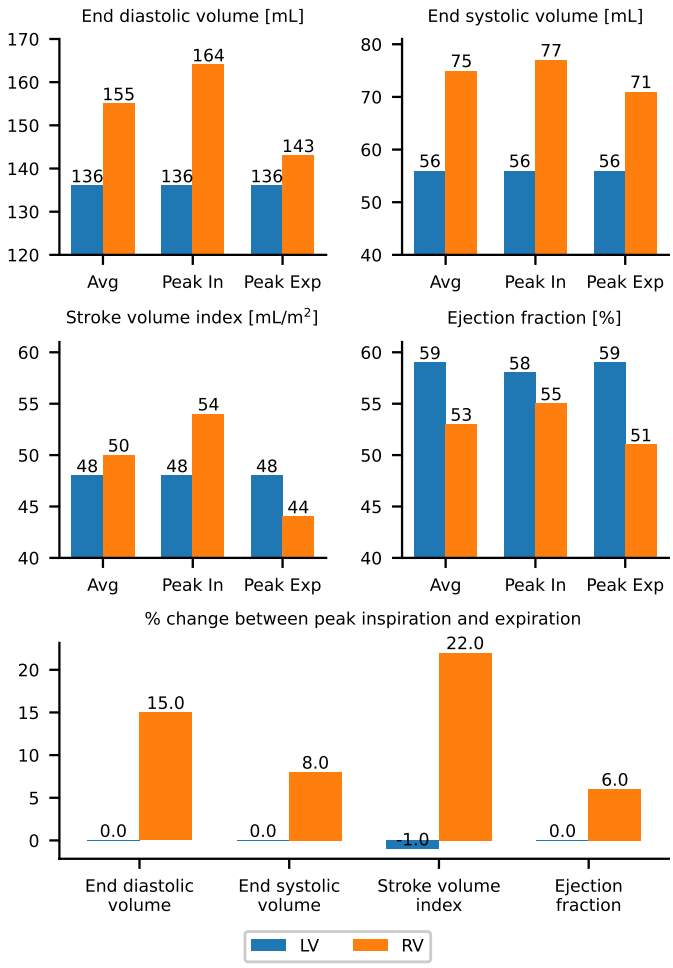

Figure 4.2: Ventricular end-diastolic and end-systolic volumes (EDV, ESV, top row), stroke volume indices and ejection fractions (SVI, EF, middle row) obtained for Scenario 2 (see section 4.1.1): average over the respiratory cycle (Avg), end-inspiratory cardiac cycle (it includes also the first 0.1 s of expiration, Peak In), end-expiratory cardiac cycle (Peak Exp). Bottom row shows the percentage changes of these quantities between peak inspiration and expiration, computed using the end-expiratory value as reference.

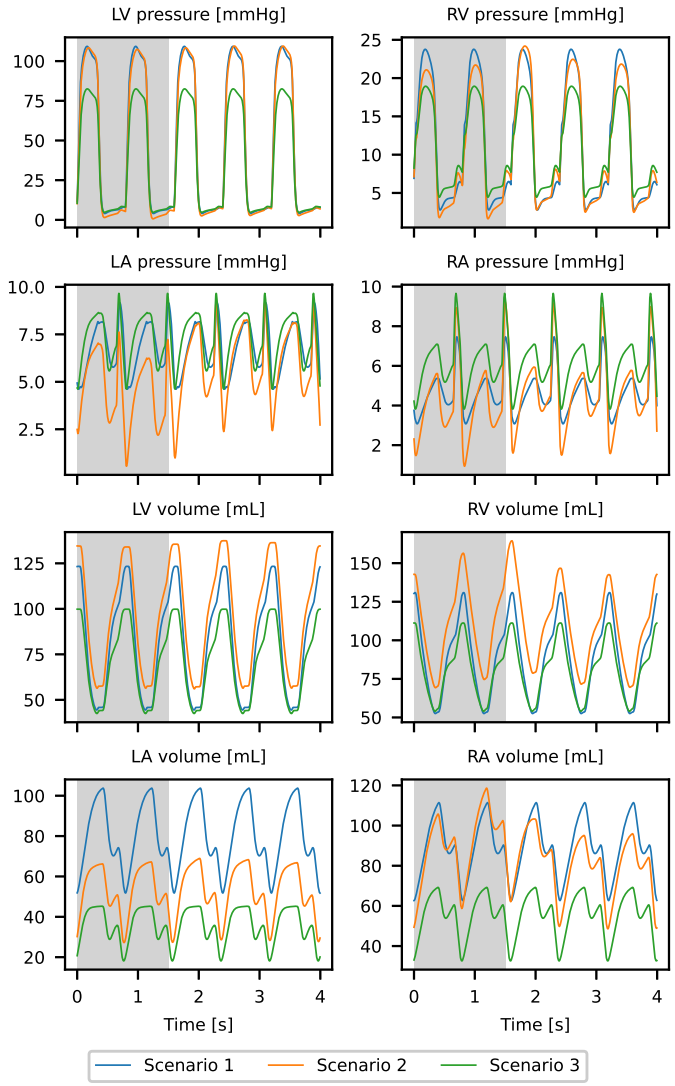

Figure 4.3: Haemodynamic waveforms for cardiac chambers, scenarios 1-3 (see section 4.1.1). From top to bottom: ventricular pressures; atrial pressures; ventricular volumes; atrial volumes. LV/RV are left/right ventricle, LA/RA are left/right atrium. The grey-shaded area highlights inspiration. We depict scenarios 1, 2, 3 respectively through blue, orange and green full lines.

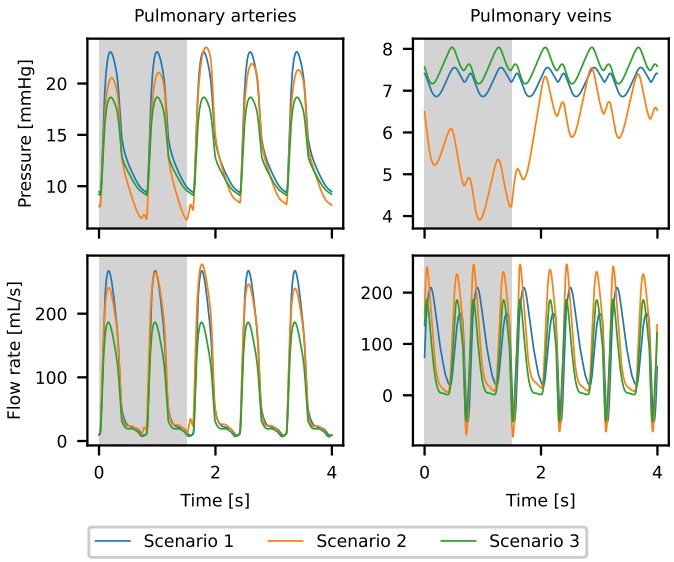

Figure 4.4: Haemodynamic waveforms for the pulmonary circulation. Top row shows pressure waveforms for pulmonary arteries (left) and veins (right). Bottom row shows flow waveforms for pulmonary arteries (left) and veins (right). The grey-shaded area highlights inspiration. We depict scenarios 1, 2, 3 respectively through blue, orange and green full lines.

In particular, figures 4.8 and 4.10 report wave intensity profiles for selected arteries and veins, highlighting forward and backward components, while figure 4.12 shows overall peak forward and backward wave intensities along the arteriovenous paths via the head and the left lower limb. Analogously, figures 4.9 and 4.11 report wave power profiles for selected arteries and veins, while figure 4.13 shows overall peak forward and backward wave power values along the arteriovenous paths via the head and the left lower limb.

4.1.2.5 Sensitivity analysis

Local sensitivity indices were computed for variables $\mathcal{M} = \{\text{CO, CVP, MAP, PPA, LAV}\}$:

- CO [L/min] is the cardiac output, which can be computed as the cardiac-cycle averaged flow rate in the ascending aorta.
- CVP [mmHg] is the central venous pressure, computed as the cardiac cycle-averaged right atrial pressure.
- MAP [mmHg] is the mean arterial pressure, computed as the cardiac-cycle averaged aortic pressure.
- PPA [mmHg] is the central pulse pressure, computed in the ascending aorta at each cardiac cycle as the difference between systolic and diastolic blood pressure.
- LAV [mL] is the cardiac cycle averaged left atrial volume.

To account for respiratory variability, we then averaged each variable over one respiratory

cycle. The sensitivity analysis was performed for all model parameters: 118 for Scenario 2, 97 for Scenarios 1 and 3. In figures 4.14, 4.15, 4.16, 4.17, 4.18, we compare the sensitivity indices estimated through Scenarios 1, 2 and 3 in response to the variation of the 15 most influential parameters pertaining to Scenario 1.

4.1.3 Discussion

In this section, we discuss our results and highlight how they compare to physiological observations. We analyse the impact of breathing on cardiovascular variables of interest, with a particular focus on the respiratory pump function. In addition, we compare waveforms obtained with and without respiration to understand the contribution of respiratory pressures in different regions of our body. Finally, we discuss the results obtained through local sensitivity analysis and highlight the main determinants of assessed variables.

4.1.3.1 Main findings

The main findings of the present study, which will be discussed in detail in the next subsections, are the following. Respiration

- has a fundamental effective pumping action, aiding the cardiac contractility in that function;
- affects mainly the average of haemodynamic variables on the arterial side, while it produces significant beat-to-beat variability on the venous side;
- triggers a complex interplay in terms of waveform conformation, mainly on the venous side;
- alleviates the energy transfer through the arterial system;
- stresses more the venous vasculature.

4.1.3.2 Haemodynamic indices

Indices and variations Var 1 and Var 2 reported in table 4.3 allow us to assess the ability of our model to characterise cardiac volumes and pressures, the interplay between cardiac function and the arterial system, and blood flow distribution in coronary and cerebral vessels. The new parametrisation reported in table 4.2 was devised to approximate, in the presence of respiration (Scenario 2), the original values of the considered indices (Scenario 1). As we can see, we were able to reproduce most of these indices $\mathcal{I}$ satisfactorily, observing a variation Var 1 above 0.15 for only four of them. In particular, we underestimate the left ventricular elastance index and the left atrial volume index, and we overestimate

the ventriculo-arterial coupling index and the API. Except for the ventriculo-arterial coupling index, which is slightly lower than expected, these quantities are still physiologically acceptable. It is important to mention that acceptable ranges for haemodynamic indices reported in the literature are highly variable, due to the use of different populations and measurement/estimation techniques. The large multiplicative factors used for atrial elastances were necessary since our atrial model assumes a linear relation between pressure and volume. While this is an accurate model to describe dynamics at a given pressure range, it fails to reproduce the nonlinear mechanical behaviour of atrial walls when shifting to a significantly different pressure range. This can also be inferred from atrial-related quantities reported in table A.1, comparing Scenario A to Scenario 1: for a central venous pressure that is half of the original one, we have a RAVI that is 50% higher than the original one and, similarly, for a mean left atrial pressure that is 30% lower than the original one we have a LAVI that is about 40% higher than the original one.

The comparison between haemodynamic indices obtained through Scenarios 2 and 3, moreover, allows us to assess how these quantities are affected by pressure fluctuations induced by respiration. In particular, ventriculo-arterial coupling indices and ventricular ejection fractions are not significantly affected by respiration (Claessen et al., 2014), with variations between Scenarios 2 and 3 below 10%. Atrial volumes and pressures, and the API, are, conversely, highly affected by the respiratory effort, with variations above 30%. Finally, systemic pressures (represented in table 4.3 by mean arterial pressure and peripheral systolic, diastolic and pulse pressures) and stroke volumes decrease between 20% and 30% in Scenario 3, when respiration is deactivated and the same parameters are used. We refer to results reported in table A.1 (Scenarios 2 and B) for a quantification of the individual contribution of intrathoracic and intra-abdominal pressure variations. The high impact of respiration on cardiac volumes is related to the inspiratory increase in the pressure gradient between the atria and the systemic vessels above and below the thorax. Indeed, during inspiration, the pressure in thoracic vessels and the heart decreases due to the decrease in pleural pressure, favouring venous return Jozwiak and Teboul (2024). As we can see in figures 4.1 and 4.2, this results in a 15%, 8% and 22% inspiratory increase in right ventricular end-diastolic, end-systolic and stroke volumes, which is consistent with what is reported by (Claessen et al., 2014). Respiratory changes in left ventricular volumes are negligible due to the compliance of the pulmonary vasculature, which dampens fluctuations in left ventricular inflow (Conway, 1975). As for the atria, we can observe, as expected (Magder, 2018), that right atrial pressure is minimal during inspiration (see figure 4.1), and that transmural right atrial pressure, which was computed as the difference between the external pressures acting on the heart (intrathoracic and pericardial) and chamber pressure, increases during inspiration.

From this analysis, we can conclude that our model can reproduce the blood pumping function of respiration (Evans, 2015). Additionally, parameter modifications required to reproduce indices obtained without respiration suggest that purely cardiovascular models

compensate the lack of the respiratory pump function through effective parameters that characterise an effective cardiac function.

4.1.3.3 Haemodynamic waveforms

In this section we discuss haemodynamic waveforms, their spectra and WIA results. We start by focussing on the heart and pulmonary circulation (figures 4.3, 4.4), and then move to systemic arteries (figures 4.5, 4.7, 4.8, 4.9) and veins (figures 4.6, 4.7, 4.10, 4.11).

4.1.3.3.1 Heart and pulmonary circulation

Figures 4.3 and 4.4 collect pulmonary and cardiac waveforms of interest, which are obtained through the 0D models for the heart and pulmonary circulation. As expected, the pressure and flow rate waveforms in the pulmonary arteries mirror the pressure and volume waveforms in the right ventricle (Ragosta and Kennedy, 2017). No literature is available, to our knowledge, regarding the respiratory influence on pulmonary venous pressure, which, according to results reported in figure 4.3, seems relevant. Indeed, our model suggests that this quantity markedly decreases during inspiration, and stabilises during expiration on a slightly lower value than its baseline value without respiration. This behaviour is reflected, albeit less markedly, by left atrial pressure.

4.1.3.3.2 Systemic arteries

Figure 4.5 shows systemic arterial pressure, flow rate, and area waveforms in several regions of the body. As we can see, respiration seems to act consistently on all reported vessels: in the absence of respiration (Scenario 3), average pressures, flow rates and areas are significantly lower than those obtained for Scenario 2 (i.e. with the same parametrisation as Scenario 3 and active respiration). Moreover, if respiration is active we can observe a slight inspiratory decrease in all waveforms, followed by a slight expiratory increase. The impact of respiration on wave periodicity, nonetheless, is negligible compared to that of cardiac periodicity. Indeed, as we can see looking at the pressure and flow spectra for the thoracic aorta obtained for Scenario 2 (see figure 4.7, panel (a)), the fifth harmonic, which corresponds to the cardiac period, is by far the most pronounced, for both pressure and flow rate. This is consistent with available physiological information: in particular, while a small inspiratory fall in systolic arterial pressure is expected, a large one (> 10 mmHg) would usually be associated with pathological conditions such as cardiac tamponade (Feihl and Broccard, 2009).

4.1.3.3.3 Systemic veins

Physiological literature suggests that venous pressure, flow rate and area waveforms are more affected by respiration than arterial ones, and that their variations depend on the considered vessel. We will discuss here features of the waveforms in the venae cavae, internal jugular and femoral veins, comparing them with available literature information. It is worth mentioning that, to our knowledge, very few physiological studies that assess the impact of respiration on venous flow/area/pressure in healthy, non-ventilated patients are available in the literature.

Venae Cavae

Multiple studies performed on healthy subjects report an inspiratory decrease of inferior caval diameters (Nakamura et al., 2016; Molokoane-Mokgoro et al., 2018; Grant et al., 1980; Wallace et al., 2010; Kimura et al., 2010), consistently with what can be observed in figure 4.6 (panel (f)). The magnitude of this variation, which is expressed in the literature in terms of collapsibility or distensibility indices, is highly variable depending on the individual patient's characteristics, on the difference in diaphragmatic excursion associated with the type of inspiration (diaphragmatic, abdominal, deep, shallow, etc.), and on the measurement location (Grant et al., 1980; Kimura et al., 2010). Choosing, for reproducibility reasons, the collapsibility index (CI) range of $30\% \pm 21\%$ reported in Wallace et al. (2010) as reference, we computed the minimum diameter of the vein during inspiration, and the maximum diameter during any other point in the respiratory cycle. We then estimated $\text{CI} = \frac{(\text{Max d. - Min d.})}{\text{Max d.}} \cdot 100$, and obtained an 18% inspiratory decrease in the diameter of the IVC at the level of the hepatic vein, which is physiologically acceptable. As for the flow rate, numerous studies suggest that, in most individuals, it increases in both venae cavae during inspiration and decreases during expiration, although variability is present depending on the respiratory pattern (Kuzo et al., 2007; Smith et al., 1985; Wexler et al., 1968). Pulsatility can be mainly influenced by cardiac periodicity, by the breathing cycle, or by both of them in variable proportions (Joseph et al., 2020). In our case, as we can see in figure 4.6 (panel (f)) and from the negative phase of the first flow rate harmonic in figure 4.7 (panel (g)), there is an increase in inspiratory inferior caval flow. Moreover, the similarity between the amplitudes of the first and tenth flow harmonics shows that both cardiac and respiratory pulsatility have a pronounced impact on the resulting waveform. Additionally, the very high amplitude of the tenth harmonic compared to the fifth one highlights the biphasic nature of both flow and pressure waveforms, which can be clearly observed in figure 4.6 and is one of the defining features of waveform profiles in most veins, distinguishing them from typical arterial signals. The analysis of the flow spectrum for the superior vena cava reported in figure 4.7 (panel (e)), instead, suggests a negligible effect of respiration on the flow rate, since the amplitude of the first harmonic is close to zero. This effect, which can be seen also in figure 4.6 (panel (d)), is consistent with the observation that the respiratory variation in the IVC flow rate is generally significantly larger than in

the SVC reported by Kuzo et al. (2007). It is worth mentioning, moreover, that we can recover the systolic dominance of superior caval flow during both inspiration and expiration, while systolic and diastolic values are very close to each other in the IVC (Appleton et al., 1987).

Internal jugular vein

The quantification of respiratory variations in the flow rate of the internal jugular veins is of interest for the clinical practice because its impairment might be related to neurodegenerative and neuroinflammatory pathologies (Laganà et al., 2017). Laganà et al. (2017) showed for a sample of 19 healthy patients that, while cardiac modulation of flow is generally marked, respiratory modulation in the supine position is variable. Additionally, Laganà et al. (2022a), Laganà et al. (2022b) and Kollmeier et al. (2022) provided a spectral analysis of the flow rate measured via RT-PC MRI for 16/30 young healthy subjects, showing that, for normal respiration, the effect of cardiac periodicity is significantly larger than that of respiratory periodicity. Our results, as we can appreciate looking at figures 4.6 (panel (b)) and 4.7 (panel (c)), are in agreement with these clinical observations: the first harmonic, i.e. the respiratory harmonic, has a negligible amplitude compared to the 5th and 10th harmonics, i.e. those corresponding to cardiac cycle and half-cardiac cycle duration. As for pressure, it has been documented that its average value is lower during inspiration (Applefeld, 1990). In our simulations we observe a mean inspiratory pressure of 4.6 mmHg, and a mean expiratory one of 5.1 mmHg. The inspiratory pressure decrease, moreover, is reflected by the positive phase of the first harmonic in the pressure spectrum (see figure 4.7).

Femoral vein

Several works are available in the literature that examine flow phasicity in the veins of the lower limbs. Abu-Yousef et al. (1997) analysed the common femoral veins of 12 young volunteers through spectral Doppler sonography, and observed that during normal breathing the flow rate is modulated by both cardiac and respiratory phasicity in different ratios: cardiac dominance was observed in 6 patients, respiratory dominance in 4, and in the other two patients the two components were balanced. Moreover, they observed a generalised inspiratory decrease in flow velocity, and the opposite behaviour during expiration. Similarly, Osada et al. (2002) showed for eight healthy males that, during quiet breathing, expiratory blood flow is significantly higher than the inspiratory one, reporting a null blood flow during inspiration, and a blood flow between 4.2 and 11.45 mL/s during expiration. Results reported in figures 4.6 (panel (g)) and 4.7 (panel (h)) show that, in our case, flow in the proximal part of the femoral vein is highly influenced by respiration. The positive phase of the first harmonic indicates that flow decreases during inspiration and, in particular, we obtained an inspiratory average of 2.84 mL/s and an expiratory one of 6.22 mL/s, which is consistent with the one reported by Osada et al. (2002).

Superior sagittal sinus, subclavian vein, coronary sinus

We chose not to devote separate paragraphs for these vessels due to the scarcity of available literature to validate our results. As expected (Laganà et al., 2022b), we can observe in figures 4.6 (panel (a)) and 4.7 (panel (b)) that in the superior sagittal sinus cardiac modulation of flow prevails over the respiratory one during normal respiration. A more accurate validation regarding this vessel will be possible once we include control mechanisms and are thus able to reproduce respiratory manoeuvres such as the Valsalva and Müller manoeuvres. As for the subclavian vein, Patel et al. (1999) show an increased wave amplitude during inspiration, which is confirmed by results reported in figure 4.6 (panel (c)). Literature review delivered no information regarding respiratory variations in the coronary sinus and, more in general, in coronary veins.

4.1.3.4 WIA for selected vessels

We discuss here wave intensity results for selected arteries and veins, as reported in figures 4.8, 4.10. Arterial wave intensity profiles have in general very similar shapes with and without respiration. An early-systolic forward compression wave (dark red) dominates in all reported vessels, with a decrease in its intensity moving towards the periphery. Additionally, a forward expansion wave (light red) is present at all locations during mid-late systole, and it is particularly pronounced in the common femoral artery, where we can observe a very marked decrease in flow rate (see figure 4.5, panel (g)). Similarly, venous wave intensity profiles are, for Scenario 1, qualitatively very similar among each other, albeit with differences in timings and amplitudes. They present marked backward components: an expansion wave which is associated with the systolic flow acceleration caused by the filling of the right atrium, and a more pronounced backward compression wave, which is caused by atrial contraction and is associated with the late diastolic flow reduction (see figure 4.6). The observed wave intensity profile is consistent with the considerations made by Mynard and Smolich (2015a). When considering Scenario 2, so when respiration is active, we can instead observe marked differences depending on the location of the vessel within the vascular network. In general, we can see very dampened wave intensities during inspiration in the lower body, with very small waves at the level of the femoral vein while intrathoracic and intra-abdominal pressures are far from their end-expiratory baseline value. This is not the case, instead, for vessels in the upper body, where wave intensity profiles are comparable with and without respiration, with an overall increase in wave intensity in the presence of respiration. These results were expected from our previous observations but, to the best of our knowledge, no literature is available to validate them.

Figure 4.12 allows us to analyse the behaviour of waves along the vasculature. Looking at the panels for Scenario 2, we can observe the negligible impact that respiration has on wave propagation in the considered arteries, both in the arteriovenous path via the

head and via the left lower limb. We can also observe, consistently with what can be seen analysing the spectra in figure 4.7, how respiration has a more marked impact in the lower body than in the upper body veins, even though marked forward compression waves are observed at end-inspiration and during the first part of expiration in the proximal portion of the IJV, due to the temporary full closure of one of the venous valves, which is instead always either open or only partially closed in the absence of respiration. The general behaviour of forward and backward waves along the vasculature is similar in all considered scenarios and, in particular, we can observe that, consistently with what was observed by Mynard and Smolich (2015a), forward waves slightly decrease as we move towards more peripheral arteries, while backward ones are, in the arteries, around one order of magnitude smaller. Venous wave intensities are, in general, lower than arterial ones, and backward waves are larger than forward waves, with the exception of the superior sagittal sinus, where they are comparable. Indeed, flow in the superior sagittal sinus is conditioned by the action of intracranial pressure in combination with Starling resistors, which results in a predominantly systolic pattern, similar to that observed in the arteries. As one moves toward central veins, there is a marked increase in the backward wave intensity (one order of magnitude for the arteriovenous path via the head, and around 2.5 orders of magnitude for the path through the lower limb).

4.1.3.5 WPA for selected vessels

We compare here wave power results for selected arteries and veins to analogous results obtained in terms of wave intensity. Comparing figure 4.8 to figure 4.9 and figure 4.10 to figure 4.11, we can notice that wave power profiles are very similar to wave intensity ones: forward and backward compressive waves are the most pronounced in arteries and veins, respectively. Additionally, we can confirm that respiration tends to alleviate energy transfer in arteries and, conversely, stresses the venous circulation more. Despite these similarities, we need to point out that the absolute values for wave power and wave intensity are, as expected, markedly different. Indeed, if we were to assume linear flow conditions, $d\pi$ could be expressed as the product of cross-sectional area and wave intensity.

Some other interesting considerations can be made comparing wave power and intensity along the arteriovenous paths via the head and legs (figures 4.12 and 4.13). The first observation regards the much steeper decline in wave power compared to wave intensity moving from central to peripheral arteries, in both considered vascular chains. This is likely due to the fact that, as demonstrated by Mynard and Smolich (2016), total wave power, like flow rate, is preserved at junctions. This is not the case instead for wave intensity, which might be higher in daughter branches compared to parent ones. This behaviour, while still evident, is less marked on the venous side, likely because the venous network we are considering is not as anatomically detailed as its arterial counterpart.

4.1.3.6 Sensitivity analysis

We discuss here the local sensitivity of cardiac output, central venous pressure, mean arterial pressure, central pulse pressure, and left atrial volume to variations in model parameters. In particular, we compare results obtained for the three considered scenarios, to assess on the one hand whether our reparametrisation has a significant impact on the sensitivities and, on the other hand, how sensitivities change turning off respiration (see figures 4.14, 4.15, 4.16, 4.17, 4.18).

Except for the pulse pressure, all variables are mainly influenced by variations in stretched blood volume ($V_{\text{str}}^{\text{set}}$), which has an impact that is 1.5-3 times higher than that of the following parameters (right ventricular free-wall elastance $E_{\text{fw,RV}}^{\text{min}}$, systemic venous compliance $C_{\text{sys,v}}$, and peripheral resistances R_{per}). Other influential parameters include the free-wall elastances of the left ventricle and the atria, the onset of atrial contraction and, for Scenario 2, the end-expiratory value of pleural pressure. These results confirm the strong relation between arterial and venous districts previously demonstrated by Müller et al. (2023) also in the presence of respiration. It is also interesting to note how, compared to results obtained with the original parametrisation from Müller et al. (2023) (Scenario 1), the impact of a 10% increase in the onset of atrial contraction ($t_{\text{onset}^{\text{RA}}}+$, $t_{\text{onset}^{\text{LA}}}+$) tends to be lower in both Scenarios 2 and 3. In the following, we analyse in detail the sensitivity of each variable.

4.1.3.6.1 Sensitivity of CO

As previously mentioned, cardiac output is mostly influenced by variations in stretched blood volume in all considered scenarios. The following four most influential parameters regard the venous circulation and the right heart, with the exception of minimum left ventricular free-wall elastance. Looking at figure 4.14, we can observe how CO responses to variations in stretched blood volume and systemic venous compliance are more pronounced in Scenarios 1 and 3 than in Scenario 2, with sensitivity indices that are 1.5-2 times higher, suggesting that these parameters play a very relevant role in compensating for the absence of respiration. In other words, respiration makes CO less sensitive to variations in these model parameters. Changes in other parameters yield comparable CO variations in all scenarios, except for the 10% delay of right and left atrial contraction, ranked respectively 5th and 11th for Scenario 1, which have instead a minimal impact in Scenarios 2 and 3.

4.1.3.6.2 Sensitivity of CVP

According to the literature, central venous pressure depends on blood volume, peripheral venous tone, intrathoracic pressure and right ventricular function (Didebotham, 2017). Consistently with this expectation, we can observe that, in our model, this variable is extremely influenced by variations in stretched blood volume, in particular in the presence

of respiration. Moreover, in all scenarios, the next most influential parameters are all related to venous circulation (systemic venous compliance is ranked third in all scenarios) or to the right heart, with the exception of the reference-volume elastance of pulmonary veins $E_{0,\mathrm{puv}}$. Additionally, in Scenario 2, end-expiratory pleural pressure, which is ranked 8th, plays a significant role.

4.1.3.6.3 Sensitivity of MAP

The important role of stretched blood volume is observed also for mean arterial pressure, which, in our model, is directly linked to the total blood volume. The third-ranked parameter for Scenarios 1 and 2 is the total peripheral resistance, which is ranked fourth for Scenario 3, with an extremely similar sensitivity. Systemic venous compliance, which is the third-ranked parameter for Scenario 3, is ranked, instead respectively 5th and 7th for Scenarios 1 and 2. It is worth noting, moreover, that the sensitivity of MAP to this parameter in Scenarios 1 and 3 is over 60% higher than that obtained in Scenario 2. This shows that, in the absence of respiration, a more relevant role seems to be played by venous properties, while respiration slightly enhances the effect of the conditions encountered in the peripheral vasculature. Additionally, similarly to what was observed for the CO, the sensitivity of MAP to a 10% delay of atrial contraction in Scenarios 2 and 3 is significantly lower than that in Scenario 1, indicating that this different behaviour is primarily related to our choice of parametrisation.

4.1.3.6.4 Sensitivity of PPA

The variation of central pulse pressure is highly impacted by parameters related to the tube law and to the arterial system. In particular, while for Scenarios 1 and 2 the most influential parameter remains the stretched blood volume, for Scenario 3 it is overtaken by the reference elastin Young modulus E_e. The impact of venous circulation remains non-negligible, with systemic venous compliance being the 7th, 11th and 12th-ranked parameter in Scenarios 1, 2 and 3, respectively.

4.1.3.6.5 Sensitivity of LAV

In addition to the stretched blood volume, which is the most influential parameter, left atrial volume is mostly determined by cardiac properties, with a high influence of left atrial, left ventricular and right ventricular minimum free-wall elastances. The impact of these quantities is comparable in all scenarios. Similarly to what was observed for MAP and CO, LAV obtained in Scenario 1 is also particularly sensitive to a delay in atrial contraction.

4.1.3.6.6 Further remarks

Local sensitivities, defined as the change in model output resulting from a small perturbation of a given input parameter, provide a direct and intuitive measure of model responsiveness, facilitating the identification of dominant parameters and supporting mechanistic interpretation. In contrast, global sensitivity approaches require the specification of plausible parameter ranges. For highly complex models, these ranges are often difficult to justify, as many parameters lack a direct physical interpretation or are not measurable. Moreover, global methods rely on extensive sampling of the multidimensional parameter space, resulting in computational demands exceeding the resources available for this study. A global analysis would thus require for example the use of Gaussian process emulators as surrogates for the full haemodynamic model (Strocchi et al., 2023). Nevertheless, global sensitivity analyses remain preferable when parameter uncertainty is substantial or when interactions among parameters are expected to play a major role in driving variability in model outputs. A pragmatic strategy is therefore to first employ a local approach to identify a subset of influential parameters, and subsequently apply global sensitivity analysis to this reduced parameter set (Eck et al., 2016; Schäfer et al., 2024). This, however, was outside the scope of the present work.

4.1.4 Limitations

This study has some potential limitations. On the one hand, the validation of our model was focused just on some physiological aspects of interest for which we could find a satisfactory amount of data from different sources. We need to reiterate, though, that acceptable ranges for haemodynamic indices, and features of haemodynamic waveforms reported in the literature are highly variable, due to the use of different populations and measurement/estimation techniques. Additionally, while our simulations are based on the anatomical and physiological features of a healthy young male at rest, it would be advisable to perform analogous simulations for a female subject and for subjects of different ages. Indeed, nowadays, medicine is providing increasing evidence about the fundamental role of sex in the pathophysiology of the cardiovascular system (Susin, 2023; Comunale et al., 2020; Corsini et al., 2017; Zaid et al., 2023), and it is well documented that age plays a fundamental role as well (Hirschhorn et al., 2021; Charlton et al., 2019).

Moreover, in order to facilitate the comparison of our results with those obtained through the baseline ADAVN model (Müller et al., 2023), we chose to operate under some assumptions that are valid under physiological conditions, but could be improved in the future. As an example, in the next chapter we show simulation results obtained introducing within the current cardiac model a nonlinear end-diastolic pressure-volume relationship, which, according to the literature, better represents the cardiac performance in diverse pathological conditions.

Furthermore, this work includes no assessment of model behaviour when considering pathological situations and respiratory manoeuvres. Indeed, while our model integrates a detailed description of a one-way mechanical coupling between the vasculature and a lung mechanics module, such simulations require a description of gas exchange and transport, as well as of local cardiorespiratory control mechanisms. Additionally, the effect of gravity has been neglected.

Index	Scenario 1	Scenario 2		Scenario 3		References	
	Val.	Val.	Var 1	Val.	Var 2		
Ventriculo-arterial coupling indices and stroke work							
LV elastance index [mmHg/mL]	2.85	2.12	-0.26	2.25	0.06	2.3 ± 1	(Chen et al., 1998)
Aortic elastance index [mmHg/mL]	1.24	1.23	-0.01	1.27	0.03	2.2 ± 0.8	(Chen et al., 1998)
Ventriculo-arterial coupling index	0.44	0.58	0.32	0.57	-0.02	1.0 ± 0.36	(Chen et al., 1998)
Aortic Pulsatility Index	4.21	5.0	0.19	3.3	-0.34	>1.45	(Belkin et al., 2021)
LV stroke work [J]	1.03	1.05	0.02	0.55	-0.48		
Chamber volumes and related quantities							
Cardiac output [L/min]	5.81	5.86	+0.01	4.18	-0.29	5.0 ± 1.1	(Patel et al., 2021)
LV stroke volume index [mL/m^2]	47.9	48.49	0.01	34.8	-0.28	44.3 ± 8.7	(Patel et al., 2021)
LV ejection fraction [%]	64.01	58.67	-0.08	57.48	-0.02	60.7 ± 4.2	(Kovalova et al., 2006)
RV stroke volume index [mL/m^2]	47.57	49.81	0.05	34.74	-0.3	39.4 ± 4.55	(Kovalova et al., 2006)
RV ejection fraction [%]	59.9	52.98	-0.12	51.49	-0.03	53.9 ± 7.1	(Kovalova et al., 2006)
LA volume index [mL/m^2]	48.42	31.98	-0.34	21.74	-0.32	39 (26,53)	(Maceira et al., 2010)
RA volume index [mL/m^2]	53.91	50.94	-0.06	33.46	-0.34	55 (33,78)	(Maceira et al., 2013)
Blood pressure							
Central venous pressure [mmHg]	4.67	4.49	-0.04	6.17	0.37	(1-8)	(De Vecchis et al., 2016)
Mean left atrial pressure [mmHg]	6.74	5.41	-0.2	7.23	0.34	(2-12)	(Fowler, 1980)
Mean arterial pressure [mmHg]	92.8	93.31	0.01	69.97	-0.25	89 ± 8	(McEniery et al., 2005)
Peripheral SBP [mmHg]	127.88	127.6	-0.0	97.59	-0.24	124 ± 10	(McEniery et al., 2005)
Peripheral DBP [mmHg]	73.28	74.39	0.02	54.34	-0.27	75 ± 8	(McEniery et al., 2005)
Peripheral PP [mmHg]	54.6	53.21	-0.03	43.25	-0.19	49 ± 9	(McEniery et al., 2005)
Blood flow distribution							
Cerebral flow [mL/s]	12.38	12.48	0.01	9.13	-0.27	12.18 ± 2.12	(Ford et al., 2005)
Coronary flow [mL/s]	4.91	5.32	0.08	3.57	-0.33	4.5 ± 1.36	(Sakamoto et al., 2013)

Table 4.3: Main cardiac and haemodynamic indices $\mathcal{I}$ obtained for scenarios 1-3 (see section 4.1.1). LA/RA/LV/RV: left atrium/right atrium/left ventricle/right ventricle; SBP/DBP/PP: systolic/-diastolic/pulse pressure. Indices were computed averaging over the respiratory cycle. The relative variation Var 1 = $(\mathcal{I}_{sc2} - \mathcal{I}_{sc1})/\mathcal{I}_{sc1}$ is computed with respect to results without respiration, and the relative variation Var 2 = $(\mathcal{I}_{sc3} - \mathcal{I}_{sc2})/\mathcal{I}_{sc2}$ with respect to results obtained with respiration and our best parametrisation. Reference values, if not otherwise specified, are expressed as mean ± SD. Reference left/right atrial volume indices are expressed as mean, (95% confidence interval). Reference mean left/right atrial pressures are expressed in terms of a reasonable range accepted in the clinical practice.

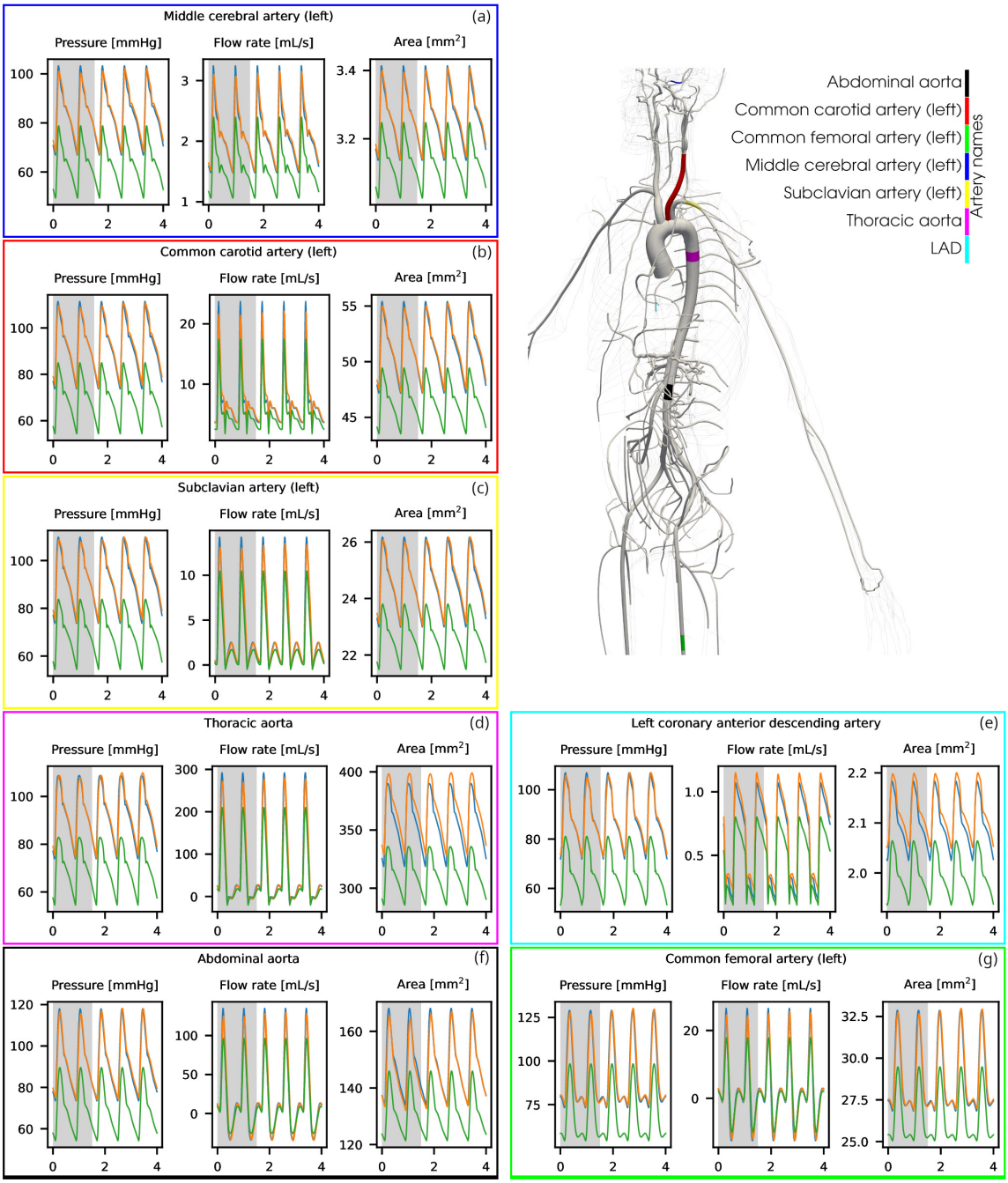

Figure 4.5: Haemodynamic waveforms for selected arteries. We depict pressure, flow rate and area waveforms for scenarios 1, 2, 3 respectively through blue, orange and green lines.

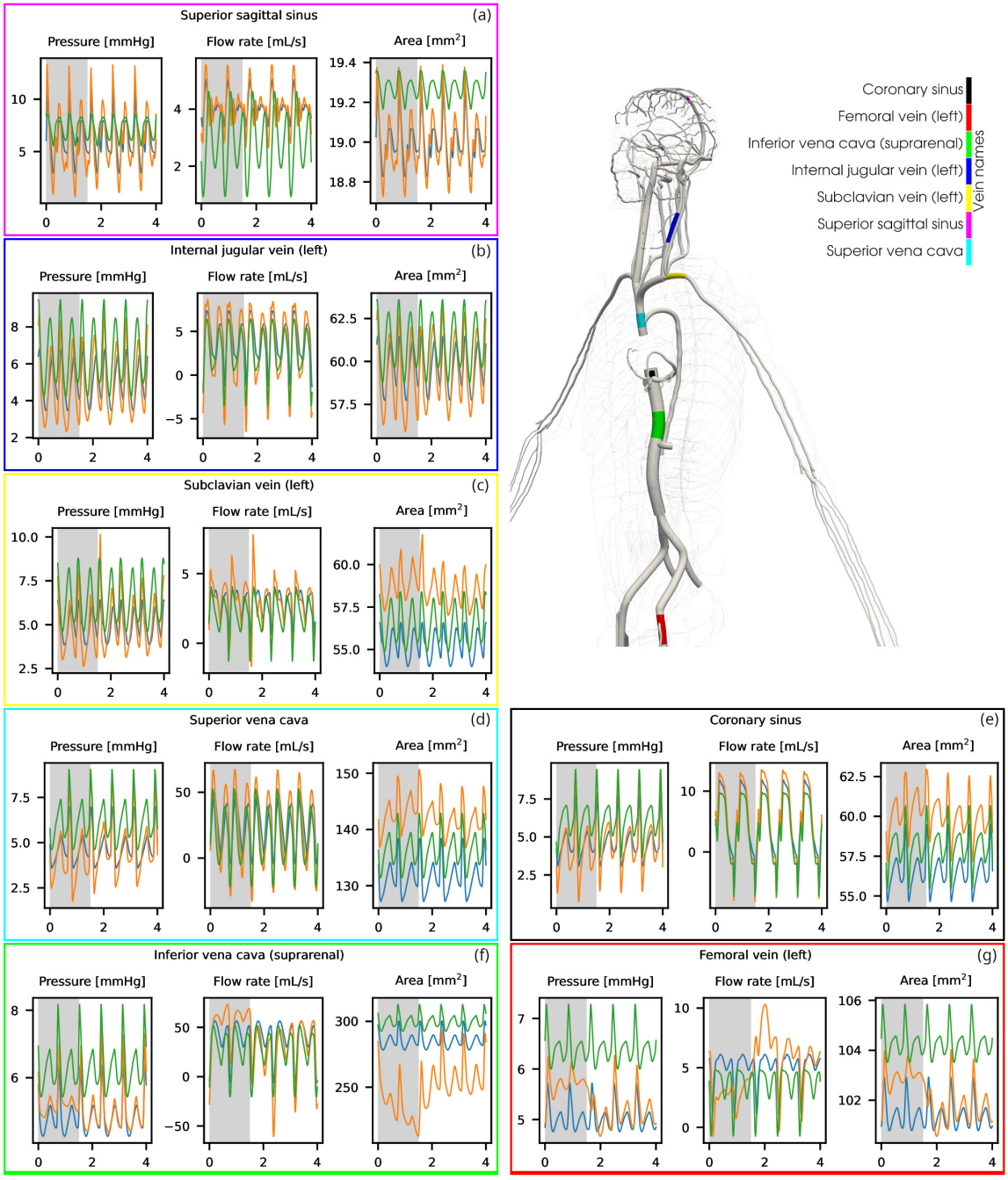

Figure 4.6: Haemodynamic waveforms for selected veins. We depict pressure, flow rate and area waveforms for scenarios 1, 2, 3 respectively through blue, orange and green.

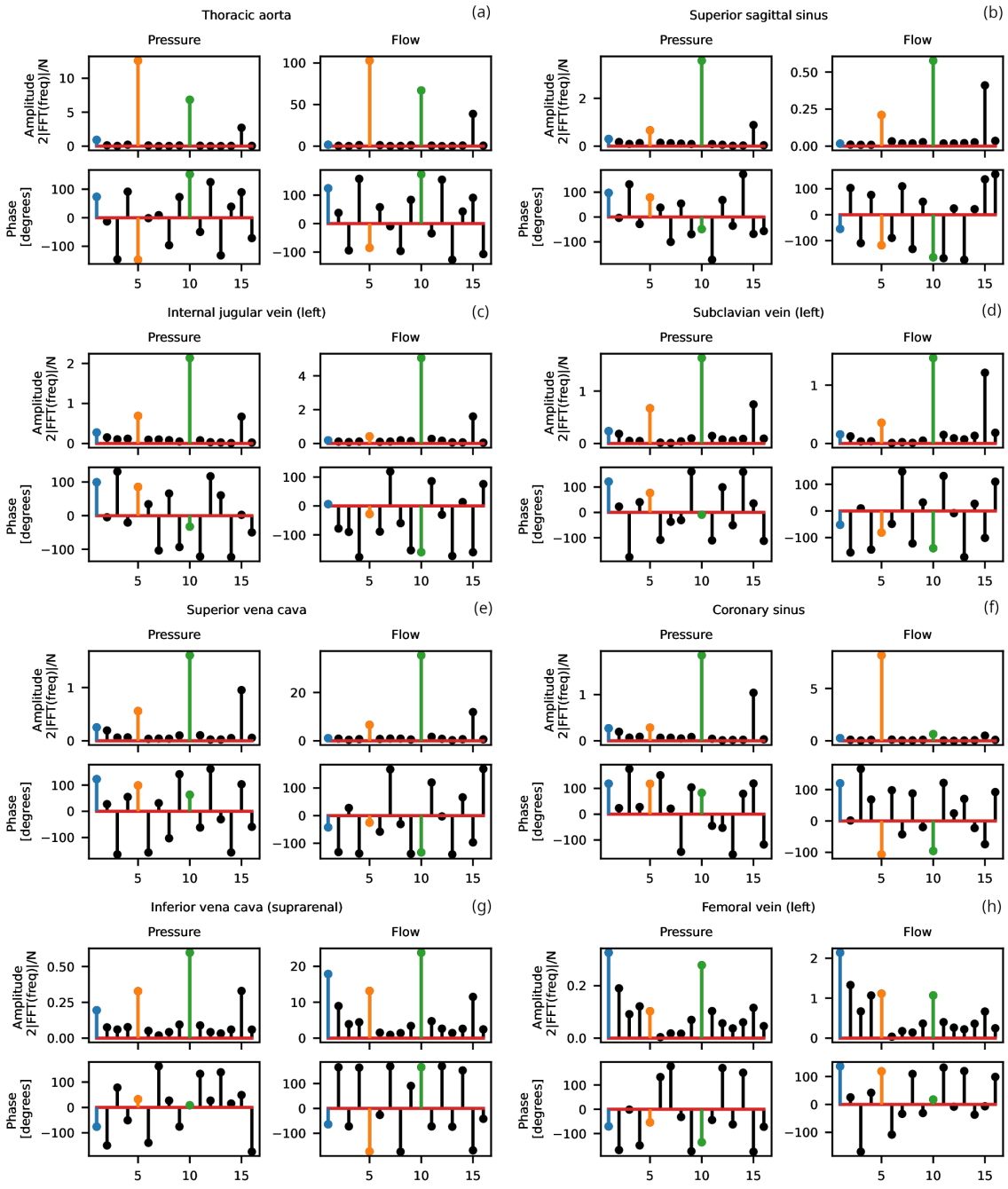

Figure 4.7: Spectra of pressure and flow rate waveforms for Scenario 2. The fundamental frequency (first harmonic, in blue) of the wave corresponds to respiratory periodicity, while the fifth (in orange) and tenth (in green) harmonics correspond to cardiac cycle and half cardiac cycle periodicity, respectively.

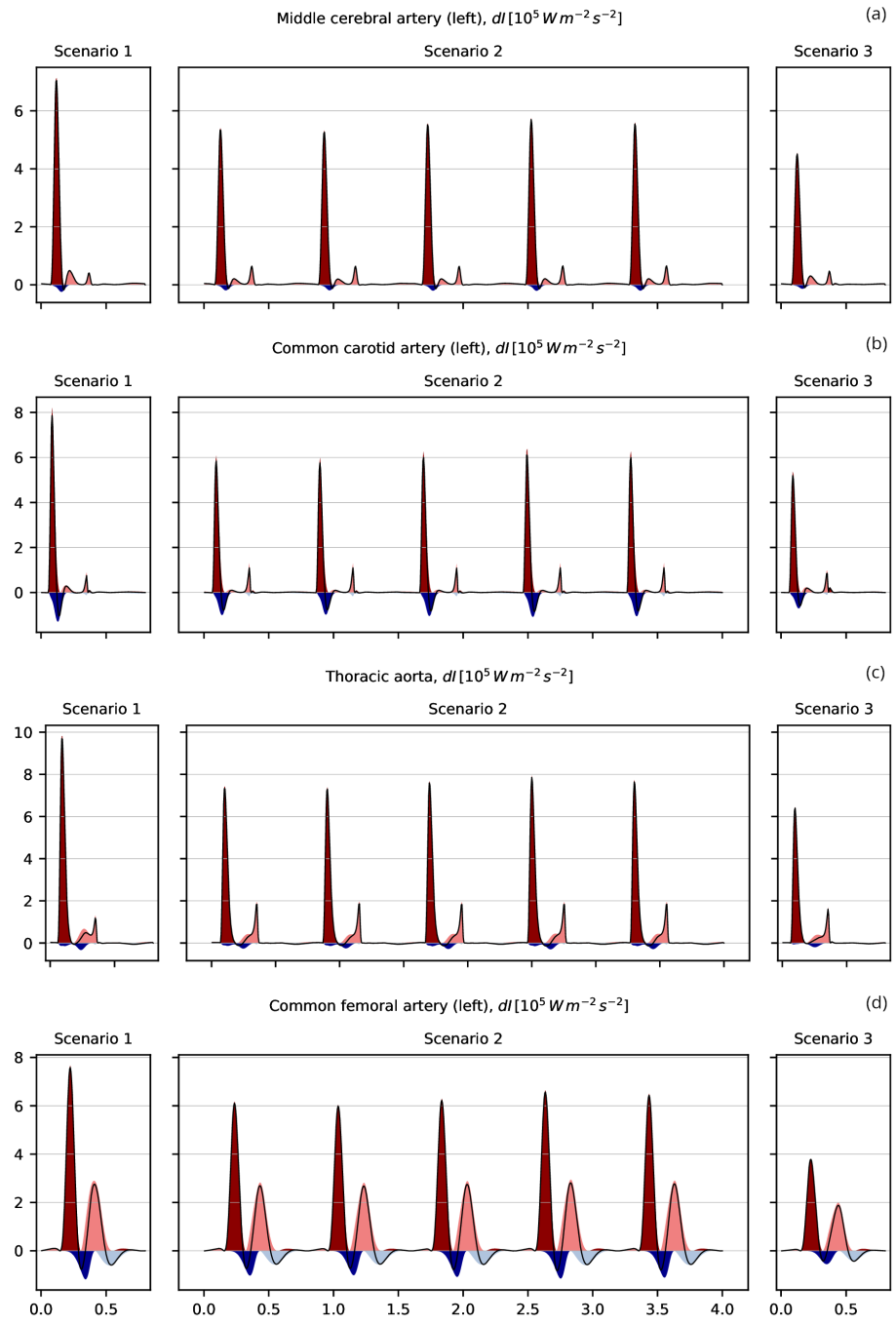

Figure 4.8: Wave intensity analysis for scenarios 1-3 in selected arteries. Dark red shaded areas indicate FCW, dark blue shaded areas BCW. Light red shaded areas denote FEW and light blue shaded areas BEW.

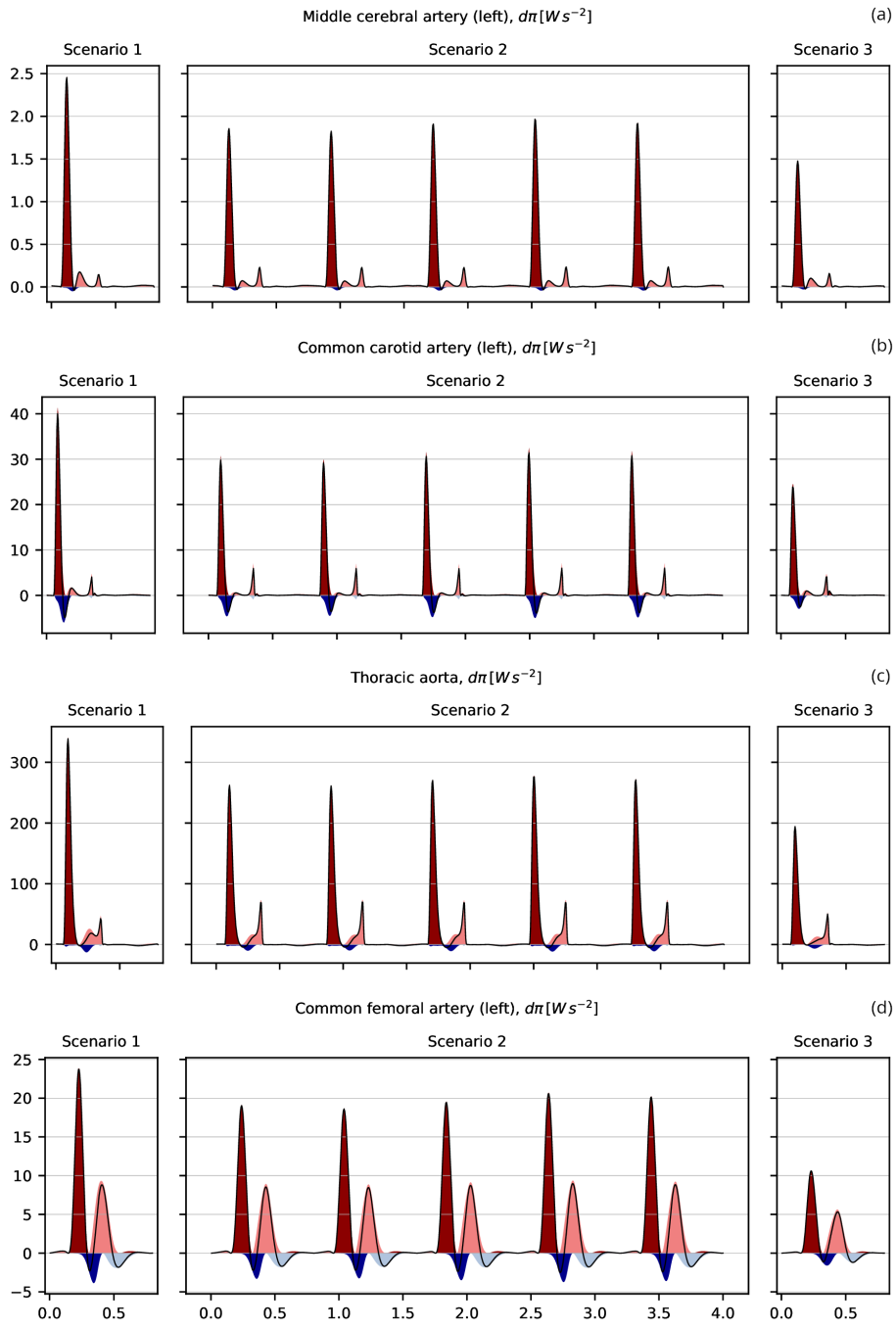

Figure 4.9: Wave power analysis for scenarios 1-3 in selected arteries. Dark red shaded areas indicate FCW, dark blue shaded areas BCW. Light red shaded areas denote FEW and light blue shaded areas BEW.

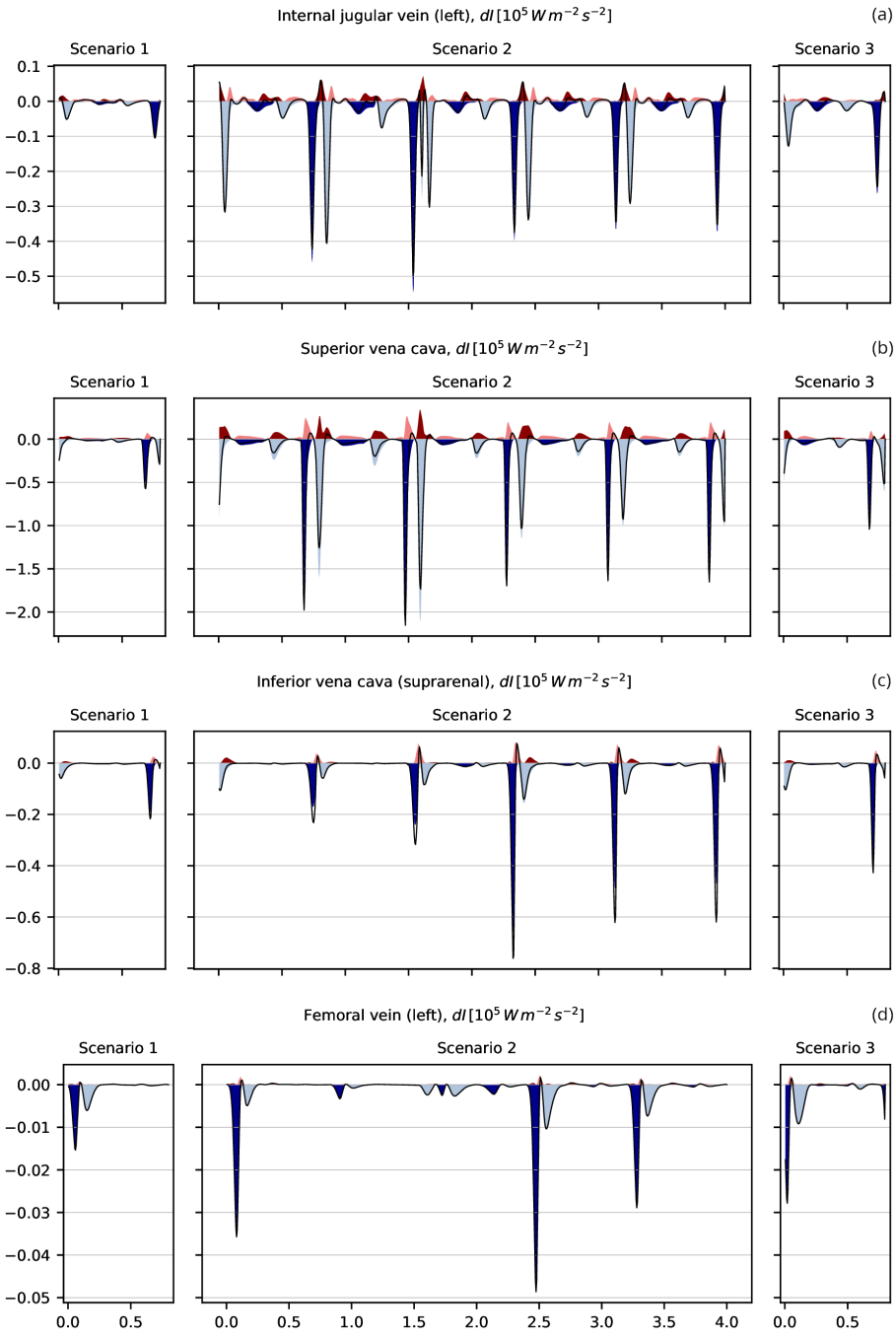

Figure 4.10: Wave intensity analysis for scenarios 1-3 in selected veins. Dark red shaded areas indicate FCW, dark blue shaded areas BCW. Light red shaded areas denote FEW and light blue shaded areas BEW.

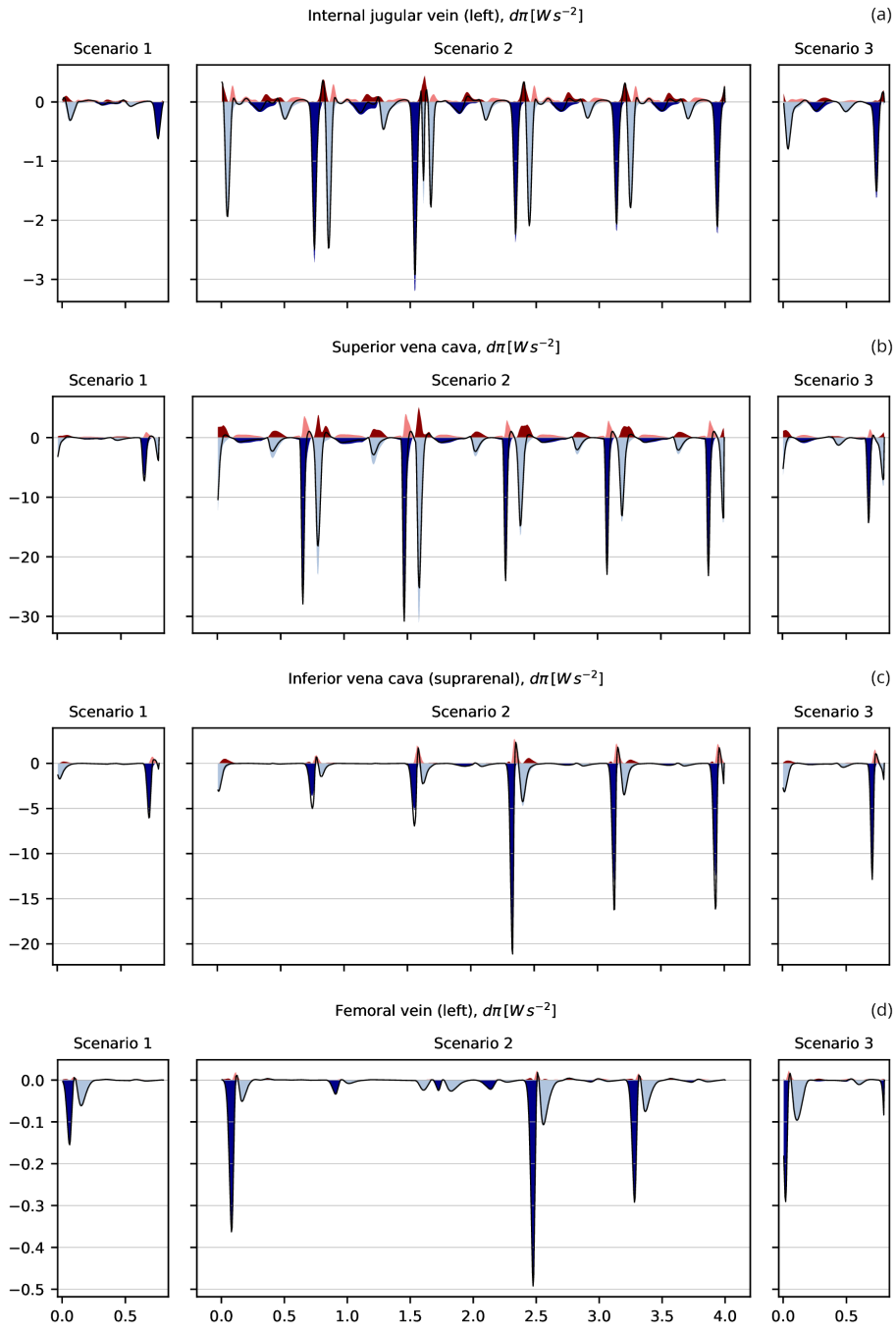

Figure 4.11: Wave power analysis for scenarios 1-3 in selected veins. Dark red shaded areas indicate FCW, dark blue shaded areas BCW. Light red shaded areas denote FEW and light blue shaded areas BEW.

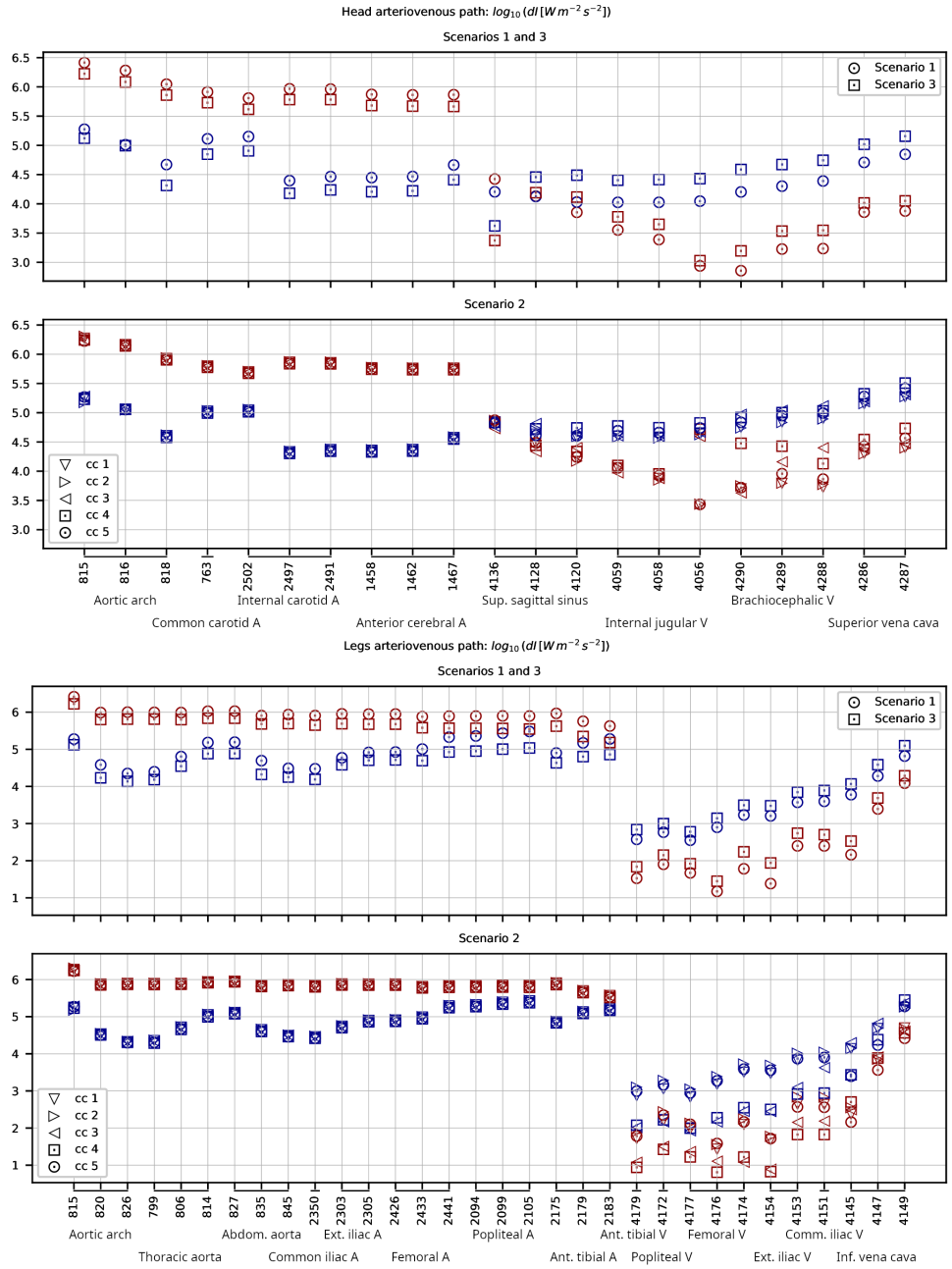

Figure 4.12: Peak forward (red) and backward (blue) wave intensity along the arteriovenous path via the head (top panels for scenarios 1, 2 and 3, correspondingly) and lower limb (bottom panels for scenarios 1, 2 and 3, correspondingly). For scenarios 1 and 3 we report the single cardiac cycle-invariant values, while for Scenario 2 we report the values for the five cardiac cycles cc 1 - cc 5 that compose each respiratory cycle.

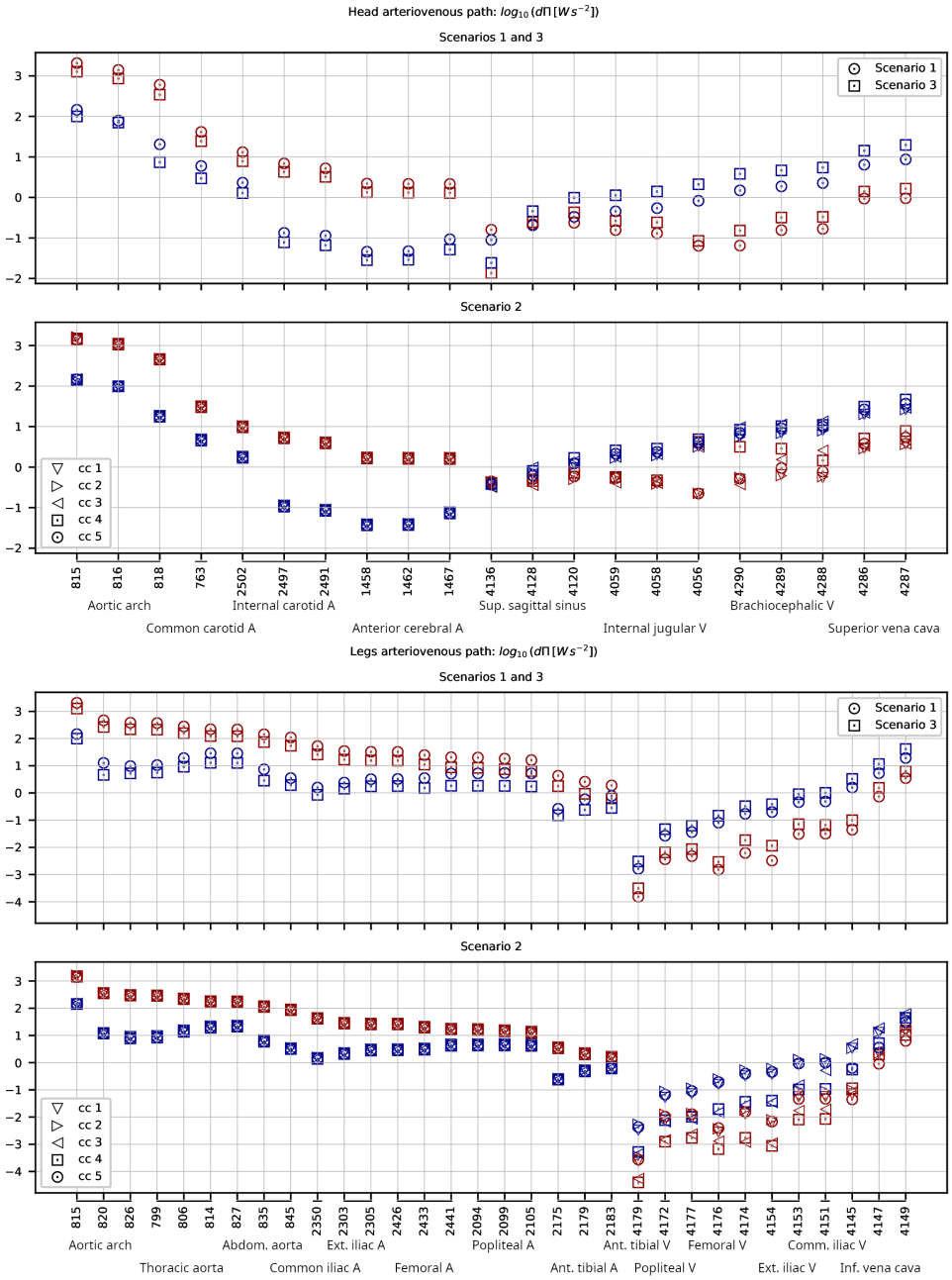

Figure 4.13: Peak forward (red) and backward (blue) wave power along the arteriovenous path via the head (top panels for scenarios 1, 2 and 3, correspondingly) and lower limb (bottom panels for scenarios 1, 2 and 3, correspondingly). For scenarios 1 and 3 we report the single cardiac cycle-invariant values, while for Scenario 2 we report the values for the five cardiac cycles cc 1 - cc 5 that compose each respiratory cycle.

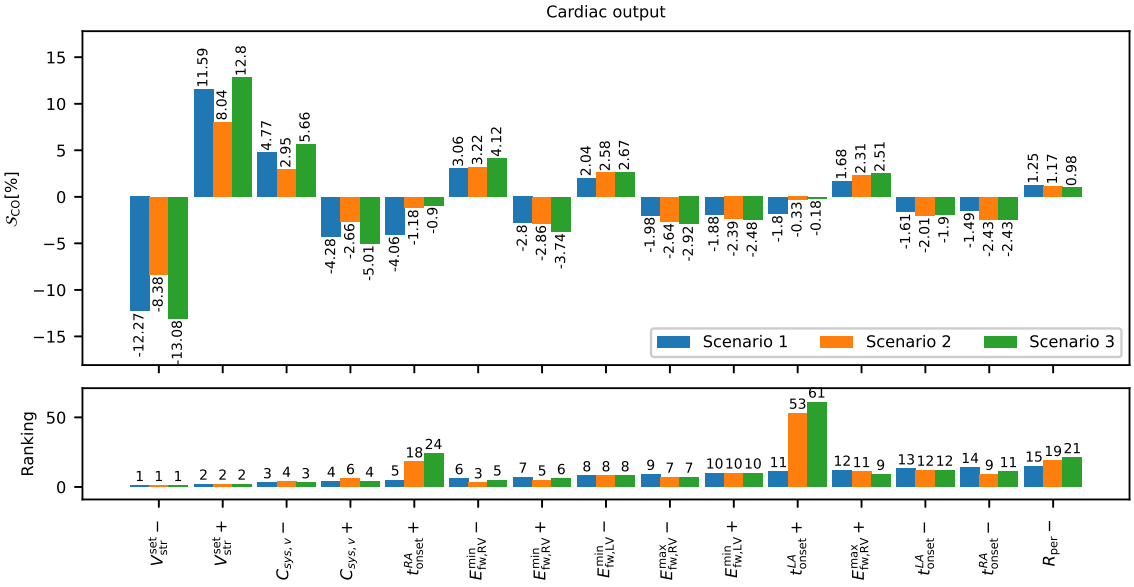

Figure 4.14: Comparison between sensitivity indices for cardiac output in scenarios 1, 2 and 3. Top panel shows the sensitivity indices for CO, bottom panel shows the rankings in scenarios 1, 2 and 3 of the 15 most influential parameters pertaining to Scenario 1.

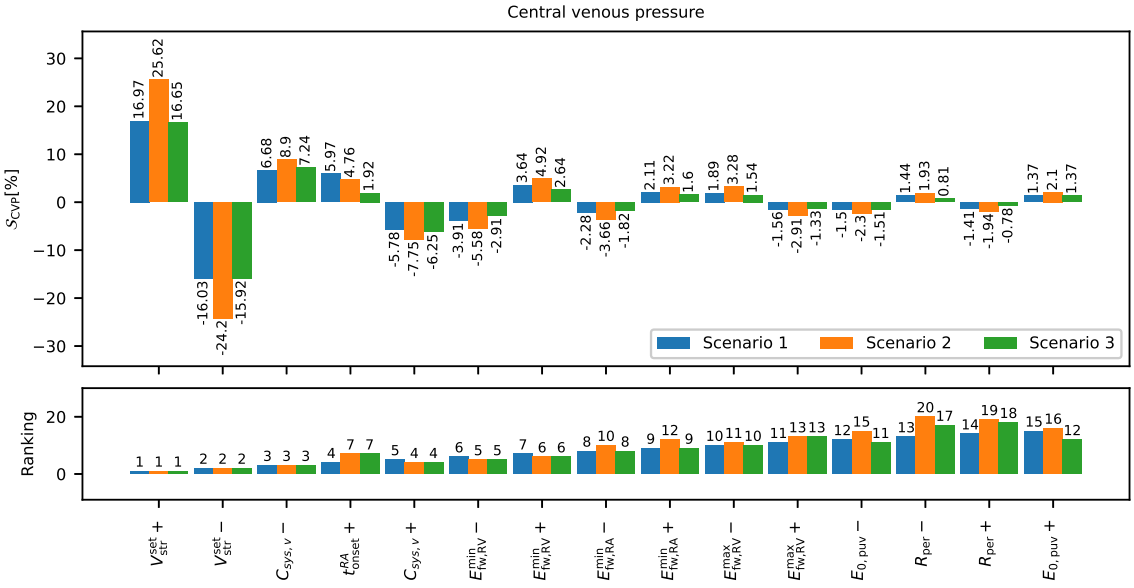

Figure 4.15: Comparison between sensitivity indices for central venous pressure in scenarios 1, 2 and 3. Top panel shows the sensitivity indices for central venous pressure, bottom panel shows the rankings in scenarios 1, 2 and 3 of the 15 most influential parameters pertaining to Scenario 1.

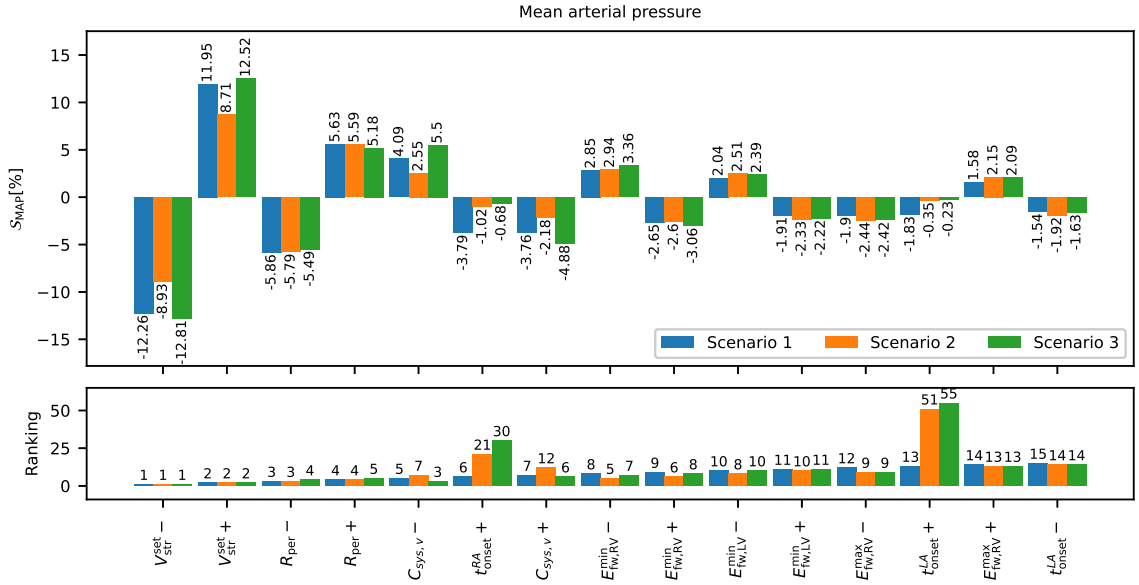

Figure 4.16: Comparison between sensitivity indices for mean arterial pressure in scenarios 1, 2 and 3. Top panel shows the sensitivity indices for MAP, bottom panel shows the rankings in scenarios 1, 2 and 3 of the 15 most influential parameters pertaining to Scenario 1.

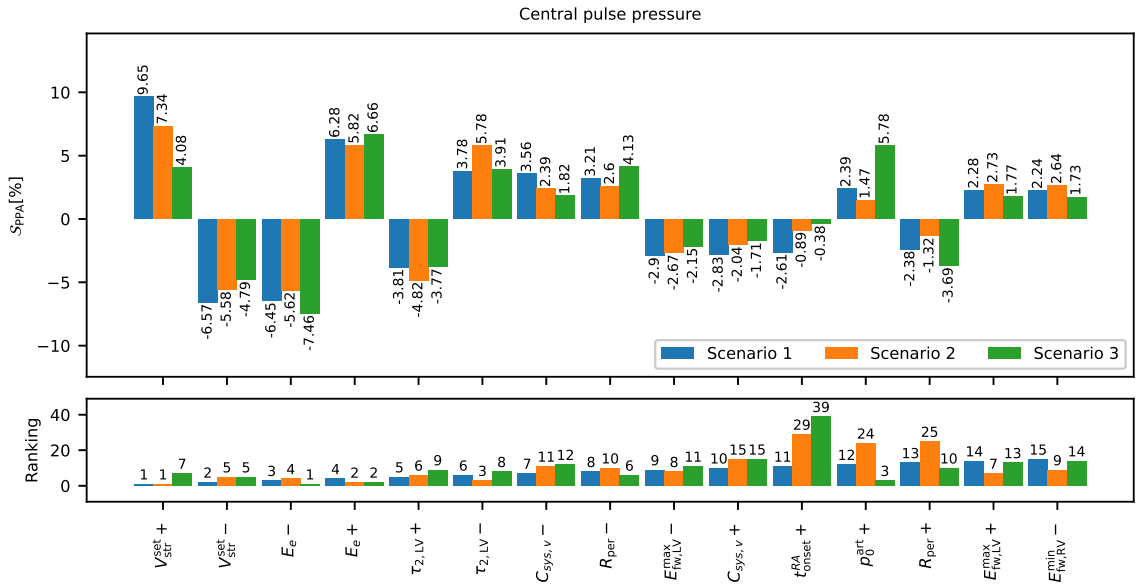

Figure 4.17: Comparison between sensitivity indices for pulse pressure in scenarios 1, 2 and 3. Top panel shows the sensitivity indices for PPA, bottom panel shows the rankings in scenarios 1, 2 and 3 of the 15 most influential parameters pertaining to Scenario 1.

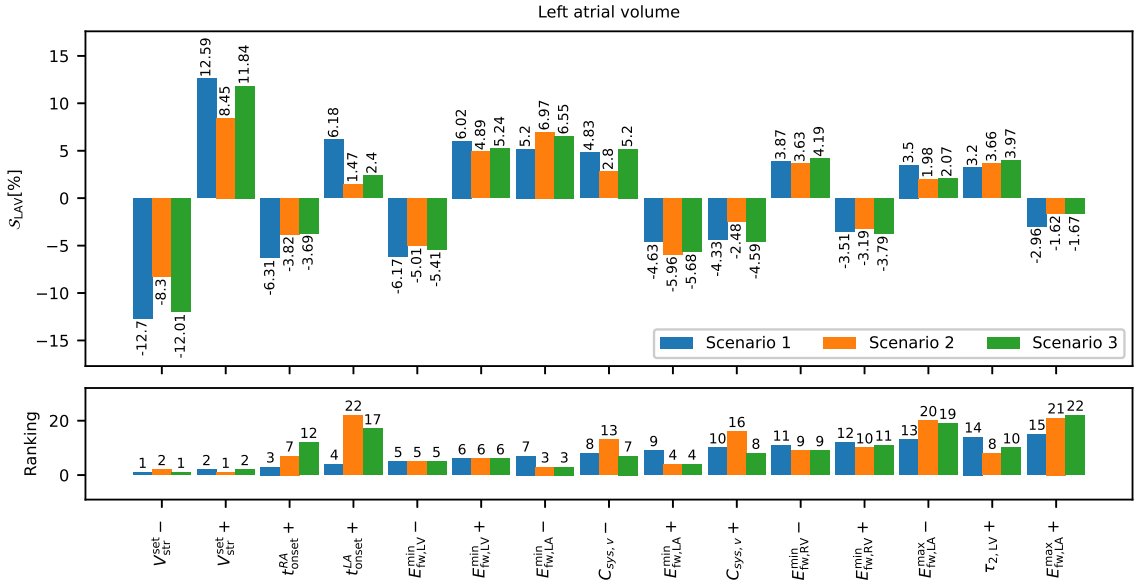

Figure 4.18: Comparison between sensitivity indices for left atrial volume in scenarios 1, 2 and 3. Top panel shows the sensitivity indices for LAV, bottom panel shows the rankings in scenarios 1, 2 and 3 of the 15 most influential parameters pertaining to Scenario 1.

4.2 ADAVN86 vascular network and nonlinear cardiac model: model parametrisation and verification

In this section, we outline the parametrisation procedure used for the ADAVN86 model (section 2.1.4) and assess its performance by comparing simulations with and without respiration to those produced by the ADAVN model. We then present the parameters employed in simulations that incorporate both respiration and the nonlinear cardiac model introduced in section 2.3.1.2, and we evaluate the resulting behaviour relative to simulations performed without respiration using the linear cardiac model.

4.2.1 ADAVN86 vascular network

The construction of a truncated network requires the modeller to lump the truncated regions into peripheral compartments by appropriately adjusting compliances and resistances, so as to preserve physiologically reasonable blood flow distributions across the various peripheral districts.

4.2.1.1 Parametrisation

With the objective of comparing results obtained through the ADAVN and ADAVN86 vascular networks, we parametrise the ADAVN86 model following the approach proposed in Blanco et al. (2020) for the arterial ADAN86 network. To ensure consistency between the two models, blood supply to major organs is initially kept identical to that prescribed in ADAVN (see table 4.4).

Encephalon: 12%	Coronary vessels: 4.5%
Liver: 6.5%	Kidneys: $9.5\% \cdot 2$
Intestines: 13.25%	Spleen: 3%
Stomach: 1%	Pancreas: 1%

Table 4.4: Blood flow fractions to major organs.

Organ flow is computed as

$$Q_o = \frac{\mathrm{BF}}{100} Q_T, \tag{4.11}$$

where Q_T is the cardiac output obtained from a reference simulation performed without respiration with the ADAVN model, and BF is the considered blood flow fraction. The total resistance associated with each organ is then computed using the mean arterial pressure

(MAP) at the aortic arch as reference:

$$R_o = \frac{\text{MAP}}{Q_o}. \tag{4.12}$$

This resistance is distributed among all vessels supplying the organ according to Murray's law

$$R_i = \frac{\text{MAP}}{\alpha_i Q_o},\ \alpha_i = \frac{r_i^3}{\sum_j r_j^3}. \tag{4.13}$$

For coronary vessels, we consider the resistances used in the ADAVN network (Müller et al., 2023) and rescale them to match the prescribed 4.5% blood flow fraction to the heart.

Blood flow to extracranial territories via the external carotid artery and to the intercostal region via intercostal arteries is determined so that these vessels carry the same flow Q_i^{ADAVN} as in ADAVN

$$R_i = \frac{\text{MAP}}{Q_i^{\text{ADAVN}}}. \tag{4.14}$$

Similarly, vessels that supply the upper and lower limbs carry the same blood flow fraction as in ADAVN, which is then split among them according to Murray's law. Any remaining flow is allocated to intercostal vessels and to vessels perfusing the liver, intestines, and kidneys.

Compliances are adjusted so that the characteristic constants satisfy $\tau_{\text{ADAVN86}} = R_{\text{ADAVN86}} C_{\text{ADAVN86}} = \beta_C \tau_{\text{ADAVN}}$, with $\beta_C = 6$, chosen to ensure that the difference in pulse pressure between the two models remains below 10%.

After an initial simulation, all resistances were uniformly scaled by a factor of 0.832 to better match the MAP obtained with the ADAVN model.

4.2.1.2 Results and discussion

We compare haemodynamic results obtained with the ADAVN and ADAVN86 networks in the absence of respiration to show that the proposed parametrisation yields haemodynamic indices and waveforms consistent with those of the original model. After performing an analogous comparison in the presence of respiration, we further deepen the analysis by examining the spectra associated with pressure and flow rate waveforms.

Table 4.5 reports a selection of haemodynamic indices obtained with the ADAVN and ADAVN86 models, without respiration and using the same cardiac model adopted in Müller et al. (2023); Dalmaso et al. (2025a). The two networks exhibit very good agreement, with discrepancies not exceeding 9% (aortic pulsatility index and peripheral pulse pressure).

Small differences with respect to the results presented in section 4.1 arise from a modification of the coronary connectivities in the vascular network, which required a subsequent reparametrisation. Table 4.6 reports the corresponding haemodynamic indices obtained in the presence of respiration. In this case, we observe a 14% difference in the average right atrial pressure between the two networks, although both values remain within physiological bounds.

Figures 4.19 and 4.20 show pressure, area and flow rate waveforms for selected arteries and veins, obtained without respiration. The comparison confirms a good agreement in both pressure and flow rate waveforms. Differences in cross-sectional area stem from the fact that vessels in ADAVN are tapered, whereas those in ADAVN86 have a constant cross-sectional area. Figures 4.21 and 4.22 report analogous plots obtained in the presence of respiration, while figure 4.23 reports the associated spectra for the two networks, confirming the agreement between the two models also when external pressures are applied to the thoracic and abdominal compartments.

4.2.2 Nonlinear heart model

When assessing cardiopulmonary interactions using a cardiac model with a linear end-diastolic PV relationship, we showed that a marked change in cardiac free-wall elastances was required to maintain atrial volumes within reasonable ranges. Consequently, we chose to introduce an exponential end-diastolic PV relationship for all cardiac chambers (Artrip et al., 2001; Burkhoff and Tyberg, 1993; Burkhoff et al., 2005; Abi-Abdallah Rodriguez et al., 2015; Shimizu et al., 2018; Santamore and Burkhoff, 1991), which reflects the expected increase in diastolic stiffness in response to increased loading (Ten Brinke et al., 2010). Indeed, this relationship is inherently nonlinear due to the different types of structural fibres being stretched in different pressure-volume ranges (Burkhoff et al., 2005; Diamond et al., 1971). This choice allows us to obtain reasonable end-diastolic volumes while keeping chamber minimum and maximum free-wall elastances closer to that considered without respiration.

4.2.2.1 Parametrisation

We report in table 4.7 only the parameters that differ or are added with respect to the original cardiac model used for simulations with respiration in Dalmaso et al. (2025a), i.e. minimum and maximum chamber free wall elastances $E_{\mathrm{fw},\alpha}^{\mathrm{min}}$ and $E_{\mathrm{fw},\alpha}^{\mathrm{max}}$, and parameters $A_{0,\alpha}$, β_α and n_α introduced in equations (2.117), (2.116), (2.118), reported in section 2.3.1.2.3. Parameter values were empirically adjusted from literature data (Santamore and Burkhoff, 1991; Burkhoff and Tyberg, 1993; Morley et al., 2007; Kaye et al., 2014) following a local sensitivity analysis, in order to match the original waveforms in Dalmaso

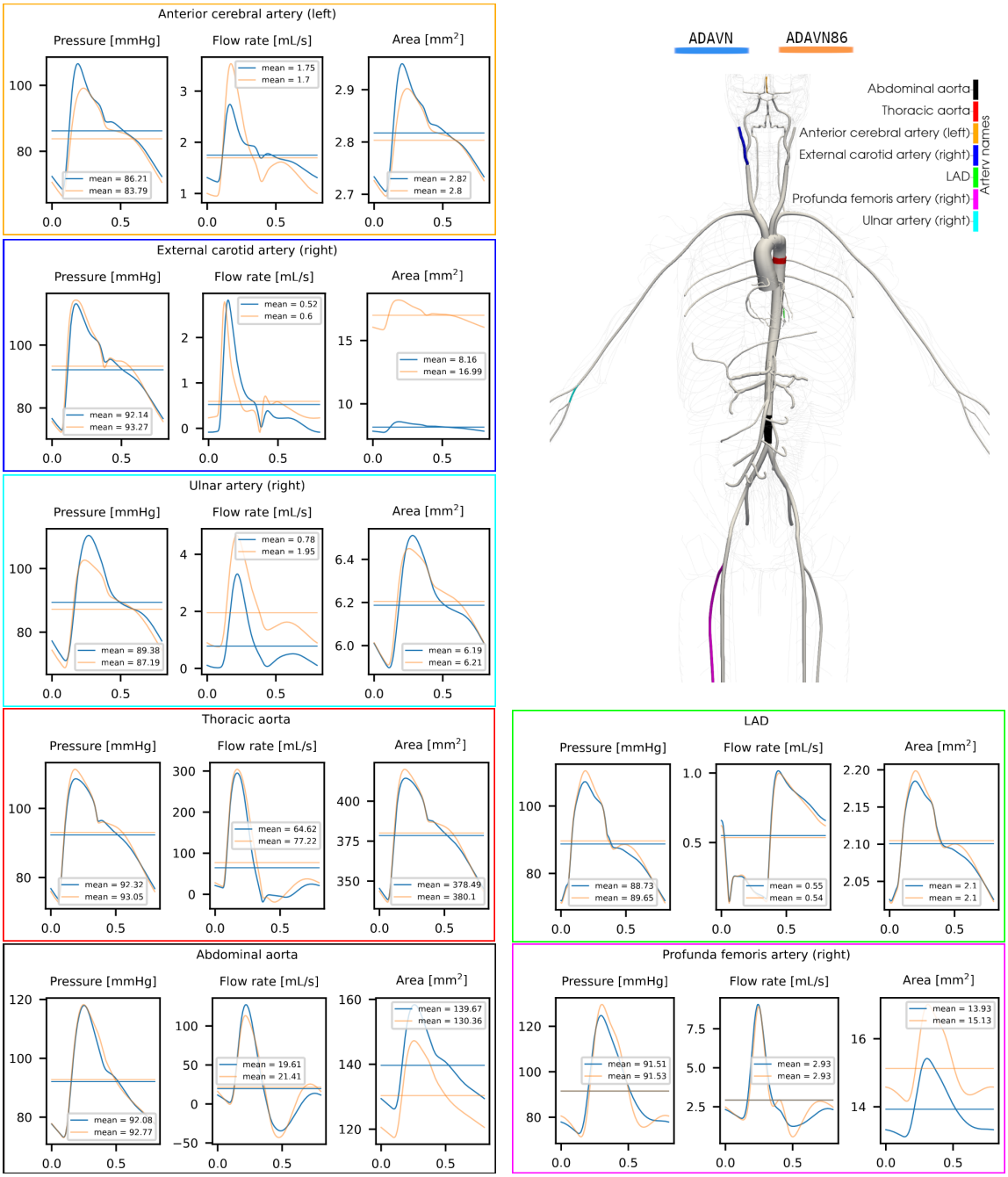

Figure 4.19: Pressure, flow rate and area waveforms for selected arteries in the absence of respiration. These simulations were performed under the assumption of null terminal unstressed volumes. Results for ADAVN are in blue, and for ADAVN86 in orange.

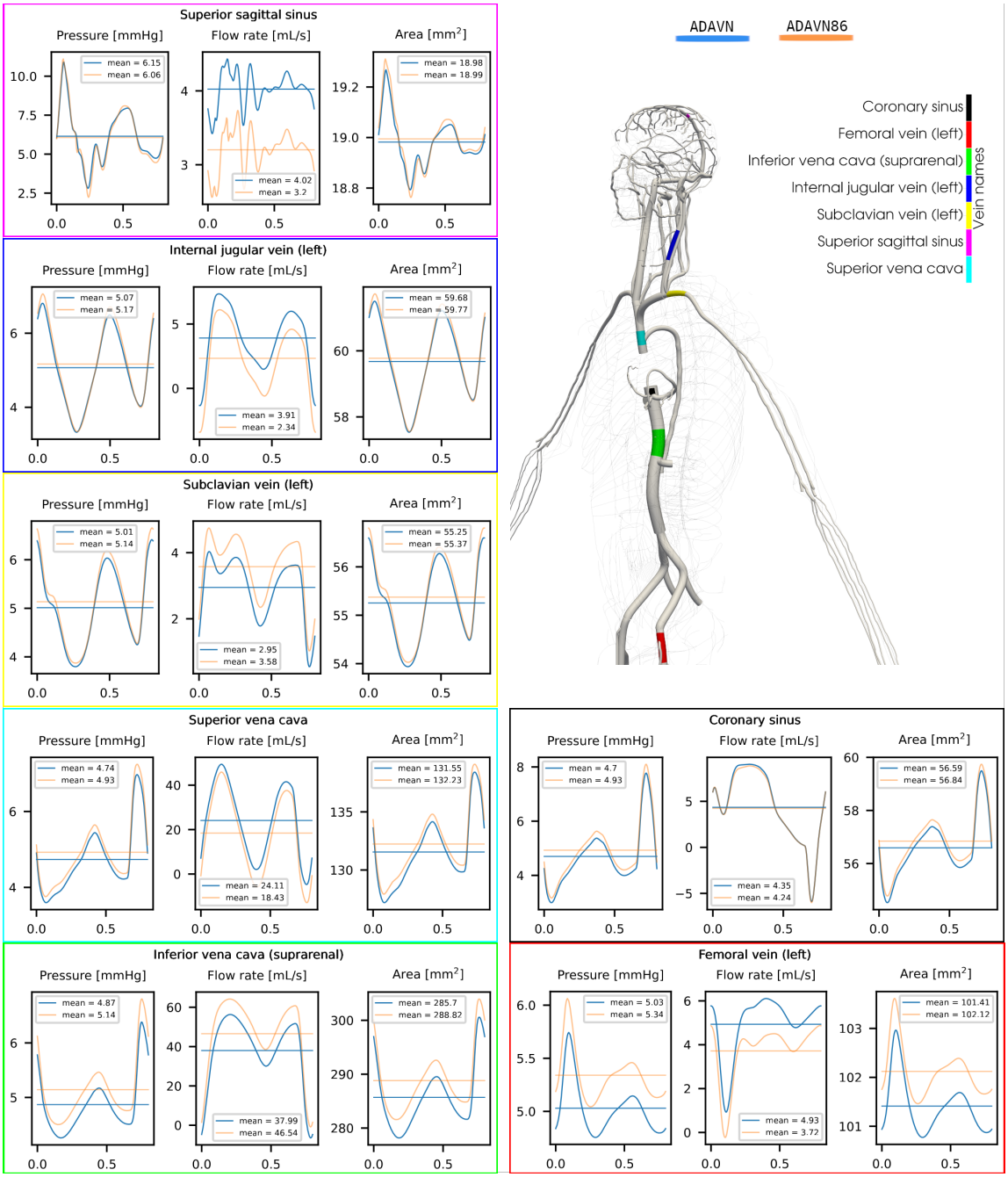

Figure 4.20: Pressure, flow rate and area waveforms for selected veins in the absence of respiration. These simulations were performed under the assumption of null terminal unstressed volumes. Results for ADAVN are in blue, and for ADAVN86 in orange.

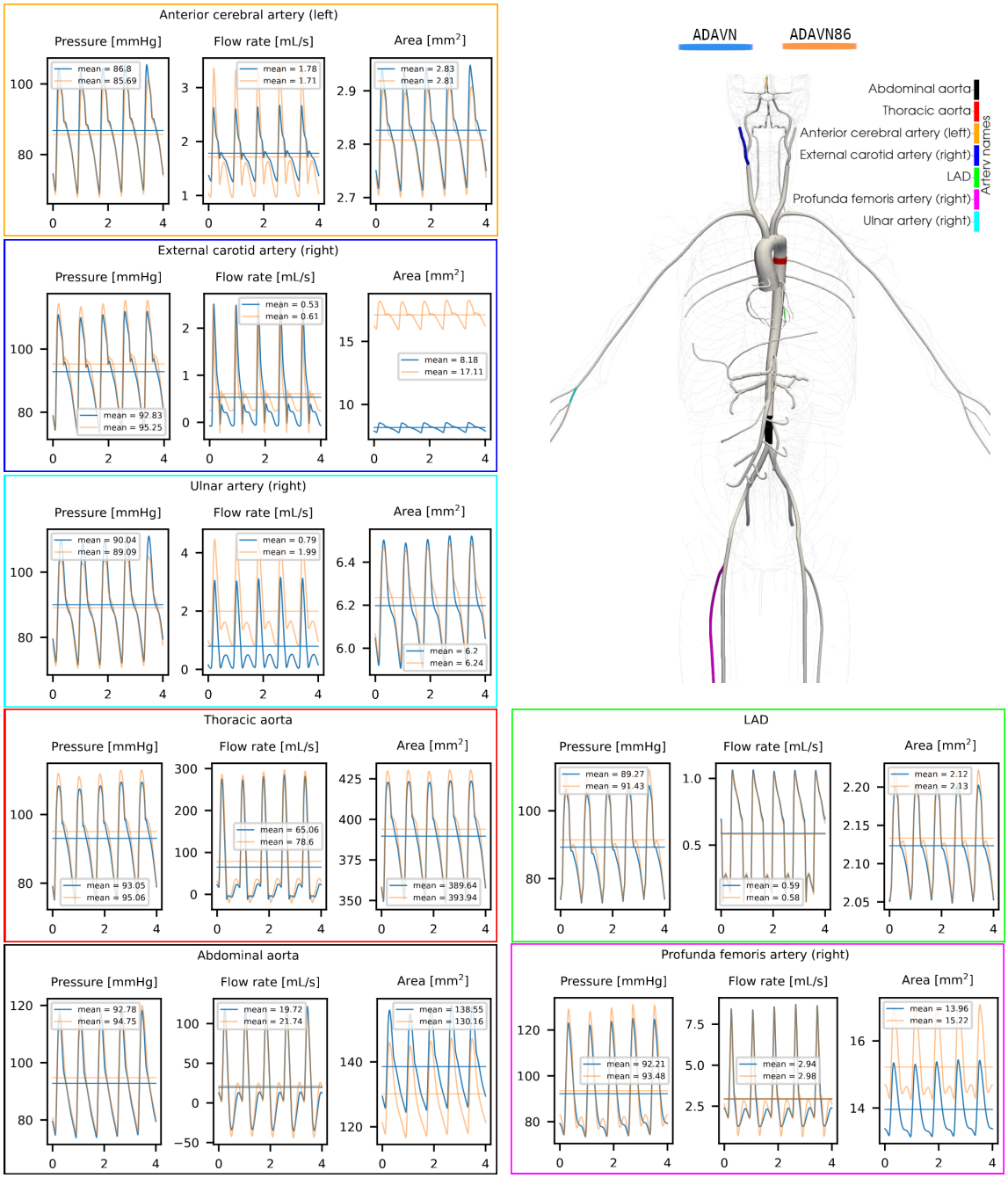

Figure 4.21: Pressure, flow rate and area waveforms for selected arteries in the presence of respiration. These simulations were performed under the assumption of non-zero terminal unstressed volumes. Results for ADAVN are in blue, and for ADAVN86 in orange.

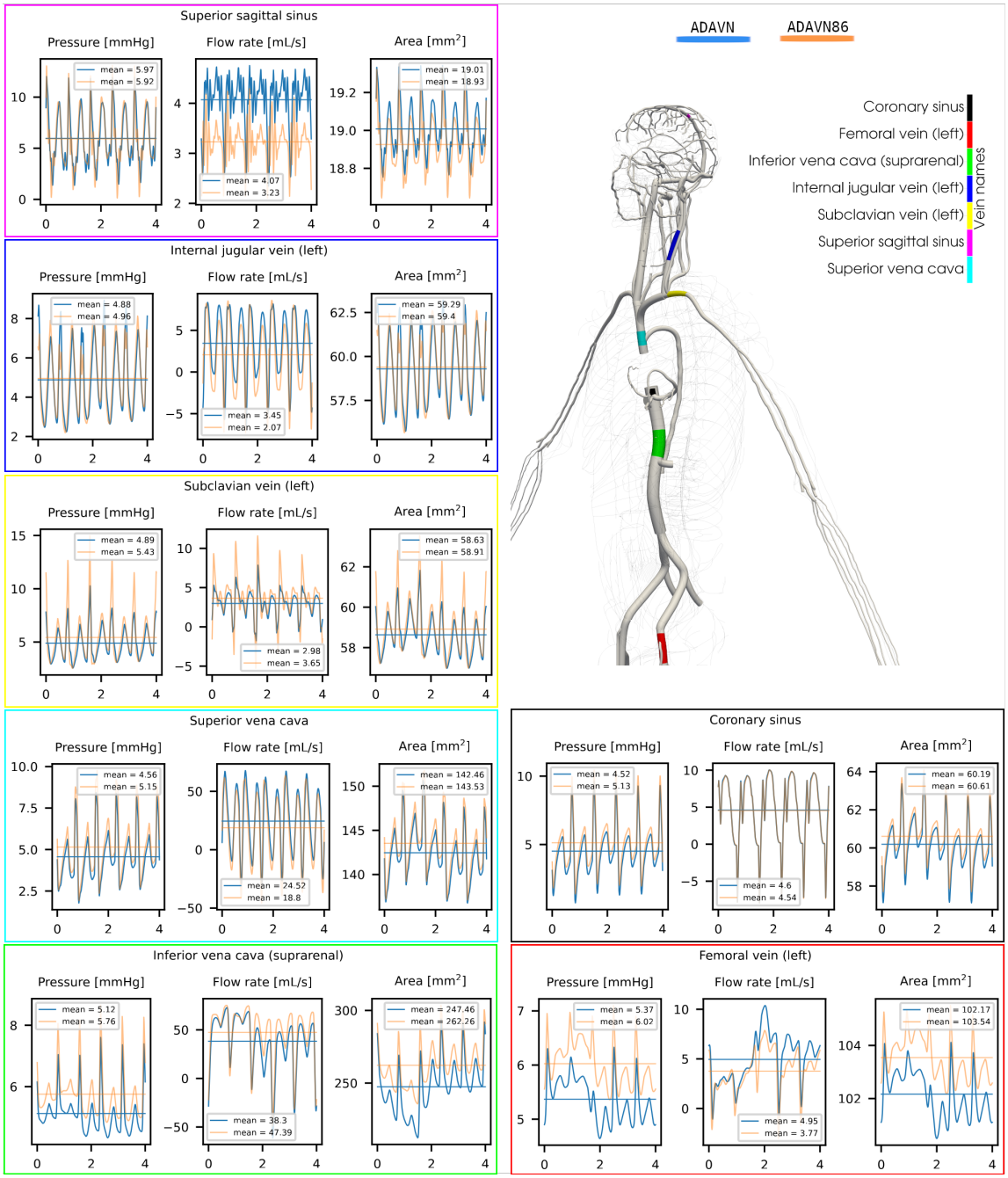

Figure 4.22: Pressure, flow rate and area waveforms for selected veins in the presence of respiration. These simulations were performed under the assumption of non-zero terminal unstressed volumes. Results for ADAVN are in blue, and for ADAVN86 in orange.

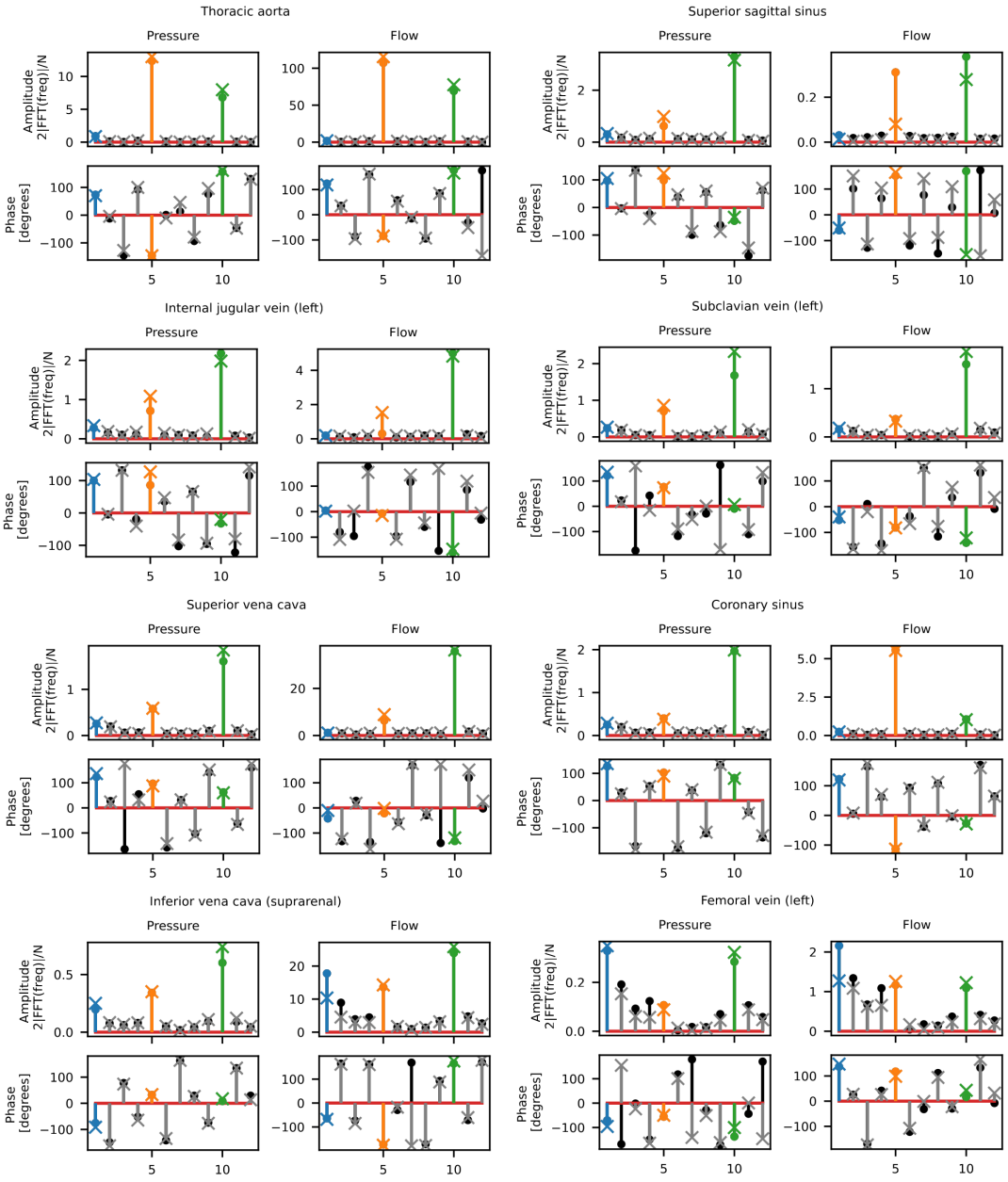

Figure 4.23: Spectra of pressure and flow rate waveforms in the presence of respiration. These simulations were performed under the assumption of non-zero terminal unstressed volumes. The fundamental frequency (first harmonic, in blue) of the wave corresponds to respiratory periodicity, while the fifth (in orange) and tenth (in green) harmonics correspond to cardiac cycle and half cardiac cycle periodicity, respectively. We denote with a dot results obtained with the ADAVN model, and with an X results obtained with ADAVN86.

et al. (2025a). For a list of the remaining parameter values, we refer to Müller et al. (2023).

4.2.2.2 Results and discussion

We compare here the haemodynamic indices and pressure/flow rate waveforms obtained for the ADAVN86 and ADAVN models using the linear and nonlinear cardiac models introduced in sections 2.3.1.1 and 2.3.1.2.

Table 4.8 reports a selection of indices obtained with the linear cardiac model without respiration and with the nonlinear cardiac model with respiration, for both vascular networks. As in Chapter 4.1, the parametrisation was chosen so that the nonlinear model with respiration reproduces the indices obtained with the linear model without respiration. Overall, the agreement is satisfactory, with the largest discrepancies appearing in ventriculo-arterial coupling indices, which remain within physiological ranges, with percentage variations that are almost identical to those reported in table 4.3, section 4.1.2.3.

Extending the comparison to the results obtained with the reparametrised linear cardiac model in the presence of respiration, figures 4.24 and 4.25 show haemodynamic waveforms for the pulmonary circulation and the heart, respectively, and figures 4.26 and 4.27 collect waveforms for selected arteries and veins. Both sets of figures report simulation results obtained through the ADAVN86 network, and show a satisfactory agreement, in the presence of respiration, between results obtained using the linear cardiac model parametrised as illustrated in table 4.2 (section 4.1.1.1.2), and the nonlinear cardiac model parametrised as in table 4.7.

Compared to the results reported in chapter 4.1, it is worth noting that the nonlinear formulation of the end diastolic pressure-volume relationship allows us to reproduce the haemodynamic indices using elastance values that are closer to those reported in Müller et al. (2023). This avoids the larger parameter adjustments that were necessary in Dalmaso et al. (2025a) and suggests that the nonlinear model provides a more physiologically consistent parametrisation.

Further insight is provided by the results reported in table 4.9, obtained by using, in both cardiac models and in the presence of respiration, the original elastances from Müller et al. (2023), which were calibrated to reproduce physiological behaviour in the absence of respiration. Indeed, the introduction of respiratory effects into the linear cardiac model produces substantial deviations from the baseline, particularly in chamber volumes, and in atrial and systemic pressures. In contrast, the inclusion of a nonlinear end-diastolic PV relationship allows the cardiac model to better control variations in central venous and systemic pressures, with variations that are 3-4 times smaller, remaining around 10%. This difference arises because variations in venous return are more readily accommodated when the ventricle is modelled with a linear end-diastolic PV relationship, reflecting constant

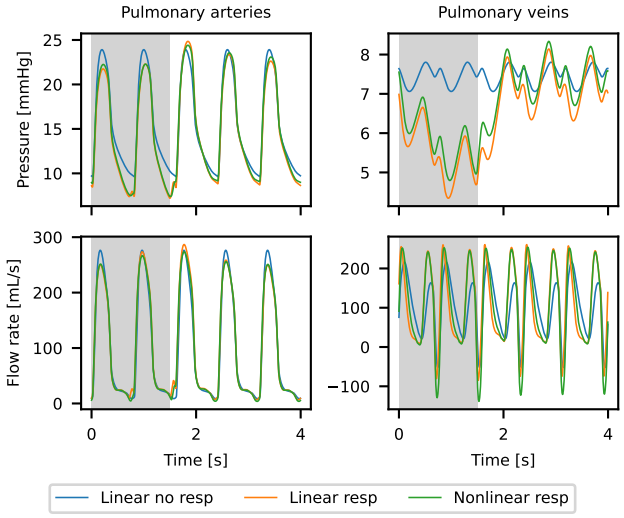

Figure 4.24: Haemodynamic waveforms for the pulmonary circulation, obtained without respiration and the linear cardiac model (blue line), with respiration and the linear cardiac model (orange line), and with respiration and the nonlinear cardiac model (green line). Top row shows pressure waveforms for pulmonary arteries (left) and veins (right). Bottom row shows flow waveforms for pulmonary arteries (left) and veins (right). The grey-shaded area highlights inspiration.

diastolic compliance and resulting in large ventricular volume changes that propagate into significant systemic pressure variations. Conversely, a nonlinear end-diastolic PV relationship introduces a physiological constraint on volume changes, since as filling increases, the steeper pressure rise limits further expansion, thus effectively reducing ventricular compliance (Ten Brinke et al., 2010). This indicates that nonlinear elastance dynamics induced by the values for $A_{0,\alpha}$, β_α and n_α reported in table 4.7 provides a more accurate description of chamber function over a wider range of transmural pressure values. The only exception concerns atrial volumes which, in the presence of respiration, increase by 26% and 34%, for left and right atria, respectively. This observation motivates the reparametrisation of chamber elastances (table 4.7) compared to the original values employed for the linear cardiac model in the absence of respiration (Müller et al., 2023).

In summary, the results presented in this section demonstrate that a nonlinear end-diastolic PV relationship provides a more physiologically consistent framework for simulating haemodynamics across a wider range of conditions, including respiration. Although the linear model can be tuned to reproduce selected indices also in the presence of respiration (albeit requiring large parameter adjustments), the nonlinear model exhibits an improved ability to control variations in central venous and systemic pressures and allows the use of chamber elastance values closer to those reported in the literature for purely cardiovascular simulations. Together, these findings support its adoption as the preferred modelling choice.

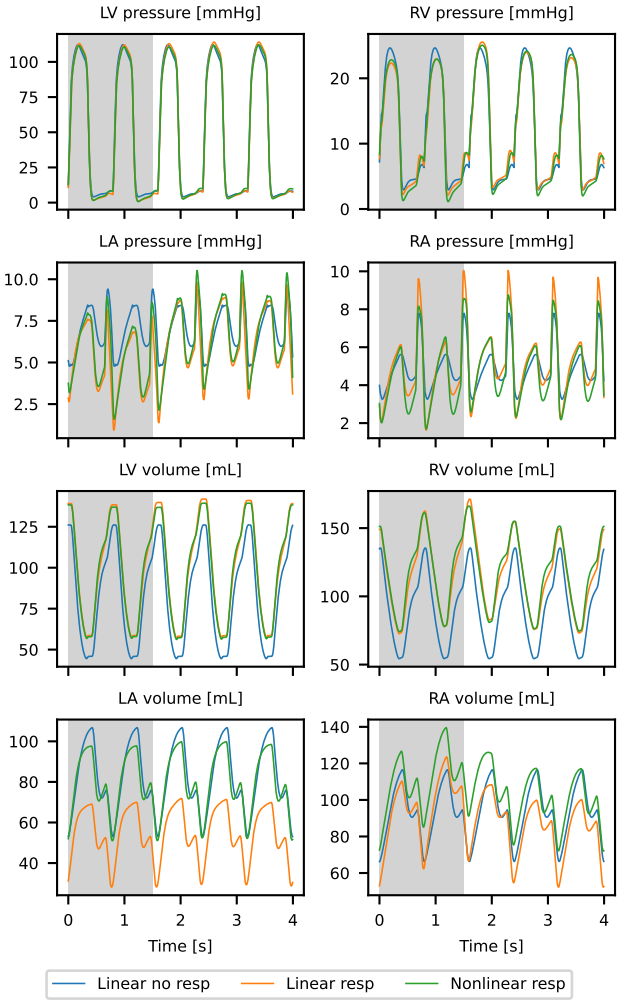

Figure 4.25: Haemoynamic waveforms for cardiac chambers, obtained without respiration and the linear cardiac model (blue line), with respiration and the linear cardiac model (orange line), and with respiration and the nonlinear cardiac model (green line). From top to bottom: ventricular pressures; atrial pressures; ventricular volumes; atrial volumes. LV/RV are left/right ventricle, LA/RA are left/right atrium. The grey-shaded area highlights inspiration.

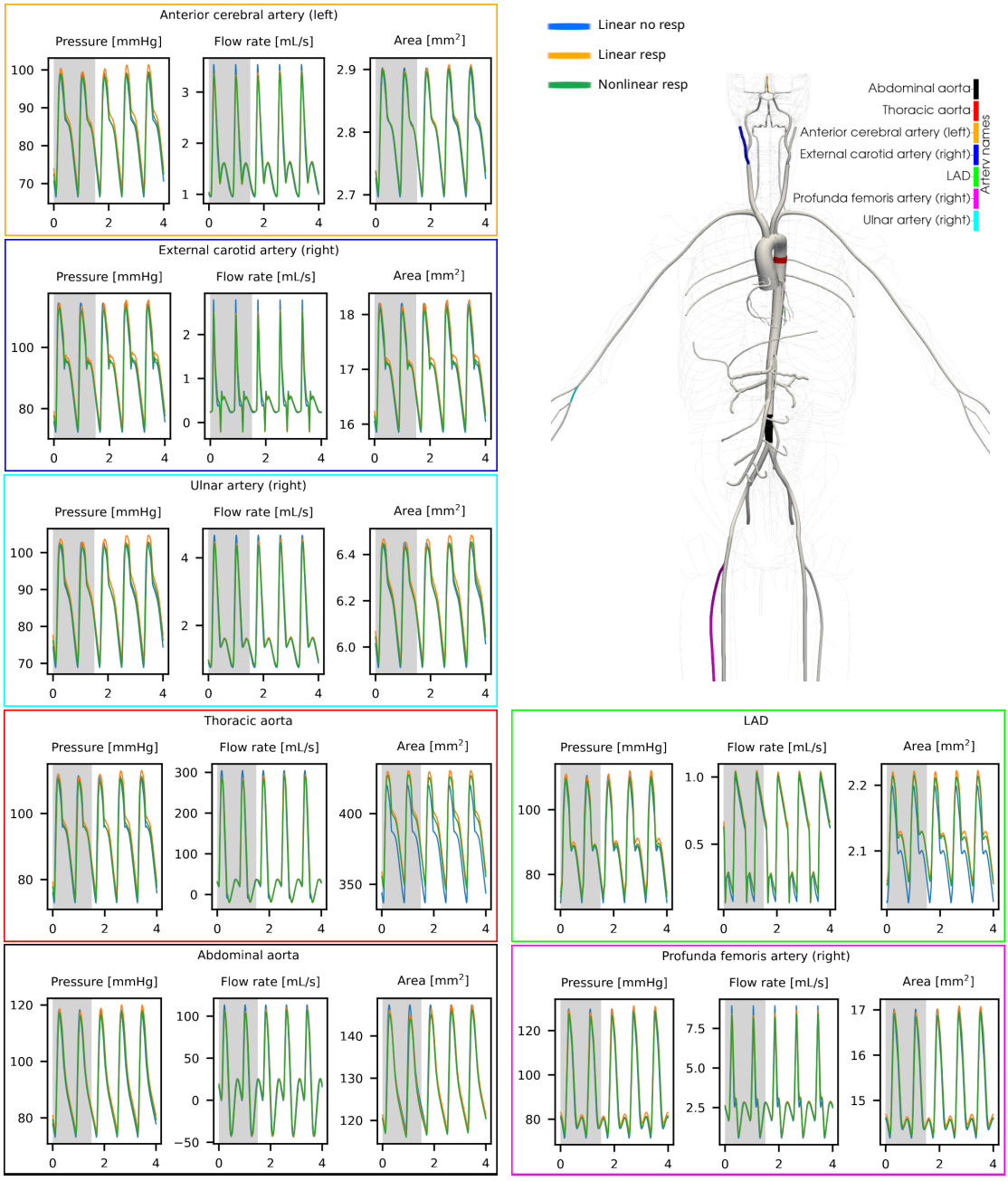

Figure 4.26: Haemodynamic waveforms for selected arteries, obtained without respiration and the linear cardiac model (blue line), with respiration and the linear cardiac model (orange line), and with respiration and the nonlinear cardiac model (green line). These simulations were performed under the assumption of non-zero terminal unstressed volumes.

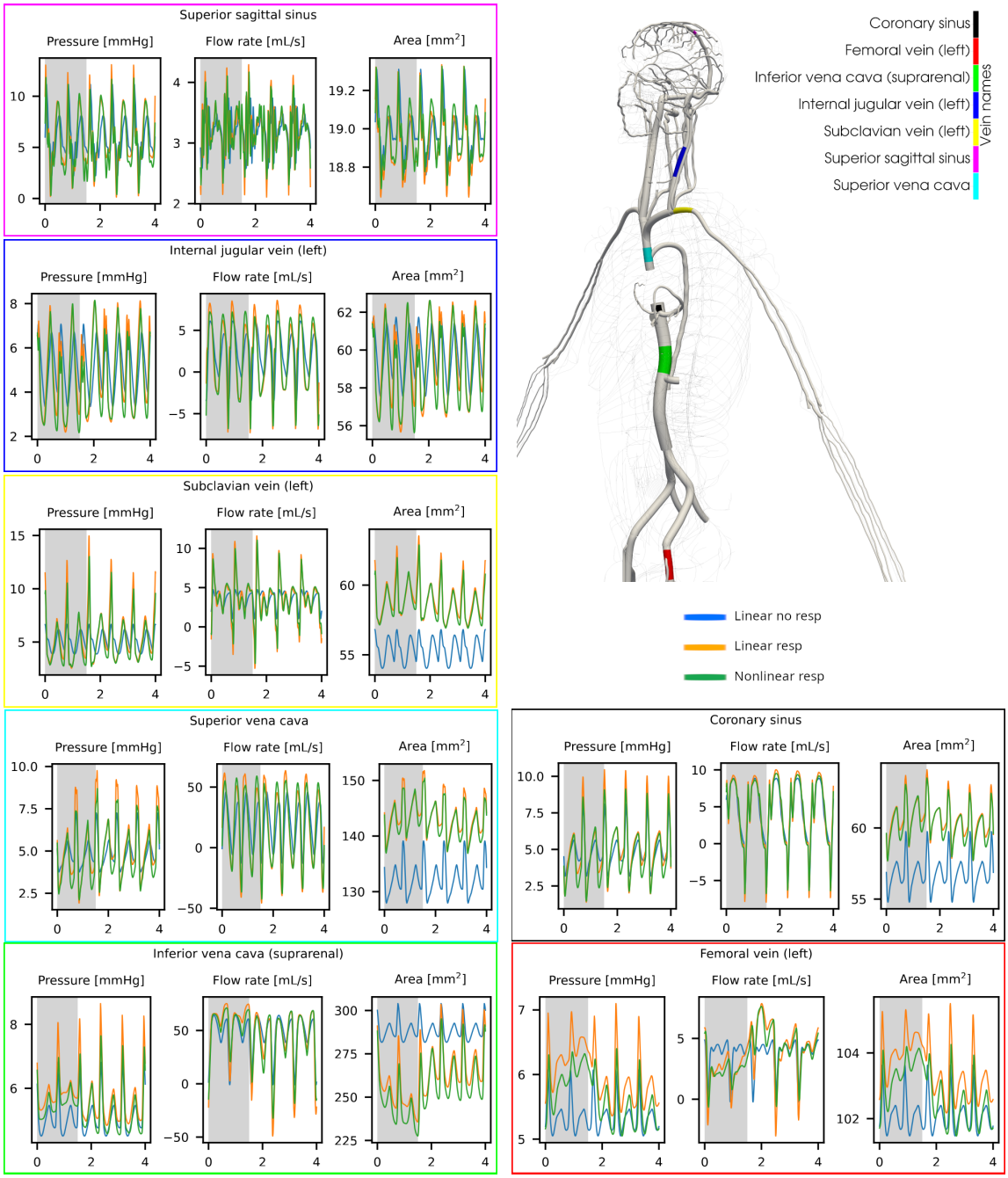

Figure 4.27: Haemodynamic waveforms for selected veins obtained without respiration and the linear cardiac model (blue line), with respiration and the linear cardiac model (orange line), and with respiration and the nonlinear cardiac model (green line). These simulations were performed under the assumption of non-zero terminal unstressed volumes.

Index	ADAVN	ADAVN86	Var.	References	
Ventriculo-arterial coupling indices and stroke work					
LV elastance index [mmHg/mL]	2.85	2.80	-0.02	2.3 ± 1	(Chen et al., 1998)
Aortic elastance index [mmHg/mL]	1.24	1.18	-0.05	2.2 ± 0.8	(Chen et al., 1998)
Ventriculo-arterial coupling index	0.43	0.42	-0.02	1.0 ± 0.36	(Chen et al., 1998)
Aortic Pulsatility Index	4.24	4.62	+0.09	>1.45	(Belkin et al., 2021)
LV stroke work [J]	1.03	1.08	+0.05	–	–
Chamber volumes and related quantities					
Cardiac output [L/min]	5.82	6.02	+0.03	5.0 ± 1.1	(Patel et al., 2021)
LV stroke volume index [mL/m^2]	47.90	49.52	+0.03	44.3 ± 8.7	(Patel et al., 2021)
LV ejection fraction [%]	64.04	64.77	+0.01	60.7 ± 4.2	(Kovalova et al., 2006)
RV stroke volume index [mL/m^2]	47.57	49.18	+0.03	39.4 ± 4.55	(Kovalova et al., 2006)
RV ejection fraction [%]	59.90	59.91	+0.00	53.9 ± 7.1	(Kovalova et al., 2006)
LA volume index [mL/m^2]	48.40	49.62	+0.02	39 (26,53)	(Maceira et al., 2010)
RA volume index [mL/m^2]	53.81	56.55	+0.05	55 (33,78)	(Maceira et al., 2013)
Blood pressure					
Central venous pressure [mmHg]	4.66	4.90	+0.05	(1–8)	(De Vecchis et al., 2016)
Mean left atrial pressure [mmHg]	6.74	6.94	+0.03	(2–12)	(Fowler, 1980)
Mean arterial pressure [mmHg]	92.60	93.39	+0.01	89 ± 8	(McEniery et al., 2005)
Peripheral SBP [mmHg]	127.62	122.87	-0.04	124 ± 10	(McEniery et al., 2005)
Peripheral DBP [mmHg]	73.07	73.43	+0.005	75 ± 8	(McEniery et al., 2005)
Peripheral PP [mmHg]	54.55	49.43	-0.09	49 ± 9	(McEniery et al., 2005)
Blood flow distribution					
Cerebral flow [mL/s]	12.37	11.36	-0.08	12.18 ± 2.12	(Ford et al., 2005)
Coronary flow [mL/s]	4.34	4.22	-0.03	4.5 ± 1.36	(Sakamoto et al., 2013)

Table 4.5: Main cardiac and haemodynamic indices $\mathcal{I}$ with the ADAVN and ADAVN86 networks in the absence of respiration. LA/RA/LV/RV: left atrium/right atrium/left ventricle/right ventricle; SBP/DBP/PP: systolic/diastolic/pulse pressure. These simulations were performed under the assumption of null terminal unstressed volumes. Indices were computed averaging over the cardiac cycle. Var $= (\mathcal{I}_{\text{ADAVN86}} - \mathcal{I}_{\text{ADAVN}})/\mathcal{I}_{\text{ADAVN}}$. We color in green variations with $|\text{Var}| < 0.05$, and in yellow variations with $0.05 \leq |\text{Var}| < 0.1$ No variations with $|\text{Var}| > 0.1$ are present in this table.

Index	ADAVN	ADAVN86	Var.	References	
Ventriculo-arterial coupling indices and stroke work					
LV elastance index [mmHg/mL]	2.12	2.07	-0.02	2.3 ± 1	(Chen et al., 1998)
Aortic elastance index [mmHg/mL]	1.23	1.17	-0.05	2.2 ± 0.8	(Chen et al., 1998)
Ventriculo-arterial coupling index	0.58	0.57	-0.02	1.0 ± 0.36	(Chen et al., 1998)
Aortic Pulsatility Index	5.04	5.34	+0.06	>1.45	(Belkin et al., 2021)
LV stroke work [J]	1.05	1.12	+0.07	–	–
Chamber volumes and related quantities					
Cardiac output [mL/s]	5.78	6.04	+0.05	5.0 ± 1.1	(Patel et al., 2021)
LV stroke volume index [mL/m^2]	48.54	50.58	+0.04	44.3 ± 8.7	(Patel et al., 2021)
LV ejection fraction [%]	58.69	59.23	+0.01	60.7 ± 4.2	(Kovalova et al., 2006)
RV stroke volume index [mL/m^2]	49.85	51.74	+0.04	39.4 ± 4.55	(Kovalova et al., 2006)
RV ejection fraction [%]	52.98	52.69	-0.01	53.9 ± 7.1	(Kovalova et al., 2006)
LA volume index [mL/m^2]	32.01	33.10	+0.03	39 (26,53)	(Maceira et al., 2010)
RA volume index [mL/m^2]	50.88	53.97	+0.06	55 (33,78)	(Maceira et al., 2013)
Blood pressure					
Central venous pressure [mmHg]	4.49	5.10	+0.14	(1–8)	(De Vecchis et al., 2016)
Mean arterial pressure [mmHg]	93.24	95.30	+0.02	89 ± 8	(McEniery et al., 2005)
Peripheral SBP [mmHg]	127.53	124.98	-0.02	124 ± 10	(McEniery et al., 2005)
Peripheral DBP [mmHg]	74.28	75.81	+0.02	75 ± 8	(McEniery et al., 2005)
Peripheral PP [mmHg]	53.25	49.17	-0.08	49 ± 9	(McEniery et al., 2005)
Blood flow distribution					
Cerebral blood flow [mL/s]	12.40	11.42	-0.08	12.18 (2.12)	(Ford et al., 2005)
Coronary blood flow [mL/s]	4.62	4.57	-0.01	4.5 (1.36)	(Sakamoto et al., 2013)

Table 4.6: Main cardiac and haemodynamic indices $\mathcal{I}$ with the ADAVN and ADAVN86 networks in the presence of respiration. LA/RA/LV/RV: left atrium/right atrium/left ventricle/right ventricle; SBP/DBP/PP: systolic/diastolic/pulse pressure. Indices were computed averaging over the respiratory cycle. These simulations were performed under the assumption of non-zero terminal unstressed volumes. Var $= (\mathcal{I}_{\text{ADAVN86}} - \mathcal{I}_{\text{ADAVN}})/\mathcal{I}_{\text{ADAVN}}$. We color in green variations with $|\text{Var}| < 0.05$, in yellow variations with $0.05 \leq |\text{Var}| < 0.1$, and in red variations with $|\text{Var}| > 0.1$.

	RA	RV	LA	LV
$E_{\mathrm{fw},\alpha}^{\min}$	90.	71.5	180.	102.3
$E_{\mathrm{fw},\alpha}^{\max}$	255.	640.	357.	3580.8
$A_{0,\alpha}$	0.02	0.015	0.02	0.015
β_α	0.22	0.22	0.22	0.22
n_α	10^{-5}	$5 \cdot 10^{-5}$	10^{-5}	$5 \cdot 10^{-5}$

Table 4.7: Parameters for the nonlinear heart model. Elastances are expressed in dyn/cm^5, $A_{0,\alpha}$ in mL^{-1}, β_α in mmHg and n_α in mL^{-2}.

Index	ADAVN86			ADAVN		
	No resp. linear model	Resp., nonlinear model	Var.	No resp. linear model	Resp., nonlinear model	Var.
Ventriculo-arterial coupling indices and stroke work						
LV elastance index [mmHg/mL]	2.80	2.07	-0.26	2.85	2.12	-0.26
Aortic elastance index [mmHg/mL]	1.18	1.17	-0.01	1.24	1.23	-0.01
Ventriculo-arterial coupling index	0.42	0.56	+0.33	0.43	0.58	+0.35
Aortic Pulsatility Index	4.62	3.86	-0.16	4.24	3.27	-0.23
LV stroke work [J]	1.08	1.08	+0.00	1.03	1.05	+0.02
Chamber volumes and related quantities						
Cardiac output [L/min]	6.02	6.04	+0.00	5.81	5.88	+0.01
LV stroke volume index [mL/m^2]	49.56	49.85	+0.01	47.90	48.54	+0.01
LV ejection fraction [%]	64.78	59.25	-0.09	64.04	58.74	-0.08
RV stroke volume index [mL/m^2]	49.22	50.53	+0.03	47.57	49.61	+0.04
RV ejection fraction [%]	59.91	52.05	-0.13	59.90	52.53	-0.12
LA volume index [mL/m^2]	49.66	48.20	-0.03	48.41	46.88	-0.03
RA volume index [mL/m^2]	56.62	63.84	+0.13	53.81	60.46	+0.12
Blood pressure						
Central venous pressure [mmHg]	4.90	4.70	-0.04	4.67	4.04	-0.14
Mean left atrial pressure [mmHg]	6.95	6.23	-0.10	6.74	5.74	-0.15
Mean arterial pressure [mmHg]	93.48	93.80	+0.00	92.60	93.10	+0.01
Peripheral SBP [mmHg]	122.98	122.93	+0.00	127.62	127.33	+0.00
Peripheral DBP [mmHg]	73.51	74.56	+0.01	73.08	74.12	+0.01
Peripheral PP [mmHg]	49.47	48.36	-0.02	54.55	53.21	-0.02
Blood flow distribution						
Cerebral flow [mL/s]	11.37	11.31	-0.01	12.37	12.41	+0.00
Coronary flow [mL/s]	4.24	4.40	+0.04	4.34	4.58	+0.06

Table 4.8: Main cardiac and haemodynamic indices $\mathcal{I}$ with the linear and nonlinear heart model using the ADAVN and ADAVN86 networks. These simulations were performed in the presence of nonzero terminal unstressed volumes. LA/RA/LV/RV: left atrium/right atrium/left ventricle/right ventricle; SBP/DBP/PP: systolic/diastolic/pulse pressure. Indices were computed averaging over the cardiac cycle. Var $= (\mathcal{I}_{\mathrm{NL}} - \mathcal{I}_{\mathrm{L}})/\mathcal{I}_{\mathrm{L}}$. We color in green variations with $|\mathrm{Var}| < 0.05$, in yellow variations with $0.05 \leq |\mathrm{Var}| < 0.1$, and in red variations with $|\mathrm{Var}| > 0.1$.

Index	Linear no resp	Linear resp	Var_L	Nonlinear resp	Var_NL
Ventriculo-arterial coupling indices and stroke work					
LV elastance [mmHg/mL]	2.80	2.60	-0.07	2.67	-0.05
Aortic elastance [mmHg/mL]	1.18	1.15	-0.03	1.18	+0.00
Ea / E_{LV} ratio	0.42	0.44	+0.05	0.44	+0.05
Aortic Pulsatility Index	4.62	7.57	+0.64	4.95	+0.07
LV stroke work [J]	1.08	1.76	+0.63	1.24	+0.15
Chamber volumes and related quantities					
Cardiac output [L/min]	6.025	7.68	+0.27	6.39	+0.06
LV SVI [mL/m^2]	49.56	63.10	+0.27	52.78	+0.06
LV EF [%]	64.78	64.99	+0.00	64.27	-0.01
RV SVI [mL/m^2]	49.22	63.77	+0.30	53.79	+0.09
RV EF [%]	59.91	59.74	-0.00	58.03	-0.03
LA volume index [mL/m^2]	49.66	68.51	+0.38	62.38	+0.26
RA volume index [mL/m^2]	56.62	84.71	+0.50	76.09	+0.34
Blood pressure					
Central venous pressure [mmHg]	4.90	2.77	-0.43	4.31	-0.12
Mean arterial pressure [mmHg]	93.48	115.77	+0.24	98.86	+0.06
Peripheral SBP [mmHg]	122.98	159.50	+0.30	130.31	+0.06
Peripheral DBP [mmHg]	73.51	88.37	+0.20	77.94	+0.06
Peripheral PP [mmHg]	49.47	71.13	+0.44	52.36	+0.06
Blood flow distribution					
Cerebral blood flow [mL/s]	11.37	14.39	+0.27	11.70	+0.03
Coronary blood flow [mL/s]	4.24	5.68	+0.34	4.65	+0.10

Table 4.9: Main cardiac and haemodynamic indices $\mathcal{I}$ obtained with the linear and nonlinear heart model, using the elastances reported in Müller et al. (2023). These simulations were performed in the presence of nonzero terminal unstressed volumes. LA/RA/LV/RV: left atrium/right atrium/left ventricle/right ventricle; SBP/DBP/PP: systolic/diastolic/pulse pressure. Indices were computed averaging over the respiratory cycle. Var_L = (Linear resp – Linear no resp)/Linear no resp; Var_NL = (Nonlinear resp – Linear no resp)/Linear no resp. We color in green variations with $|\text{Var}| < 0.1$, in yellow variations with $0.1 \leq |\text{Var}| \leq 0.3$, and in red variations with $|\text{Var}| > 0.3$.

4.3 Modelling gas transport and exchange: model parametrisation, verification and validation

We describe in this section the parametrisation and validation of the gas transport and exchange modules presented in sections 2.2.2 and 2.3.6. In particular, in addition to reporting the parametrisation adopted for the baseline lung gas-exchange model described in section 2.3.6.1, we present our parametrisation strategy for the peripheral exchange model illustrated in section 2.3.6.2, which leverages the anatomical detail provided by the ADAVN86 vascular network. In section 4.3.2, we test the resulting modelling framework.

4.3.1 Parametrisation

4.3.1.1 Gas exchange in the lungs

The parametrisation employed for the lung exchange module is the same as that proposed by Albanese et al. (2016). Table 4.10 reports the considered parameters.

		Oxygen	Carbon dioxide
	Dissociation curves		
Gas saturation capacity	$\phi_{\text{sat,gas}}$ $\left[\frac{\text{mL}_{\text{gas}}}{(\text{mL}_{\text{blood}})}\right]$	0.2045	1.9564
Hill coefficient	h_{gas}	0.3836	1.819
Dissociation slope	α_{gas} [mmHg^{-1}]	0.0320	0.0559
Dissociation intercept	β_{gas} [mmHg^{-1}]	0.0083	0.0326
Dissociation constant	k_{gas} [mmHg]	14.99	194.4
	Lung gas exchange		
Fraction of inspired gas	$F_{i,\text{gas}}$ [%]	21.04	0.0421
Gas exchange coefficient	K_{gas} $\left[\frac{\text{mL}_{\text{gas}}}{(\text{mL}_{\text{blood}} \cdot s \cdot \text{mmHg})}\right]$	2.28	65.60
Constant for volume conversion	K		1.2103
Atmospheric pressure	P_{atm} [mmHg]		760
Water vapour pressure	P_{ws} [mmHg]		47
Haemoglobin concentration	hgb [$\text{g} \cdot \text{mL}^{-1}$]		0.15

Table 4.10: Parameters employed for the lung exchange module.

4.3.1.2 Gas exchange in peripheral capillaries

Two distinct parametrisations of the peripheral exchange model are examined. The first follows the formulation introduced in Albanese et al. (2016) (Parametrisation 1), whereas

	O_2 consumption [mL/min]	CO_2 production [mL/min]	Tissue volume [mL]
Splanchnic	108.4190	91.0720	2673
Extrasplanchnic	14.6830	12.3337	262
Skeletal muscle	51.60	43.3440	31200
Brain	47.5020	39.9017	1300
Coronaries	24	20.16	284

Table 4.11: Tissue gas exchange parameters (Parametrisation 1).

the second is constructed to take advantage of the anatomical resolution offered by the ADAVN86 vascular network (Parametrisation 2). In particular, we need to provide suitable definitions for the metabolic gas production and consumption rates, namely $\dot{M}_{CO_2}$ and $\dot{M}_{O_2}$ in equations (2.152) and (2.151) (section 2.3.6.2), and for the tissue volumes employed in equation (2.153) (section 2.3.6.2) to derive gas concentrations in peripheral terminals.

4.3.1.2.1 Parametrisation 1

Albanese et al. (2016) considers five regions (coronary vessels, brain vessels, skeletal muscle vessels, splanchnic and extrasplanchnic vessels) corresponding to the venous pool subdivision. Compartmental tissue volumes V_{tissue} are assigned based on literature data. Values for the oxygen consumption rates $\dot{M}_{O_2}$ in the cerebral, coronary and skeletal muscle compartments are based on those reported by Albanese et al. (2016); Ursino and Magosso (2000); Magosso and Ursino (2001), and those for the splanchnic and extrasplanchnic compartments are computed under the assumption of a total oxygen uptake of 250 ml/min, together with the reported ratio $\dot{M}_{O_2,sp}/\dot{M}_{O_2,ep} = 7.384$ (Ottesen et al., 2004). The values for $\dot{M}_{CO_2}$ are computed assuming a respiratory quotient of 0.84. Parameters are reported in table 4.11. It is worth noting that the total tissue volume represented in Albanese et al. (2016) amounts to 35719 mL, which implies that the perfusion of adipose tissue, bone, bone marrow, cartilage, and skin is not included. From a modelling perspective, adopting the Albanese framework requires distributing both the perfused tissue volume and the metabolic gas production/consumption rates across all terminals present in the ADAVN86 vascular network within each considered region in a physiologically meaningful manner, for example, proportionally to the fraction of blood flow entering their venous compartment.

4.3.1.2.2 Parametrisation 2

The parametrisation presented above is tailored to a compartmental model, where circulatory districts are described through few compartments. Thanks to the anatomical detail encoded in the ADAVN86 vascular network, we propose different parametrisation approach. In what follows, we outline the derivation of suitable gas metabolic rates and tissue volumes for each terminal.

Metabolic rates

Oxygen delivery from the lungs to the tissues depends on cardiac output, haemoglobin concentration, and on the efficiency of pulmonary oxygenation. Importantly, only a portion of the oxygen carried in the blood is actually released to tissues. The Fick's principle provides a way to quantify oxygen consumption by relating it to the cardiac output or the flow to a specific tissue, and the arteriovenous difference in oxygen content (Raikhelkar et al., 2011)

$$\dot{M}_{O_2} = q \times (\phi_{\text{artery},O_2} - \phi_{\text{vein},O_2}). \tag{4.15}$$

Under typical physiological conditions, $\phi_{\text{artery},O_2} \simeq 20\text{vol}\%$ and $\phi_{\text{vein},O_2} \simeq 15\text{vol}\%$, implying that tissues consume on average around 5vol% of the delivered oxygen (that is, 50 mL of O_2 per litre of blood). For a cardiac output of approximately 5L/min this yields

$$\dot{M}_{O_2} = 5\text{L/min} \times 50\text{mL/L} = 250\text{mL/min}. \tag{4.16}$$

Clearly, oxygen extraction increases with exercise, and it is well established that metabolically active organs such as the heart and brain have higher oxygen extraction rates.

We report in table 4.12 literature values for the arteriovenous oxygen difference in six regions of the body, combining the skeletal muscle-skin compartments, since their perfusion cannot be distinguished in our model. Reported values are not sex-specific, and the author acknowledges the presence of considerable inter-individual variation. The oxygen consumption rate associated with each terminal is computed using equation (4.15), where q denotes the blood flow entering the terminal venous compartment, and $\phi_{\text{artery},O_2} - \phi_{\text{vein},O_2}$ represents the expected arterio-venous oxygen difference in the region in which the terminal is located. Here, each terminal belongs to at most one region. Metabolic CO_2 production is computed under the assumption of a 0.84 respiratory quotient, which indicates a balanced metabolism

$$\dot{M}_{CO_2} = 0.84\dot{M}_{O_2}. \tag{4.17}$$

Table 4.13 shows the metabolic rates obtained for each region with the ADAVN86 model along with the total flow rates entering the venous compartments present in each region. These metabolic rates are not the result of a full simulation. Rather, they arise directly from the parametrisation procedure, being computed as the product of the haemodynamically simulated flow entering each region and the corresponding arteriovenous oxygen difference.

Tissue volumes

Tissue volumes perfused by each terminal, which are required to estimate venous gas concentration according to equation (2.153) in section 2.3.6.2, are defined in such a way that takes advantage of the anatomical definition of both the ADAVN and ADAVN86 networks. They are defined from mass literature data for adult males (Valentin, 2002)

Region	Arteriovenous O_2 difference	Venous O_2 content	Reference
Coronary	12.5 mL/dL	6.5 mL/dL	Kung-Ming (2026)
Brain	6.7 mL/dL	12.3 mL/dL	Kung-Ming (2026)
Splanchnic	4.2 mL/dL	14.8 mL/dL	Kung-Ming (2026)
Renal	1.4 mL/dL	17.6 mL/dL	Kung-Ming (2026)
Skeletal muscle	7.1 mL/dL	11.9 mL/dL	Kung-Ming (2026)
Skin	1.2 mL/dL	17.8 mL/dL	Kung-Ming (2026)
Other	3.0 mL/dL	16 mL/dL	Kung-Ming (2026)

Table 4.12: Arteriovenous oxygen difference and venous oxygen content in the main vascular regions. The way our model is structured makes it impossible to split the skeletal muscle and cutaneous circulations. Consequently, we define the metabolic rate for the combined skin-muscle compartment accounting for the fact that of CO perfusing these two tissues, 77% perfuses the muscle, and 23% the skin (Valentin, 2002). A reasonable overall arteriovenous oxygen difference can be computed as $\phi_{\text{artery},O_2} - \phi_{\text{vein},O_2} = 0.77 \times 7.1 + 0.23 \times 1.2 = 5.743$ mL/dL.

Region	O_2 consumption rate [mL/min]	Total flow rate [mL/s]	O_2 consumption rate [mL/min] (Albanese et al. (2016))
Coronary	31.66	4.22	24
Brain	41.06	10.21	47.5020
Splanchnic	76.73	30.44	108.4190
Renal	21.31	25.37	14.683
Skin-muscle	103.55	30.05	51.60

Table 4.13: Metabolic rates and total flow rates entering the venous compartments present in each region (Parametrisation 2). Total metabolic rate with the new parametrisation is 274.32 mL/min, for a CO of 6.02 L/min. This results in an average arteriovenous oxygen difference of 4.56 mL/dL.

under the assumption that the tissue density is uniform and equal to 1 g/cm^3, so that the total tissue mass is equal to the total tissue volume. Analogous datasets for newborns, children, adolescent and adult females, and adolescent males are also provided in Valentin (2002). The assumption of 1 g/cm^3 average tissue density may be refined, depending on the application, to incorporate variations in body-fat composition related e.g. to age and sex, as well as differences in individual tissue densities (Durnin and Womersley, 1974; Zemel, 2022). We consider a total tissue volume of 73L, 63L of which (86.43%) are involved in gas exchange (see table 4.14). We exclude separable connective tissues and certain lymphatic tissues, the contents of the stomach, intestines and gallbladder, the upper airways and lungs, and blood. The volume involved in gas exchange is split among 25 regions, 8 of which do not contain 0D terminals in the ADAVN86 model. We assume that excess volume in the limb is distributed among the existing limb terminals, while volume associated to the adrenals and diaphragm is distributed among the intercostal, liver, intestine and kidney regions, similar to the approach we followed for distributing excess flow rate during the calibration of the haemodynamics. Tissue volumes are distributed among the venous compartments of each terminal proportionally to the blood flow fraction entering them:

$$\mathrm{TV}^{j}_{i,\mathrm{reg}} = \mathrm{TV}_{\mathrm{reg}} \frac{q^{j}_{in,v,i}}{\sum_{j\in \mathrm{reg}} \sum_{i\in j} q^{j}_{in,v,i}}, \tag{4.18}$$

with $\mathrm{TV}^{j}_{i,\mathrm{reg}}$ tissue volume perfused by the $i-th$ compartment of the $j-th$ terminal in region reg, $\mathrm{TV}_{\mathrm{reg}}$ total tissue volume in region reg, and $q^{j}_{in,v,i}$ flow entering the $i-th$ venous compartment of terminal j in region reg. $\sum_{j\in \mathrm{reg}} \sum_{i\in j} q^{j}_{in,v,i}$ corresponds to the total flow rate entering the venous compartments of terminals present in region reg. Flow rates are precomputed from a reference haemodynamic simulation. In the ADAVN86 network, due to the low anatomical resolution of the abdominal vasculature, the stomach, intestines, liver and pancreas are perfused by the same terminal. As a consequence, TV^{j}_{i} is actually the sum of per-region contributions.

4.3.2 Results and discussion

4.3.2.1 Transport model

We evaluate the transport module using a test bolus, a procedure commonly employed in the clinical practice to determine, prior to contrast-enhanced CT and MRI examinations, the time required for the contrast agent to travel from the injection site to the target vessel (Fischer et al., 2022; Bae, 2010). In order to reproduce this scenario, we simulate the injection of 20 mass units (UM) of contrast medium into the antecubital vein (see figure 4.28), at a constant rate, over 1, 5, and 10 seconds. Bolus injection start at time $t = 50$ s, and the simulation ends at time $t = 400$ s. Simulations are performed on both the

	Mass [g]	% of total mass	ADAVN regions	Presence in ADAVN86
Organs	**5621**	**7.7**		
Adrenals	14	0.02	32, 33	X
Stomach	150	0.21	35	✓
Intestines	1020	1.4	40	✓
Liver	1800	2.47	34	✓
Pancreas	140	0.19	37	✓
Brain	1450	1.99	2,3,4,5,6	✓
Heart	330	0.45	26,27,28	✓
Spleen	150	0.21	36	✓
Kidneys	310	0.42	38,39	✓
Diaphragm	256	0.35	25	X
Head	2813	3.85	1,7,8,9	✓
Distributed organs	**57472**	**78.73**		
Trunk	16616	22.76	20,21,22,23,24,29,30,31 41,42,43,44,45,46,47,48	✓
Right arm	1876	2.57	10,11,12	X
Right forearm	1098	1.5	13	✓
Right hand	408	0.56	14	X
Left arm	1876	2.57	15,16,17	X
Left forearm	1098	1.5	18	✓
Left hand	408	0.56	19	X
Pelvis	10016	13.72	49	✓
Right thigh	7069	9.68	50,51,52,53	✓
Right leg	2766	3.79	54	✓
Right foot	797	1.09	55	X
Left thigh	7069	9.68	56,57,58,59	✓
Left leg	2766	3.79	60	✓
Left foot	797	1.09	61	X

Table 4.14: Tissue regions involved in gas exchange. Note that eight of them do not contain terminals in ADAVN86.

ADAVN86 (sections 2.1.4, 4.2.1.1) and ADAVN (section 2.1.3) vascular networks, in the presence of respiration, using the nonlinear cardiac model introduced in section 2.3.1.2.

We perform the injection of a mass $M_{\phi_i,j}$ of tracer i at the level of a vessel junction j by enforcing that

$$\dot{M}^{TOT}_{\phi_i,j,In} = \dot{M}^{BLOOD}_{\phi_i,j,In} + \dot{M}^{INJ}_{\phi_i,j,In}, \tag{4.19}$$

where $\dot{M}^{TOT}_{\phi_i,j,In}$ is the total incoming tracer mass flow (UM/s), composed of the tracer already present in the blood ($\dot{M}^{BLOOD}_{\phi_i,j,In}$) and by the injected one ($\dot{M}^{INJ}_{\phi_i,j,In}$). The injection term $\dot{M}^{INJ}_{\phi_i,j,In}$ is defined so that the desired mass $M_{\phi_i,j}$ of tracer is injected over the specified time interval.

Assuming uniform mixing at the junction, the tracer concentration $\phi_{i,j}$ in outlet vessels (in this case the antecubital vein) is computed as

$$\phi_{i,j} = -\frac{\dot{M}^{TOT}_{\phi_i,j,In}}{Q_{j,Out}} \tag{4.20}$$

whenever $Q_{j,Out} \neq 0$.

For this test, we are not injecting a volume of fluid along with the tracer mass, i.e. we are not perturbing total fluid volume within the circulation. This choice was motivated by the fact that small boluses, such as the ones we are considering, do not perturb the haemodynamics (Bae, 2010).

Through this test, we aim to verify the following hypotheses:

(1) At steady state, the distribution of tracer mass across the system (arteries, veins, terminals, heart, pulmonary circulation) is expected to mirror the underlying blood volume distribution, with total mass conserved over time.

(2) Following bolus injection, the time to peak (TTP) tracer mass in the aortic arch should be approximately 19.1 ± 3.5 seconds for a 20 UM bolus administered over 5 seconds, consistent with reported values (Fischer et al., 2022). This peak time, measured from the beginning of the injection, is expected to increase with longer injection durations. Furthermore, for a fixed total amount of contrast medium, a faster injection rate should produce a higher peak value (Weininger et al., 2011; Bae, 2010; Erturk et al., 2008). Note that TTPs are reported in the literature for aortic enhancement (HU), which can be regarded as proportional to tracer mass.

Figure 4.29 compares the tracer mass and blood volume distributions across vascular compartments, demonstrating close agreement and thereby supporting hypothesis (1). Figure 4.31 shows the percent relative error in total tracer mass, which remains on the order of 10^{-9}, verifying mass conservation (for additional considerations we refer to section 3.1.1).

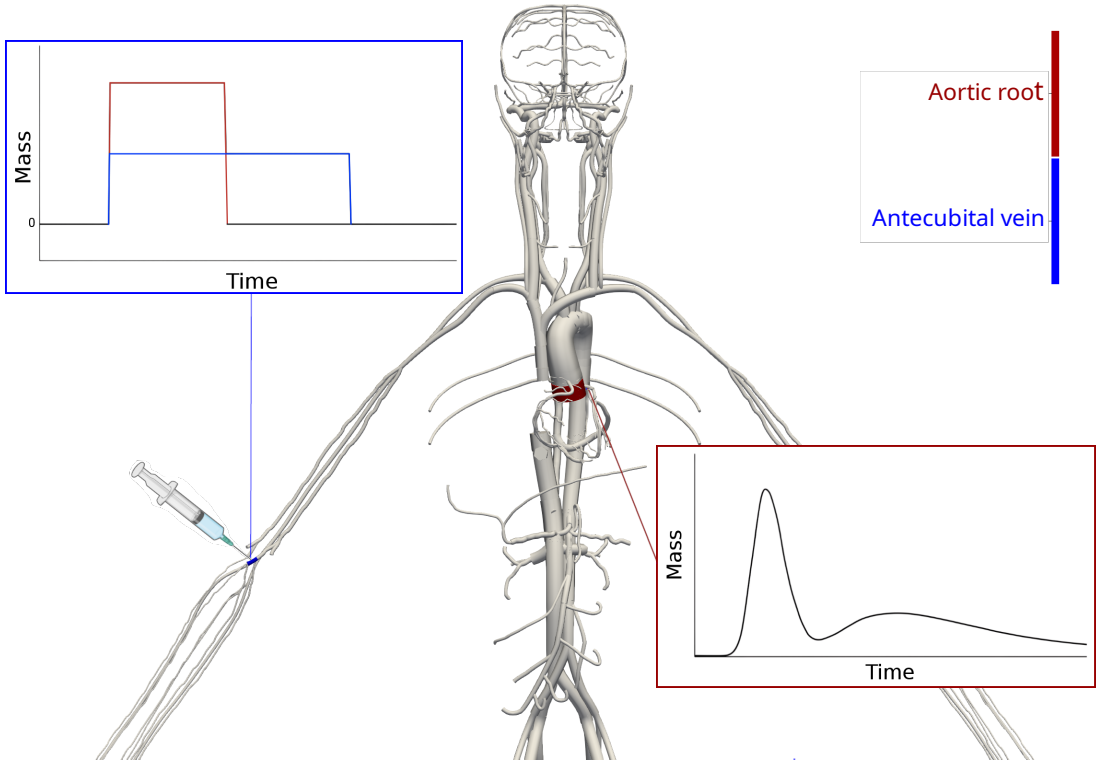

Figure 4.28: Setup of the bolus test: tracer is injected into the antecubital vein, transit times are measured in the aortic arch.

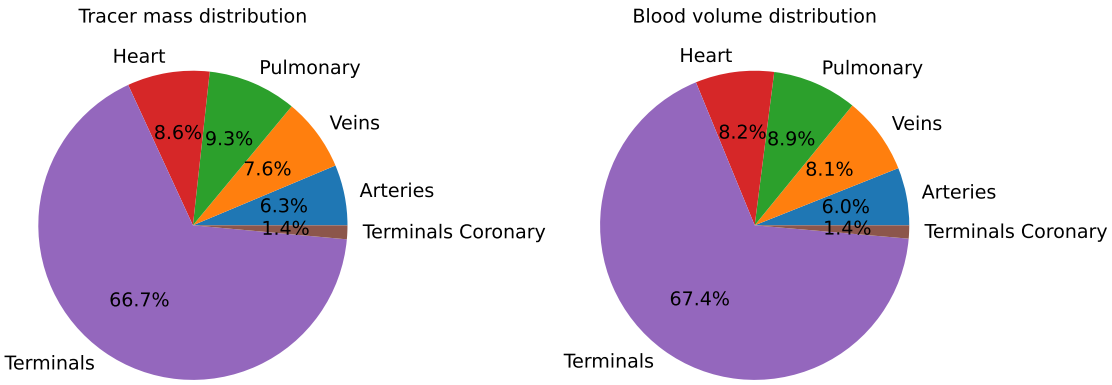

Figure 4.29: Comparison between tracer mass and blood volume distributions at the final respiratory cycle.

We report in figure 4.30 the transient distribution of tracer mass following the start of the injection.

Figure 4.33 shows the tracer mass arrival in the aortic arch following injections lasting 1, 5 and 10 seconds. Consistent with hypothesis (2), we observe that the TTP increases with longer injection durations, which are also associated with lower peak values. The TTP obtained for the 5 seconds injection, 14.8 s, is lower than the 19.1 ± 3.5 seconds reported by Fischer et al. (2022). However, the reported value corresponds to a cohort of patients aged 62 ± 16, who underwent CCTA for suspected coronary artery disease. Results reported by François et al. (2003) show that TTPs are significantly longer (approximately 33%) for patients with CAD, suggesting that a reasonable comparison value would be on the order of $\frac{19.1}{1.33} \simeq 14.4$ seconds, which is in close agreement with the 14.8 s obtained in our simulation.

In addition, we compare in figure 4.34 results obtained with the ADAVN86 network to results obtained using the ADAVN one, confirming that, even though there is a slight difference in peak timing and amplitude, the parametrisation adopted for the reduced network generates satisfactory results. Indeed, the parametrisation strategy illustrated in section 4.2.1.1 for the ADAVN86 network was specifically devised to ensure that the resulting upper and lower limb blood flow fractions remain consistent with those produced by the original ADAVN model.

In order to expand our validation, we report in figure 4.35 results obtained by injecting a

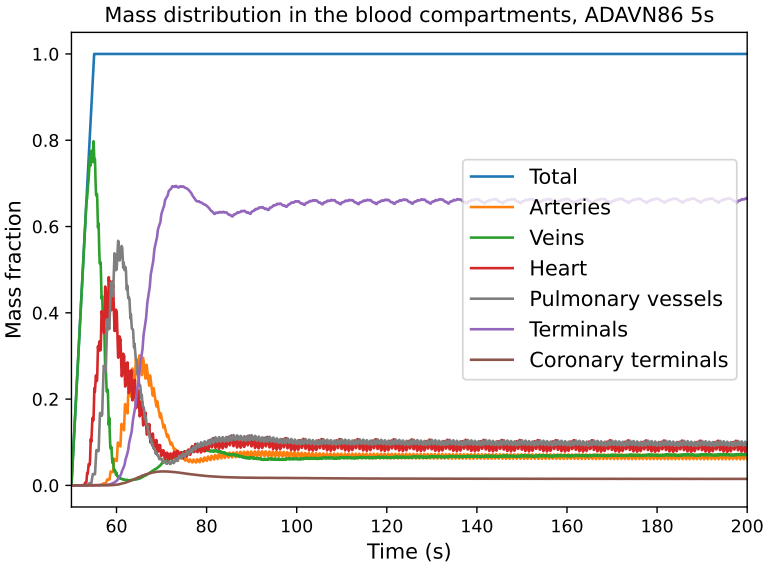

Figure 4.30: Tracer mass distribution in the blood compartments.

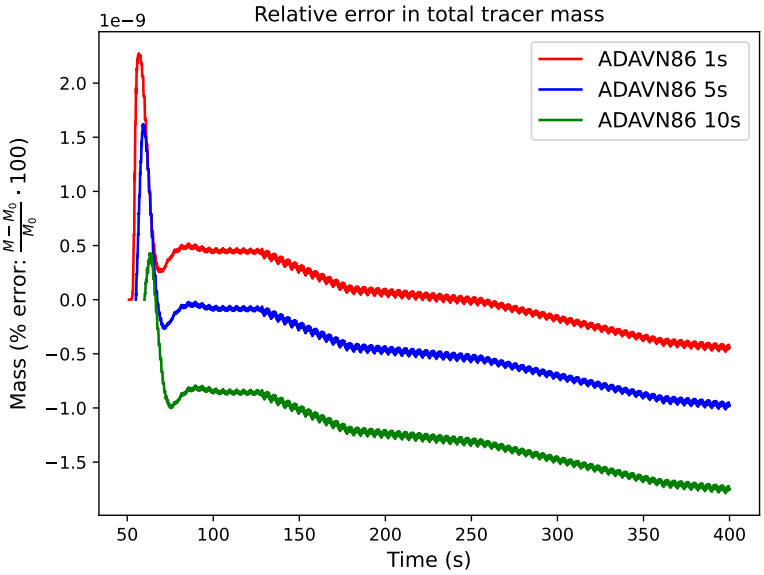

Figure 4.31: Percent relative error in total tracer mass.

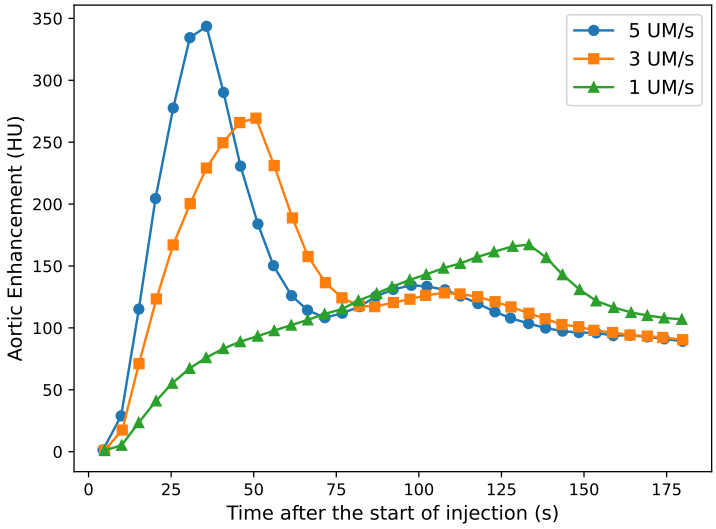

Figure 4.32: Aortic root enhancement curves adapted from Bae (2010) for three injection protocols: 125 UM of tracer injected at a constant rate over 25, 41, 125 seconds, i.e. at 5 UM/s, 3 UM/s, 1 UM/s.

larger amount of tracer medium (125 UM) over longer injection periods, namely 25, 41 and 125 seconds, showing a good correspondence with the computer simulation data obtained by Bae (2010) through a physiologically based pharmacokinetic model, reported in figure 4.32 for an analogous setup. In particular, times to peak contrast enhancement reported by Bae (2010) are around 35, 50 and 135 seconds after the start of injection, while the ones we obtain are 31.6, 47.6 and 131.6 seconds.

Additionally, we obtain comparable mass profiles. A more direct comparison with results reported by Bae (2010) would require modelling the redistribution of tracer from the vascular to the interstitial spaces, as well as incorporating tracer clearance mechanisms. We currently only account for mixing effects at junctions and in lumped parameter models such as peripheral terminals, heart and pulmonary circulation. In addition, we would have to account for haemodynamic perturbation caused by bolus injections.

4.3.2.2 Cardiopulmonary model with gas transport and exchange

We evaluate the combined gas transport and exchange model by simulating a physiological condition that includes a 1.7% pulmonary shunt, consistent with the setup used by Albanese et al. (2016), which accounts for the oxygen partial pressure drop that is commonly observed between the alveoli and systemic arteries (Hantzidiamantis and Amaro, 2019; Hall and Halle, 2020). As the haemodynamic portion of the model is not affected, at this stage, by the presence of gas transport and exchange, we refer to section 4.2 for the parametrisation and verification of the model obtained combining the ADAVN86 vascular network (section 2.1.4) with the nonlinear cardiac model introduced in section 2.3.1.2, and to section 4.1

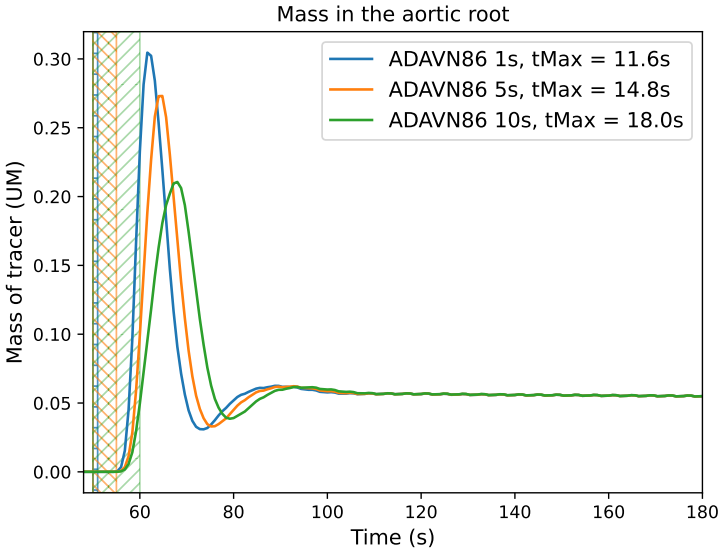

Figure 4.33: Tracer mass arrival in the aortic root for three injection protocols: 20 UM of tracer injected at a constant rate over 1, 5, 10 seconds. tMax denotes the TTP. Shaded regions denote injection periods.

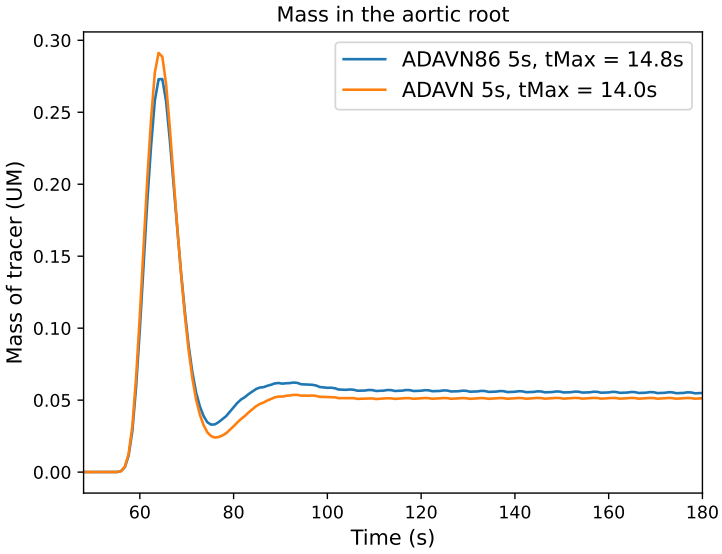

Figure 4.34: Tracer mass arrival in the aortic root: 20 UM of tracer injected at a constant rate over 5 seconds with the ADAVN86 and ADAVN models. tMax denotes the TTP.

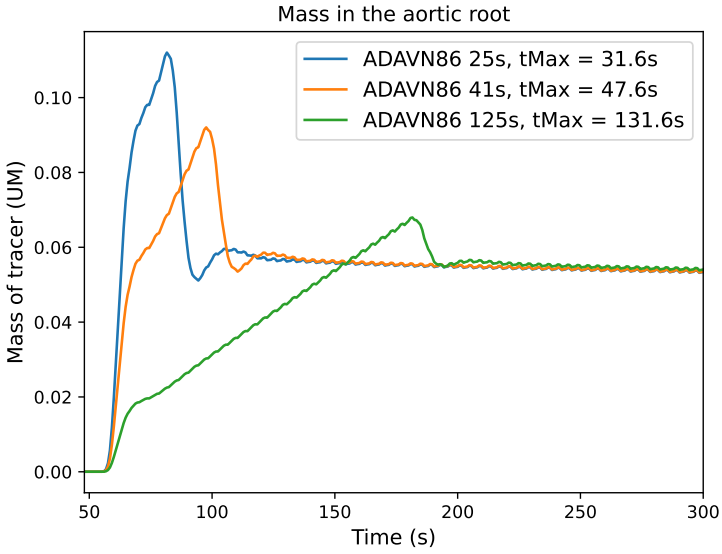

Figure 4.35: Tracer mass arrival in the aortic root for three injection protocols: 125 UM of tracer injected at a constant rate over 25, 41, 125 seconds, i.e. at 5 UM/s, 3 UM/s, 1 UM/s. tMax denotes the TTP.

for a validation against physiological literature data for the ADAVN vascular network. Simulations are initialized by prescribing in all 0D lumped parameter models the gas concentration values obtained through our implementation of the model by Albanese et al. (2016) [1].

Table 4.15 summarizes the main outputs of the model, reported as average values over a respiratory cycle. In addition, figure 4.36 shows the time profiles of gas partial pressures in the alveoli, pulmonary circulation, heart, aortic root, and inferior vena cava.

Alveolar partial pressures (figure 4.36, ALV) follow the expected physiological behaviour described in the literature (Comroe et al., 1977) and are consistent with previous modelling studies (Albanese et al., 2016). At the onset of inspiration, when dead-space air enters the alveoli, P_{A,O_2} drops to a minimum while P_{A,CO_2} peaks. Shortly after, as inspired air reaches the alveoli, P_{A,O_2} rapidly increases and P_{A,CO_2} decreases, with their respective maximum and minimum values occurring at end-inspiration. During expiration, when no fresh air enters the alveoli, the opposite behaviour is observed. As noted by Albanese et al. (2016), a direct comparison with physiological pressure tracings is not possible, since computational results include cardiac-induced pressure variations. These oscillations generate plateau-like segments superimposed on the otherwise monotonic inspiratory and expiratory patterns, and are typically omitted in physiological textbook representations. Therefore, our observations refer to the overall trend of the simulated gas partial pressure waveforms.

[1] Laudenzi et al. (2025b)

Gas exchange occurs across the haemato-alveolar membrane in the pulmonary capillaries (figure 4.36, PC), where P_{PC,O_2} rises from 37.19 mmHg to 104.3 mmHg, and P_{PC,CO_2} decreases from about 36.01 mmHg to 34.98 mmHg. The oxygenated blood then flows through the pulmonary veins, where oxygen partial pressure differs markedly between the simulations with (81.94 mmHg) and without (103.21 mmHg) a pulmonary shunt. Blood subsequently enters the left atrium and ventricle before being ejected into the aortic root.

Peripheral gas exchange is reflected in the steep drop in oxygen partial pressure between the aortic and caval compartments, with deoxygenated blood returning to the right atrium via the coronary sinus and venae cavae. In particular, as illustrated in (figure 4.36, IVC), P_{O_2} in the IVC is approximately 40.13 mmHg, consistent with literature data, and P_{CO_2} is 35.37 mmHg, lower than the expected 46 mmHg Nevertheless, the corresponding CO_2 concentration remains close to the physiological reference (0.48 $\mathrm{mL_{gas}/mL_{blood}}$ compared with an expected 0.52 $\mathrm{mL_{gas}/mL_{blood}}$). These discrepancies in partial pressures arise from the fact that the dissociation functions we employ are extremely sensitive to small variations in concentration ($< 10^{-3}$). As a consequence, a simulation where gas concentrations have not reached a perfect steady state, as seems true in our case for CO_2 (see figure 4.36, panel PA), may produce biased partial pressure values.

Compared to the model by Albanese et al. (2016), our formulation explicitly represents gas transit within the pulmonary arteries, capillaries, veins, and the heart, whereas Albanese's approach treats these pathways as instantaneous. We also drop the assumption of instantaneous equilibrium between the alveolar space and capillary blood. As a result, we observe a temporal shift between the partial pressure curves in the pulmonary capillaries and in the aortic root of around 3-4 s. These results are consistent with the pulmonary transit times (time blood takes to pass from the right ventricle to the left ventricle via pulmonary circulation) of 5.9-7.9 s reported by Segeroth et al. (2023). Previous work suggests that roughly 70% of this interval is spent in the pulmonary capillaries and veins (Moore et al., 2023), corresponding to ≈ 4.25 s. Subtracting a capillary transit time of ≈ 0.75 s (Patel and Patel, 2023) yields an estimate of ≈ 3.5 s for the pulmonary venous transit time, under the simplifying assumption of negligible intracardiac transit. Since right- and left-ventricular transit times at rest are each on the order of 0.4-0.6 s, this assumption slightly overestimates venous transit, but does not affect our interpretation of the observed 3-4 s temporal shift. Indeed, this delay already encompasses pulmonary venous and intracardiac transit, so no additional correction is required when comparing it to literature-based estimates of the post-capillary pulmonary compartment.

Variable	Model simulation		Reference
	No shunt	1.7% shunt	
Aortic P_{O_2} [mmHg]	103.23	82.03	75-100 (McGee and Franco-McKinney)
Aortic P_{CO_2} [mmHg]	34.42	32.92	35-45 (McGee and Franco-McKinney)
Aortic C_{O_2} [mL_{gas}/mL_{blood}]	0.19	0.2	0.17-0.2 (McGee and Franco-McKinney)
Aortic C_{CO_2} [mL_{gas}/mL_{blood}]	0.46	0.45	0.48 (Arthurs and Sudhakar, 2005)
IVC P_{O_2} [mmHg]	41.92	40.13	40 (Albanese et al., 2016)
IVC P_{CO_2} [mmHg]	36.3	35.37	46 (Albanese et al., 2016)
IVC C_{O_2} [mL_{gas}/mL_{blood}]	0.16	0.16	0.12-0.15 (McGee and Franco-McKinney)
IVC C_{CO_2} [mL_{gas}/mL_{blood}]	0.48	0.48	0.52 (Arthurs and Sudhakar, 2005)
Alveolar P_{O_2} [mmHg]	106.05	106.28	104 (Albanese et al., 2016)
Alveolar P_{CO_2} [mmHg]	34.36	34.93	38-42 (Arthurs and Sudhakar, 2005)

Table 4.15: Mean values of main gas composition variables obtained in the presence and absence of the pulmonary shunt.

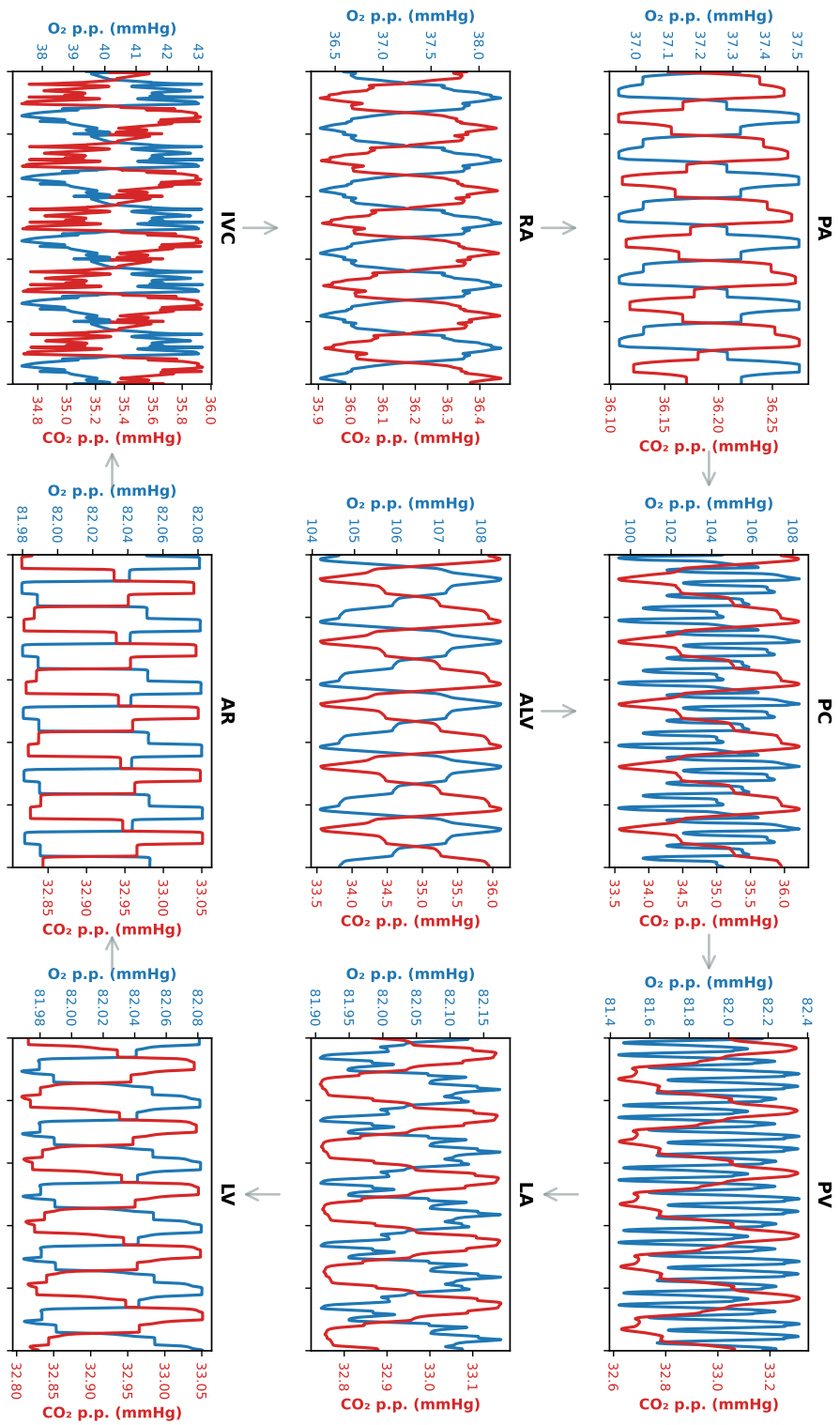

Figure 4.36: Gas transport and exchange in the main circulatory compartments over 5 respiratory cycles (x-axis ticks denote the beginning of each respiratory cycle) in the presence of a 1.7% pulmonary shunt: p.p - partial pressure, PA - pulmonary arteries, PC - pulmonary capillaries, PV - pulmonary veins, LA - left atrium, LV - left ventricle, AR - aortic root, IVC - inferior vena cava, RA - right atrium, ALV - alveoli. Arrows denote the path followed by respiratory gases, starting from the alveolar compartment.

4.4 Cerebral local autoregulation

This section focuses on validating the cerebral local autoregulation models we presented in section 2.3.7.

Before presenting the validation results, we briefly recall the main physiological mechanisms underlying cerebral autoregulation. As illustrated by Payne (2016), steady-state cerebral blood flow (CBF) remains relatively constant across a broad range of arterial blood pressure values (MAP), yet it also responds dynamically to several additional stimuli. Notably, alterations in Pa_{CO_2} can cause substantial changes in CBF, while variations in cardiac output and shifts in neural activity further modulate cerebral perfusion. These regulatory behaviours arise from three principal mechanisms of cerebral autoregulation which interact to maintain adequate and stable cerebral blood flow and oxygenation under varying physiological conditions: myogenic, metabolic, and neurogenic pathways (Payne, 2016; Claassen et al., 2021). The myogenic response reflects the intrinsic ability of cerebral vessels to actively adjust their tone in reaction to changes in MAP, thereby stabilizing flow. In response to reductions in MAP, vessels reduce their myogenic tone and increase their diameter, thus reducing resistance. The opposite occurs in response to an increase in MAP. The metabolic response is triggered when a mismatch develops between oxygen supply and the metabolic demands of neural tissue. In particular, brain perfusion is very sensitive to hypercapnia, which produces vasodilation, and hypocapnia, which reduces CBF. In addition, the cerebral vasculature responds to variations in Pa_{O_2}: hypoxia leads to vasodilation, which is strengthened in the presence of hypercapnia, and attenuated in the presence of hypocapnia Claassen et al. (2021). The neurogenic component of cerebral autoregulation remains less well understood.

Model validation will follow the structure outlined below. We start by testing, on the ADAVN86 network, the myogenic autoregulation model by Ursino and Giannessi (2010), which will be applied in chapter 4.5 to reproduce the hyperaemic response observed in foot angiosomes following a cuff-induced ischaemia test. We then incorporate the metabolic autoregulation model proposed in the same work, and test it under hypercapnic conditions. Finally , we test the metabolic autoregulation model by Magosso and Ursino (2001), in order to assess how it responds both to perturbations in gas concentrations and to perturbations in mean arterial pressure.

4.4.1 Myogenic autoregulation model

In this section, we validate the myogenic autoregulation model introduced in section 2.3.7.1. This model responds to variations in cerebral arterial flow rate by modulating terminal compliances. The variation of compliance in time alters terminal stretched blood volumes. Given that stretched blood volume is proportional to the inverse square root of resistance

(Toro et al., 2022), variations in compliance translate directly into adjustments of terminal vascular resistances.

A classical test for assessing the validity of a myogenic autoregulation model is its ability to reproduce the static autoregulation curve first introduced by Lassen (1959) (Lassen curve), which relates changes in cerebral perfusion pressure to corresponding changes in cerebral blood flow. This curve is characterised by a lower limit, where vessels reach maximal dilation; an upper limit, where they achieve maximal constriction; and a broad plateau region in which CBF varies very little despite substantial changes in MAP. This behaviour arises from active adjustments in vascular compliance, which modulate vessel diameter and thereby stabilize flow.

4.4.1.1 Simulations setup

Since our simulations are performed within a closed-loop framework, mean arterial pressure cannot be treated as an external input to the system, unlike in traditional assessments of cerebral autoregulation. As a consequence, to explore how autoregulation behaves without directly forcing pressure changes, we adjust all peripheral resistances except those in the brain, thus shifting systemic haemodynamic in a controlled way. We examine several setups, grouping them according to whether ICP is kept constant and whether respiration is active:

(1) Inactive respiration, constant ICP;

(2) Inactive respiration, ICP modulated according to the model in Müller et al. (2023);

(3) Active respiration, constant ICP;

(4) Active respiration, ICP modulated according to the model in Müller et al. (2023).

In setups (2) and (3), we also compare the outcomes obtained when autoregulation monitors the cardiac/respiratory-cycle averaged flow rate versus its instantaneous value. Since the myogenic response is modelled through a low-pass filter, both choices should provide enough smoothing for the mechanism to behave consistently.

Autoregulation parameters are chosen as illustrated in table 4.16, and all peripheral resistances except for cerebral ones are multiplied by factors 0.4, 0.6, 0.8, 1.0, 1.2, 1.4, 1.6, 1.8, 2.0. Simulations are performed over 200 seconds, with ICP modulation starting at $t = 40$ s, resistances being modified at $t = 72$ s, and myogenic autoregulation being activated at $t = 50$ s.

Terminal vessels where autoregulation is applied are shown in black in figure 4.37.

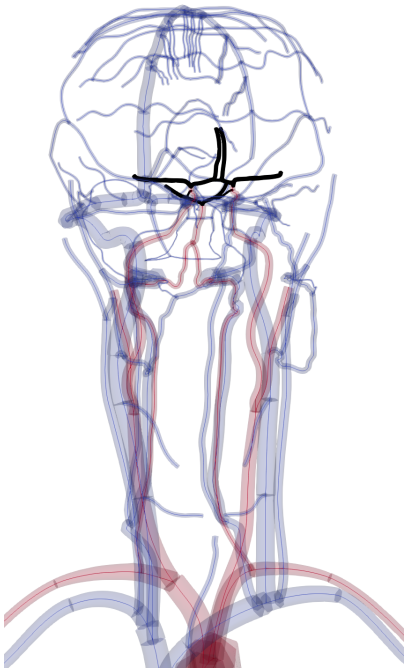

Figure 4.37: Cerebral arteries (black). Autoregulation is applied to the terminal compartments that connect them to cerebral veins (in blue).

Parameter	sat_1 [-]	sat_2 [-]	G_{reg} [-]	τ [s]	k_{mult} [-]	CBF_{ref} [mL/s]
Value	0.4	2.	0.9	20.	0.5	10.25

Table 4.16: Parameters employed for the validation of the myogenic autoregulation model by Ursino and Giannessi (2010).

4.4.1.2 Results and discussion

We report in figure 4.38 the static autoregulation curve obtained for setups (1) and (2), and in figures 4.39, 4.40 the response of cerebral vasculature to a sudden variation in mean arterial pressure. Finally, in figures 4.41 and 4.42 we report the corresponding time profiles of intracranial pressure and total cerebral blood volume, obtained respectively with constant and variable ICP models.

These results lead to several observations, especially regarding the impact of the ICP model employed for simulations. Indeed, while we can reasonably reproduce the static autoregulatory behaviour, especially for setup (1), we note a significant difference between results obtained with constant (setup (1)) and variable (setup (2)) intracranial pressures.

When ICP is treated as a fixed quantity, as in the generation of autoregulation curves reported by Ursino and Lodi (1998), the only mechanism available to buffer increases in cerebral blood volume is arteriolar vasoconstriction. This test allows us to assess, as a consequence, the impact of MAP fluctuations on CBF, without other mechanisms entering into play. Under these conditions, any rise in MAP produces an immediate increase in cerebral perfusion pressure (CPP = MAP − ICP) and therefore a transient increase in cerebral blood flow. This initial overshoot is followed by autoregulatory vasoconstriction, which decreases cerebral compliances, increases cerebrovascular resistance and reduces CBF from its peak back toward baseline levels. As MAP continues to rise and autoregulatory capacity becomes saturated, which in our case occurs for MAP levels above 122 mmHg (figure 4.39), arteriolar compliance can no longer decrease. Beyond this point, further increases in MAP lead to passive vascular distension, producing a pronounced rise in CBF, accompanied by a marked increase in cerebral blood volume (figure 4.41). This is consistent with the reduction in cerebrovascular resistance observed at very high MAP levels (figure 4.39).

The behaviour changes when ICP is allowed to vary, mirroring cerebral physiology more closely. We recall that the time rate of change of intracranial pressure, in this case, is given by a monoexponential relationship

$$\mathrm{ICP} = \mathrm{ICP}_{ref} \exp(k_{\mathrm{ICP}}(V_{IC} - V_{IC,ref})), \tag{4.21}$$

with $V_{IC}, V_{IC,ref}$ current and reference intracranial volumes, ICP_{ref} reference intracranial pressure and k_{ICP} experimentally determined coefficient, which we assume equal to 0.15 mL^{-1} (Toro et al., 2022). As mentioned above, as MAP increases, cerebral vessels constrict in response to the transient rise in cerebral blood flow, restoring it toward baseline. The initial rise in CBF is accompanied by transient increases in both ICP and cerebral blood volume; however, as long as autoregulatory capacity is preserved, both variables return close to baseline (figure 4.42). Once the upper limit of autoregulation is exceeded (MAP $>$ 123 mmHg), further vasoconstriction is no longer possible, and neither resistance nor compliance can adjust further (figure 4.40). As a result, CBF increases, although to a lesser

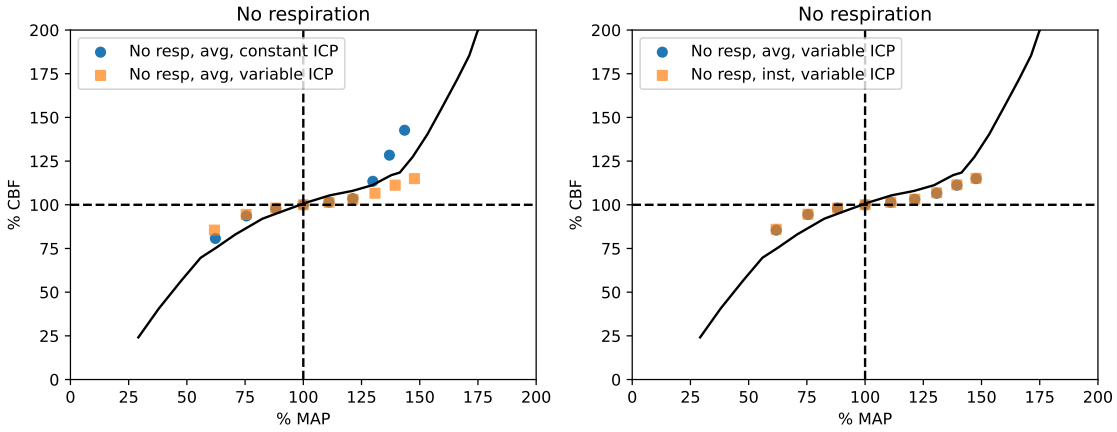

Figure 4.38: Static autoregulation curve obtained for simulation setups (1) and (2).

extent than in the constant ICP case, giving the impression of a stronger autoregulatory effect (figure 4.38). This apparent enhancement is explained by the marked increase in ICP observed at high MAP values, expected when autoregulation is impaired due to the passive dilation of vessels (Tsigaras et al., 2023; Ruesch et al., 2021). Indeed, because cerebral perfusion pressure is defined as CPP = MAP − ICP, the rise in ICP partially offsets the increase in MAP, thereby buffering the increase in CPP and limiting the corresponding rise in CBF (Chan et al., 1992). This behaviour can be related to several reasons: on the one hand, we might be considering an excessively stiff cranial compartment, which would result in steeper pressure variations. On the other hand, we are neglecting the effect of CSF reabsorption on ICP, whose rate depends on the difference between intracranial and dural sinus pressure (Toro et al., 2022).

The behaviour observed in the presence of respiration is in general very similar. Indeed, figure 4.43, which collects the static autoregulation curves for scenarios (2) and (4), demonstrates a consistent steady-state behaviour of autoregulation with and without respiration. We report for completeness, in figure 4.44, curves for mean arterial pressure, total CBF, cerebral resistances and compliances at varying resistance values, obtained for scenario (4). However, the choice of averaged monitored quantities poses some problems: the duration of the respiratory cycle, in this case 4 s, is too close to the autoregulation time constant $\tau = 20$ s. When the autoregulatory mechanism is far from saturation, this causes spurious oscillations which disappear for larger values of τ (figures 4.45, 4.46). As a consequence, simulations presented in the following section, which require the presence of respiration, will be performed with instantaneous monitored quantities.

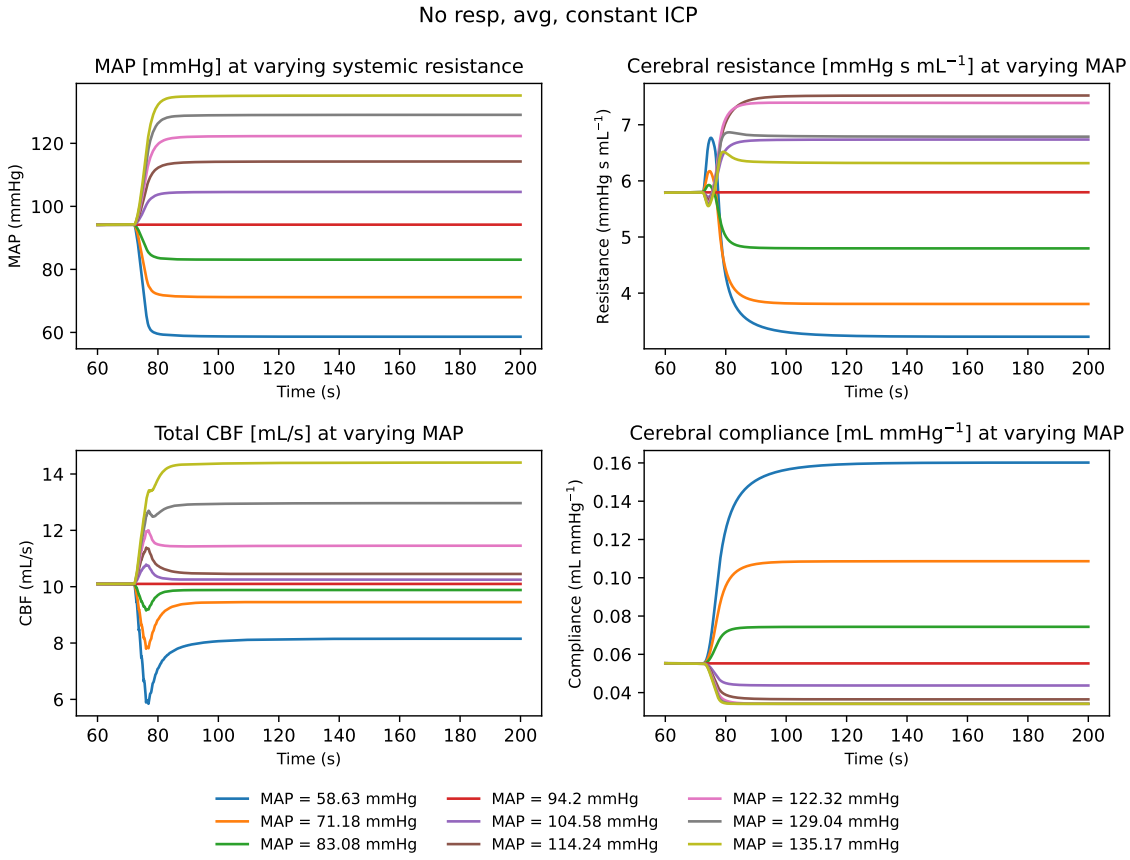

Figure 4.39: Mean arterial pressure, total cerebral blood flow and total cerebral resistances and compliances at varying resistance values, setup (1).

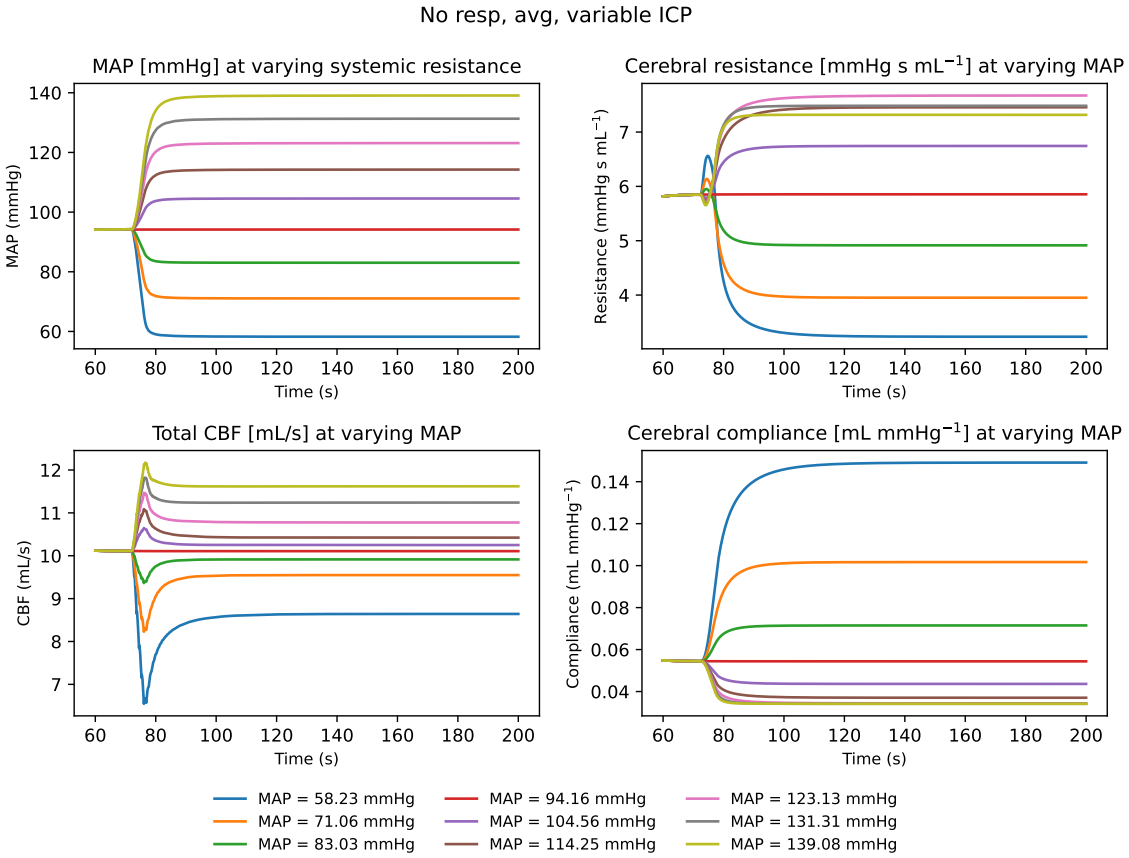

Figure 4.40: Mean arterial pressure, total cerebral blood flow and total cerebral resistances and compliances at varying resistance values, setup (2).

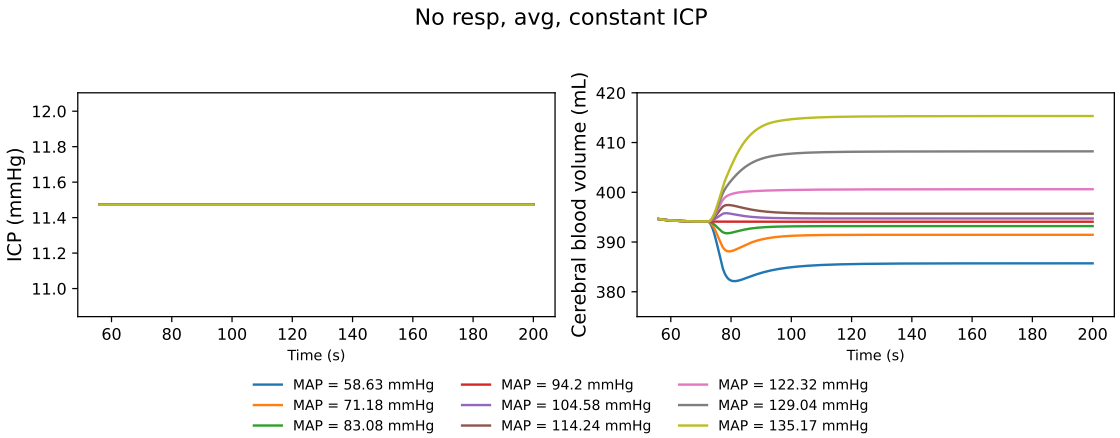

Figure 4.41: Intracranial pressure and volume at different levels of MAP, in the absence of respiration, with constant ICP.

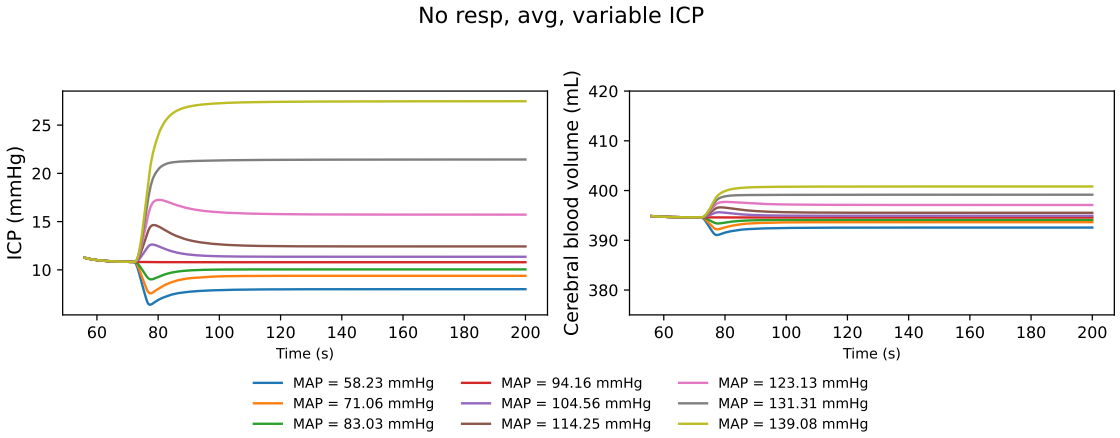

Figure 4.42: Intracranial pressure and volume at different levels of MAP, in the absence of respiration, with variable ICP (Müller et al., 2023).

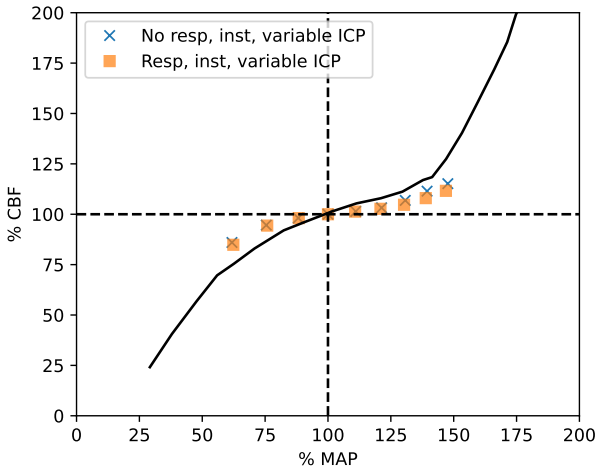

Figure 4.43: Static autoregulation curve obtained for simulation setups (2) and (4).

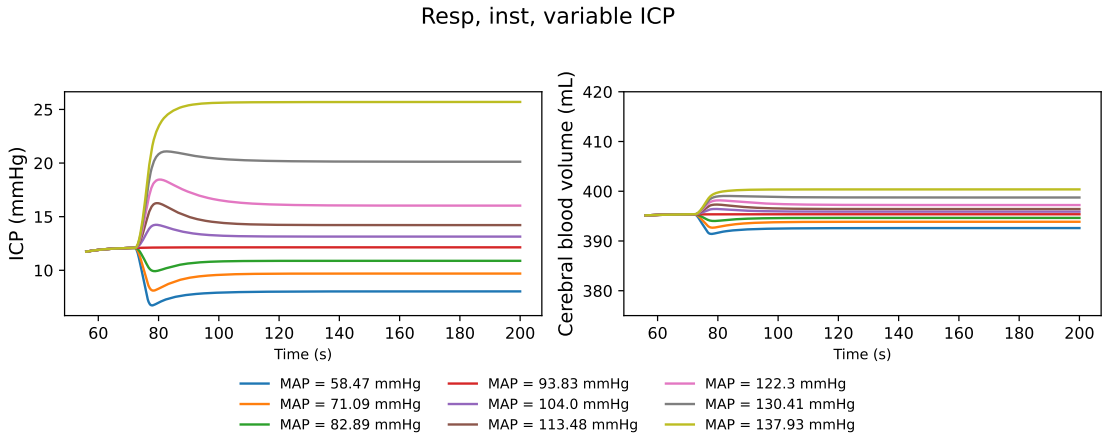

Figure 4.44: Mean arterial pressure, total cerebral blood flow and total cerebral resistances and compliances obtained for setup (4) at varying MAP levels.

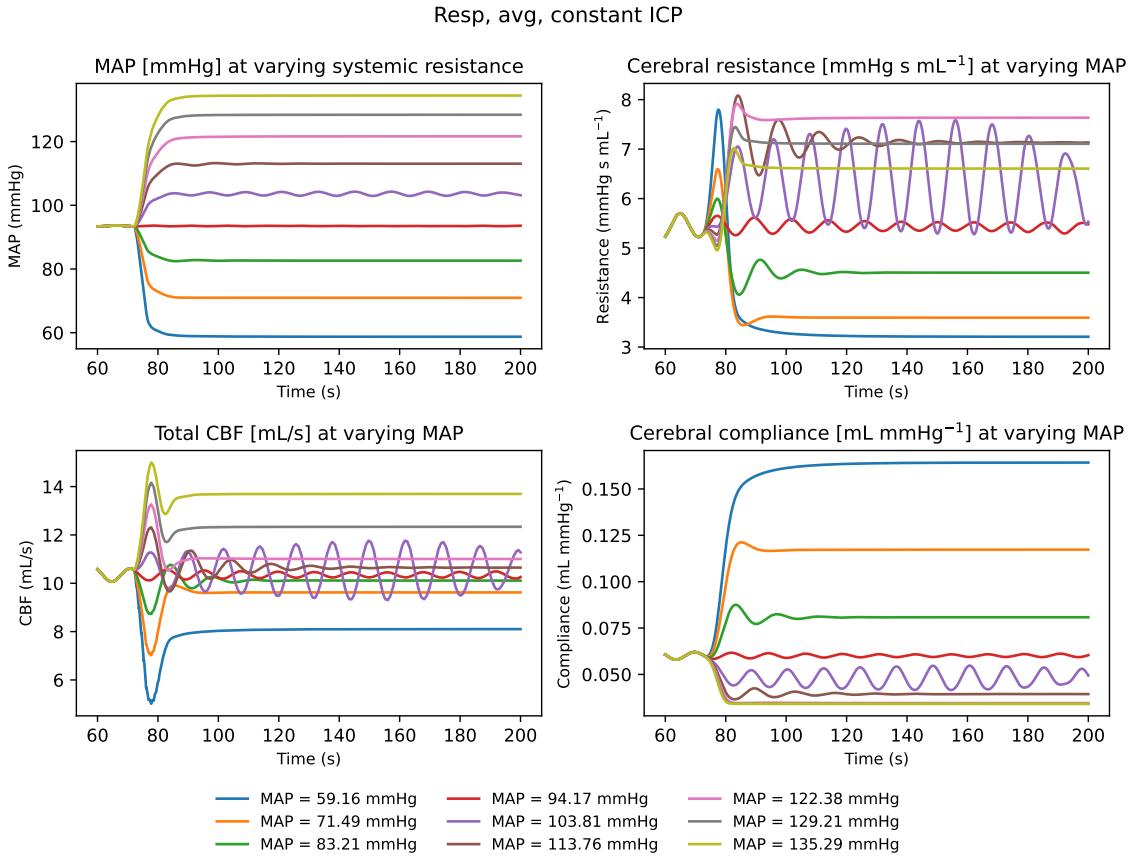

Figure 4.45: Mean arterial pressure, total cerebral blood flow and total cerebral resistances and compliances obtained for setup (3) at varying MAP levels.

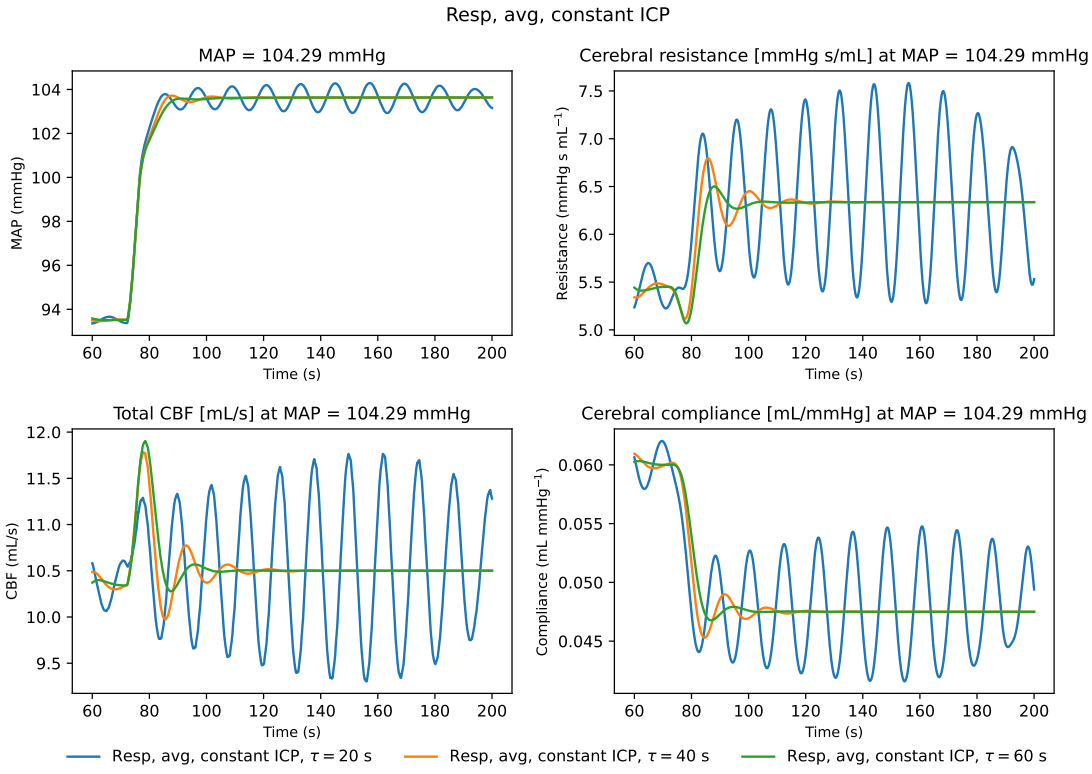

Figure 4.46: Mean arterial pressure, total cerebral blood flow and total cerebral resistances and compliances obtained for setup (3) at varying values of τ.

4.4.1.3 Main findings

We evaluated the myogenic autoregulation model by reproducing Lassen's static autoregulation curve, which relates changes in MAP to corresponding changes in CBF.

- The model successfully reproduced the autoregulation curve, both in the presence and absence of respiration, provided that instantaneous monitored blood flow was used.
- When ICP was held constant, the model reproduced the expected autoregulatory plateau until saturation occurred; beyond this point, further increases in MAP produced proportional increases in CBF and cerebral blood volume.
- When ICP was allowed to vary, it rose substantially at high MAP values, once the upper limit of autoregulation was exceeded, thus partially counteracting the MAP increase, and limiting the associated increase in CBF.

4.4.2 Metabolic autoregulation models

CBF is strongly affected by changes in arterial blood gas levels: an increase in arterial CO_2 causes vasodilation, leading to an increase in CBF, with a considerably larger sensitivity than that to changes in arterial blood pressure (Reivich, 1964). In addition, hypocapnia lowers and lengthens the myogenic autoregulation plateau, while hypercapnia moves it upwards, shortening it. As a result, hypercapnia is often used as a means of simulating an impaired autoregulation (Payne, 2016).

4.4.2.1 CO_2 reactivity model by Ursino and Giannessi (2010)

We validate in this section the CO_2 reactivity model presented in section 2.3.7.2.1, which integrates the myogenic autoregulation model validated in the previous section to account for the effect of derangements of Pa_{CO_2} from a baseline state. A decrease in flow and an increase in Pa_{CO_2} induce vasodilation, represented in the model by an increase in terminal compliance and the resulting reduction in terminal resistance. The opposite behaviour occurs in response to increased flow or reduced Pa_{CO_2}. The myogenic and metabolic regulatory mechanisms interact in a nonlinear manner. In particular, severe ischaemia drastically reduces the gain of CO_2 regulation.

We test our implementation by reproducing the CBF percent change vs Pa_{CO_2} curve reported in Ursino and Giannessi (2010). Similarly to the approach followed to validate the myogenic autoregulation model, since we are performing closed-loop simulations we cannot directly impose variations in Pa_{CO_2} to simulate hypercapnia, as this quantity depends on the inspired gas fraction, the CO_2 metabolic production rate and the ventilatory drive.

As a consequence, since both ventilation and metabolic gas production are assumed to be constant, we implement a simple feedback loop that continuously adjusts the inspired CO_2 fraction Fi_{CO_2} to keep Pa_{CO_2} around a steady target.

The controller adjusts Fi_{CO_2} to regulate Pa_{CO_2} toward a target value. At each update step, the deviation from the target is computed as

$$e(t) = Pa_{CO_2}^{\text{target}} - Pa_{CO_2}(t). \tag{4.22}$$

The desired change in Fi_{CO_2} is computed using a proportional law

$$\Delta Fi_{CO_2}^{\text{des}}(t) = K_p(t)\tilde{e}(t)\Delta t_u(t). \tag{4.23}$$

The proportional gain $K_p(t)$ increases with the magnitude of the error

$$K_p(t) = K_p^{\text{near}} + \alpha(t)(K_p^{\text{far}} - K_p^{\text{near}}), \tag{4.24}$$

where the scaling factor

$$\alpha(t) = \min\left(1, \frac{|e(t)|}{E_b}\right) \tag{4.25}$$

ensures smooth interpolation between "near-target" and "far-from-target" gains. Here E_b is the considered error band. The controller updates more frequently when the error is large and less frequently when the system is near the target:

$$\Delta t_u(t) = \Delta t_{\min} + (1 - \alpha(t))(\Delta t_{\max} - \Delta t_{\min}). \tag{4.26}$$

To avoid unnecessary oscillations, small errors are suppressed

$$\tilde{e}(t) = \begin{cases} 0, & \text{if } |e(t)| < E_{\text{small}}, \\ e(t), & \text{otherwise.} \end{cases} \tag{4.27}$$

The Fi_{CO_2} rate of change is limited at each update interval, to prevent abrupt variations, as

$$\gamma(t) = 1 + \min\left(4, \frac{|e(t)|}{E_b}\right), \tag{4.28}$$

$$\Delta Fi_{CO_2}^{\max}(t) = \gamma(t)\Delta Fi_{CO_2}^{\text{base}}, \tag{4.29}$$

$$\Delta Fi_{CO_2}(t) = \max\Big(-\Delta Fi_{CO_2}^{\max}(t),\ \min\left(\Delta Fi_{CO_2}^{\text{des}}(t),\ \Delta Fi_{CO_2}^{\max}(t)\right)\Big). \tag{4.30}$$

Finally, the inspired CO_2 fraction is updated and constrained within user-defined limits

$$Fi_{CO_2}(t^+) = \max\Big(Fi_{CO_2}^{\min},\ \min\left(Fi_{CO_2}(t) + \Delta Fi_{CO_2}(t),\ Fi_{CO_2}^{\max}\right)\Big). \tag{4.31}$$

After 200 s, following a fast increase, the resulting partial pressure stabilizes around the desired value (figure 4.47), which we consider satisfactory for this batch of tests. A direct

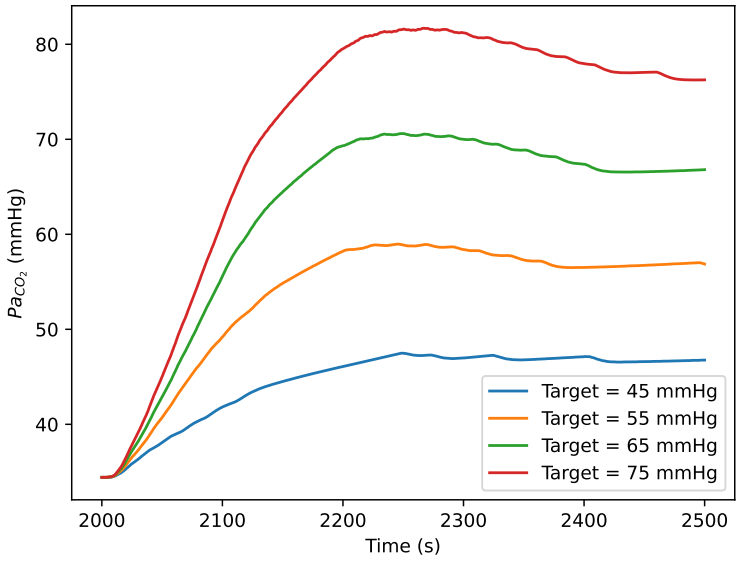

Figure 4.47: Arterial partial pressure curves generated by regulating Fi_{CO_2}.

Parameter	k_{CO_2} [-]	b_{CO_2} [-]	τ_{CO_2} [s]	G [-]	sat_2 [-]
Value	15.	0.5	40.	4.	7.

Table 4.17: Parameters employed for the validation of the CO_2 reactivity model by Ursino and Giannessi (2010).

adjustment of Fi_{CO_2} to obtain the desired Pa_{CO_2} would be possible, but would require much longer simulation times.

We perform simulations with prescribed $Pa_{CO_2} = 34.4$ (baseline value), $45, 55, 65, 75$ mmHg, turning on the autoregulation model after 200 s. We compare results obtained for the model with active respiration, gas transport and exchange, and

(1) Constant ICP, full autoregulation model,

(2) Variable ICP, full autoregulation model.

The CO_2 reactivity model is parametrised as illustrated in table 4.17. In order to improve simulation results, we chose to adopt a higher upper saturation value compared to the purely myogenic model, consistent with the one reported in Ursino and Giannessi (2010).

Figure 4.48 shows the CBF percent change vs Pa_{CO_2} curves obtained for tests (1) and (2), together with the model results reported by Ursino and Giannessi (2010).

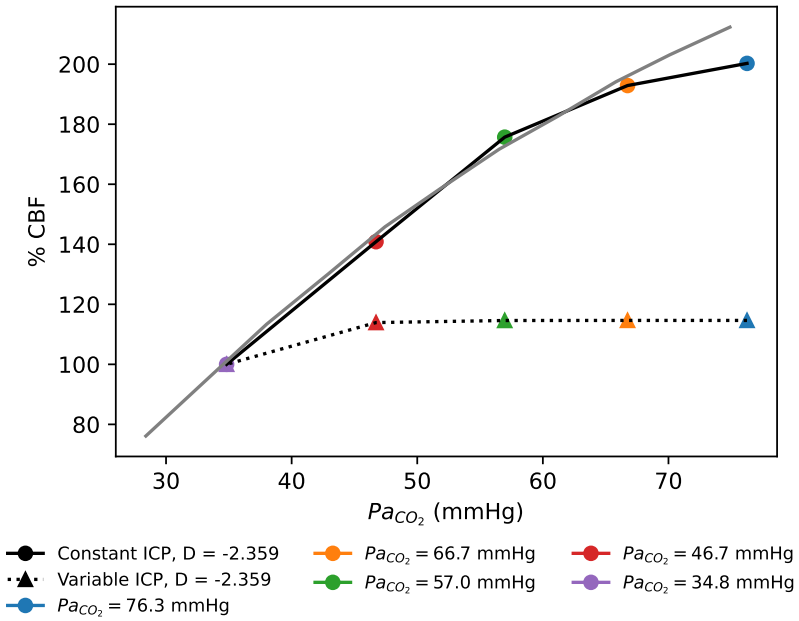

Figure 4.48: CBF percent change vs Pa_{CO_2} curves obtained for tests (1) and (2). In grey, we report results by Ursino and Giannessi (2010).

We observe a markedly different behaviour arising from the assumption of constant versus variable ICP. Imposing constant ICP yields the expected monotonic increase in CBF in response to hypercapnia, with cerebral blood volume varying between 410 and 465 mL. However, as already observed for the myogenic autoregulation model, allowing ICP to vary introduces a strong flow-limiting effect. In this case, the increase in cerebral blood volume leads to a substantial rise in ICP, which exceeds 25 mmHg at saturation. This in turn opposes the vasodilatory response elicited by elevated Pa_{CO_2} values, limiting the achievable flow increase, and producing the extremely attenuated response visible in the dotted curve in Figure 4.48.

Figure 4.49 reports the Lassen curves (% change in CBF vs change in MAP) obtained by multiplying all peripheral resistances except for cerebral ones by factors 0.4, 0.6, 0.8, 1.0, 1.2, 1.4, 1.6, 1.8, 2.0 at varying Pa_{CO2} values. Results show how hypercapnia affects myogenic autoregulation. We can observe the expected increase of CBF associated with hypercapnia, as well as the shift of the lower autoregulation limit toward higher pressure values reported by Ursino and Lodi (1998); Paulson et al. (1972); Raichle and Stone (1971). Indeed, cerebral vessels are nearly maximally dilated due to increased Pa_{CO_2}, and cannot dilate further in response to decreased MAP.

Since future simulations involving myogenic and metabolic autoregulation will be performed with variable ICP, and currently the variation in ICP seemingly dominates metabolic CBF autoregulation, in order to improve simulation results we will need to re-evaluate our parametrisation of the ICP model, currently taken from Müller et al. (2023),

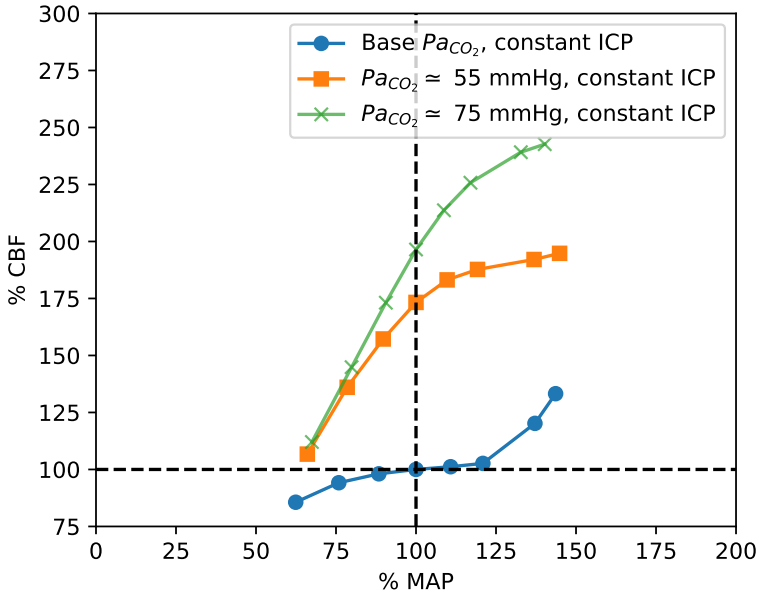

Figure 4.49: Lassen curves obtained by multiplying all peripheral resistances except for cerebral ones by factors 0.4, 0.6, 0.8, 1.0, 1.2, 1.4, 1.6, 1.8, 2.0. at varying Pa_{CO2} values.

and include CSF production and drainage, which have been proven significant for limiting ICP increases related to vasodilation (Ursino and Lodi, 1997; Giulioni and Ursino, 1996). Additionally, we plan to explore the possibility of including a nonlinear pressure-volume relationship for both arterial and venous terminal compartments, similar to the one proposed by Celant et al. (2021), in order to assess whether this assumption can improve our results for scenarios that are far from physiological states.

4.4.2.2 Metabolic autoregulation model by Magosso and Ursino (2001)

We test in this section the purely metabolic autoregulation model introduced in section 2.3.7.2.2, which is commonly used in the literature alongside other control mechanisms. To do so, we aim to replicate the CBF percent change vs Pa_{CO_2} curve reported in Ursino and Giannessi (2010) for hypercapnic stimulation, as we expect the response of both models to be comparable. This model accounts for changes in peripheral resistances caused by deviations from the baseline of both oxygen and carbon dioxide concentrations. In contrast, terminal compliances remain fixed and are not influenced by any regulatory mechanism.

Starting from the original parametrisation proposed by Magosso and Ursino (2001), reported in table 4.18, we first examine how the choice of parameters affects the strength of metabolic autoregulation. With these baseline values, the contribution of autoregulation is almost negligible. To illustrate this, recall that the strength of the CO_2-driven modulation

of cerebral autoregulation is encoded in the static nonlinear relationship

$$\Psi_{\text{brain}}(Pa_{CO_2}) = \frac{A + \frac{B}{1+C\exp(D\log(Pa_{CO_2}))}}{A + \frac{B}{1+C\exp(D\log(Pa^{ref}_{CO_2}))}} - 1. \tag{4.32}$$

Figure 4.50 shows the resulting values of $\Psi_{\text{brain}}(Pa_{CO_2})$ for a range of Pa_{CO_2} and for cartesian parameter sweeps in which A, B, C, and D are independently varied between 0.3 and 3 times their baseline values. The corresponding autoregulatory response x_{brain,CO_2} and the resulting vascular resistance R_{av} are also reported, both obtained under the assumption of constant ICP. These simulations represent the behaviour of the left middle cerebral artery under open-loop conditions, allowing us to isolate the effect of different parameter combinations on the strength of metabolic autoregulation. It is evident that the original parametrisation by Magosso and Ursino (2001) (in red), produces an almost null effect (<10%) on vascular resistances, even at extremely high values of Pa_{CO_2}, making it unsuitable for reproducing the CBF percent change vs Pa_{CO_2} curve reported in Ursino and Giannessi (2010). The black dashed line illustrates the open-loop response obtained after setting parameter D to its optimal value $D = -2.359$, i.e. the value that, when keeping the other parameters fixed, produces the strongest autoregulatory response at lower Pa_{CO_2} values.

We report in figure 4.51 cerebral blood flow variation obtained, in this case, with the full closed-loop simulation, and in figure 4.52 the corresponding $\Psi_{\text{brain}}(Pa_{CO_2}), x_{\text{brain},CO_2}$ and R_{av} values in the left middle cerebral artery, obtained under the assumption of constant ICP. As we can see, for a 50% decrease in vascular resistance, the corresponding flow rate increases only by around 30%. This discrepancy may stem from our assumption of a non-zero ICP, which differs from the model by Magosso and Ursino (2001), where ICP and Starling resistors are not included. This point will be examined further in future work.

As a consequence, in order to obtain a reasonable flow modulation, the action of autoregulation needs to be much stronger. Following our parameter sweep, we determined that stronger effects are obtained, for the optimal D value, by decreasing parameter A, and increasing B and C. We report in figure 4.53 results obtained with $D = -2.359$, $A = 3.48$, $B = 556.8$, $C = 66000$, showing that they match the expected CBF increase in response to hypercapnia better. Further work will be needed to improve the calibration, but we consider it satisfying at this stage.

Additional simulations were performed to evaluate whether the purely metabolic autoregulation model could reproduce, on its own, the characteristic autoregulatory response to changes in MAP. Because metabolic feedback depends on venous oxygen concentration, any MAP-driven change in blood flow should, in principle, modulate ϕ_{v,O_2} and thereby trigger a compensatory vascular response. However, as shown in figure 4.54, the expected static autoregulation curve does not emerge. The MAP perturbations produce only minimal changes in ϕ_{v,O_2} over the considered 400 s simulation window, and these small deviations

Parameter	A [-]	B [-]	C [-]	D [-]	g_{b,O_2} [-]	τ_{b,O_2} [s]	τ_{b,CO_2} [s]
Value	20.9	92.8	10570	-5.251	10	10	20

Table 4.18: Parametrisation by Magosso and Ursino (2001) for the autoregulation model.

are insufficient to trigger a sufficiently strong autoregulatory adjustment. These results indicate that a model combining myogenic and metabolic responses, such as the framework proposed by Ursino and Giannessi (2010), is more appropriate when the modelling objective is to reproduce responses across multiple physiological challenges. The myogenic component provides the rapid, pressure/flow-sensitive response necessary for reproducing autoregulation during hyper and hypotension, while the metabolic component governs the adjustments to changes in gas availability. These observations are consistent with the physiological assumption that myogenic and metabolic mechanisms are distinct yet interacting mechanisms that maintain adequate cerebral blood flow and oxygenation (Payne, 2016).

4.4.2.3 Main findings

In this section, we assessed the performance of two autoregulation models that account for changes in arterial and venous blood gas levels. The first model, adapted from Ursino and Giannessi (2010), combines a myogenic response to a CO_2 reactivity model, thereby allowing the characterization of responses to both hyper/hypotension and hyper/hypocapnia. The second model (Magosso and Ursino, 2001) is instead purely metabolic, and accounts for the response to changes in Pa_{CO_2} and venous oxygen concentration.

- When ICP was held constant, we were able to reproduce, with both models, the expected increase in CBF in response to hypercapnia. However, the purely metabolic autoregulation model required substantial reparametrization.
- When ICP was allowed to vary, its increase in response to vasodilation acted as a flow-limiting factor, thereby producing an extremely attenuated response. Future studies will further investigate these observed behaviours.
- Metabolic autoregulatory mechanisms alone were not able to recover the static CBF-MAP relationship, underlining the need for a combined myogenic-metabolic framework to capture the impact of both hyper/hypotension and hyper/hypocapnia.

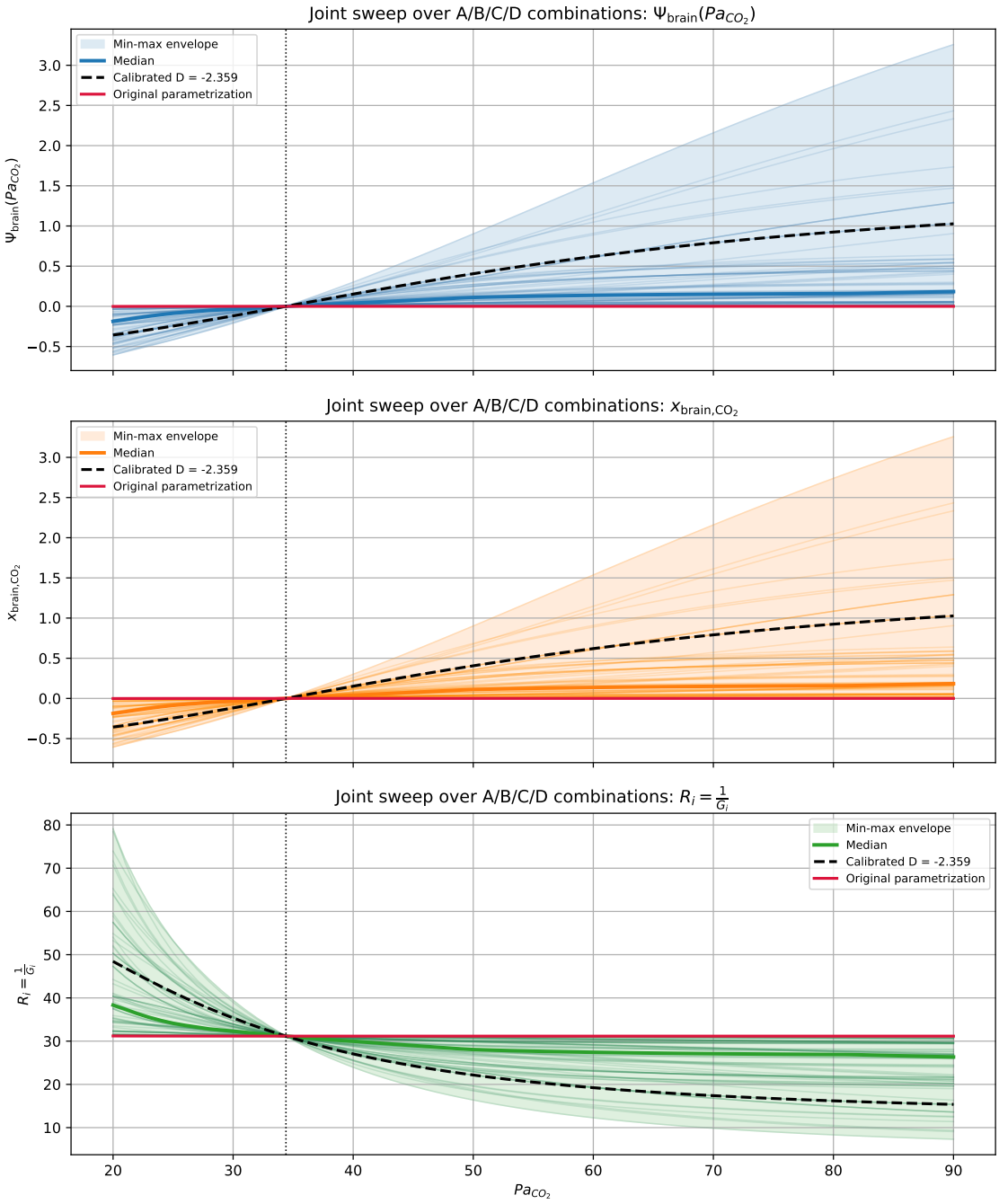

Figure 4.50: Values of $\Psi_b(Pa_{CO_2})$, x_{brain,CO_2} and R_{av} obtained for a range of Pa_{CO_2} and for parameter sweeps in which A, B, C, and D are independently varied between 0.3 and 3 times their baseline values.

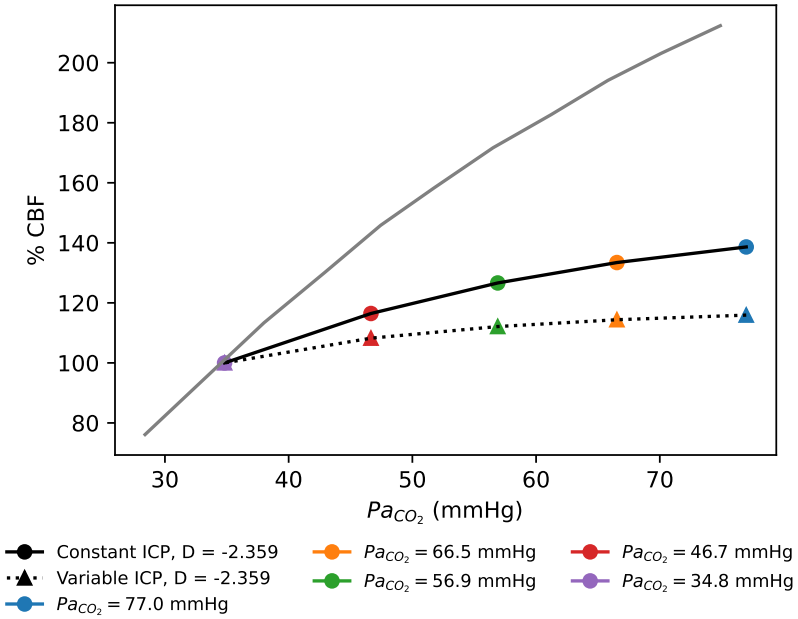

Figure 4.51: Cerebral blood flow variation obtained with the full closed-loop simulation at different Pa_{CO_2} values with $D = -2.359$. . In grey, we report results by Ursino and Giannessi (2010).

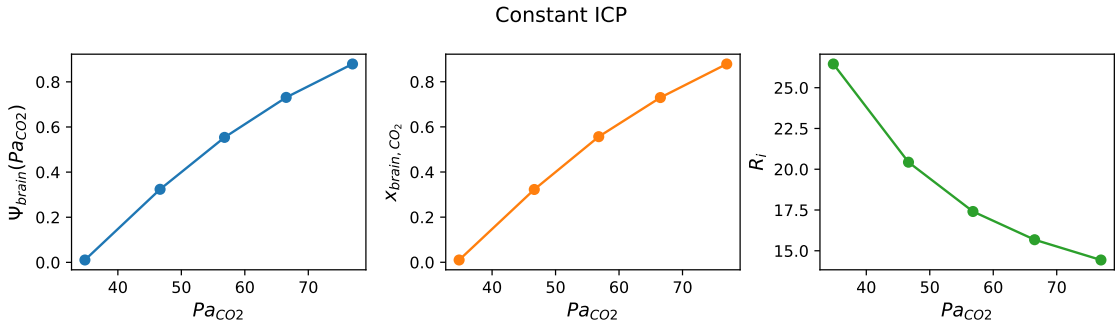

Figure 4.52: $\Psi_b(Pa_{CO_2}), x_{\text{brain},CO_2}$ and R_{av} values in the left middle cerebral artery, obtained for $D = -2.359$ under the assumption of constant ICP.

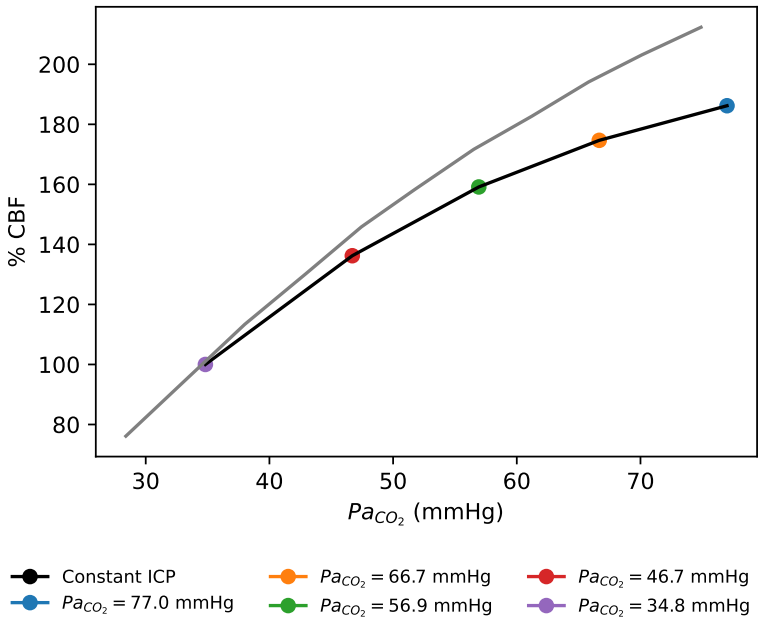

Figure 4.53: Cerebral blood flow variation obtained with the full closed-loop simulation at different Pa_{CO_2} values with $D = -2.359$, $A = 3.48$, $B = 556.8$, $C = 66000$, and constant ICP. In grey, we report results by Ursino and Giannessi (2010).

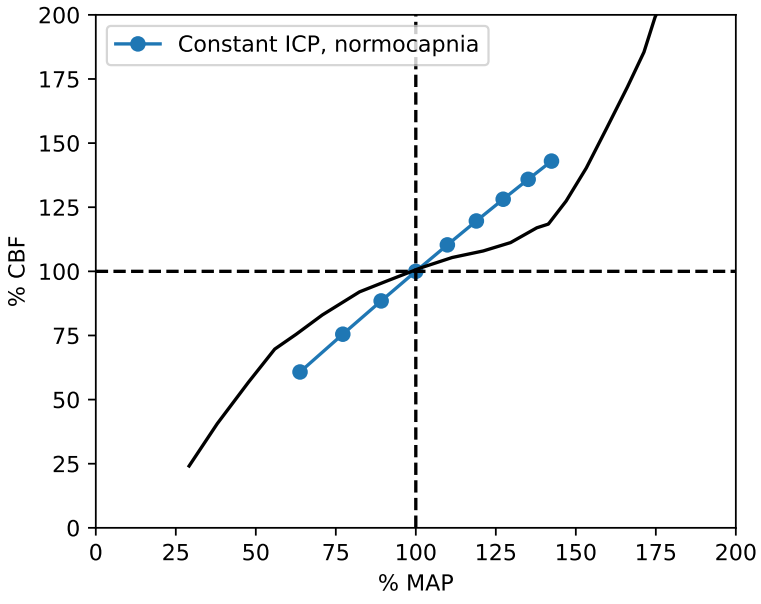

Figure 4.54: Lassen curve obtained at constant ICP by multiplying all peripheral resistances except for cerebral ones by factors 0.4, 0.6, 0.8, 1.0, 1.2, 1.4, 1.6, 1.8, 2.0, and using the fully metabolic autoregulation model by Magosso and Ursino (2001).

4.5 Modelling foot perfusion in the presence of occlusions and collateral impairment

This section is adapted from: Bisgaard, M.*, Dalmaso, C.*, Nygaard, J. V., Precht, H., Houlind, K. C., Müller, L. O., Blanco, P. J. (2026). Foot perfusion. Insights from an anatomically detailed arterial network model. Journal of Biomechanics, 113336. (*equal contributors)

More than 202 million people worldwide suffer from peripheral artery disease (PAD), making this pathology the third most common clinical manifestation of atherosclerosis after coronary artery disease and stroke (Song et al., 2019). This pathology is characterized by the narrowing and blockage of arteries supplying the lower extremities caused by the formation of atherosclerotic plaques and the presence of thrombosis and/or embolism. In addition, endothelial dysfunction may impair the ability of peripheral vessels to vasodilate in response to increased oxygen demand, which further amplifies the functional impact of this disease. PAD can be asymptomatic, or can be accompanied by symptoms such as cramping pain or discomfort in the legs during walking or exercise (Aboyans et al., 2025). For some patients with PAD, the disease manifests as critical limb-threatening ischaemia (CLTI), which is characterized by pain at rest, non-healing wounds or gangrene: their mortality risk increases (Van den Berg, 2018), and it is necessary to restore perfusion to damaged tissues to avoid amputation. To guide vascular surgeons in selecting the best treatment, patients will have an ankle-brachial index (ABI) or a toe-brachial index (TBI) measured. In addition, the leg vessels will be imaged using ultrasound, subtraction angiography, computed tomography, or magnetic resonance imaging (MRI). These examinations allow surgeons to visualize occlusions and stenoses, as well as the largest collateral vessels, thereby providing information on blood flow to the leg and foot. Based on them, the best revascularisation or conservative treatment is decided (Norgren et al., 2007).

If revascularisation is pursued, clinicians must decide between direct revascularisation of the affected angiosome (three-dimensional tissue block with one feeding artery (Taylor and Palmer, 1987)) and indirect revascularisation via the best-preserved vessel crossing the ankle. Several retrospective studies and meta-analyses have been performed to evaluate the effect of revascularisation based on the angiosome theory, mostly assessing wound healing and amputation-free survival (see Špillerová et al. (2017); Neville et al. (2009); Popitiu et al. (2024); Van den Berg (2018); Biancari and Juvonen (2014); Bosanquet et al. (2014); Sumpio et al. (2013) and references therein for details). They generally agree that the greatest value of direct angiosome-based revascularisation is in patients with lesions limited to a single angiosome, which comprises only a small part of patients (in 35% to 55% of patients wounds may involve two to three angiosomes (Alexandrescu, 2014)), and in patients with an inadequate distal distribution system (Špillerová et al., 2017; Neville et al., 2009; Palena et al., 2014). However, if a wound covers more than one angiosome,

the perfusion status in each angiosome would be relevant to guide the revascularisation procedure.

In the last few years, even though it has been possible to image the perfusion in all modalities that produce angiography (Boonen and Aerden, 2023; Caroca et al., 2021; Reekers et al., 2016; Souza et al., 2024), these measurements have not yet become a clinical standard. Several reasons are behind this: new software is required for generating and evaluating the images, staff need to be trained, and examinations can be time-consuming and painful for the patient.

As an alternative, computer simulations may provide estimates about the perfusion level in each foot angiosome based on information from angiographic images. This study aims to characterise how occlusions in the main feeding arteries impact perfusion, in order to assess the applicability of the angiosome-targeted and "best-vessel" paradigms for revascularisation under varying degrees of collateral impairment. Indeed, several works have noted that indirect revascularisation may be sufficient when collateral pathways are preserved (Venermo and Settembre, 2024; Van den Berg, 2018; Kim et al., 2021), with outcomes comparable to those of direct revascularisation.

Addressing this problem requires models endowed with a sufficiently detailed representation of the vascular topology of the leg and the foot, so that both direct and alternative feeding routes to the different angiosomes can be faithfully captured (Varela et al., 2017). In particular, in addition to the main feeding arteries, such models should include arterial-arterial connections, notably the plantar arch and the distal peroneal branches, which play a key role in redistributing flow when proximal vessels are compromised. For this reason, we chose to employ the Anatomically-Detailed Arterial Network (ADAN) model, presented in section 2.1.1, which includes 2142 vessels, comprising almost every named arterial vessel and providing a level of anatomical accuracy that is absent in other 1D vascular networks available in the literature (Avolio, 1980; Stergiopulos et al., 1992; Liang et al., 2009; Mynard and Smolich, 2015b). In particular, the topology of the vascular architecture in the lower limb is extremely realistic, with 154 vascular segments in the foot and calf. This anatomical detail provides a baseline (healthy/lesion-free) characterisation of blood flow to the different vascular territories of the foot (see figure 4.57). Moreover, we incorporate autoregulatory capacity of peripheral compliances and resistances (see section 2.3.3.1 for a description of peripheral terminals, and section 2.3.7.1 for a description of the autoregulation model), a component rarely included in large-scale arterial networks, which enables us to reproduce the transient hyperaemic response following cuff release (reactive hyperaemia) and to simulate the dynamic adjustments of peripheral resistances and compliances under reduced flow. This component is essential for assessing microvascular function, since an impaired reactive hyperaemia indicates microvascular dysfunction (Rosenberry and Nelson, 2020), and reflects the inability of the vessels to display an autoregulatory response.

To the best of our knowledge, only one previous study has pursued a related goal in

the context of diabetic foot ischaemia (Sun et al., 2025). However, the vascular model adopted there includes only the posterior tibial artery and plantar vessels, thereby focusing primarily on toe perfusion and neglecting several collateral pathways that could influence distal perfusion. Moreover, simulations performed by Sun et al. (2025) reproduce the haemodynamic waveforms in plantar vessels of an ideal diabetic patient at rest by tuning the values of inlet pressure in the posterior tibial artery and plantar arch, the brachial-ankle pulse wave velocity and blood viscosity, without modelling stenoses, occlusions, luminal narrowing, or autoregulatory responses.

Building on these considerations, we advance the state of the art in the assessment of foot perfusion by combining an extremely realistic vascular network with autoregulatory mechanisms and a systematic simulation of stenoses and occlusions in the major feeding arteries to the foot, while explicitly accounting for collateral pathways and their progressive impairment. This integrated approach enables, for the first time, an in-silico comparison of angiosome-targeted and best-vessel strategies within a realistic, whole-limb vascular architecture, thereby offering new mechanistic insights into revascularisation planning.

4.5.1 Clinical problem

Here, we outline the main features of the clinical problem, describe the expected behaviour of foot perfusion during cuff-induced ischaemia tests, and illustrate the two main theories guiding the choice of vessels that need revascularisation.

4.5.1.1 Foot angiosomes

Angiosomes can be defined as areas of tissue (skin, subcutaneous tissue, fascia, muscle and bone) supplied and drained by specific arteries and veins. According to the most common subdivision, the foot can be decomposed into 5 different angiosomes, perfused by the medial plantar artery (MPA), lateral plantar artery (LPA), dorsal pedal artery (DPA), medial calcaneal artery (MCA), and lateral calcaneal artery (LCA) (Houlind and Christensen, 2013). Furthermore, the first toe is supplied by DPA, MPA, and LPA. In figure 4.55 these angiosomes are depicted, respectively, in light blue, orange, red, yellow and blue. The presence of a well-developed collateral network in the foot provides alternative perfusion/drainage routes, allowing angiosomes to receive blood from neighbouring regions in the case of obstructive disease.

4.5.1.2 revascularisation guidelines and clinical practice

In the case of CLTI patients, perfusion can be restored to damaged tissues via revascularisation. Two main theories have emerged regarding which vessels should be treated in order to

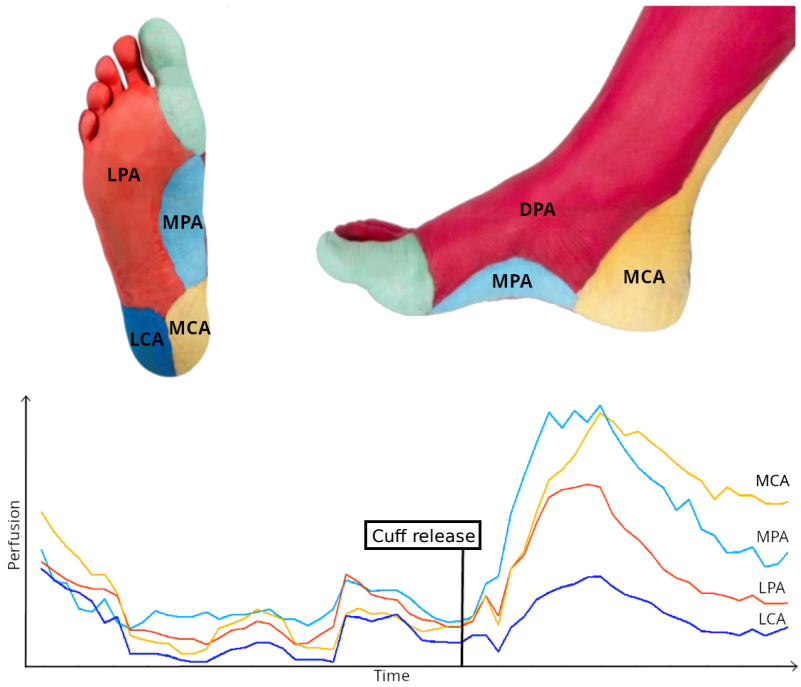

Figure 4.55: Foot angiosomes and example of perfusion curves obtained using a Flow-sensitive Alternating Inversion Recovery (FAIR) sequence. Light blue: angiosome perfused by the MPA; orange: angiosome perfused by the LPA; red: angiosome perfused by the DPA; yellow: angiosome perfused by the MCA; blue: angiosome perfused by the LCA. Adapted from (Houlind and Christensen, 2013).

provide the best outcome. Some clinicians claim that perfusion to the ischemic angiosome should be obtained by direct revascularisation of the relevant feeding artery (Houlind and Christensen, 2013). An alternative view claims that one should aim for revascularisation of the best preserved vessel that crosses the ankle, regardless of whether or not this vessel provides direct flow to the relevant angiosome (Norgren et al., 2007). The main objective of this section of the thesis is, consequently, to explore the validity and applicability of these two theories in a controlled, physiologically realistic setting.

4.5.1.3 Perfusion in a cuff-induced ischaemia test

In recent years, various imaging modalities have demonstrated potential for assessing perfusion or oxygenation in the feet. These modalities include positron emission tomography–computed tomography (PET-CT) (Christensen et al., 2024; Burchert et al., 1997), digital subtraction angiography (Reekers et al., 2016), computed tomography (Boonen et al., 2023), ultrasound (Sommerset et al., 2019; Souza et al., 2024), near-infrared spectroscopy (Meertens et al., 2021), indocyanine green fluorescence imaging (Fang et al., 2022; Tange et al., 2023, 2024), thermal imaging (Gatt et al., 2018; Petrova et al., 2018), and MRI (Caroca et al., 2021). However, to the best of our knowledge, none of these techniques have been implemented in routine clinical practice. A promising method for measuring foot perfusion is arterial spin labeling (ASL), measured with MRI. This technique enables quantitative perfusion measurements without the use of gadolinium-based contrast agents (Leithner et al., 2008). Since the ASL signal is proportional to perfusion, which is low at rest in the foot, this approach requires a cuff-induced ischaemia test, to increase perfusion for a short time period (Lopez et al., 2015). In particular, ASL allows the generation of perfusion curves, as illustrated in figure 4.55, depicting baseline perfusion levels and time to peak (TTP), defined as the interval between cuff release and the attainment of maximum perfusion.

4.5.2 Simulations setup

Simulations were performed to reproduce a cuff-induced ischaemia test, in both a baseline lesion-free scenario, and in multiple pathological cases, defined by occlusions placed in different foot arteries. Pathological cases were constructed to evaluate the validity of the angiosome theory and the best-vessel theory in a fully controlled, physiologically realistic setting. Indeed, the substantial heterogeneity of patients affected by CLTI, arising from diverse risk factors, comorbidities and highly variable collateral networks (including the presence of choke vessels, arterial-arterial connections such as the plantar arch, and the effect that occlusive disease has on collateral capacity), makes it challenging to clearly demonstrate the superiority of one revascularisation strategy over the other, and has been evidenced as a limitation in most analyses available in the literature (Popitiu et al., 2024;

Van den Berg, 2018; Palena et al., 2014).

4.5.2.1 Cuff protocol

We model the pressure cuff as a two-vessel junction where energy is not conserved. In particular, setting vessel 1 as the vessel sharing its outlet with the junction, we enforce that

$$P_1 + \frac{\rho}{2}\left(\frac{Q_1}{A_1}\right)^2 = P_2 + \frac{\rho}{2}\left(\frac{Q_2}{A_2}\right)^2 + R_{\text{cuff}}Q_2, \tag{4.33}$$

Here, R_{cuff} changes depending on the state of the cuff: it is null while the cuff is deactivated, maximal while the cuff is activated, and varies according to an exponential profile during cuff activation and deactivation

$$R_{\text{cuff}} = R_{max}\frac{R_{\text{coeff}}^{\frac{t-t_{\text{act,ini}}}{t_{\text{act,dur}}}} - 1}{R_{\text{coeff}} - 1}, \qquad t \in [t_{\text{act,ini}}, t_{\text{act,ini}} + t_{\text{act,dur}}], \tag{4.34}$$

$$R_{\text{cuff}} = R_{max}\frac{R_{\text{coeff}}^{1+\frac{t_{\text{deact,ini}}-t}{t_{\text{deact,dur}}}} - 1}{R_{\text{coeff}} - 1}, \qquad t \in [t_{\text{deact,ini}}, t_{\text{deact,ini}} + t_{\text{deact,dur}}]. \tag{4.35}$$

Here, $t_{act,ini}$ and $t_{\text{deact,ini}}$ are the times at which cuff activation and deactivation begin, and $t_{\text{act,dur}}$ and $t_{\text{deact,dur}}$ are the durations of the activation and deactivation phases. R_{coeff} is a coefficient that determines the speed of activation/deactivation, and R_{max} is the maximum resistance reached when the cuff is fully activated.

The cuff was applied in all cases to the medial portions of the anterior tibial, posterior tibial, and fibular arteries (see figure 4.57, panel (B)). We assume that R_{max} in equations (4.34) and (4.35) is equal to $1e^7[dyn \cdot s/cm^5]$, so that flow to the angiosomes of the foot during cuff activation is nearly zero. Moreover, we set R_{coeff} to $1e^4$ and $t_{\text{act,dur}} = t_{\text{deact,dur}}$ to $50s$ to obtain reasonably slow cuff activation/deactivation phases. Since after $150s$ all baseline simulations reach a steady-state condition, meaning a periodic regime in which haemodynamic variables such as pressure and flow rate remain unchanged from one heartbeat to the next, we assume that cuff inflation starts at $t = 175s$. The cuff remains fully closed for $275s$, and, after that, cuff deactivation begins at $t = 500s$. An illustration can be found in figure 4.56.

4.5.2.2 Occlusions and collateral impairment

Simulations were designed to assess the extent to which the best vessel and angiosome theories are valid at different degrees of collateral impairment, when lesions are present in

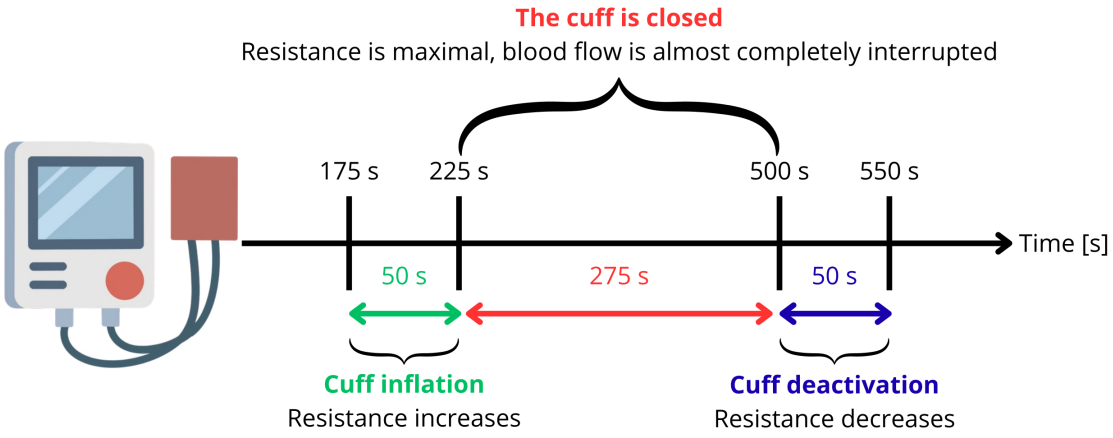

Figure 4.56: Cuff protocol. Cuff inflation and deactivation phases are highlighted also in figure 4.58, top left panel.

the main foot arteries. As a consequence, we considered six different lesion configurations, characterised by the presence of at most two occlusions at the level of DPA, MPA and LPA. We chose to place lesions in the proximal segment of each vessel, in order to obtain the maximum perfusion impairment, enforcing no-flow conditions across them.

We performed simulations assuming that foot collaterals are fully patent (scenarios $1a$ - $6a$) and compared them with simulations with reduced collateral diameters. We distinguished two different collateral configurations, one in which the plantar arch is treated as a collateral vessel (see figure 4.57, panel (D)), and one in which it is assumed to be fully patent (see figure 4.57, panel (C)). Indeed, the plantar arch connects the two circulatory pathways that, arising from the anterior and posterior tibial arteries, supply the dorsum of the foot (via the medial tarsal arteries and several perforating branches) and the posterior and plantar areas, respectively. In particular, cases $1b_1 - 6b_1$, $1c_1 - 6c_1$, $1d_1 - 6d_1$ denote scenarios where the plantar arch is assumed to be fully patent, while other collaterals have a diameter that is, respectively, 60%, 30%, and 5% of the original diameter. Cases $1b_2 - 6b_2$, $1c_2 - 6c_2$, $1d_2 - 6d_2$ denote scenarios where all collaterals (including the plantar arch) have a diameter that is, respectively, 60%, 30%, and 5% of the original diameter. The resulting simulation scenarios are summarized in table 4.19.

4.5.2.3 Perfusion estimation

The proposed model allows us to compute the time evolution of flow rates at the level of different foot angiosomes. We can derive reasonable perfusion values in each angiosome from model-generated flow rates by multiplying the flow rate by angiosome weight, which

Lesion configurations

Case	DPA	MPA	LPA	Case	DPA	MPA	LPA
0	Lesion-free baseline scenario						
	One lesion			Multiple lesions			
1	Occl.	-	-	4	Occl.	Occl.	-
2	-	Occl.	-	5	-	Occl.	Occl.
3	-	-	Occl.	6	Occl.	-	Occl.

Collateral configurations and impairment

$1-6a$	Patent collaterals		
	Collateral diameters	$1-6b_1, c_1, d_1$	$1-6b_2, c_2, d_2$
$1-6b$	$D_b = 0.6D_0$	Patent pl. arch	Obstr. pl. arch
$1-6c$	$D_c = 0.3D_0$	Patent pl. arch	Obstr. pl. arch
$1-6d$	$D_d = 0.05D_0$	Patent pl. arch	Obstr. pl. arch

Table 4.19: Location of lesions in the dorsalis pedis (DPA), medial plantar (MPA) and lateral plantar (LPA) arteries and collateral configurations (see figure 4.57). The 42 pathological scenarios are determined by the combination of 6 types of occlusions (Lesion configurations, 1-6) and 7 types of collateral impairment (Collateral configurations and impairment $a, b_1, c_1, d_1, b_2, c_2, d_2$). D_0 is vessel diameter in the baseline lesion-free configuration.

Angiosome	Area [cm^2]	TAF (%)	VF (%)	Volume [cm^3]	Weight [g]
MPA	12.3	0.075	0.0474	24.59	24.59
1 toe region	20.0	0.122	0.0773	40.10	40.10
LPA	80.7	0.490	0.3111	161.47	161.47
DPA	160.7	0.976	0.6197	321.63	321.63
MCA	48.1	0.292	0.1855	96.27	96.27
LCA	38.4	0.233	0.1481	76.85	76.85
LM	24.4	0.148	0.0941	48.85	48.85
Total	384.6	2.337	1.4831	769.77	769.77

Table 4.20: Area, volume and weight of foot angiosomes. TAF: total area fraction, computed as the ratio between angiosome area and total body surface area ($16460cm^2$ for the ADAN model); VF: volume fraction, computed as the product between TAF and a scaling factor equal to 0.6347 (Blanco et al., 2014); MPA: medial plantar artery; LPA: lateral plantar artery; DPA: dorsalis pedis artery; MCA: medial calcaneal artery; LCA: lateral calcaneal artery; LM: lateral malleolar artery.

is computed from angiosome volume under the assumption of a constant tissue density of $1g/cm^3$. We report in table 4.20 the volumes and weights of foot territories in the ADAN model (Blanco et al., 2015, 2014).

4.5.2.4 Autoregulation model

We employ the myogenic autoregulation model described in section 2.3.7.1, based on Ursino and Lodi (1997), which provides feedback when the flow rate departs from a homeostatic state, defined here by the baseline model state. This control model acts upon peripheral resistances and compliances whenever the flow through the corresponding peripheral Windkessel models is affected as a consequence of modifications in the vascular network (see section 2.3.3.1 for a description of peripheral terminals for the ADAN vascular network). This allows us to reproduce the hyperaemic response after cuff opening, caused by vasodilation, as well as the ability of the vessels to preserve an adequate flow rate if their calibre is reduced due to pathological conditions. Indeed, equations (2.155) and (2.156) imply that a decrease in blood flow below its baseline value $\bar{Q}_o^B$, such as the one observed during cuff activation, causes vasodilation, which is modelled through an increase in terminal compliance. While the cuff is active, terminal resistances temporarily increase due to a decreased blood volume. Right after cuff deactivation, instead, the increase in arteriolar blood volume caused by increased compliances results in a reduction of resistances below their baseline value.

Parameter	Regions			
	1: pink	2: yellow	3: green	4: blue
τ	$40s$	$40s$	$40s$	$40s$
sat_1	0.4	0.4	0.4	0.4
sat_2	4.5	4.5	4.5	4.5
k_{mult}	8.	8.	8.	8.
$G_{\mathcal{R}}$	0.102	0.017	0.014	0.009

Table 4.21: Parameters employed for the autoregulation model. See color-coded regions in figure 4.57.

Parameter values were determined empirically to reproduce the magnitude and time scales of hypereaemic responses observed in the clinical practice, and are available in table 4.21. The choice of a $k_{mult} = 8$ results in a central gain $\mathcal{G}_{\mathcal{R}} = -G_{\mathcal{R}}/16$.

4.5.2.5 Numerical methods

We briefly summarize the numerical methods employed to discretize the 1D blood flow equations and to couple them to 0D lumped parameter models. We refer to relevant references for further details. The blood flow equations (2.2), with tube law (2.3), (2.4) form an advection–diffusion–reaction system of PDEs. Under suitable assumptions on parameters and state variables, this system can be recast as a first-order hyperbolic system with stiff source terms (Montecinos et al., 2014; Müller et al., 2016a,b). Each 1D vessel segment was discretised using the second-order, finite-volume, path-conservative scheme described in Müller et al. (2016a). Time stepping followed the local time-step strategy of Müller et al. (2016a), with a maximum allowable local step of $\Delta t_{\max} = 1$ ms and a Courant–Friedrichs–Lewy number of 0.9. Spatial discretisation used a characteristic mesh size of 1 cm; vessels shorter than this threshold were represented by a single computational cell. Ordinary differential equations associated with lumped parameter components were solved using either the explicit Euler method.

4.5.3 Results

We report in table 4.22 the baseline perfusion values in each foot angiosome for the lesion-free scenario (Case 0) and their percent variations computed for all considered pathological scenarios (Cases 1-6) with respect to Case 0. table 4.23 reports the time to peak (TTP) after cuff release in each foot angiosome for Case 0, and its percent variations computed

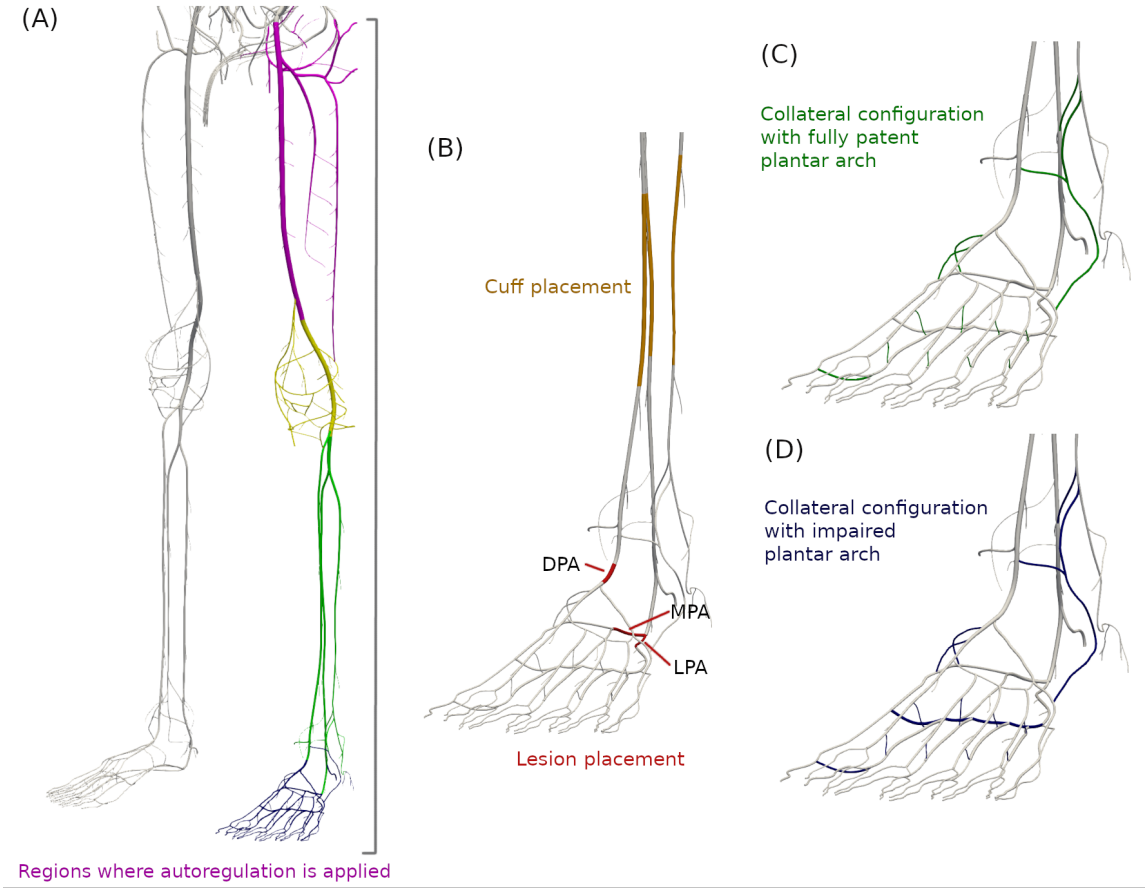

Figure 4.57: Arterial vasculature in the leg. Panel (A): regions where the autoregulation model is applied (each color corresponds to a different parametrisation, see table 4.20); Panel (B): cuff and lesion placement (DPA, MPA, LPA stand, respectively, for dorsalis pedis, medial plantar, lateral plantar artery); Panels (C) and (D): foot collaterals.

for all considered pathological scenarios compared to Case 0, since longer TTPs can be associated with CLTI. Percent variations are computed as

$$\Delta = \frac{\mathcal{I} - \mathcal{I}_{\text{ref}}}{\mathcal{I}_{\text{ref}}} \cdot 100, \tag{4.36}$$

where $\mathcal{I}$ is the considered quantity, and $\mathcal{I}_{\text{ref}}$ is the corresponding reference value obtained for Case 0. Figures 4.58 and 4.59 show how cardiac-cycle averaged perfusion values vary in time in the DPA, LPA and MPA angiosomes for all considered scenarios.

4.5.4 Discussion

We discuss here the computational results presented in section 4.5.3, highlighting their clinical implications to explore the capability of our model to characterise both the angiosome and "best-vessel" theories for revascularisation.

4.5.4.1 Model verification

The haemodynamic model in baseline conditions (without cuff, stenoses, or occlusions) was parametrised according to established vascular territories to ensure, among other features, a lower-limb blood-flow fraction of 8.5% of the cardiac output. Validation against clinical data is reported in Blanco et al. (2014). Moreover, the perfusion fractions predicted by our model for the foot angiosomes show very good agreement with those obtained by Bisgaard et al. (2024) using ASL-MRI sequences, with differences of 3% in the DPA, 2% in the MPA, 0% in the LPA, and 1% in the calcaneal region. The myogenic autoregulation model adopted here has been previously validated against clinical data for the cerebral circulation (Toro et al., 2022), demonstrating its ability to reproduce the characteristic sigmoidal cerebral blood flow-mean arterial pressure (CBF-MAP) relationship. Our parametrisation was further designed to capture the qualitative features of the hyperaemic response, including the peak occurring approximately 30–60 s after cuff deflation (Arvidsson et al., 2023; Wu et al., 2009). In addition, the model reproduces the expected increase in TTP with progressively more severe pathological conditions (Arvidsson et al., 2023; Bajwa et al., 2014). In particular, compared to the original formulation reported by Toro et al. (2022), we increased the time constant τ from 20 to 40 s, the upper saturation value sat_2 from 1.5 to 4.5, and increased the parameter k_{mult}, which regulates the steepness of the sigmoid function, from 0.5 to 8 (see equations (2.156), (2.165), (2.166)). These parameters are region-independent. Validation against absolute perfusion values derived from ASL-MRI sequences is inherently challenging. The MRI-based perfusion estimates come from a single slice of the foot and are postprocessed under the assumption that the perfusion per 100 g is uniform throughout the entire foot, an assumption that does not hold. This leads to a scale mismatch between model predictions and MRI-derived measurements, one that cannot be

	LCA	**MCA**	**DPA**	**LPA**	**MPA**		**LCA**	**MCA**	**DPA**	**LPA**	**MPA**
Case 0: lesion-free baseline perfusion											
	3.65	4.06	3.76	3.01	2.52						
Case 1: % variations with respect to Case 0											
a	-0.29	-1.68	-6.96	-4.53	-3.78						
b_1	-0.01	-1.98	-25.72	-5.03	-4.18	b_2	0.89	-0.98	-28.59	-3.32	-3.22
c_1	1.28	0.44	-86.78	1.63	-0.13	c_2	1.3	0.52	-88.65	-10.25	-0.19
d_1	1.34	0.78	-	2.48	0.53	d_2	1.46	1.84	-	-77.01	2.59
Case 2: % variations with respect to Case 0											
a	-0.02	0.22	-0.41	-0.57	-1.3						
b_1	1.06	0.75	1.39	0.39	-2.85	b_2	1.07	0.99	0.93	-1.84	-7.8
c_1	1.1	0.52	1.65	-0.68	-4.24	c_2	1.2	1.46	1.37	-34.41	-70.14
d_1	1.1	0.49	1.69	-0.8	-4.4	d_2	1.26	1.95	1.83	-77.24	-
Case 3: % variations with respect to Case 0											
a	-0.02	0.18	-0.57	-1.41	-0.26						
b_1	1.06	0.7	1.48	0.21	-0.19	b_2	1.07	0.77	1.19	-2.5	0.04
c_1	1.1	0.54	1.66	-0.32	-0.58	c_2	1.14	0.91	1.46	-36.15	0.43
d_1	1.1	0.52	1.68	-0.37	-0.62	d_2	1.24	1.8	1.8	-	2.61
Case 4: % variations with respect to Case 0											
a	-0.45	-1.4	-12.26	-9.12	-11.26						
b_1	0.89	-0.78	-34.28	-7.57	-12.06	b_2	0.91	-0.29	-44.7	-15.61	-29.65
c_1	1.29	0.42	-87.71	-1.88	-5.65	c_2	1.42	1.59	-95.04	-43.8	-85.82
d_1	1.35	0.72	-	-0.52	-4.14	d_2	1.51	2.17	-	-77.29	-
Case 5: % variations with respect to Case 0											
a	-0.08	0.95	-2.4	-4.75	-4.04						
b_1	1.11	1.98	-1.09	-19.86	-20.46	b_2	1.11	1.98	-1.1	-20.23	-20.14
c_1	1.26	2.08	1.18	-83.13	-83.36	c_2	1.26	2.08	1.19	-83.06	-83.14
d_1	1.29	2.11	1.86	-	-	d_2	1.29	2.11	1.86	-	-
Case 6: % variations with respect to Case 0											
a	-0.36	-1.54	-9.48	-8.36	-5.0						
b_1	0.89	-0.9	-30.53	-6.57	-4.49	b_2	0.89	-0.78	-33.41	-12.75	-4.14
c_1	1.28	0.43	-87.24	-1.34	-1.16	c_2	1.34	0.89	-90.6	-44.54	0.09
d_1	1.35	0.75	-	-0.1	-0.38	d_2	1.49	2.02	-	-	2.84

Table 4.22: Baseline perfusion values in the foot angiosomes for a lesion-free baseline scenario (Case 0) and percent changes in baseline perfusion values compared to a model with no occlusion or stenosis (Cases 1-6). Cases $1a-6a$ denote scenarios where all collaterals are assumed to be patent. Cases $1b_1-6b_1$, $1c_1-6c_1$, $1d_1-6d_1$ denote cases where the plantar arch is assumed to be fully patent, while other collaterals have a diameter that is, respectively, 60%, 30%, and 5% of the original diameter. Cases $1b_2-6b_2$, $1c_2-6c_2$, $1d_2-6d_2$ denote cases where all collaterals (including the plantar arch) have a diameter that is, respectively, 60%, 30%, and 5% of the original diameter.

	LCA	**MCA**	**DPA**	**LPA**	**MPA**		**LCA**	**MCA**	**DPA**	**LPA**	**MPA**
Case 0: lesion-free TTP											
	38.59	37.53	40.57	40.59	38.55						
Case 1: % variations with respect to Case 0											
a	-0.12	2.66	7.52	4.96	5.21						
b_1	-5.4	5.33	24.88	4.96	5.25	b_2	-7.89	5.34	26.5	4.94	5.21
c_1	-10.6	2.73	-	0.06	2.67	c_2	-10.57	2.68	-	7.38	0.04
d_1	-10.63	2.72	-	0.05	2.66	d_2	-10.6	0.01	-	-7.42	-2.58
Case 2: % variations with respect to Case 0											
a	-0.03	-0.07	0.02	0.0	0.13						
b_1	-7.88	0.01	0.0	0.02	5.25	b_2	-7.88	-0.03	0.01	2.4	8.03
c_1	-10.63	2.64	-2.43	2.46	7.83	c_2	-10.61	-2.68	0.0	2.37	-
d_1	-10.65	2.64	-2.44	2.48	7.85	d_2	-10.63	-2.69	-2.43	-7.5	-
Case 3: % variations with respect to Case 0											
a	-0.03	-0.04	0.01	0.06	-0.01						
b_1	-7.88	0.04	0.0	2.49	0.06	b_2	-7.88	0.01	0.0	4.96	0.01
c_1	-10.64	2.66	-2.44	2.53	2.61	c_2	-10.63	0.0	-2.43	19.71	-0.04
d_1	-10.65	2.66	-2.44	2.53	2.61	d_2	-10.64	-2.65	-2.43	-	-5.17
Case 4: % variations with respect to Case 0											
a	-0.14	2.6	9.98	7.38	10.53						
b_1	-7.89	2.68	41.56	4.95	10.53	b_2	-7.89	0.01	-	4.89	23.51
c_1	-10.57	2.66	-	2.5	7.91	c_2	-10.54	-2.65	-	2.37	-
d_1	-10.6	2.66	-	2.49	7.88	d_2	-10.56	-2.66	-	-7.49	-
Case 5: % variations with respect to Case 0											
a	-0.1	-2.76	2.51	5.09	5.36						
b_1	-7.89	-5.34	2.46	22.37	21.03	b_2	-7.89	-5.34	2.46	22.43	20.92
c_1	-10.6	-5.34	0.0	-	-	c_2	-10.6	-5.34	0.0	-	-
d_1	-10.63	-5.34	-2.43	-	-	d_2	-10.63	-5.34	-2.43	-	-
Case 6: % variations with respect to Case 0											
a	-0.13	2.62	9.93	7.49	5.17						
b_1	-7.89	2.7	26.72	7.43	5.2	b_2	-7.89	2.69	29.13	9.94	5.15
c_1	-10.59	2.69	-	2.56	2.65	c_2	-10.56	0.03	-	19.71	-0.01
d_1	-10.61	2.69	-	2.55	2.63	d_2	-10.59	-2.64	-	-	-5.16

Table 4.23: Time to peak after cuff release in the foot angiosomes for a lesion-free baseline scenario (Case 0) and percent changes in time to peak compared to a model with no occlusion or stenosis (Cases 1-6). If the peak did not occur within the first $75s$ after cuff opening, we assume that no peak occurs. Cases $1a-6a$ denote scenarios where all collaterals are assumed to be patent. Cases $1b_1-6b_1$, $1c_1-6c_1$, $1d_1-6d_1$ denote cases where the plantar arch is assumed to be fully patent, while other collaterals have a diameter that is, respectively, 60%, 30%, and 5% of the original diameter. Cases $1b_2-6b_2$, $1c_2-6c_2$, $1d_2-6d_2$ denote cases where all collaterals (including the plantar arch) have a diameter that is, respectively, 60%, 30%, and 5% of the original diameter.

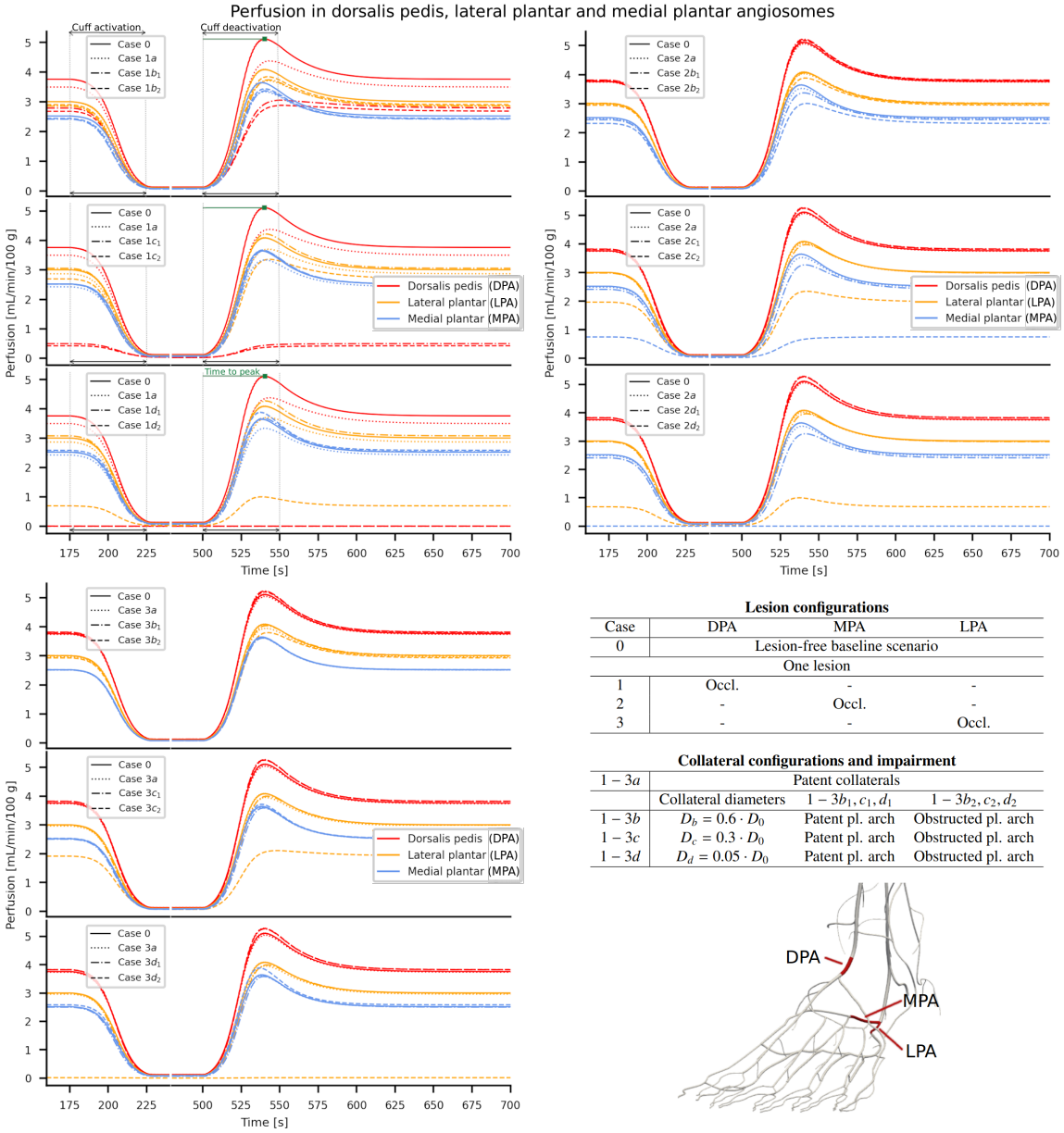

Lesion configurations

Case	DPA	MPA	LPA
0	Lesion-free baseline scenario		
	One lesion		
1	Occl.	-	-
2	-	Occl.	-
3	-	-	Occl.

Collateral configurations and impairment

$1-3a$	Patent collaterals		
	Collateral diameters	$1-3b_1, c_1, d_1$	$1-3b_2, c_2, d_2$
$1-3b$	$D_b = 0.6 \cdot D_0$	Patent pl. arch	Obstructed pl. arch
$1-3c$	$D_c = 0.3 \cdot D_0$	Patent pl. arch	Obstructed pl. arch
$1-3d$	$D_d = 0.05 \cdot D_0$	Patent pl. arch	Obstructed pl. arch

Figure 4.58: Time variation of cardiac-cycle averaged perfusion values in the DPA, LPA and MPA angiosomes for cases 1-3. Cases $1a - 3a$ denote scenarios where all collaterals are assumed to be patent. Cases $1b_1 - 3b_1$, $1c_1 - 3c_1$, $1d_1 - 3d_1$ denote cases where the plantar arch is assumed to be fully patent, while other collaterals have a diameter that is, respectively, 60%, 30%, and 5% of the original diameter. Cases $1b_2 - 3b_2$, $1c_2 - 3c_2$, $1d_2 - 3d_2$ denote cases where all collaterals (including the plantar arch) have a diameter that is, respectively, 60%, 30%, and 5% of the original diameter. In the top left panel, we highlight cuff activation, deactivation and the time to peak.

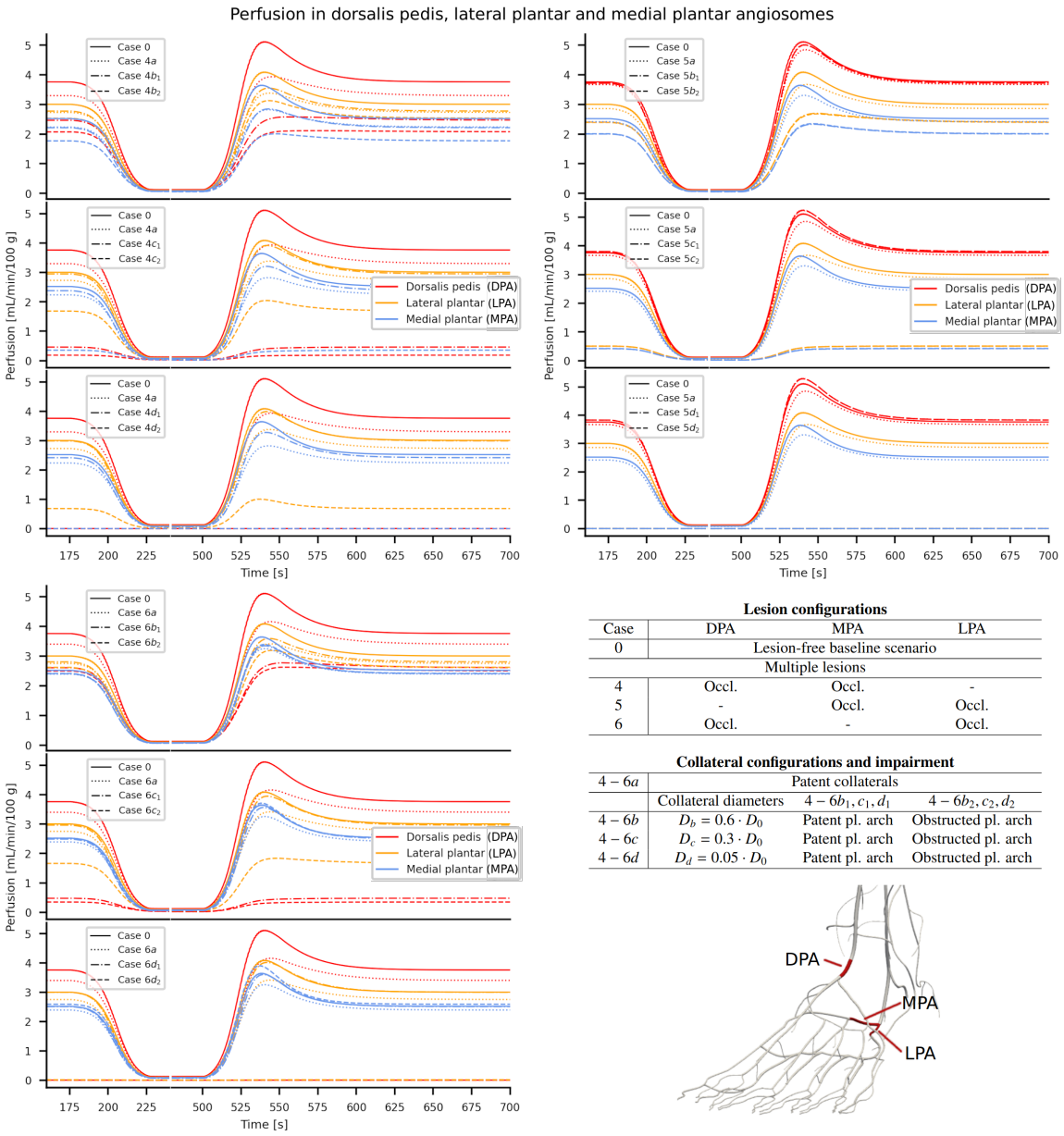

Lesion configurations

Case	DPA	MPA	LPA
0	Lesion-free baseline scenario		
	Multiple lesions		
4	Occl.	Occl.	-
5	-	Occl.	Occl.
6	Occl.	-	Occl.

Collateral configurations and impairment

$4-6a$	Patent collaterals		
	Collateral diameters	$4-6b_1, c_1, d_1$	$4-6b_2, c_2, d_2$
$4-6b$	$D_b = 0.6 \cdot D_0$	Patent pl. arch	Obstructed pl. arch
$4-6c$	$D_c = 0.3 \cdot D_0$	Patent pl. arch	Obstructed pl. arch
$4-6d$	$D_d = 0.05 \cdot D_0$	Patent pl. arch	Obstructed pl. arch

Figure 4.59: Time variation of cardiac-cycle averaged perfusion values in the DPA, LPA and MPA angiosomes for cases 4-6. Cases $4a-6a$ denote scenarios where all collaterals are assumed to be patent. Cases $4b_1-6b_1$, $4c_1-6c_1$, $4d_1-6d_1$ denote cases where the plantar arch is assumed to be fully patent, while other collaterals have a diameter that is, respectively, 60%, 30%, and 5% of the original diameter. Cases $4b_2-6b_2$, $4c_2-6c_2$, $4d_2-6d_2$ denote cases where all collaterals (including the plantar arch) have a diameter that is, respectively, 60%, 30%, and 5% of the original diameter.

reliably quantified. In summary, although the model is firmly rooted in established physiological principles and aligned with current research, the scarcity of direct angiosome-level perfusion data limits the extent to which its predictions can be fully validated.

4.5.4.2 Clinical interpretation and implications

The discussion will focus on the impact of lesions in the DPA, LPA and MPA on their respective angiosomes. In tables 4.22 and 4.23 we also report results for the LCA and MCA angiosomes, which are characterised by a low variation in baseline perfusion for all considered scenarios, due to the absence of lesions in their feeding arteries.

4.5.4.2.1 Perfusion under single-artery occlusion

Simulation results suggest that TTP in the angiosomes can serve as a functional readout of collateral sufficiency. Indeed, when collateralisation is preserved (collateral diameter $\geq$ 60% of the baseline geometry in cases 2 and 3, and not impaired in case 1), ΔTTP remains $\leq$10% in the affected angiosome under the condition of a single feeding artery occlusion. This pattern is consistent with maintained tissue perfusion through collaterals (Δ baseline perfusion $\leq$10%). In contrast, when the collateral calibre falls below a subcritical range (in case 1, 60% of the baseline diameter), the hyperaemic TTP response disappears, indicating that the autoregulatory capacity of the model was exhausted independently of cuff application due to the severity of the pathological condition. From a clinical perspective, this is consistent with the observed loss of perfusion. In cases 2 and 3, assuming all other arteries remain patent, TTP changes are primarily observed when the plantar arch is occluded, underscoring the arch's role as the cross-angiosome conduit that distributes flow across MPA and LPA.

Placed in a clinical context, these findings offer a physiological bridge between the angiosome targeted strategy and the "best-vessel" paradigm. Prior observational studies have reported improved healing when revascularisation is directed to the artery feeding the wounded angiosome (Kim et al., 2021). They also observed that when the wound-bearing angiosome received blood flow via angiographically visible collaterals, outcomes were generally comparable to those achieved with direct angiosome perfusion (Špillerová et al., 2017; Chuter et al., 2024; Berchiolli et al., 2023). Our simulations explain how both strategies can be correct, conditional on arch patency and collateral sufficiency: if the plantar arch is patent and collaterals are functionally adequate (ΔTTP$\leq$10%), indirect or "best-vessel" revascularisation may restore sufficient perfusion to the wound angiosome via blood redistribution. If the arch is occluded, collaterals are absent, or the collateral diameter is, in our model, below 60% of its original value, simulations suggest that a direct angiosome-targeted revascularisation would be preferable. However, simulations are restricted to macrovascular architecture and vessel calibre, without incorporating microvascular dysfunction. In

clinical reality, microvascular impairment, particularly in patients with diabetes, edema, or renal failure (Kim et al., 2021; Norgren et al., 2007), can significantly limit vasodilatory capacity and compromise collateral flow. This discrepancy between macrovascular and microvascular behaviour likely contributes to the observed variability in wound healing among patients with comparable angiographic findings.

4.5.4.2.2 Perfusion under dual-artery occlusion

When two of the three feeding arteries to the foot are occluded (cases 4-6), model predictions show a marked deterioration in perfusion, reflected by a substantial increase in TTP within the angiosomes with occluded inflow vessels, even when collateral diameters remain at 60% of the reference model for a healthy individual. When collateral diameter is reduced further to 30% or 5% of its original value, the TTP response is almost completely eliminated, indicating near-complete loss of functional perfusion, which is also confirmed by a reduction in baseline perfusion $\geq$40% in the affected angiosomes. This contrasts sharply with single-occlusion scenarios, where ΔTTP remained below 10% under collateralisation with a diameter above 60% of the standard model, suggesting that the physiological reserve provided by collaterals is insufficient once inflow is severely restricted. Interestingly, whether the plantar arch is patent or occluded only has a minimal effect in these dual-occlusion scenarios, underscoring that the dominant determinant of perfusion failure is the severe reduction in inflow rather than redistribution capacity. From a clinical perspective, in such scenarios, reliance on indirect strategies, even in the presence of visible collaterals, may be insufficient to achieve wound healing or limb salvage.

4.5.5 Limitations

The present study is characterised by several limitations. In particular, we perform a purely computational study employing an idealised vascular configuration, derived from clinical textbooks, which was modified to reproduce the application of a pressure cuff and a set of idealised pathological scenarios. These scenarios do not account for the various stenosis degrees that could be observed in clinical practice, nor for microvascular impairment, which is a fundamental flow-limiting factor, especially in the presence of comorbidities such as diabetes and oedema. Moreover, we reproduce the expected hyperaemic response after cuff release through a very simplistic description of control mechanisms. Finally, while the model reflects established physiological knowledge and current research, the absence of direct perfusion measurements at the angiosome level remains a key barrier to full validation. For these reasons, our model is currently not suitable for providing patient-level outcomes, and the findings reported in this study may not directly translate to patients with multilevel disease, severe infection/oedema, or extensive tissue loss.

5 Conclusions

In his chapter we discuss the main contributions presented in this thesis, outline some limitations, and propose several extensions and improvements.

5.1 Contributions

This work, motivated by the lack of integrated 1D-0D models of the cardiorespiratory system, has resulted in the following main contributions, which bring together methodological developments in numerical analysis and the progressive construction of a 1D-0D cardiopulmonary modelling framework:

(1) The development of a high-order well-balanced finite-volume scheme for non-conservative hyperbolic systems;

(2) The construction of a progressively integrated cardiopulmonary model including lung mechanics, gas transport and exchange, and local control mechanisms.

(3) The application of such a model to a clinically relevant problem, i.e. the study of foot perfusion in the presence of stenoses and occlusions.

5.1.1 Well-balanced high-order method for non-conservative hyperbolic PDEs with source terms

In section 2.2.3, we proposed a high-order well-balanced numerical scheme for the solution of non-conservative systems of hyperbolic PDEs with source terms. The method is based on the GRP reconstruction by Montecinos et al. (2025), which is well-balanced by construction

up to third order of accuracy, provided that boundary states belong to the same family of the steady-state solution of the considered PDEs and the conservation property holds. In addition, it incorporates a modification of the DET solver (Dumbser et al., 2008) along the same lines as those proposed by Guerrero Fernández et al. (2022). Numerical tests performed on the Burgers' equation and on the hyperbolized BFEs (Müller et al., 2016a) with friction (section 3.2), gravity and variable geometrical properties demonstrate the well-balanced property of the scheme and highlight its accuracy and efficiency in complex scenarios. However, it is important to mention that in this work we employ the GRP-based reconstruction without making use of any limiter, which is linear in Godunov's sense. As a consequence, spurious oscillations might arise in the presence of discontinuities. A possible strategy to overcome this issue would be to employ an a-posteriori limiter such as the Multi-dimensional Optimal Order Detection (MOOD) strategy (Clain, 2011). In addition, the proposed scheme does not guarantee the physical admissibility of the numerical solution. In particular, it does not belong to the class of positivity-preserving schemes and therefore provides no control on the positivity of physically relevant quantities, such as the cross-sectional area in the BFEs system. Nevertheless, in all the numerical experiments presented in this work, no loss of positivity of the cross-sectional area has been observed. This behaviour is likely related to the choice of physically relevant initial and boundary conditions, as well as to the time step restrictions adopted in the simulations. The design of suitable positivity-preserving modifications of the present method represents a relevant direction for future research (Huang et al., 2024).

5.1.2 Towards an integrated cardiopulmonary model

A large part of this work focused on the progressive construction of an integrated cardiopulmonary model. We started by assessing cardiopulmonary mechanical interactions, and later added descriptions of gas transport and exchange, and of a first set of short-term control mechanisms.

Cardiopulmonary mechanical interactions. Insights from an anatomically detailed arterial-venous network model

We presented a 1D-0D model that couples a 0D description of respiratory mechanics (section 2.3.4) to the closed-loop ADAVN model (sections 2.1.3, 2.3.1.1, 2.3.2, and 2.3.3.2). In section 4.1 we showed that, with the appropriate parametrisation, our model can satisfactorily reproduce cardiac and haemodynamic variables of interest for young healthy males at rest, and we placed emphasis on the diverse model responses obtained in different scenarios with and without the respiratory coupling, thus highlighting the blood-pumping function of respiration. Particularly of interest was the marked change in cardiac free-wall elastances required to maintain atrial volumes within reasonable ranges, which motivated

the later development of the cardiac model illustrated in section 2.3.1.2 and verified in section 4.2.2. We then assessed how the respiratory effort impacts haemodynamic waveforms in arteries and veins located in different areas of the body. We did so through a three-fold assessment: we analysed haemodynamic signals and their spectra to characterise the contribution of cardiac and respiratory pulsatility, and the intensity of their forward and backward components to assess whether their magnitude was impacted by respiration. Results showed that the impact of respiration on the intensity and periodicity of waveforms in the systemic arteries is negligible, and, conversely, that it is highly variable in systemic veins. In particular, respiratory influence is highly marked in lower body veins, while it is not as marked, albeit still noticeable, in the upper body. Finally, we reported local sensitivity indices obtained for the cardiac output, central venous pressure, mean arterial pressure, central pulse pressure and left atrial volume in response to variations in model parameters. Through this analysis, we confirmed the previously proven strong relationship between arterial and venous districts also in the presence of respiration.

Modelling gas transport and exchange

Following the introduction of cardiopulmonary mechanical interactions, we focused on the inclusion in our model of gas transport and exchange mechanisms. Due to the long time scales that are necessary for these simulations, associated with the slow gas exchange dynamics, we chose to develop a reduced vascular network (ADAVN86), comprising 109 arteries and 129 veins, which we presented in section 2.1.4, and verified in section 4.2.1 against simulation results obtained with the ADAVN model. We described gas transport in the 1D vascular network by coupling the 1D BFEs with spatially varying geometrical and mechanical properties with a system of n advection equations describing the passive transport of n scalars. The numerical solution of this system, for which we proposed a first order (section 2.2.2.1.1) and a second order (section 2.2.2.1.2) numerical scheme, posed several challenges, in particular regarding mass conservation at a discrete level. Indeed, we showed in section 3.1 that substance mass was conserved, with our framework, only when adopting a conservative numerical method for the solution of the transport problem, due to the presence of highly nonlinear integrand functions in the computation of numerical fluctuations. Gas transport in lumped parameter models of the heart, pulmonary circulation and peripheral terminals was described by enforcing mass conservation (section 2.3.5). We validated the resulting setup by simulating a test bolus (section 4.3.2.1), a procedure commonly used in clinical practice to determine contrast transit times prior to CT and MRI scans. We compared the model-generated times to peak in the aortic arch following contrast injections performed at different injection rates against data from a cohort of 32 patients (Fischer et al., 2022) and against simulation results obtained with physiology-based pharmacokinetic models (Bae, 2010), observing good agreement in both cases even though we neglect the redistribution of tracer from the vascular to the interstitial spaces and tracer clearance mechanisms.

After validating our transport model, we introduced descriptions of gas exchange at the level of pulmonary and peripheral capillaries. Lung gas exchange was based on the work by Albanese et al. (2016), from which we adapted model equations (section 2.3.6.1) and parametrization (section 4.3.1.1). The main difference in model equations lies in the fact that we explicitly account for gas transport in the heart, pulmonary arteries and pulmonary capillaries, while the former two compartments are bypassed in Albanese's model. The description of gas exchange in peripheral capillaries (section 2.3.6.2) required the definition of three parameters, the metabolic gas production and consumption rates, and the perfused tissue volumes. We chose to parametrize the model in a way that allowed us to take advantage of the anatomical resolution of the ADAVN86 vascular network (section 4.3.1.2.2), by defining metabolic rates over five vascular regions and partitioning the tissue volume involved in gas exchange into 25 subregions. We evaluated the performance of our model by simulating a physiological situation, showing in section 4.3.2.2 a good agreement between model-generated gas composition variables and physiological literature data. Further validation will require the introduction of local control mechanisms, in order to assess the performance of the model for respiratory manoeuvres and conditions such as hypoxia, hypercapnia and haemorrhage.

Modelling cerebral local autoregulation

We coupled our 1D-0D cardiopulmonary model with descriptions of myogenic and metabolic cerebral autoregulation mechanisms. Indeed, thanks to myogenic autoregulation, cerebral blood flow remains relatively constant over a wide range of mean arterial pressure values, and due to metabolic modulation, it responds to perturbations in blood gas levels. These mechanisms are fundamental to protect the brain from damage resulting from hypo- and hyper-perfusion. In section 4.4.1.2, we assessed the behaviour of the myogenic autoregulation model presented in section 2.3.7.1 by comparing model-generated results with the static autoregulation curve first introduced by Lassen (1959), observing good agreement both in the presence and in the absence of respiration. We compared results obtained under the assumption of constant and variable intracranial pressure, observing that increases in ICP that are observed when the upper limit of autoregulation is exceeded partially offset the increase in MAP, thereby apparently enhancing the autoregulatory response. Additionally, we were able to satisfactorily reproduce the impact of hypercapnia on Lassen curves, showing that the lower limit of regulation shifts towards higher pressure values in response to increased Pa_{CO_2} levels. We verified the CO_2 reactivity model described in section 2.3.7.2.1 and the fully metabolic autoregulation model described in section 2.3.7.2.2 by reproducing results by Ursino and Giannessi (2010). As for the myogenic autoregulation model, we observed that a variable ICP introduces an extremely strong flow-limiting effect. Future studies will address this limitation: we plan to analyse the impact of changes in the ICP model parametrization, and to include a description of CSF production and drainage.

5.1.3 Foot perfusion. Insights from an anatomically detailed arterial network model

We proposed a novel computational framework for the characterisation of foot angiosome perfusion following a cuff-induced ischaemia test. Our aim was to improve the understanding of the fundamental mechanisms that underlie the angiosome and best-vessel theories for revascularization, by providing quantitative results obtained in a fully controlled, physiologically realistic situation. Indeed, a major drawback highlighted in clinical studies available in the literature is the substantial heterogeneity of patients affected by CLTI, arising from diverse risk factors, comorbidities and highly variable collateral networks. In particular, we used this model to study the impact of 42 pathological scenarios, characterised by occlusions placed in either the DPA, the MPA, or the LPA, and by different degrees of collateral impairment. As illustrated in section 4.5.4, if collateralization between foot angiosomes is preserved, occlusions in one of the three feeding arteries of the foot have little influence on overall foot perfusion, underlining the importance of blood redistribution in maintaining adequate perfusion levels. In this case, good patient outcomes can be achieved by revascularising the best-preserved vessel that crosses the ankle. When collateral vessels are impaired, instead, perfusion decreases in the angiosome corresponding to the occluded feeding artery. Additionally, perfusion in the MPA and LPA angiosomes is highly dependent on the level of patency of the plantar arch, which acts as a cross-angiosome conduit. In this case, it is important for the surgeon to revascularise the relevant feeding artery. Instead, when two of the three feeding arteries to the foot are occluded, there is a significant reduction in perfusion even when collaterals are patent, caused by the insufficient inflow. These considerations highlight the strong influence of network structure on simulation results, suggesting that meaningful comparisons with clinical data and the applicability of such a model in the clinical practice via the definition of thresholds for TTP and baseline perfusion variations will require an accurate definition of the patients' foot vasculature or, at least, a characterisation of the degree of collateral impairment. In addition, the model would benefit from the knowledge of patient-specific vessel wall thickness and stiffness, or at least from a characterization of how these properties are affected by age and comorbidities commonly associated with peripheral artery disease. Future extensions of the model will include the addition of an explicit description of foot oxygenation and metabolic autoregulation phenomena. Moreover, we plan to study the impact of bypass surgeries on foot perfusion.

5.1.4 Limitations and perspectives

Several limitations characterise the work presented in this thesis. On the one hand, as evidenced when discussing simulation results, the scarcity of physiological data limits the extent to which the model can be fully validated and applied clinically. On the other hand, the presented cardiopulmonary model relies on several simplifying assumptions. Our

lung-mechanics model cannot reproduce ventilation heterogeneity, which plays a fundamental role in pathological conditions such as asthma, lung fibrosis and COPD (Bruce et al., 2021; Gibson et al., 2024; Teague et al., 2014; Barjaktarevic et al., 2026). Several approaches can be adopted to address this limitation. As an example, the adopted 0D model can be extended as in Christensen and Dræby to account for the presence of multiple alveolar branches, which would allow the simulation of scenarios in which alveolar compliances differ or airflow is restricted in some areas. Additionally, 1D descriptions of the upper airways can be adopted, e.g. following the approaches proposed by Choi et al. (2019) or Grandmont et al. (2025). The gas exchange model is implemented only in the 0D terminals and lacks explicit representations of membrane transport properties, pH regulation, and acid-base balance. In future work, we plan to include the gas dissociation and pH regulation models employed by Christensen and Dræby; Trenhago et al. (2015), which can be useful for the characterisation e.g. of cardiogenic shock, assocciated with acidosis and high lactate levels (Jentzer et al., 2022). Moreover, only local autoregulation mechanisms were included, while central nervous system-mediated respiratory and cardiovascular control mechanisms, and hormonal regulation were not considered. In particular, for short timescale simulations, the role of baroreflex (Herring and Paterson, 2018; Lanfranchi and Somers, 2002; Di Rienzo et al., 2009; Fu and Ogoh, 2019), chemoreflex (Kara et al., 2003; Kamra et al., 2025; Gabutti et al., 2001) and lung stretch reflex (Kam and Power, 2020) responses cannot be neglected, both in physiological and pathological conditions. When considering longer timescales, such as those associated with the sleep-wake cycle, additional mechanisms need to be considered. Indeed, during sleep, heart and respiratory rates decrease, and drops in cardiac output and systemic pressures are observed (Coote, 1982; Guilleminault et al., 1976; Cheng et al., 2010). Additionally, metabolic processes such as glucose-insulin-fatty acid regulation become non-negligible when considering multi-day simulations, as illustrated by (Cheng et al., 2010), as they influence both autonomic control and cardiovascular function, thereby affecting systemic pressures.

Despite these constraints, this thesis provides methodological advances and offers mechanistic insights into clinically relevant problems, such as perfusion in peripheral artery disease, and into complex physiological phenomena, such as cardiopulmonary interactions. Having outlined the main limitations, we now describe the specific extensions we will pursue in the immediate future.

To start, we plan to include the baroreflex and chemoreflex regulation mechanisms employed by Albanese et al. (2016); Fernandes et al. (2021), enabling the simulation of realistic responses to hypoxia, hypercapnia, haemorrhage, and to the Müller and Valsalva manoeuvres. These challenges will provide a deeper validation of the model and allow us to assess its behaviour under conditions that strongly perturb the baseline "at-rest" condition (Cheng et al., 2016). In addition, we will integrate the description of gravitational effects proposed by Colombo et al. (2026), in order to characterise the system's response to orthostasis and, ultimately, to physical exercise. In this context, we will also analyse

the implications of adopting either an arterial (Albanese et al., 2016; Blanco et al., 2012) or an integrated arterial-cardiopulmonary (Celant et al., 2023; Fois et al., 2022) baroreflex model.

Furthermore, we plan to improve the description of the brain-CSF compartment, with the aim of using the integrated model to investigate how respiration and orthostasis influence brain waste clearance, an increasingly relevant topic given the rising clinical burden of neurodegenerative diseases. Achieving this goal will require additional numerical developments, including the characterisation of CSF flow in the perivascular space, potentially extending strategies such as those proposed by Toro et al. (2019), and the simulation of solute diffusion from and into 1D domains.

Together, these directions outline an ambitious research programme. They build on the methodological and physiological foundations established in this thesis and point toward increasingly comprehensive models capable of addressing both fundamental scientific questions and clinically relevant scenarios.

A

Appendix

A.1 Cardiopulmonary mechanical interactions. Insights from an anatomically detailed arterial-venous network model

A.1.1 Haemodynamic indices

We report here the definitions of the haemodynamic indices in table 4.2 along with a description of the populations for which the literature values were provided (sections A.1.1, A.1.1). Moreover, in section A.1.1 we report haemodynamic indices obtained for the following additional scenarios:

A. Respiration (both intrathoracic and intra-abdominal pressures applied as external pressures respectively in the thoracic and abdominal compartments), original parametrisation from (Müller et al., 2023);

B. Reduced respiration (only intrathoracic pressure applied as external pressure respectively in the thoracic compartment), modified parametrisation reported in table 4.2.

Definitions

Ventriculo-arterial coupling indices and stroke work

- Left ventricle elastance index [mmHg/mL] (Holm et al., 2022). It describes the contractility of the left ventricle and can be computed as the ratio between end-systolic pressure and end-systolic volume. It is affected by chamber stiffness, mass and geometry. In our case, we consider, for computations, only the end-systolic

stretched volume.

$$\text{LV elastance index} = \frac{P_{LV}^{\text{end-systolic}}}{V_{LV}^{\text{end-systolic}} - V_{0,LV}}$$

- Aortic elastance index [mmHg/mL] (Holm et al., 2022). It describes the arterial load on the left ventricle, and is defined as the ratio between end-systolic pressure and stroke volume. It is influenced by vascular resistance, pulsatile load and heart rate.

$$\text{Aortic el. index} = \frac{P_{LV}^{\text{end-systolic}}}{V_{LV}^{\text{end-diastolic}} - V_{LV}^{\text{end-systolic}}}$$

- Ventriculo-arterial coupling index (Holm et al., 2022). This index helps evaluate arterial and myocardial function, and plays and important role in the diagnosis of heart failure. It is computed as the ratio between arterial and ventricular elastances.

$$\text{Ventriculo-arterial coupling index} = \frac{\text{Aortic elastance index}}{\text{LV elastance index}}$$

- Aortic pulsatility index (Belkin et al., 2021). This haemodynamic index, which can be computed as the ratio between central pulse pressure and pulmonary capillary wedge pressure, characterises cardiac filling pressures and contractility, and can be used to assess the severity of heart failure. Since in the clinical practice pulmonary capillary wedge pressure serves as a surrogate for left ventricular end-diastolic pressure, for the computation of this index we employ the latter.

$$\text{Aortic pulsatility index} = \frac{\text{Central PP}}{P_{LV}^{\text{end-diastolic}}}$$

- Left ventricle stroke work [J] (Gilbert-Kawai and Wittenberg, 2014), i.e. the work that each ventricle does to eject a certain volume of blood. It can be computed as the area of the left ventricular PV loop (as we do here) or approximated as the product between stroke volume, the difference between mean arterial pressure and pulmonary capillary wedge pressure, and a factor of 0.0136 to convert units of pressure and volume to units of work.

Volumes of interest and related quantities

- Cardiac output [L/min]. The amount of volume pumped by the left ventricle per minute. We computed it as the average flow entering the systemic arteries during one respiratory cycle.

$$\text{CO} = \frac{1}{T_{\text{resp}}} \int_0^{T_{\text{resp}}} q_{\text{aorta}}\, dt$$

- Left/right ventricular stroke volume indices [mL/m^2]. The volume of blood ejected by each ventricle with each contraction divided by the body surface area of the subject, which we assumed to be equal to 1.6488m^2 (Blanco et al., 2015). The volume of blood ejected by each ventricle with each contraction can be computed as the difference between their end-diastolic and end-systolic volumes.

$$\text{LV/RV SVI} = \frac{V_{LV/RV}^{\text{end-diastolic}} - V_{LV/RV}^{\text{end-systolic}}}{\text{BSA}}$$

- Left/right ventricular ejection fractions [%]. This index is computed as the ratio between the stroke volume and the end-diastolic volume and is employed in the clinical practice as a measure of ventricular systolic function. A low ejection fraction might denote heart failure, while very high values might indicate heart conditions like hypertrophic cardiomyopathy.

$$\text{LV/RV EF} = \frac{V_{LV/RV}^{\text{end-diastolic}} - V_{LV/RV}^{\text{end-systolic}}}{V_{LV/RV}^{\text{end-diastolic}}}$$

- Left/right atrial volume index [mL/m^2]. Left atrial volume index is employed in the clinical practice to assess the severity of pathological conditions such as valvular heart diseases, left ventricular systolic or diastolic dysfunction and atrial fibrillation. Indeed, LA enlargement is associated with a higher risk of heart failure, stroke and death. Both indices are computed as the average atrial volumes during one cardiac cycle divided by the body surface area.

$$\text{LA/RA VI} = \frac{1}{\text{BSA} \cdot T_{\text{c. cycle}}} \int_0^{T_{\text{c. cycle}}} V_{LA/RA} dt$$

  To account for respiratory variability, we then average over the respiratory cycle.

Pressures of interest

- Central venous pressure [mmHg]. This pressure, which corresponds to the mean right atrial pressure, is determined by the balance between systemic venous return and right ventricular output, and depends on blood volume, peripheral venous tone, intrathoracic pressure and right ventricular function (Didebotham, 2017). It is computed as the cardiac cycle-averaged pressure in the right atrium.

$$\text{CVP} = \frac{1}{T_{\text{c. cycle}}} \int_0^{T_{\text{c. cycle}}} P_{RA} dt$$

  To account for respiratory variability, we then average over the respiratory cycle.

- Mean left atrial pressure [mmHg]. It is computed as the cardiac cycle-averaged pressure in the left atrium.

$$\text{MLAP} = \frac{1}{T_{\text{c. cycle}}} \int_0^{T_{\text{c. cycle}}} P_{LA} dt$$

  To account for respiratory variability, we then average over the respiratory cycle.

- Mean arterial pressure [mmHg]. Cardiac-cycle average of pressure in the aorta.

$$\text{CVP} = \frac{1}{T_{\text{c. cycle}}} \int_0^{T_{\text{c. cycle}}} P_{\text{aorta}}\, dt$$

  To account for respiratory variability, we then average over the respiratory cycle.

- Peripheral systolic, diastolic and pulse pressure [mmHg]. Peripheral systolic and diastolic pulse pressure are computed, respectively, as the maximum and minimum pressure values in the femoral artery over one cardiac cycle. Pulse pressure is computed as the difference between PSBP and PDBP.

$$\begin{aligned} \text{PSBP} &= \max_{\text{c. cycle}} P_{\text{fem. artery}}, \\ \text{PDBP} &= \min_{\text{c. cycle}} P_{\text{fem. artery}}, \\ \text{PPP} &= \text{PSBP} - \text{PDBP}. \end{aligned}$$

  To account for respiratory variability, we then average these three quantities over the respiratory cycle.

Population characteristics

- In Patel et al. (2021), they considered 1450 healthy adult subjects, enrolled in 15 countries, with an even distribution among sex and age groups. Given the availability of sex and age-stratified data, we consider as reference the CO and LVSVI measured for 320 young male subjects (18-40 years).
- In Kovalova et al. (2006), they considered 91 healthy normotensive volunteers with an average age of 39 years (range 17-62), 46 of which were men. No age stratification was provided, but data was provided separately for men and women, so we consider as reference the ejection fractions and RVSVI measured for males.
- in Maceira et al. (2010) and Maceira et al. (2013) they consider a population of 60 healthy males with an average age of 49 years (standard deviation 17 years). Data was acquired through cardiac magnetic resonance. We chose to refer to this kind of measurement since it matched the behaviour of the model without respiration better, due to the fact that echocardiographic reference values are about 20 mL/m^2

lower. Moreover, cardiac magnetic resonance is regarded as the gold standard for measurement of ventricular dimension and function, suggesting that the same can hold for the atria.

- In McEniery et al. (2005) they considered 4001 healthy, normotensive individuals between 18 and 90 years selected from the 10096 individuals enrolled in the ACCT study, and reported sex and age-stratified values for all considered haemodynamic parameters. We chose as reference the MAP, PSBP, PDBP and PPP reported for 178 males between 20-29 years.
- In Ford et al. (2005) they considered 17 young healthy volunteers (16 males) at rest in supine position.
- In Sakamoto et al. (2013) they considered 1322 coronary vessels from 496 patients enrolled in the PREDICTION study.

Additional scenarios

In table A.1 we compare results obtained with (Scenario A) and without (Scenario 1) respiration using the parametrisation reported in (Müller et al., 2023). Additionally, we compare results obtained through the parametrisation reported in table 4.2 using the full respiration model (Scenario 2) or neglecting the contribution of intra-abdominal pressure (Scenario B), as is done in most available literature.

A.2 Sensitivity analysis

In table A.2, we report sensitivity indices obtained for Scenarios 1, 2 and 3.

Table A.1: Main cardiac and haemodynamic indices $\mathcal{I}$ obtained for scenarios 1, A, 2, B. LA/RA/LV/RV: left atrium/right atrium/left ventricle/right ventricle; SBP/DBP/PP: systolic/-diastolic/pulse pressure. Indices were computed averaging over the respiratory cycle. The relative variation Var A = $(\mathcal{I}_{\mathrm{scA}} - \mathcal{I}_{\mathrm{sc1}})/\mathcal{I}_{\mathrm{sc1}}$ is computed with respect to results without respiration, and the relative variation Var B = $(\mathcal{I}_{\mathrm{scB}} - \mathcal{I}_{\mathrm{sc2}})/\mathcal{I}_{\mathrm{sc2}}$ with respect to results obtained with respiration and our best parametrisation. Reference values, if not otherwise specified, are expressed as mean ± SD. Reference left/right atrial volume indices are expressed as mean, (95% confidence interval). Reference mean left/right atrial pressures are expressed in terms of a reasonable range accepted in the clinical practice

Index	Scenario 1	Scenario A		Scenario 2	Scenario B	
	Val.	Val.	Var A	Val.	Val.	Var B
Ventriculo-arterial coupling indices and stroke work						
LV elastance index [mmHg/mL]	2.85	2.66	-0.7	2.12	2.12	0
Aortic elastance index [mmHg/mL]	1.24	1.21	-0.02	1.23	1.22	-0.01
Ventriculo-arterial coupling index	0.44	0.46	0.05	0.58	0.57	-0.02
Aortic Pulsatility Index	4.21	7.2	0.71	5.0	5.35	0.07
LV stroke work [J]	1.03	1.69	0.64	1.05	0.94	-0.1
Volumes of interest and related quantities						
Cardiac output [L/min]	5.81	7.49	0.29	5.86	5.56	-0.05
LV stroke volume index [mL/m^2]	47.9	61.61	0.29	48.49	45.94	-0.05
LV ejection fraction [%]	64.01	64.33	0	58.67	58.61	0
RV stroke volume index [mL/m^2]	47.57	62.5	0.31	49.81	47.25	-0.05
RV ejection fraction [%]	59.9	60.12	0	52.98	53.19	0
LA volume index [mL/m^2]	48.42	67.54	0.39	31.98	30.25	-0.05
RA volume index [mL/m^2]	53.91	81.47	0.51	50.94	47.73	-0.06
Pressures of interest						
Central venous pressure [mmHg]	4.67	2.32	-0.5	4.49	3.82	-0.15
Mean left atrial pressure [mmHg]	6.74	4.53	-0.33	5.41	4.74	-0.12
Mean arterial pressure [mmHg]	92.8	114.73	0.24	93.31	87.88	-0.06
Peripheral SBP [mmHg]	127.88	164.74	0.29	127.6	120.46	-0.06
Peripheral DBP [mmHg]	73.28	88.13	0.2	74.39	69.69	-0.06
Peripheral PP [mmHg]	54.6	76.61	0.4	53.21	50.76	-0.05
Blood flow distribution						
Cerebral flow [mL/s]	12.38	16.31	0.32	12.48	12.05	-0.03
Coronary flow [mL/s]	4.91	6.67	0.36	5.32	4.97	-0.07

Table A.2: Local sensitivities $\mathcal{S}^{\pm}_{\mathcal{M},\mathcal{P}}$ of variables $\mathcal{M} = \{\text{CO, CVP, MAP, PPA, LAV}\}$ obtained for Scenarios 1 (top third), 2 (mid third), 3 (bottom third) and ranked according to their absolute values.

Rk	CO	CVP	MAP	PPA	LAV
	Scenario 1: no respiration, original parametrisation from (Müller et al., 2023)				
1	$V_{\text{str}}^{\text{set}} - (-12.27\%)$	$V_{\text{str}}^{\text{set}} + (+16.97\%)$	$V_{\text{str}}^{\text{set}} - (-12.26\%)$	$V_{\text{str}}^{\text{set}} + (+9.65\%)$	$V_{\text{str}}^{\text{set}} - (-12.70\%)$
2	$V_{\text{str}}^{\text{set}} + (+11.59\%)$	$V_{\text{str}}^{\text{set}} - (-16.03\%)$	$V_{\text{str}}^{\text{set}} + (+11.95\%)$	$V_{\text{str}}^{\text{set}} - (-6.57\%)$	$V_{\text{str}}^{\text{set}} + (+12.59\%)$
3	$C_{\text{sys,v}} - (+4.77\%)$	$C_{\text{sys,v}} - (+6.68\%)$	$R_{\text{per}} - (-5.86\%)$	$E_e - (-6.45\%)$	$t_{\text{onset}}^{RA} + (-6.31\%)$
4	$C_{\text{sys,v}} + (-4.28\%)$	$t_{\text{onset}}^{RA} + (+5.97\%)$	$R_{\text{per}} + (+5.63\%)$	$E_e + (+6.28\%)$	$t_{\text{onset}}^{LA} + (+6.18\%)$
5	$t_{\text{onset}}^{RA} + (-4.06\%)$	$C_{\text{sys,v}} + (-5.78\%)$	$C_{\text{sys,v}} - (+4.09\%)$	$\tau_{2,\text{LV}} + (+3.81\%)$	$E_{\text{fw,LV}}^{\text{min}} - (-6.17\%)$
6	$E_{\text{fw,RV}}^{\text{min}} - (+3.06\%)$	$E_{\text{fw,RV}}^{\text{min}} - (-3.91\%)$	$t_{\text{onset}}^{RA} + (-3.79\%)$	$\tau_{2,\text{LV}} - (+3.78\%)$	$E_{\text{fw,LV}}^{\text{min}} + (+6.02\%)$
7	$E_{\text{fw,RV}}^{\text{min}} + (-2.80\%)$	$E_{\text{fw,RV}}^{\text{min}} + (+3.64\%)$	$C_{\text{sys,v}} + (-3.76\%)$	$C_{\text{sys,v}} - (+3.56\%)$	$E_{\text{fw,LA}}^{\text{min}} - (+5.20\%)$
8	$E_{\text{fw,LV}}^{\text{min}} - (+2.04\%)$	$E_{\text{fw,RA}}^{\text{min}} - (-2.28\%)$	$E_{\text{fw,RV}}^{\text{min}} - (+2.85\%)$	$R_{\text{per}} - (+3.21\%)$	$C_{\text{sys,v}} - (+4.83\%)$
9	$E_{\text{fw,RV}}^{\text{max}} - (-1.98\%)$	$E_{\text{fw,RA}}^{\text{min}} + (+2.11\%)$	$E_{\text{fw,RV}}^{\text{min}} + (-2.65\%)$	$E_{\text{fw,LV}}^{\text{max}} - (-2.90\%)$	$E_{\text{fw,LA}}^{\text{min}} + (-4.63\%)$
10	$E_{\text{fw,LV}}^{\text{min}} + (-1.88\%)$	$E_{\text{fw,RV}}^{\text{max}} - (+1.89\%)$	$E_{\text{fw,LV}}^{\text{min}} - (+2.04\%)$	$C_{\text{sys,v}} + (-2.83\%)$	$C_{\text{sys,v}} + (-4.33\%)$
	Scenario 2: respiration, modified parametrisation reported in table 4.2				
1	$V_{\text{str}}^{\text{set}} - (-8.38\%)$	$V_{\text{str}}^{\text{set}} + (+25.62\%)$	$V_{\text{str}}^{\text{set}} - (-8.93\%)$	$V_{\text{str}}^{\text{set}} + (+7.34\%)$	$V_{\text{str}}^{\text{set}} + (+8.45\%)$
2	$V_{\text{str}}^{\text{set}} + (+8.04\%)$	$V_{\text{str}}^{\text{set}} - (-24.20\%)$	$V_{\text{str}}^{\text{set}} + (+8.71\%)$	$E_e + (+5.82\%)$	$V_{\text{str}}^{\text{set}} - (-8.30\%)$
3	$E_{\text{fw,RV}}^{\text{min}} - (+3.22\%)$	$C_{\text{sys,v}} - (+8.90\%)$	$R_{\text{per}} - (-5.79\%)$	$\tau_{2,\text{LV}} - (+5.78\%)$	$E_{\text{fw,LA}}^{\text{min}} - (+6.97\%)$
4	$C_{\text{sys,v}} - (+2.95\%)$	$C_{\text{sys,v}} + (-7.75\%)$	$R_{\text{per}} + (+5.59\%)$	$E_e - (-5.62\%)$	$E_{\text{fw,LA}}^{\text{min}} + (-5.96\%)$
5	$E_{\text{fw,RV}}^{\text{min}} + (-2.86\%)$	$E_{\text{fw,RV}}^{\text{min}} - (-5.58\%)$	$E_{\text{fw,RV}}^{\text{min}} - (+2.94\%)$	$V_{\text{str}}^{\text{set}} - (-5.58\%)$	$E_{\text{fw,LV}}^{\text{min}} - (-5.01\%)$
6	$C_{\text{sys,v}} + (-2.66\%)$	$E_{\text{fw,RV}}^{\text{min}} + (+4.92\%)$	$E_{\text{fw,RV}}^{\text{min}} + (-2.60\%)$	$\tau_{2,\text{LV}} + (-4.82\%)$	$E_{\text{fw,LV}}^{\text{min}} + (+4.89\%)$
7	$E_{\text{fw,RV}}^{\text{max}} - (-2.64\%)$	$t_{\text{onset}}^{RA} + (+4.76\%)$	$C_{\text{sys,v}} - (+2.55\%)$	$E_{\text{fw,LV}}^{\text{max}} + (+2.73\%)$	$t_{\text{onset}}^{RA} + (-3.82\%)$
8	$E_{\text{fw,LV}}^{\text{min}} - (+2.58\%)$	$P_{pl,ee} + (-4.66\%)$	$E_{\text{fw,LV}}^{\text{min}} - (+2.51\%)$	$E_{\text{fw,LV}}^{\text{max}} - (-2.67\%)$	$\tau_{2,\text{LV}} + (+3.66\%)$
9	$t_{\text{onset}}^{RA} - (-2.43\%)$	$P_{pl,ee} - (+4.64\%)$	$E_{\text{fw,RV}}^{\text{max}} - (-2.44\%)$	$E_{\text{fw,RV}}^{\text{min}} - (+2.64\%)$	$E_{\text{fw,RV}}^{\text{min}} - (+3.63\%)$
10	$E_{\text{fw,LV}}^{\text{min}} + (-2.39\%)$	$E_{\text{fw,RA}}^{\text{min}} - (-3.66\%)$	$E_{\text{fw,LV}}^{\text{min}} + (-2.33\%)$	$R_{\text{per}} - (+2.60\%)$	$E_{\text{fw,RV}}^{\text{min}} + (-3.19\%)$
	Scenario 3: no respiration, modified parametrisation reported in table 4.2				
1	$V_{\text{str}}^{\text{set}} - (-13.08\%)$	$V_{\text{str}}^{\text{set}} + (+16.65\%)$	$V_{\text{str}}^{\text{set}} - (-12.81\%)$	$E_e - (-7.46\%)$	$V_{\text{str}}^{\text{set}} - (-12.01\%)$
2	$V_{\text{str}}^{\text{set}} + (+12.80\%)$	$V_{\text{str}}^{\text{set}} - (-15.92\%)$	$V_{\text{str}}^{\text{set}} + (+12.52\%)$	$E_e + (+6.66\%)$	$V_{\text{str}}^{\text{set}} + (+11.84\%)$
3	$C_{\text{sys,v}} - (+5.66\%)$	$C_{\text{sys,v}} - (+7.24\%)$	$C_{\text{sys,v}} - (+5.50\%)$	$p_0^{\text{art}} + (+5.78\%)$	$E_{\text{fw,LA}}^{\text{min}} - (+6.55\%)$
4	$C_{\text{sys,v}} + (-5.01\%)$	$C_{\text{sys,v}} + (-6.25\%)$	$R_{\text{per}} - (-5.49\%)$	$p_0^{\text{art}} - (-5.12\%)$	$E_{\text{fw,LA}}^{\text{min}} + (-5.68\%)$
5	$E_{\text{fw,RV}}^{\text{min}} - (+4.12\%)$	$E_{\text{fw,RV}}^{\text{min}} - (-2.91\%)$	$R_{\text{per}} + (+5.18\%)$	$V_{\text{str}}^{\text{set}} - (-4.79\%)$	$E_{\text{fw,LV}}^{\text{min}} - (-5.41\%)$
6	$E_{\text{fw,RV}}^{\text{min}} + (-3.74\%)$	$E_{\text{fw,RV}}^{\text{min}} + (+2.64\%)$	$C_{\text{sys,v}} + (-4.88\%)$	$R_{\text{per}} - (+4.13\%)$	$E_{\text{fw,LV}}^{\text{min}} + (+5.24\%)$
7	$E_{\text{fw,RV}}^{\text{max}} - (-2.92\%)$	$t_{\text{onset}}^{RA} + (-1.92\%)$	$E_{\text{fw,RV}}^{\text{min}} - (+3.36\%)$	$V_{\text{str}}^{\text{set}} + (+4.08\%)$	$C_{\text{sys,v}} - (+5.20\%)$
8	$E_{\text{fw,LV}}^{\text{min}} - (+2.67\%)$	$E_{\text{fw,RA}}^{\text{min}} - (-1.82\%)$	$E_{\text{fw,RV}}^{\text{min}} + (-3.06\%)$	$\tau_{2,\text{LV}} - (+3.91\%)$	$C_{\text{sys,v}} + (-4.59\%)$
9	$E_{\text{fw,RV}}^{\text{max}} + (+2.51\%)$	$E_{\text{fw,RA}}^{\text{min}} + (+1.60\%)$	$E_{\text{fw,RV}}^{\text{max}} - (-2.42\%)$	$\tau_{2,\text{LV}} + (-3.77\%)$	$E_{\text{fw,RV}}^{\text{min}} - (+4.19\%)$
10	$E_{\text{fw,LV}}^{\text{min}} + (-2.48\%)$	$E_{\text{fw,RV}}^{\text{max}} - (+1.54\%)$	$E_{\text{fw,LV}}^{\text{min}} - (+2.39\%)$	$R_{\text{per}} + (-3.69\%)$	$\tau_{2,\text{LV}} + (+3.97\%)$

Bibliography

D. Abi-Abdallah Rodriguez, E. Durand, L. De Rochefort, Y. Boudjemline, and E. Mousseaux. Simultaneous pressure–volume measurements using optical sensors and mri for left ventricle function assessment during animal experiment. *Medical engineering & physics*, 37(1):100–108, 2015.

V. Aboyans, M. E. Canonico, L. Chastaingt, S. S. Anand, M. Brodmann, T. Couffinhal, M. H. Criqui, E. S. Debus, L. Mazzolai, M. M. McDermott, et al. Peripheral artery disease. *Nature Reviews Disease Primers*, 11(1):68, 2025.

M. Abu-Yousef, M. Mufid, K. Woods, B. Brown, and T. Barloon. Normal lower limb venous doppler flow phasicity: is it cardiac or respiratory? *American Journal of Roentgenology*, 196(6), 1997. doi: 10.2214/ajr.169.6.9393197.

J. Alastruey, K. H. Parker, S. J. Sherwin, et al. Arterial pulse wave haemodynamics. In *11th international conference on pressure surges*, volume 30, pages 401–443. Virtual PiE Led t/a BHR Group Lisbon, Portugal, 2012.

J. Alastruey, A. A. Hunt, and P. D. Weinberg. Novel wave intensity analysis of arterial pulse wave propagation accounting for peripheral reflections. *International journal for numerical methods in biomedical engineering*, 30(2):249–279, 2014.

A. Albanese, L. Cheng, M. Ursino, and N. Chbat. An integrated mathematical model of the human cardiopulmonary system: model development. *Am. J. Physiol. Heart Circ. Physiol.*, 310(7):H899–H921, 2016. doi: 10.1152/ajpheart.00230.2014.

V.-A. Alexandrescu. Myths and proofs of angiosome applications in cli: where do we stand? *Journal of Endovascular Therapy*, 21(5):616–624, 2014.

K. Anjana, S. Saha, and N. Selvaganesan. Simulation and analysis of an integrated cardiopulmonary gas exchange model under different pathological conditions. *IEEE Access*, 2025.

M. Applefeld. The jugular venous pressure and pulse contour. In H. Walker, W. Hall, and J. Hurst, editors, *Clinical Methods: The History, Physical, and Laboratory Examinations. 3rd edition.*, chapter 19. Boston: Butterworths, 1990.

P. Appleton, L. Hatle, and R. Popp. Superior vena cava and hepatic vein doppler echocardiography in healthy adults. *J. Am. Coll. Cardiol.*, 10:1032–1039, 1987. doi: 10.1016/s0735-1097(87)80343-1.

G. Arthurs and M. Sudhakar. Carbon dioxide transport. *Continuing education in anaesthesia, critical care & pain*, 5(6):207–210, 2005.

J. H. Artrip, M. C. Oz, and D. Burkhoff. Left ventricular volume reduction surgery for heart failure: a physiologic perspective. *The Journal of thoracic and cardiovascular surgery*, 122(4):775–782, 2001.

J. Arvidsson, S. Eriksson, E. Johansson, and K. Lagerstrand. Arterial occlusion duration affects the cuff-induced hyperemic response in skeletal muscle bold perfusion imaging as shown in young healthy subjects. *Magnetic Resonance Materials in Physics, Biology and Medicine*, 36(6):897–910, 2023.

A. Athanasiades, F. Ghorbel, J. Clark Jr, S. Niranjan, J. Olansen, J. Zwischenberger, and A. Bidani. Energy analysis of a nonlinear model of the normal human lung. *Journal of Biological Systems*, 8(02):115–139, 2000.

A. Avolio. Multi-branched model of the human arterial system. *Med. Biol. Eng. Comput.*, 18(6):709–718, 1980. doi: 10.1007/BF02441895.

K. Azer. Taylor diffusion in time-dependent flow. *International journal of heat and mass transfer*, 48(13):2735–2740, 2005.

K. T. Bae. Intravenous contrast medium administration and scan timing at ct: considerations and approaches. *Radiology*, 256(1):32–61, 2010.

A. Baird, R. A. Umoren, S. A. White, M. Gray, and T. L. Sawyer. A whole-body physiology model to investigate respiratory function during exercise across different age cohorts. *Journal of Respiration*, 5(1):1, 2025.

A. Bajwa, R. Wesolowski, A. Patel, P. Saha, F. Ludwinski, A. Smith, E. Nagel, and B. Modarai. Assessment of tissue perfusion in the lower limb: current methods and techniques under development. *Circulation: Cardiovascular Imaging*, 7(5):836–843, 2014.

I. Barjaktarevic, B. Kuhn, and C. B. Cooper. The evolving science of ventilation heterogeneity: From pathophysiology to personalized therapeutic approaches. *Respiratory Medicine*, page 108811, 2026.

J. B. Bassingthwaighle and H. R. Warner. Indicator dispersion in the circulation. *American heart journal*, 69:838, 1965.

M. Belkin, S. Kalantari, A. Kanelidis, T. Miller, B. Smith, S. Besser, D. Tehrani, B. Chung, A. Nguyen, N. Sarswat, J. Blair, D. Burkhoff, G. Sayer, S. Pinney, N. Uriel, G. Kim,

and J. Grinstein. Aortic pulsatility index: A novel hemodynamic variable for evaluation of decompensated heart failure. *J. Card. Fail.*, 27(10):1045–1052, 2021. doi: 10.1016/j.cardfail.2021.05.010.

R. Berchiolli, G. Bertagna, D. Adami, F. Canovaro, L. Torri, and N. Troisi. Chronic limb-threatening ischemia and the need for revascularization. *Journal of clinical medicine*, 12 (7):2682, 2023. doi: https://doi.org/10.3390/jcm12072682.

A. Bermudez, X. López, and M. E. Vázquez-Cendón. Numerical solution of non-isothermal non-adiabatic flow of real gases in pipelines. *J. Comp. Phys.*, 323:126–148, 2016. doi: 10.1016/j.jcp.2016.07.020.

F. Biancari and T. Juvonen. Angiosome-targeted lower limb revascularization for ischemic foot wounds: systematic review and meta-analysis. *European Journal of Vascular and Endovascular Surgery*, 47(5):517–522, 2014.

M. Bisgaard, K. C. Houlind, A. D. Blankholm, S. Ringgaard, J. Christensen, and H. Precht. Validation of mri assessment of foot perfusion for improving treatment of patients with peripheral artery disease. *Radiography*, 30(4):1116–1124, 2024.

P. Blanco, P. Trenhago, L. Fernandes, and R. Feijóo. On the integration of the baroreflex control mechanism in a heterogeneous model of the cardiovascular system. *International journal for numerical methods in biomedical engineering*, 28(4):412–433, 2012.

P. Blanco, L. Müller, S. Watanabe, and R. Feijóo. Computational modeling of blood flow steal phenomena caused by subclavian stenoses. *Journal of Biomechanics*, 49(9): 1593–1600, 2016.

P. J. Blanco, S. M. Watanabe, E. A. Dari, M. A. R. Passos, and R. A. Feijóo. Blood flow distribution in an anatomically detailed arterial network model: criteria and algorithms. *Biomechanics and modeling in mechanobiology*, 13(6):1303–1330, 2014. doi: https://doi.org/10.1007/s10237-014-0574-8.

P. J. Blanco, S. M. Watanabe, M. A. R. F. Passos, P. A. Lemos, and R. A. Feijóo. An anatomically detailed arterial network model for one-dimensional computational hemodynamics. *IEEE Trans. Biomed. Eng.*, 62(2):736–753, 2015.

P. J. Blanco, L. O. Müller, S. M. Watanabe, and R. A. Feijóo. On the anatomical definition of arterial networks in blood flow simulations: comparison of detailed and simplified models. *Biomech. Model Mechan.*, 19:663–1678, 2020. doi: 10.1007/s10237-020-01298-4.

E. Boileau, S. Pant, C. Roobottom, I. Sazonov, J. Deng, X. Xie, and P. Nithiarasu. Estimating the accuracy of a reduced-order model for the calculation of fractional flow reserve (ffr). *International journal for numerical methods in biomedical engineering*, 34 (1):e2908, 2018.

P. T. Boonen and D. Aerden. Intraarterial four-dimensional ct angiography with soft tissue perfusion evaluation in diabetic feet. *Radiology*, 307(4):e222663, 2023. doi: https://doi.org/10.1148/radiol.222663.

P. T. Boonen, N. Buls, J. Vandemeulebroucke, G. Van Gompel, F. Van Den Bergh, T. Leiner, D. Aerden, and J. De Mey. Combined evaluation of blood flow and tissue perfusion in diabetic feet by intra-arterial dynamic 4dct imaging. *European radiology experimental*, 7(1):44, 2023. doi: https://doi.org/10.1186/s41747-023-00352-x.

D. Bosanquet, J. Glasbey, I. Williams, and C. Twine. Systematic review and meta-analysis of direct versus indirect angiosomal revascularisation of infrapopliteal arteries. *European Journal of Vascular and Endovascular Surgery*, 48(1):88–97, 2014.

J. Britton and Y. Xing. Well-balanced discontinuous Galerkin methods for the one-dimensional blood flow through arteries model with man-at-eternal-rest and living-man equilibria. *Comput. Fluids*, 203:104493, 2020. doi: 10.1016/j.compfluid.2020.104493.

C. Broyd, J. Favies, J. Escaned, A. Huges, and K. Parker. Wave intensity analysis and its application to the coronary circulation. *Glob. Cardiol. Sci. Pract.*, 2017(1):e201705, 2017. doi: 10.21542/gcsp.2017.5.

R. M. Bruce, P. A. Phan, M. Rigolli, M. C. Tran, E. Pacpaco, N. M. Rahman, and A. D. Farmery. Assessment of ventilatory heterogeneity in chronic obstructive pulmonary disease using the inspired sinewave test. *International journal of chronic obstructive pulmonary disease*, pages 401–413, 2021.

W. Burchert, S. Schellong, J. van den Hoff, G.-J. Meyer, et al. Oxygen-15-water pet assessment of muscular blood flow in peripheral vascular disease. *The Journal of Nuclear Medicine*, 38(1):93, 1997.

D. Burkhoff and J. V. Tyberg. Why does pulmonary venous pressure rise after onset of lv dysfunction: a theoretical analysis. *American Journal of Physiology-Heart and Circulatory Physiology*, 265(5):H1819–H1828, 1993.

D. Burkhoff, I. Mirsky, and H. Suga. Assessment of systolic and diastolic ventricular properties via pressure-volume analysis: a guide for clinical, translational, and basic researchers. *American Journal of Physiology-Heart and Circulatory Physiology*, 2005.

S. Caroca, D. Villagran, and S. Chabert. Four functional magnetic resonance imaging techniques for skeletal muscle exploration, a systematic review. *European journal of radiology*, 144:109995, 2021. doi: https://doi.org/10.1016/j.ejrad.2021.109995.

J. M. Carson, C. Roobottom, R. Alcock, and P. Nithiarasu. Computational instantaneous wave-free ratio (ifr) for patient-specific coronary artery stenoses using 1d network models. *International Journal for Numerical Methods in Biomedical Engineering*, 35(11):e3255, 2019. doi: https://doi.org/10.1002/cnm.3255.

M. Castro, J. M. Gallardo, J. A. López-GarcÍa, and C. Parés. Well-balanced high order extensions of Godunov method for linear balance laws. *SIAM J. Numer. Anal.*, 46(2): 1012–1039, 2008.

M. J. Castro and C. Parés. Well-balanced high-order finite volume methods for systems of balance laws. *J. Sci. Comput.*, 82(2):48, 2020. doi: 10.1007/s10915-020-01149-5.

M. J. Castro Díaz, T. Chacón Rebollo, E. D. Fernández-Nieto, and C. Parés. On well-balanced finite volume methods for nonconservative nonhomogeneous hyperbolic systems. *SIAM J. Sci. Comput.*, 29(3):1093–1126, 2007. doi: 10.1137/040607642.

M. Celant, E. F. Toro, and L. O. Müller. Total effective vascular compliance of a global mathematical model for the cardiovascular system. *Symmetry*, 13(10):1858, 2021.

M. Celant, E. Toro, G. Bertaglia, S. Cozzio, V. Caleffi, A. Valiani, P. Blanco, and L. Müller. Modeling essential hypertension with a closed-loop mathematical model for the entire human circulation. *Int. J. Numer. Meth. Biomed. Eng.*, 39(11):e3748, 2023. doi: 10.1002/cnm.3748.

K.-H. Chan, J. D. Miller, and I. R. Piper. Cerebral blood flow at constant cerebral perfusion pressure but changing arterial and intracranial pressure: relationship to autoregulation. *Journal of Neurosurgical Anesthesiology*, 4(3):188–193, 1992.

P. Charlton, J. Harana, S. Vennin, Y. Li, P. Chowienczyk, and J. Alastruey. Modeling arterial pulse waves in healthy aging: a database for in silico evaluation of hemodynamics and pulse wave indexes. *Am. J. Physiol. Heart Circ. Physiol.*, 317(5):H1062–H1085, 2019. doi: 10.1152/ajpheart.00218.2019.

C. Chen, M. Nakayama, E. Nevo, B. Fetics, W. Maughan, and D. Kass. Coupled systolic-ventricular and vascular stiffening with age: Implications for pressure regulation and cardiac reserve in the elderly. *J. Am. Coll. Cardiol.*, 32(5):1221–1227, 1998. doi: 10.1016/S0735-1097(98)00374-X.

L. Cheng and M. C. Khoo. Modeling the autonomic and metabolic effects of obstructive sleep apnea: a simulation study. *Frontiers in Physiology*, 2:111, 2012.

L. Cheng, O. Ivanova, H.-H. Fan, and M. C. Khoo. An integrative model of respiratory and cardiovascular control in sleep-disordered breathing. *Respiratory physiology & neurobiology*, 174(1-2):4–28, 2010.

L. Cheng, A. Albanese, M. Ursino, and N. Chbat. An integrated mathematical model of the human cardiopulmonary system: model validation under hypercapnia and hypoxia. *Am. J. Physiol. Heart Circ. Physiol.*, 310(7):H922–H937, 2016. doi: 10.1152/ajpheart.00923.2014.

L. Chiari, G. Avanzolini, F. Grandi, and G. Gnudi. A simple model of the chemical regulation of acid-base balance in blood. In *Proceedings of 16th Annual International Conference of the IEEE Engineering in Medicine and Biology Society*, volume 2, pages 1025–1026. IEEE, 1994.

S. Choi, S. Yoon, J. Jeon, C. Zou, J. Choi, M. H. Tawhai, E. A. Hoffman, R. Delvadia, A. Babiskin, R. Walenga, et al. 1d network simulations for evaluating regional flow and pressure distributions in healthy and asthmatic human lungs. *Journal of Applied Physiology*, 127(1):122–133, 2019.

N. L. Christensen, J. Sørensen, K. Bouchelouche, M. A. Madsen, C. S. Buhl, and L. P. Tolbod. Repeatability of [15o] h2o pet imaging for lower extremity skeletal muscle perfusion: a test–retest study. *EJNMMI research*, 14(1):11, 2024. doi: https://doi.org/10.1186/s13550-024-01073-x.

T. G. Christensen and C. Dræby. *8. Respiration*, chapter 8, pages 197–247. doi: 10.1137/1.9780898718287.ch8. URL `https://epubs.siam.org/doi/abs/10.1137/1.9780898718287.ch8`.

D. Chung, S. Niranjan, J. Clark Jr, A. Bidani, W. Johnston, J. Zwischenberger, and D. Traber. A dynamic model of ventricular interaction and pericardial influence. *American Journal of Physiology-Heart and Circulatory Physiology*, 272(6):H2942–H2962, 1997.

V. Chuter, N. Schaper, J. Mills, R. Hinchliffe, D. Russell, N. Azuma, C.-A. Behrendt, E. J. Boyko, M. S. Conte, M. D. Humphries, et al. Effectiveness of revascularisation for the ulcerated foot in patients with diabetes and peripheral artery disease: A systematic review. *Diabetes/metabolism research and reviews*, 40(3):e3700, 2024. doi: https://doi.org/10.1002/dmrr.3700.

S. Cirovic, C. Walsh, and W. D. Fraser. A mathematical model of cerebral perfusion subjected to gz acceleration. *Aviation, space, and environmental medicine*, 71(5):514–521, 2000.

J. A. Claassen, D. H. Thijssen, R. B. Panerai, and F. M. Faraci. Regulation of cerebral blood flow in humans: physiology and clinical implications of autoregulation. *Physiological reviews*, 101(4):1487–1559, 2021.

G. Claessen, P. Claus, M. Delcroix, J. Bogaert, A. La Gerche, and H. Heidbuchel. Interaction between respiration and right versus left ventricular volumes at rest and during exercise: a real-time cardiac magnetic resonance study. *Am. J. Physiol. Heart Circ. Physiol.*, 306(6):H816–H824, 2014. doi: 10.1152/ajpheart.00752.2013.

R. L. Clain, S. Diot. A high-order finite volume method for systems of conservation laws-Multi-dimensional Optimal Order Detection (MOOD). *J. Comp. Phys.*, 230(10):4028–4050, 2011. doi: 10.1016/j.jcp.2011.02.026.

W. Cobb, J. Burns, K. Kercher, B. Matthews, H. Norton, and B. Heniford. Normal intraabdominal pressure in healthy adults. *J. Surg. Res.*, 129(2):231–235, 2005. doi: 10.1016/j.jss.2005.06.015.

C. Colombo, A. Siviglia, E. F. Toro, D. Bia, Y. Zócalo, and L. O. Müller. Tube law parametrization using in vitro data for one-dimensional blood flow in arteries and veins: Tube law parametrization in arteries and veins. *International Journal for Numerical Methods in Biomedical Engineering*, 40(4):e3803, 2024.

C. Colombo et al. Development of a multiscale 1d-0d cardiovascular model to investigate orthostatic stress responses. 2026.

J. Comroe, R. Foster, A. Dubois, W. Briscoe, and E. Carlsen. Alveolar ventilation. *Physiology of Respiration*, pages 8–21, 1977.

G. Comunale, F. Susin, and J. Mynard. A female-specific cardiovascular lumped-parameter model. *2020 42nt Annual International Conference of the IEEE EMBC*, 2020. doi: 10.1109/EMBC44109.2020.9175427.

C. Conway. Haemodynamic effects of pulmonary ventilation. *Br. J. Anaesth.*, 47:761–766, 1975.

J. Cooley and J. Tukey. An algorithm for the machine calculation of complex fourier series. *Math. Comput.*, 19:297–301, 1965.

J. Coote. Respiratory and circulatory control during sleep. *Journal of Experimental Biology*, 100(1):223–244, 1982.

C. Corsini, E. Cervi, F. Migliavacca, S. Schievano, H. Tain-Yen, and G. Pennati. Mathematical modelling of the maternal cardiovascular system in the three stages of pregnancy. *Medical Engineering & Physics*, 47:55–63, 2017. doi: 10.1016/j.medengphy.2017.06.025.

W. Cui, T. Wang, Z. Xu, J. Liu, S. Simakov, and F. Liang. A numerical study of the hemodynamic behavior and gas transport in cardiovascular systems with severe cardiac or cardiopulmonary failure supported by venoarterial extracorporeal membrane oxygenation. *Frontiers in Bioengineering and Biotechnology*, 11:1177325, 2023.

J. Cushway, L. Murphy, J. G. Chase, G. M. Shaw, and T. Desaive. Modelling patient specific cardiopulmonary interactions. *Computers in Biology and Medicine*, 151:106235, 2022.

J. Cushway, L. Murphy, J. G. Chase, G. Shaw, T. Desaive, and C. Zhou. Model based care in the icu: A review of potential combined cardio-pulmonary models. *Plos one*, 19(10): e0306925, 2024.

G. Dal Maso, P. G. Le Floch, and F. Murat. Definition and weak stability of nonconservative products. *J. Math. Pure Appl.*, 74(6):483–548, 1995.

C. Dalmaso, P. J. Blanco, and L. O. Müller. Cardiopulmonary mechanical interactions. insights from an anatomically detailed arterial-venous network model: C. dalmaso et al. *Biomechanics and Modeling in Mechanobiology*, 24(5):1653–1686, 2025a.

C. Dalmaso, F. E. Fossan, A. T. Bråten, and L. O. Müller. Uncertainty quantification and sensitivity analysis for non-invasive model-based instantaneous wave-free ratio prediction. *International Journal for Numerical Methods in Biomedical Engineering*, 41(1): e3898, 2025b.

M. d. B. Daly. Interactions between arterial chemoreceptors and other inputs. In *Peripheral Arterial Chemoreceptors and Respiratory-Cardiovascular Integration*. Oxford University Press, 02 1997. ISBN 9780198576754. doi: 10.1093/oso/9780198576754.003.0015. URL `https://doi.org/10.1093/oso/9780198576754.003.0015`.

A. Das, M. Haque, M. Chikhani, W. Wang, T. Ali, O. Cole, J. G. Hardman, and D. G. Bates. Development of an integrated model of cardiovascular and pulmonary physiology for the evaluation of mechanical ventilation strategies. In *2015 37th Annual International Conference of the IEEE Engineering in Medicine and Biology Society (EMBC)*, pages 5319–5322. IEEE, 2015.

R. De Vecchis, C. Baldi, G. Giandomenico, M. Di Maio, A. Giasi, and C. Cioppa. Estimating right atrial pressure using ultrasounds: An old issue revisited with new methods. *J. Clin. Med. Res.*, 8(8):569–574, 2016. doi: 10.14740/jocmr2617w.

O. Delestre and P.-Y. Lagrée. A well-balanced finite volume scheme for blood flow simulation. *Int. J. Numer. Meth. Fl.*, 72(2):177–205, 2013. doi: 10.1002/fld.3736.

M. Di Rienzo, G. Parati, A. Radaelli, and P. Castiglioni. Baroreflex contribution to blood pressure and heart rate oscillations: time scales, time-variant characteristics and nonlinearities. *Philosophical Transactions of the Royal Society A: Mathematical, Physical and Engineering Sciences*, 367(1892):1301–1318, 2009.

G. Diamond, J. S. Forrester, J. Hargis, W. W. Parmley, R. Danzig, and H. Swan. Dlastolic pressure-volume relationship in the canine left ventricle. *Circulation Research*, 29(3): 267–275, 1971.

D. Didebotham. *Cardiothoracic critical care*. Butterworth-Heinemann, Philadelphia, 2017.

J. M. Downing and D. N. Ku. Effects of frictional losses and pulsatile flow on the collapse of stenotic arteries. *Journal of Biomechanical Engineering*, 119(3):317–324, 08 1997. ISSN 0148-0731. doi: 10.1115/1.2796096. URL `https://doi.org/10.1115/1.2796096`.

D. D'Souza, T. Walizai, and P. O'Shea. Brain arterial vascular territories. URL `https://radiopaedia.org/articles/brain-arterial-vascular-territories`. Last accessed 14 Apr 2026.

M. Dumbser and E. F. Toro. A simple extension of the osher riemann solver to non-conservative hyperbolic systems. *Journal of Scientific Computing*, 48(1):70–88, 2011a. doi: https://doi.org/10.1007/s10915-010-9400-3.

M. Dumbser and E. F. Toro. On universal osher-type schemes for general nonlinear hyperbolic conservation laws. *Communications in Computational Physics*, 10(3):635–671, 2011b. doi: https://doi.org/10.4208/cicp.170610.021210a.

M. Dumbser, C. Enaux, and E. F. Toro. Finite volume schemes of very high order of accuracy for stiff hyperbolic balance laws. *J. Comput. Phys.*, 227:3971–4001, 2008. doi: 10.1016/j.jcp.2007.12.005.

J. V. Durnin and J. Womersley. Body fat assessed from total body density and its estimation from skinfold thickness: measurements on 481 men and women aged from 16 to 72 years. *British journal of nutrition*, 32(1):77–97, 1974.

V. G. Eck, W. P. Donders, J. Sturdy, J. Feinberg, T. Delhaas, L. R. Hellevik, and W. Huberts. A guide to uncertainty quantification and sensitivity analysis for cardiovascular applications. *International journal for numerical methods in biomedical engineering*, 32 (8):e02755, 2016. doi: https://doi.org/10.1002/cnm.2755.

S. Erturk, T. Ichikawa, H. Sou, T. Tsukamoto, U. Motosugi, and T. Araki. Effect of duration of contrast material injection on peak enhancement times and values of the aorta, main portal vein, and liver at dynamic mdct with the dose of contrast medium tailored to patient weight. *Clinical radiology*, 63(3):263–271, 2008.

J. Evans. *Crash Course Cardiovascular System Updated, Fourth Edition*. Elsevier, 2015.

M. M. Faghih and M. K. Sharp. Is bulk flow plausible in perivascular, paravascular and paravenous channels? *Fluids and Barriers of the CNS*, 15(1):17, 2018.

C. Fang, G. Zhu, S. Su, L. Zhu, Y. Peng, P. Chen, Y. Zhuo, L. Xu, X. Yang, and B. Li. A new precise way to guide the debridement process of diabetic foot ulcer using indocyanine green fluorescence molecular imaging. *Photodiagnosis and Photodynamic Therapy*, 40: 103095, 2022. doi: https://doi.org/10.1016/j.pdpdt.2022.103095.

F. Feihl and A. Broccard. Interactions between respiration and systemic hemodynamics. part ii: practical implications in critical care. *Intensive Care Med.*, 35:198–205, 2009. doi: 10.1007/s00134-008-1298-y.

L. Fernandes, P. Trenhago, R. Feijóo, and P. Blanco. Integrated cardiorespiratory system model with short timescale control mechanisms. *Int. J. Numer. Meth. Biomed. Eng.*, 37 (11):e3332, 2021. doi: 10.1002/cnm.3332.

E. G. Fernández, M. C. Díaz, M. Dumbser, and T. M. De Luna. An arbitrary high order well-balanced ADER-DG numerical scheme for the multilayer shallow-water model with variable density. *J. Sci. Comp.*, 90(1):52, 2022. doi: 10.1007/s10915-021-01734-2.

A. M. Fischer, J. A. Decker, J. Schoepf, A. Varga-Szemes, T. Flohr, B. Schmidt, R. Gutjahr, P. Sahbaee, D. A. Giovagnoli, T. Emrich, et al. Optimization of contrast material administration for coronary ct angiography using a software-based test-bolus evaluation algorithm. *The British Journal of Radiology*, 95(1133):20201456, 2022.

J. E. Flaherty, J. B. Keller, and S. Rubinow. Post buckling behavior of elastic tubes and rings with opposite sides in contact. *SIAM Journal on Applied Mathematics*, 23(4): 446–455, 1972. doi: https://doi.org/10.1137/0123047.

M. Fois, S. V. Maule, M. Giudici, M. Valente, L. Ridolfi, and S. Scarsoglio. Cardiovascular response to posture changes: Multiscale modeling and in vivo validation during head-up tilt. *Front. Physiol.*, 13:826989, 2022. doi: 10.3389/fphys.2022.826989.

M. Ford, A. Alperin, A. Lee, D. Holdsworth, and D. Steinman. Characterization of volumetric flow rate waveforms in the normal internal carotid and vertebral arteries. *Physiol. Meas.*, 26:477–488, 2005. doi: 10.1088/0967-3334/26/4/013.

L. Formaggia, D. Lamponi, and A. Quarteroni. One-dimensional models for blood flow in arteries. *Journal of engineering mathematics*, 47(3):251–276, 2003. doi: https://doi.org/10.1023/B:ENGI.0000007980.01347.29.

F. E. Fossan, J. Sturdy, L. O. Müller, A. Strand, A. T. Bråten, A. Jørgensen, R. Wiseth, and L. R. Hellevik. Uncertainty quantification and sensitivity analysis for computational ffr estimation in stable coronary artery disease. *Cardiovascular engineering and technology*, 9(4):597–622, 2018. doi: https://doi.org/10.1007/s13239-018-00388-w.

N. Fowler. *Cardiac Diagnosis and Treatment*. Harper & Row, 1980.

C. J. François, S. M. Shors, R. O. Bonow, and J. P. Finn. Analysis of cardiopulmonary transit times at contrast material–enhanced mr imaging in patients with heart disease. *Radiology*, 227(2):447–452, 2003.

L. Fresiello, B. Meyns, A. Di Molfetta, and G. Ferrari. A model of the cardiorespiratory response to aerobic exercise in healthy and heart failure conditions. *Frontiers in Physiology*, 7:189, 2016.

Q. Fu and S. Ogoh. Sex differences in baroreflex function in health and disease. *The Journal of Physiological Sciences*, 69(6):851–859, 2019.

E. Gaburro, M. J. Castro, and M. Dumbser. Well-balanced Arbitrary-Lagrangian-Eulerian finite volume schemes on moving nonconforming meshes for the Euler equations of gas dynamics with gravity. *Mon. Not. R. Astro. Soc.*, 477(2):2251–2275, 2018. doi: 10.1093/mnras/sty542.

A. Gabutti, L. Spicuzza, C. Porta, and L. Bernardi. Functions and changes of chemoreflex in physiological and pathological conditions. *Recenti Progressi in Medicina*, 92(7-8): 433–445, 2001.

A. Gatt, K. Cassar, O. Falzon, C. Ellul, K. P. Camilleri, J. Gauci, S. Mizzi, A. Mizzi, C. Sturgeon, N. Chockalingam, et al. The identification of higher forefoot temperatures associated with peripheral arterial disease in type 2 diabetes mellitus as detected by thermography. *Primary care diabetes*, 12(4):312–318, 2018. doi: https://doi.org/10.1016/j.pcd.2018.01.001.

X. Ge, Y. Liu, Z. Yin, S. Tu, Y. Fan, Y. Vassilevski, S. Simakov, and F. Liang. Comparison of instantaneous wave-free ratio (ifr) and fractional flow reserve (ffr) with respect to their sensitivities to cardiovascular factors: a computational model-based study. *Journal of interventional cardiology*, 2020, 2020. doi: https://doi.org/10.1155/2020/4094121.

B. Ghitti, C. Berthon, M. H. Le, and E. F. Toro. A fully well-balanced scheme for the 1D blood flow equations with friction source term. *J. Comput. Phys.*, 421:109750, 2020. doi: 10.1016/j.jcp.2020.109750.

P. G. Gibson, P. D. U. Guerrero, C. Poon, N. Rutherford, B. Brooker, A. Smith, C. Grainge, P. A. Wark, and V. M. McDonald. Ventilation heterogeneity is a treatable trait in severe asthma. *The Journal of Allergy and Clinical Immunology: In Practice*, 12(4):929–935, 2024.

E. Gilbert-Kawai and M. Wittenberg. *Essential Equations for Anaesthesia*. Cambridge University Press, 2014. doi: 10.1017/CBO9781139565387.043.

M. Giulioni and M. Ursino. Impact of cerebral perfusion pressure and autoregulation on intracranial dynamics: a modeling study. *Neurosurgery*, 39(5):1005–1015, 1996.

T. K. Goldstick, V. T. Ciuryla, and L. Zuckerman. Diffusion of oxygen in plasma and blood. In *Oxygen transport to tissue—ii*, pages 183–190. Springer, 1976.

C. Grandmont, C. Karamaoun, S. Martin, and F. Noël. Sensitivity and optimality analysis of breathing scenarios for 1d or 0d models of gas diffusion in the lung. *Journal of Theoretical Biology*, page 112235, 2025.

E. Grant, F. Rendano, E. Sevinc, J. Gammelgaard, H. Holm, and S. Gronvall. Normal inferior vena cava: Caliber changes observed by dynamic ultrasound. *American Journal of Roentgenology*, 135(2):335–338, 1980. doi: 10.2214/ajr.135.2.335.

F. S. Grodins. Integrative cardiovascular physiology: a mathematical synthesis of cardiac and blood vessel hemodynamics. *The Quarterly Review of Biology*, 34(2):93–116, 1959.

F. S. Grodins, J. S. Gray, K. R. Schroeder, A. L. Norins, and R. W. Jones. Respiratory responses to co2 inhalation. a theoretical study of a nonlinear biological regulator. *Journal of applied physiology*, 7(3):283–308, 1954.

G. Guerrero, V. Le Rolle, and A. Hernandez. Parametric analysis of an integrated model of cardio-respiratory interactions in adults in the context of obstructive sleep apnea. *Annals of biomedical engineering*, 49(12):3374–3387, 2021.

E. Guerrero Fernández, C. Escalante, and M. J. Castro Díaz. Well-balanced high-order discontinuous Galerkin methods for systems of balance laws. *Mathematics*, 10(1):15, 2022. doi: 10.3390/math10010015.

C. Guilleminault, A. Tilkian, and W. C. Dement. The sleep apnea syndromes. *Annual review of medicine*, 1976.

A. C. Guyton, T. G. Coleman, and H. J. Granger. Circulation: overall regulation. *Annual review of physiology*, 34(1):13–44, 1972.

J. E. Hall and M. E. Halle. *Text book of medical physiology*. Elsevier, 2020.

J. Halls, G. Bydawell, and U. Patel. Erectile dysfunction: the role of penile doppler ultrasound in diagnosis. *Abdominal imaging*, 34(6):712–725, 2009.

P. J. Hantzidiamantis and E. Amaro. Physiology, alveolar to arterial oxygen gradient, 2019. URL `https://www.ncbi.nlm.nih.gov/books/NBK545153/`. Last accessed 15 April 2026.

A. Harten. ENO schemes with subcell resolution. *J. Comp. Phys.*, 83(1):148–184, 1989. doi: 10.1016/0021-9991(89)90226-X.

N. Herring and D. J. Paterson. *Levick's introduction to cardiovascular physiology*. CRC Press, 2018.

M. H. Heusinkveld, W. Huberts, J. Lumens, T. Arts, T. Delhaas, and K. D. Reesink. Large vessels as a tree of transmission lines incorporated in the circadapt whole-heart model: A computational tool to examine heart-vessel interaction. *PLoS Computational Biology*, 15(7):e1007173, 2019.

M. Hirschhorn, E. Garven, J. Wells, R. Stevens, V. Tchantchaleishvili, and A. Throckmorton. The newly emerging field of pediatric engineering: Innovation for our next generation. *Artificial Organs*, 45(6), 2021. doi: 10.1111/aor.13973.

H. Holm, M. Magnusson, A. Jujic, E. Bozek, and N. Girerd. How to calculate ventricular–arterial coupling? *Eur. J. Heart Fail.*, 24(4):600–602, 2022. doi: 10.1002/ejhf.2456.

K. Houlind and J. Christensen. The role of the angiosome model in treatment of critical limb ischemia. In *Artery bypass*. IntechOpen, 2013. doi: https://doi.org/10.5772/54418.

Q.-M. Huang, H. Zhou, Y.-X. Ren, and Q. Wang. A general positivity-preserving algorithm for implicit high-order finite volume schemes solving the Euler and Navier-Stokes equations. *J. Comp. Phys.*, 508:112999, 2024. doi: 10.1016/j.jcp.2024.112999.

T. J. Hughes and J. Lubliner. On the one-dimensional theory of blood flow in the larger vessels. *Mathematical Biosciences*, 18(1-2):161–170, 1973. doi: https://doi.org/10.1016/0025-5564(73)90027-8.

J. C. Jentzer, B. Schrage, P. C. Patel, K. B. Kashani, G. W. Barsness, D. R. Holmes Jr, S. Blankenberg, P. Kirchhof, and D. Westermann. Association between the acidemia, lactic acidosis, and shock severity with outcomes in patients with cardiogenic shock. *Journal of the American Heart Association*, 11(9):e024932, 2022.

A. Joseph, D. Voit, and J. Frahm. Inferior vena cava revisited – real-time flow mri of respiratory maneuvers. *NMR in Biomedicine*, 33(4):e4232, 2020. doi: 10.1002/nbm.4232.

M. Jozwiak and J. Teboul. Heart–lungs interactions: the basics and clinical implications. *Ann. Intensive Care*, 14(122), 2024. doi: 10.1186/s13613-024-01356-5.

P. Kam and I. Power. *Principles of Physiology for the Anaesthetist*. CRC Press, 2020.

K. Kamra, Z. Xia, I. H. Zucker, H. Schultz, and H.-J. Wang. Chemoreflex function in pulmonary diseases–a review. *The Journal of Physiology*, 603(16):4461–4482, 2025.

T. Kara, K. Narkiewicz, and V. Somers. Chemoreflexes–physiology and clinical implications. *Acta Physiologica Scandinavica*, 177(3):377–384, 2003.

N. Karamolegkos, A. Albanese, and N. W. Chbat. Heart-lung interactions during mechanical ventilation: analysis via a cardiopulmonary simulation model. *IEEE Open Journal of Engineering in Medicine and Biology*, 2:324–341, 2021.

D. Kaye, S. J. Shah, B. A. Borlaug, F. Gustafsson, J. Komtebedde, S. Kubo, C. Magnin, M. S. Maurer, T. Feldman, and D. Burkhoff. Effects of an interatrial shunt on rest and exercise hemodynamics: results of a computer simulation in heart failure. *Journal of cardiac failure*, 20(3):212–221, 2014.

A. Khir, A. O'brien, J. Gibbs, and K. Parker. Determination of wave speed and wave separation in the arteries. *Journal of biomechanics*, 34(9):1145–1155, 2001.

K. G. Kim, D. H. Meshkin, A. R. Tirrell, J. C. Bekeny, E. A. Tefera, K. L. Fan, C. M. Akbari, and K. K. Evans. A systematic review and meta-analysis of endovascular angiosomal revascularization in the setting of collateral vessels. *Journal of vascular surgery*, 74(4):1406–1416, 2021. doi: https://doi.org/10.1016/j.jvs.2021.04.026.

M. Kim and S. Cirovic. A computational model of the cerebrospinal fluid system incorporating lumped-parameter cranial compartment and one-dimensional distributed spinal compartment. *Journal of biorheology*, 25(1):78–87, 2011.

B. Kimura, R. Dalugdugan, G. Gilcrease, J. Phan, B. Showalter, and T. Wolfson. The effect of breathing manner on inferior vena caval diameter. *European Journal of Echocardiography*, 12(2):120–123, 2010. doi: 10.1093/ejechocard/jeq157.

V. B. Kolachalama, N. W. Bressloff, P. B. Nair, and C. P. Shearman. Predictive haemodynamics in a one-dimensional human carotid artery bifurcation. part i: Application to stent design. *IEEE Transactions on Biomedical Engineering*, 54(5):802–812, 2007.

J. Kollmeier, L. Gürbüz-Reiss, P. Sahoo, S. Badura, B. Ellebracht, M. Keck, J. Gärtner, H. Ludwig, J. Frahm, and S. Dreha-Kulaczewski. Deep breathing couples csf and venous flow dynamics. *Sci. Rep.*, 12(2568), 2022. doi: 10.1038/s41598-022-06361-x.

S. Kovalova, J. Necas, and J. Vespalec. What is a "normal" right ventricle? *Eur. Heart J. Cardiovasc. Imaging*, 7(4):293–297, 2006. doi: 10.1016/j.euje.2005.06.010.

J. Kung-Ming. Physiology g6001 (graduate), chapter 5 (regional circulation), 2026. URL `https://www.columbia.edu/~kj3/Chapter5.htm`. Last accessed 01 March 2026.

R. Kuzo, R. Pooley, J. Crook, M. Heckman, and T. Gerber. Measurement of caval blood flow with mri during respiratory maneuvers: Implications for vascular contrast opacification on pulmonary ct angiographic studies. *American Journal of Roentgenology*, 188 (3):839–842, 2007. doi: 10.2214/AJR.06.5035.

M. Laganà, M. Di Rienzo, F. Rizzo, C. Ricci, S. D'Onofrio, L. Forzoni, and P. Cecconi. Cardiac, respiratory and postural influences on venous return of internal jugular and vertebral veins. *J. Ultras. Med. Bio.*, 43(10):1195–1204, 2017. doi: 10.1016/j.ultrasmedbio.2017.02.007.

M. Laganà, S. Di Tella, F. Ferrari, L. Pelizzari, M. Cazzoli, N. Alperin, D. Zavà, G. Baselli, and F. Baglio. Blood and cerebrospinal fluid flow oscillations measured with real-time phase-contrast mri: breathing mode matters. *Fluids Barriers CNS*, 29(100), 2022a. doi: 10.1186/s12987-022-00394-0.

M. Laganà, A. Piastru, F. Ferrari, S. Di Tella, M. Cazzoli, L. Pelizzari, N. Jin, D. Zacà, N. Alperin, G. Baselli, and F. Baglio. Cardiac and respiratory influences on intracranial and neck venous flow, estimated using real-time phase-contrast mri. *Biosensors*, 12(8): 612, 2022b. doi: 10.3390/bios12080612.

P. A. Lanfranchi and V. K. Somers. Arterial baroreflex function and cardiovascular variability: interactions and implications. *American Journal of Physiology-Regulatory, Integrative and Comparative Physiology*, 283(4):R815–R826, 2002.

G. Langewouters, K. Wesseling, and W. Goedhard. The static elastic properties of 45 human thoracic and 20 abdominal aortas in vitro and the parameters of a new model. *Journal of biomechanics*, 17(6):425–435, 1984. doi: https://doi.org/10.1016/0021-9290(84)90034-4.

N. A. Lassen. Cerebral blood flow and oxygen consumption in man. *Physiological reviews*, 39(2):183–238, 1959.

B. M. Laudenzi, A. Cucino, S. Lassola, E. Balzani, and L. O. Müller. Predicting in-hospital indicators from wearable-derived signals for cardiovascular and respiratory disease monitoring: an in silico study. *PLOS Digital Health*, 4(10):e0001041, 2025a.

B. M. Laudenzi, C. Dalmaso, and L. O. Muller. Cardio-respiratory-model, Sept. 2025b. URL `https://doi.org/10.5281/zenodo.17222758`.

C. Leithner, K. Gertz, H. Schröck, J. Priller, K. Prass, J. Steinbrink, A. Villringer, M. Endres, U. Lindauer, U. Dirnagl, et al. A flow sensitive alternating inversion recovery (fair)-mri protocol to measure hemispheric cerebral blood flow in a mouse stroke model. *Experimental neurology*, 210(1):118–127, 2008. doi: https://doi.org/10.1016/j.expneurol.2007.10.003.

C. Li and H. Cheng. A nonlinear fluid model for pulmonary blood circulation. *Journal of biomechanics*, 26(6):653–664, 1993.

G. Li, O. Delestre, and L. Yuan. Well-balanced discontinuous Galerkin method and finite volume WENO scheme based on hydrostatic reconstruction for blood flow model in arteries. *Int. J. Numer. Meth. Fl.*, 86(7):491–508, 2018. doi: 10.1002/fld.4463.

R. Li, K. Sughimoto, X. Zhang, S. Wang, Y. Hiraki, and H. Liu. Impact of respiratory fluctuation on hemodynamics in human cardiovascular system: A 0-1d multiscale model. *Fluids*, 7(1):28, 2022.

R. Li, K. Sughimoto, X. Zhang, S. Wang, and H. Liu. Impacts of respiratory fluctuations on cerebral circulation: a machine-learning-integrated 0–1d multiscale hemodynamic model. *Physiological Measurement*, 44(3):035013, 2023.

Y. Li, H. Gu, H. Fok, J. Alastruey, and P. Chowienczyk. Forward and backward pressure waveform morphology in hypertension. *Hypertension*, 69(2):375–381, 2017.

F. Liang, S. Takagi, R. Himeno, and H. Liu. Multi-scale modeling of the human cardiovascular system with applications to aortic valvular and arterial stenoses. *Med. Biol. Eng. Comput.*, 47(7):743–755, 2009. doi: 10.1007/s11517-009-0449-9.

C. Liu, S. Niranjan, J. Clark Jr, K. San, J. Zwischenberger, and A. Bidani. Airway mechanics, gas exchange, and blood flow in a nonlinear model of the normal human lung. *Journal of applied physiology*, 84(4):1447–1469, 1998.

X.-D. Liu, S. Osher, and T. Chan. Weighted essentially non-oscillatory schemes. *J. Comput. Phys.*, 115(1):200–212, 1994. doi: 10.1006/jcph.1994.1187.

D. Lopez, A. W. Pollak, C. H. Meyer, F. H. Epstein, L. Zhao, A. J. Pesch, R. Jiji, J. R. Kay, J. M. DiMaria, J. M. Christopher, et al. Arterial spin labeling perfusion cardiovascular magnetic resonance of the calf in peripheral arterial disease: cuff occlusion hyperemia vs exercise. *Journal of Cardiovascular Magnetic Resonance*, 17(1):23, 2015. doi: https://doi.org/10.1186/s12968-015-0128-y.

M. Loukas, J. Hullett, and T. Wagner. Clinical anatomy of the inferior phrenic artery. *Clinical Anatomy: The Official Journal of the American Association of Clinical Anatomists and the British Association of Clinical Anatomists*, 18(5):357–365, 2005.

K. Lu, J. W. J. Clark, F. H. Ghorbel, D. L. Ware, and A. Bidani. A human cardiopulmonary system model applied to the analysis of the valsalva maneuver. *Am. J. Physiol. Heart Circ. Physiol.*, 281(6):H2661–H2679, 2001. doi: 10.1152/ajpheart.2001.281.6.H2661.

K. Lu, J. W. J. Clark, F. H. Ghorbel, D. L. Ware, J. B. Zwischenberger, and A. Bidani. Whole-body gas exchange in human predicted by a cardiopulmonary model. *Cardiovasc. Eng.*, 3:1–19, 2003. doi: 10.1023/A:1024795417999.

K. Lu, J. W. J. Clark, F. H. Ghorbel, C. S. Robertson, D. L. Ware, J. B. Zwischenberger, and A. Bidani. Cerebral autoregulation and gas exchange studied using a human cardiopulmonary model. *Am. J. Physiol. Heart Circ. Physiol.*, 286(2):H584–H601, 2004. doi: 10.1152/ajpheart.00594.2003.

B. Lukitsch, R. Koller, P. Ecker, M. Elenkov, C. Janeczek, M. Pekovits, B. Haddadi, C. Jordan, M. Gfoehler, and M. Harasek. Water as a blood model for determination of co2 removal performance of membrane oxygenators. *Membranes*, 11(5):356, 2021.

A. Maceira, C.-S. J., M. Roughton, S. Prasad, and D. Pennell. Reference left atrial dimensions and volumes by steady state free precession cardiovascular magnetic resonance. *J. Cardiovasc. Magn. Reson.*, 12(65), 2010. doi: 10.1186/1532-429X-12-65.

A. Maceira, C.-S. J., M. Roughton, S. Prasad, and D. Pennell. Reference right atrial dimensions and volume estimation by steady state free precession cardiovascular magnetic resonance. *J. Cardiovasc. Magn. Reson.*, 15(29), 2013. doi: 10.1186/1532-429X-15-29.

S. Magder. Heart-lung interaction in spontaneous breathing subjects: the basics. *Ann. Transl. Med.*, 6(18), 2018. doi: 10.21037/atm.2018.06.19.

E. Magosso and M. Ursino. A mathematical model of co2 effect on cardiovascular regulation. *American Journal of Physiology-Heart and Circulatory Physiology*, 281(5):H2036–H2052, 2001.

E. Magosso and M. Ursino. Cardiovascular response to dynamic aerobic exercise: A methematical model. *Medical and Biological Engineering and Computing*, 40(6):660–674, 2002.

M. Malbrain, Y. Peeters, and R. Wise. The neglected role of abdominal compliance in organ-organ interactions. *Crit. Care*, 20(67), 2016. doi: 10.1186/s13054-016-1220-x.

B. A. Martin, P. Reymond, J. Novy, O. Balédent, and N. Stergiopulos. A coupled hydrodynamic model of the cardiovascular and cerebrospinal fluid system. *American Journal of Physiology-Heart and Circulatory Physiology*, 302(7):H1492–H1509, 2012.

F. K. McConnell and S. Payne. The dual role of cerebral autoregulation and collateral flow in the circle of willis after major vessel occlusion. *IEEE Transactions on Biomedical Engineering*, 64(8):1793–1802, 2016.

C. McEniery, Yasmin, I. Hall, A. Qasem, I. Wilkinson, J. Cockcroft, and I. ACCT. Normal vascular aging: differential effects on wave reflection and aortic pulse wave velocity: the anglo-cardiff collaborative trial (acct). *J. Am. Coll. Cardiol.*, 46(9):1753–1760, 2005. doi: 10.1016/j.jacc.2005.07.037.

W. T. McGee and T. Franco-McKinney. Cardiopulmonary care.

J. Mecklenburgh and W. Mapleson. Ventilatory assistance and respiratory muscle activity. 2: Simulation with an adaptive active ("aa" or "a-squared") model lung. *British journal of anaesthesia*, 80(4):434–439, 1998.

R. Meertens, K. M. Knapp, W. D. Strain, F. Casanova, S. Ball, J. Fulford, and C. Thorn. In vivo measurement of intraosseous vascular haemodynamic markers in human bone tissue utilising near infrared spectroscopy. *Frontiers in Physiology*, 12:738239, 2021. doi: https://doi.org/10.3389/fphys.2021.738239.

P. Mohammadyari, G. Gadda, and A. Taibi. Modelling physiology of haemodynamic adaptation in short-term microgravity exposure and orthostatic stress on earth. *Scientific reports*, 11(1):4672, 2021.

K. Molokoane-Mokgoro, L. Goldstein, and M. Wells. Ultrasound evaluation of the respiratory changes of the inferior vena cava and axillary vein diameter at rest and during positive pressure ventilation in spontaneously breathing healthy volunteers. *Emerg. Med. J.*, 35(5):297–302, 2018. doi: 10.1136/emermed-2016-205944.

G. Montecinos, L. Müller, and E. Toro. Hyperbolic reformulation of a 1d viscoelastic blood flow model and ader finite volume schemes. *J. Comp. Phys.*, 266:101–123, 2014. doi: 10.1016/j.jcp.2014.02.013.

G. I. Montecinos, E. F. Toro, and L. O. Müller. A generalized Riemann problem-based compact reconstruction method for finite volume schemes. *Comput. Fluids*, page Submitted, 2025.

J. E. Moore, J. W. Cerne, A. Pathrose, M. Veer, R. Sarnari, A. Ragin, J. C. Carr, and M. Markl. Quantitative assessment of regional pulmonary transit times in pulmonary hypertension. *Journal of Magnetic Resonance Imaging*, 57(3):727–737, 2023.

D. Morley, K. Litwak, P. Ferber, P. Spence, R. Dowling, B. Meyns, B. Griffith, and D. Burkhoff. Hemodynamic effects of partial ventricular support in chronic heart failure: results of simulation validated with in vivo data. *The Journal of thoracic and cardiovascular surgery*, 133(1):21–28, 2007.

L. O. Müller and P. J. Blanco. A high order approximation of hyperbolic conservation laws in networks: Application to one-dimensional blood flow. *J. Comp. Phys.*, 300:423–437, 2015. doi: 10.1016/j.jcp.2015.07.056.

L. O. Müller and E. F. Toro. Enhanced global mathematical model for studying cerebral venous blood flow. *Journal of biomechanics*, 47(13):3361–3372, 2014.

L. O. Müller, C. Parés, and E. F. Toro. Well-balanced high-order numerical schemes for one-dimensional blood flow in vessels with varying mechanical properties. *Journal of computational physics*, 242:53–85, 2013. doi: https://doi.org/10.1016/j.jcp.2013.01.050.

L. O. Müller, P. J. Blanco, S. M. Watanabe, and R. A. Feijóo. A high-order local time stepping finite volume solver for one-dimensional blood flow simulations: application to the adan model. *International Journal for Numerical Methods in Biomedical Engineering*, 32(10):e02761, 2016. doi: https://doi.org/10.1002/cnm.2761.

L. O. Müller, F. E. Fossan, A. T. Bråten, A. Jørgensen, R. Wiseth, and L. R. Hellevik. Impact of baseline coronary flow and its distribution on fractional flow reserve prediction. *International journal for numerical methods in biomedical engineering*, 37(11):e3246, 2021. doi: https://doi.org/10.1002/cnm.3246.

J. Murillo and P. Garcia-Navarro. A Roe type energy balanced solver for 1D arterial blood flow and transport. *Comput. Fluids*, 117:149–167, 2015. doi: 10.1016/j.compfluid.2015.05.003.

J. Murillo and P. Garcia-Navarro. Numerical coupling of 0D and 1D models in networks of vessels including transonic flow conditions. Application to short-term transient and stationary hemodynamic simulation of postural changes. *Int. J. Numer. Method Biomed. Eng.*, 39(11):e3751, 2023. doi: 10.1002/cnm.3751.

J. Murillo, A. Navas-Mantilla, and P. Garcia-Navarro. Formulation of exactly balanced solvers for blood flow in elastic vessels and their application to collapsed states. *Comput. Fluids*, 186:74–98, 2019. doi: 10.1016/j.compfluid.2019.04.008.

J. Mynard and J. Smolich. One-dimensional haemodynamic modeling and wave dynamics in the entire adult circulation. *Ann. Biomed. Eng.*, 43:1443–1460, 2015a. doi: 10.1007/s10439-015-1313-8.

J. Mynard and J. Smolich. Novel wave power analysis linking pressure-flow waves, wave potential, and the forward and backward components of hydraulic power. *Am. J. Physiol. Heart Circ. Physiol.*, 310(8):H1026–H1038, 2016. doi: 10.1152/ajpheart.00954.2015.

J. Mynard, M. Davidson, D. Penny, and J. Smolich. A simple, versatile valve model for use in lumped parameter and one-dimensional cardiovascular models. *Int. J. Numer. Meth. Biomed. Eng.*, 28(6-7):626–641, 2012a. doi: 10.1002/cnm.1466.

J. Mynard, M. Davidson, D. Penny, and J. Smolich. Non-linear separation of pressure, velocity and wave intensity into forward and backward components. *Med. Biol. Eng. Comput.*, 50:641–648, 2012b. doi: 10.1007/s11517-012-0897-5.

J. Mynard, D. Penny, and J. Smolich. Scalability and in vivo validation of a multiscale numerical model of the left coronary circulation. *Am. J. Physiol.*, 306(4):H517–H528, 2014. doi: 10.1152/ajpheart.00603.2013.

J. P. Mynard and J. J. Smolich. One-dimensional haemodynamic modeling and wave dynamics in the entire adult circulation. *Annals of biomedical engineering*, 43(6):1443–1460, 2015b.

L. Müller and E. Toro. Well-balanced high-order solver for blood flow in networks of vessels with variable properties. *Int. J. Numer. Meth. Biomed. Eng.*, 29(12):1388–1411, 2013. doi: 10.1002/cnm.2580.

L. Müller and E. Toro. A global multiscale mathematical model for the human circulation with emphasis on the venous system. *Int. J. Numer. Meth. Biomed. Eng.*, 30(7):681–725, 2014. doi: 10.1002/cnm.2622.

L. Müller, P. Blanco, S. Watanabe, and R. Feijóo. A high-order local time stepping finite volume solver for one-dimensional blood flow simulations: application to the adan model. *Int. J. Numer. Meth. Biomed. Eng.*, 32(10):e02761, 2016a. doi: 10.1002/cnm.2761.

L. Müller, G. Leugering, and P. Blanco. Consistent treatment of viscoelastic effects at junctions in one-dimensional blood flow models. *J. Comp. Phys.*, 314:167–193, 2016b. doi: 10.1016/j.jcp.2016.03.012.

L. Müller, S. Watanabe, E. Toro, R. Feijóo, and P. Blanco. An anatomically detailed arterial-venous network model. cerebral and coronary circulation. *Front. Physiol.*, 14: 1162391, 2023. doi: 10.3389/fphys.2023.1162391.

K. Nakamura, K. Quian, T. Ando, R. Inokuchi, K. Doi, E. Kobayashi, I. Sakuma, S. Nakajima, and N. Yahagi. Cardiac variation of internal jugular vein for the evaluation of hemodynamics. *Ultrasound Med. Biol.*, 42(8):1764–1770, 2016. doi: 10.1016/j.ultrasmedbio.2016.03.003.

R. F. Neville, C. E. Attinger, E. J. Bulan, I. Ducic, M. Thomassen, and A. N. Sidawy. Revascularization of a specific angiosome for limb salvage: does the target artery matter? *Annals of vascular surgery*, 23(3):367–373, 2009. doi: https://doi.org/10.1016/j.avsg.2008.08.022.

A. Noordergraaf, P. D. Verdouw, and H. B. Boom. The use of an analog computer in a circulation model. *Progress in Cardiovascular Diseases*, 5(5):419–439, 1963.

L. Norgren, W. R. Hiatt, J. A. Dormandy, M. R. Nehler, K. A. Harris, F. G. R. Fowkes, T. I. W. Group, et al. Inter-society consensus for the management of peripheral arterial disease (tasc ii). *Journal of vascular surgery*, 45(1):S5–S67, 2007. doi: https://doi.org/10.1016/j.jvs.2006.12.037.

J. B. Olansen, J. Clark, D. Khoury, F. Ghorbel, and A. Bidani. A closed-loop model of the canine cardiovascular system that includes ventricular interaction. *Computers and biomedical research*, 33(4):260–295, 2000.

T. Osada, T. Katsumura, T. Hamaoka, N. Murase, M. Naka, and T. Shimomitsu. Quantitative effects of respiration on venous return during single knee extension-flexion. *Int. J. Sports Med.*, 23(3), 2002. doi: 10.1055/s-2002-23177.

J. T. Ottesen, M. S. Olufsen, and J. K. Larsen. *Applied mathematical models in human physiology*. SIAM, 2004.

L. M. Palena, L. F. Garcia, C. Brigato, E. Sultato, A. Candeo, T. Baccaglini, and M. Manzi. Angiosomes: how do they affect my treatment? *Techniques in Vascular and Interventional Radiology*, 17(3):155–169, 2014.

C. Parés. Numerical methods for nonconservative hyperbolic systems: a theoretical framework. *SIAM Journal on Numerical Analysis*, 44(1):300–321, 2006. doi: https://doi.org/10.1137/050628052.

C. Parés and M. Muñoz Ruíz. On some difficulties of the numerical approximation of nonconservative hyperbolic systems. *Boletın SEMA*, 47:23–52, 2009.

H. Patel, T. Miyoshi, K. Addetia, M. Henry, R. Citro, M. Daimon, P. Fajardo, R. Kasliwal, J. Kirkpatrick, M. Monaghan, D. Muraru, K. Ogunyakin, S. Park, R. Ronderos, A. Sadeghpour, G. Scalia, M. Takeuchi, W. Tsang, E. Tucay, A. Rodrigues, and J. Hwang. Normal values of cardiac output and stroke volume according to measurement technique, age, sex, and ethnicity: Results of the world alliance of societies of echocardiography study. *J. Am. Soc. Echocardiogr.*, 34(10):1077–1085.e, 2021. doi: 10.1016/j.echo.2021.05.012.

M. Patel, L. Berman, H. Moss, and S. McPherson. Subclavian and internal jugular veins at doppler us: abnormal cardiac pulsatility and respiratory phasicity as a predictor of

complete central occlusion. *Radiology*, 211(2):579–583, 1999. doi: 10.1148/radiology.211.2.r99ma08579.

N. Patel and K. Patel. Estimation of pulmonary gas exchange in the human respiratory system under normal and abnormal conditions. *Biosciences Biotechnology Research Asia*, 20(1):255–262, 2023.

O. B. Paulson, J. Olesen, and M. S. Christensen. Restoration of autoregulation of cerebral blood flow by hypocapnia. *Neurology*, 22(3):286–286, 1972.

S. Payne. *Cerebral autoregulation: control of blood flow in the brain*, volume 15. Springer, 2016.

T. Pedley. Wave phenomena in physiological flows. *IMA journal of applied mathematics*, 32(1-3):267–287, 1984.

J. Peiró and A. Veneziani. Reduced models of the cardiovascular system. In *Cardiovascular Mathematics: Modeling and simulation of the circulatory system*, pages 347–394. Springer, 2009.

N. Petrova, A. Whittam, A. MacDonald, S. Ainarkar, A. Donaldson, J. Bevans, J. Allen, P. Plassmann, B. Kluwe, F. Ring, et al. Reliability of a novel thermal imaging system for temperature assessment of healthy feet. *Journal of foot and ankle research*, 11(1):22, 2018. doi: https://doi.org/10.1186/s13047-018-0266-1.

M. I. Popitiu, V. A. Alexandrescu, G. Clerici, S. Ionac, G. Gavrila-Ardelean, M. G. Ion, and M. E. Ionac. Angiosome-targeted infrapopliteal angioplasty: Impact on clinical outcomes—an observational study. *Journal of Clinical Medicine*, 13(3):883, 2024.

J. Prazma, S. G. Vance, and G. Rodgers. Measurement of cochlear blood flow—new technique. *Hearing research*, 14(1):21–28, 1984.

M. Ragosta and J. Kennedy. Normal waveforms, artifacts and pitfalls. In M. Ragosta, editor, *Textbook of Clinical Hemodynamics, 2nd Edition*, pages 17–33. Elsevier Health Sciences, 2017.

M. Raichle and H. Stone. Cerebral blood flow autoregulation and graded hypercapnia. *European neurology*, 6(1-6):1–5, 1971.

J. Raikhelkar, P. J. Papadakos, and D. L. Reich. *Oxygen delivery, oxygen transport, and tissue oxygen tension: Critical monitoring in the ICU*, page 98–104. Cambridge University Press, 2011.

J. A. Reekers, M. J. Koelemay, H. A. Marquering, and E. T. van Bavel. Functional imaging of the foot with perfusion angiography in critical limb ischemia. *Cardiovascular and interventional radiology*, 39(2):183–189, 2016. doi: https://doi.org/10.1007/s00270-015-1253-6.

F. Regazzoni, M. Salvador, P. C. Africa, M. Fedele, L. Dedè, and A. Quarteroni. A cardiac electromechanical model coupled with a lumped-parameter model for closed-loop blood circulation. *Journal of Computational Physics*, 457:111083, 2022.

M. Reivich. Arterial pco2 and cerebral hemodynamics. *American Journal of Physiology-Legacy Content*, 206(1):25–35, 1964.

P. Reymond, F. Merenda, F. Perren, D. Rufenacht, and N. Stergiopulos. Validation of a one-dimensional model of the systemic arterial tree. *American Journal of Physiology-Heart and Circulatory Physiology*, 297(1):H208–H222, 2009.

R. Rosenberry and M. D. Nelson. Reactive hyperemia: a review of methods, mechanisms, and considerations. *American Journal of Physiology-Regulatory, Integrative and Comparative Physiology*, 318(3):R605–R618, 2020. doi: https://doi.org/10.1152/ajpregu.00339.2019.

C. J. Roth, L. Yoshihara, M. Ismail, and W. A. Wall. Computational modelling of the respiratory system: discussion of coupled modelling approaches and two recent extensions. *Computer Methods in Applied Mechanics and Engineering*, 314:473–493, 2017.

A. Ruesch, D. Acharya, S. Schmitt, J. Yang, M. A. Smith, and J. M. Kainerstorfer. Comparison of static and dynamic cerebral autoregulation under anesthesia influence in a controlled animal model. *PLoS One*, 16(1):e0245291, 2021.

J. Ryu, X. Hu, and S. C. Shadden. A coupled lumped-parameter and distributed network model for cerebral pulse-wave hemodynamics. *Journal of biomechanical engineering*, 137 (10):101009, 2015.

S. Safaei, C. P. Bradley, V. Suresh, K. Mithraratne, A. Muller, H. Ho, D. Ladd, L. R. Hellevik, S. W. Omholt, J. G. Chase, et al. Roadmap for cardiovascular circulation model. *The Journal of physiology*, 594(23):6909–6928, 2016.

S. Sakamoto, S. Takahashi, A. Coskun, M. Papafaklis, A. Takahashi, S. Saito, P. Stone, and C. Feldman. Relation of distribution of coronary blood flow volume to coronary artery dominance. *Am. J. Cardiol.*, 111(10):1420–1424, 2013. doi: 10.1016/j.amjcard.2013.01.290.

W. P. Santamore and D. Burkhoff. Hemodynamic consequences of ventricular interaction as assessed by model analysis. *American Journal of Physiology-Heart and Circulatory Physiology*, 260(1):H146–H157, 1991.

C. A. Sarmiento, A. M. Hernández, L. Y. Serna, and M. Á. Mañanas. An integrated mathematical model of the cardiovascular and respiratory response to exercise: model-building and comparison with reported models. *American Journal of Physiology-Heart and Circulatory Physiology*, 320(4):H1235–H1260, 2021.

F. Schäfer, D. E. Schiavazzi, L. R. Hellevik, and J. Sturdy. Global sensitivity analysis with multifidelity monte carlo and polynomial chaos expansion for vascular haemodynamics. *International Journal for Numerical Methods in Biomedical Engineering*, 40(8):e3836, 2024.

M. Segeroth, D. J. Winkel, I. Strebel, S. Yang, J. G. van der Stouwe, J. Formambuh, P. Badertscher, J. Cyriac, J. Wasserthal, F. Caobelli, et al. Pulmonary transit time of cardiovascular magnetic resonance perfusion scans for quantification of cardiopulmonary haemodynamics. *European Heart Journal-Cardiovascular Imaging*, 24(8):1062–1071, 2023.

L. Y. Serna, M. A. Mañanas, A. M. Hernández, and R. A. Rabinovich. An improved dynamic model for the respiratory response to exercise. *Frontiers in physiology*, 9:69, 2018.

A. H. Shapiro. Steady Flow in Collapsible Tubes. *Journal of Biomechanical Engineering*, 99(3):126–147, 08 1977. ISSN 0148-0731. doi: 10.1115/1.3426281. URL `https://doi.org/10.1115/1.3426281`.

S. Shimizu, D. Une, T. Kawada, Y. Hayama, A. Kamiya, T. Shishido, and M. Sugimachi. Lumped parameter model for hemodynamic simulation of congenital heart diseases. *The journal of physiological sciences*, 68(2):103–111, 2018.

O. Siggaard-Andersen, P. Wimberley, I. Göthgen, and M. Siggaard-Andersen. A mathematical model of the hemoglobin-oxygen dissociation curve of human blood and of the oxygen partial pressure as a function of temperature. *Clinical chemistry*, 30(10): 1646–1651, 1984.

S. Simakov, T. Gamilov, F. Y. Kopylov, and Y. V. Vasilevskii. Evaluation of hemodynamic significance of stenosis in multiple involvement of the coronary vessels by mathematical simulation. *Bulletin of experimental biology and medicine*, 162(1):111–114, 2016.

A. Siviglia, D. Vanzo, and E. F. Toro. A splitting scheme for the coupled Saint-Venant-Exner model. *Adv. Water Resour.*, 159:104062, 2022. doi: 10.1016/j.advwatres.2021.104062.

H. Smith, P. Grottum, and S. Simonsen. Ultrasonic assessment of abdominal venous return. *Acta Radiologica Diagnosis*, 26(5):581–588, 1985. doi: 10.1177/028418518502600514.

M. Snyder and V. Rideout. Computer simulation studies of the venous circulation. *IEEE Transactions on Biomedical Engineering*, (4):325–334, 1969.

J. Sommerset, R. Karmy-Jones, M. Dally, B. Feliciano, Y. Vea, and D. Teso. Plantar acceleration time: a novel technique to evaluate arterial flow to the foot. *Annals of vascular surgery*, 60:308–314, 2019. doi: https://doi.org/10.1016/j.avsg.2019.03.002.

P. Song, D. Rudan, Y. Zhu, F. Fowkes, K. Rahimi, F. G. R. Fowkes, and I. Rudan. Global, regional, and national prevalence and risk factors for peripheral artery disease in 2015: an updated systematic review and analysis. *Lancet Glob Health*, 7(8):E1020–E1030, 2019. doi: https://doi.org/10.1016/S2214-109X(19)30255-4.

D. d. A. Souza, P. V. F. Medrado, V. A. Santos, C. X. d. Aguiar, G. S. Silva, L. P. P. d. Sousa, Y. B. D. Amando, and P. F. Saad. Duplex ultrasound and pedal acceleration time as tools to evaluate foot perfusion: a literature review. *Jornal Vascular Brasileiro*, 23:e20230017, 2024. doi: https://doi.org/10.1590/1677-5449.202300172.

J. Spencer, E. Firouztale, and R. Mellins. Computational expressions for blood oxygen and carbon dioxide concentrations. *Annals of Biomedical Engineering*, 7(1):59–66, 1979.

A. Spilimbergo, E. F. Toro, L. O. Müller, et al. One-dimensional blood flow with discontinuous properties and transport: mathematical analysis and numerical schemes. *Commun. Comput. Phys.*, 2121(3):649–697, 2021. doi: 10.4208/cicp.OA-2020-0132.

A. Spilimbergo, E. F. Toro, L. O. Muller, et al. Exact solution of the riemann problem for the one-dimensional blood flow equations with general constant momentum correction coefficient. *Communications in Computational Physics*, 2024(3):711–780, 2024.

K. Špillerová, N. Settembre, F. Biancari, A. Albäck, and M. Venermo. Angiosome targeted pta is more important in endovascular revascularisation than in surgical revascularisation: analysis of 545 patients with ischaemic tissue lesions. *European Journal of Vascular and Endovascular Surgery*, 53(4):567–575, 2017. doi: https://doi.org/10.1016/j.ejvs.2017.01.008.

B. N. Steele, J. Wan, J. P. Ku, T. J. Hughes, and C. A. Taylor. In vivo validation of a one-dimensional finite-element method for predicting blood flow in cardiovascular bypass grafts. *IEEE Transactions on Biomedical Engineering*, 50(6):649–656, 2003. doi: https://doi.org/10.1109/TBME.2003.812201.

N. Stergiopulos, D. Young, and T. Rogge. Computer simulation of arterial flow with applications to arterial and aortic stenoses. *Journal of biomechanics*, 25(12):1477–1488, 1992.

J. Stettler, P. Niederer, and M. Anliker. Theoretical analysis of arterial hemodynamics including the influence of bifurcations: Part i: Mathematical model and prediction of normal pulse patterns. *Annals of biomedical engineering*, 9(2):145–164, 1981.

M. Strocchi, C. Contarino, Q. Zhang, R. Bonmassari, and E. F. Toro. A global mathematical model for the simulation of stenoses and bypass placement in the human arterial system. *Applied Mathematics and Computation*, 300:21–39, 2017.

M. Strocchi, S. Longobardi, C. M. Augustin, M. A. Gsell, A. Petras, C. A. Rinaldi, E. J. Vigmond, G. Plank, C. J. Oates, R. D. Wilkinson, et al. Cell to whole organ global sensitivity analysis on a four-chamber heart electromechanics model using gaussian processes emulators. *PLOS Computational Biology*, 19(6):e1011257, 2023.

B. E. Sumpio, R. O. Forsythe, K. R. Ziegler, J. G. van Baal, M. J. Lepantalo, and R. J. Hinchliffe. Clinical implications of the angiosome model in peripheral vascular disease. *Journal of Vascular Surgery*, 58(3):814–826, 2013.

L. Sun, X. Geng, Y. Wang, D. Wang, X. Ma, and G. Ning. Hemodynamic simulation for plantar arteries by anatomical structure based mathematical model. *Biocybernetics and Biomedical Engineering*, 45(3):390–398, 2025.

Y. Sun, M. Beshara, R. Lucariello, and S. Chiaramida. A comprehensive model for right-left heart interaction under the influence of pericardium and baroreflex. *Am. J. Physiol. Heart. Circ. Physiol.*, 272(3):H1499–1515, 1997. doi: 10.1152/ajpheart.1997.272.3.H1499.

F. Susin. Integrating sex and gender in model simulations of cardiovascular flows: a narrative review. *J. Sex Gender Specif. Med.*, 9(1):47–52, 2023. doi: 10.1723/4031.40065.

F. P. Tange, B. R. Ferrari, P. van den Hoven, J. van Schaik, A. Schepers, C. S. van Rijswijk, R. W. van der Meer, H. Putter, A. L. Vahrmeijer, J. F. Hamming, et al. Evaluation of the angiosome concept using near-infrared fluorescence imaging with indocyanine green. *Ann Vasc Surg*, 93:283–290, 2023. doi: https://doi.org/10.1016/j.avsg.2023.01.006.

F. P. Tange, P. van den Hoven, J. van Schaik, A. Schepers, K. E. van der Bogt, C. S. van Rijswijk, H. Putter, A. L. Vahrmeijer, J. F. Hamming, and J. R. van der Vorst. Near-infrared fluorescence imaging with indocyanine green to predict clinical outcome after revascularization in lower extremity arterial disease. *Angiology*, 75(9):884–892, 2024. doi: https://doi.org/10.1177/00033197231186096.

G. I. Taylor. Dispersion of soluble matter in solvent flowing slowly through a tube. *Proceedings of the Royal Society of London. Series A. Mathematical and Physical Sciences*, 219(1137):186–203, 1953.

G. I. Taylor and J. H. Palmer. The vascular territories (angiosomes) of the body: experimental study and clinical applications. *British journal of plastic surgery*, 40(2):113–141, 1987. doi: https://doi.org/10.1016/0007-1226(87)90185-8.

W. G. Teague, N. J. Tustison, and T. A. Altes. Ventilation heterogeneity in asthma. *Journal of Asthma*, 51(7):677–684, 2014.

E. A. Ten Brinke, D. Burkhoff, R. J. Klautz, C. Tschöpe, M. J. Schalij, J. J. Bax, E. E. van der Wall, R. A. Dion, and P. Steendijk. Single-beat estimation of the left ventricular

end-diastolic pressure–volume relationship in patients with heart failure. *Heart*, 96(3): 213–219, 2010.

E. F. Toro. *Riemann Solvers and Numerical Methods for Fluid Dynamics*. Springer, 2009.

E. F. Toro and A. Siviglia. Flow in collapsible tubes with discontinuous mechanical properties: mathematical model and exact solutions. *Commun. Comput. Phys.*, 13(2):361–385, 2013a. doi: 10.4208/cicp.210611.240212a.

E. F. Toro and A. Siviglia. Flow in collapsible tubes with discontinuous mechanical properties: mathematical model and exact solutions. *Communications in Computational Physics*, 13(2):361–385, 2013b. doi: https://doi.org/doi:10.4208/cicp.210611.240212a.

E. F. Toro, B. Thornber, Q. Zhang, A. Scoz, and C. Contarino. A computational model for the dynamics of cerebrospinal fluid in the spinal subarachnoid space. *Journal of biomechanical engineering*, 141(1):011004, 2019.

E. F. Toro, M. Celant, Q. Zhang, C. Contarino, N. Agarwal, A. Linninger, and L. O. Müller. Cerebrospinal fluid dynamics coupled to the global circulation in holistic setting: Mathematical models, numerical methods and applications. *International Journal for Numerical Methods in Biomedical Engineering*, 38(1):e3532, 2022. doi: https://doi.org/10.1002/cnm.3532.

P. Trenhago, L. Fernandes, L. Müller, P. Blanco, and R. Feijóo. An integrated mathematical model of the cardiovascular and respiratory systems. *Int. J. Numer. Meth. Biomed. Eng.*, 32(1):e02736, 2015. doi: 10.1002/cnm.2736.

Z. A. Tsigaras, M. Weeden, R. McNamara, T. Jeffcote, A. A. Udy, J. Anstey, M. Plummer, J. Bellapart, A. Chow, A. Delaney, et al. The pressure reactivity index as a measure of cerebral autoregulation and its application in traumatic brain injury management. *Critical Care and Resuscitation*, 25(4):229–236, 2023.

M. Ursino. Interaction between carotid baroregulation and the pulsating heart: a mathematical model. *Am. J. Physiol. Heart Circ. Physiol.*, 275(5):H1733–H1747, 1998. doi: 10.1152/ajpheart.1998.275.5.H1733.

M. Ursino and M. Giannessi. A model of cerebrovascular reactivity including the circle of willis and cortical anastomoses. *Annals of biomedical engineering*, 38(3):955–974, 2010. doi: https://doi.org/10.1007/s10439-010-9923-7.

M. Ursino and C. A. Lodi. A simple mathematical model of the interaction between intracranial pressure and cerebral hemodynamics. *Journal of applied physiology*, 82(4): 1256–1269, 1997.

M. Ursino and C. A. Lodi. Interaction among autoregulation, co2 reactivity, and intracranial pressure: a mathematical model. *American Journal of Physiology-Heart and Circulatory Physiology*, 274(5):H1715–H1728, 1998.

M. Ursino and E. Magosso. Acute cardiovascular response to isocapnic hypoxia. i. a mathematical model. *Am. J. Physiol. Heart Circ. Physiol.*, 279(1):H149–H165, 2000. doi: 10.1152/ajpheart.2000.279.1.H149.

M. Ursino and E. Magosso. A theoretical analysis of the carotid body chemoreceptor response to o2 and co2 pressure changes. *Respiratory physiology & neurobiology*, 130(1): 99–110, 2002.

M. Ursino, E. Magosso, and G. Avanzolini. An integrated model of the human ventilatory control system: the response to hypoxia. *Clinical Physiology*, 21(4):465–477, 2001.

M. Ursino, E. Magosso, and G. Avanzolini. An integrated model of the human ventilatory control system: the response to hypercapnia. *Clin. Physiol. Heart Circ. Physiol.*, 21(4): 447–464, 2008. doi: 10.1046/j.1365-2281.2001.00349.x.

J. Valentin. Basic anatomical and physiological data for use in radiological protection: reference values: Icrp publication 89: Approved by the commission in september 2001. *Annals of the ICRP*, 32(3-4):1–277, 2002.

F. Van de Vosse and N. Stergiopulos. Pulse wave propagation in the arterial tree. *Annual Review of Fluid Mechanics*, 43(1):467–499, 2011. doi: 10.1146/annurev-fluid-122109-160730.

J. Van den Berg. Angiosome perfusion of the foot: An old theory or a new issue? *Seminars in Vascular Surgery*, 31(2):56–65, 2018. doi: https://doi.org/10.1053/j.semvascsurg.2018.12.002.

C. Van Ertbruggen, C. Hirsch, and M. Paiva. Anatomically based three-dimensional model of airways to simulate flow and particle transport using computational fluid dynamics. *Journal of applied physiology*, 98(3):970–980, 2005.

B. Van Leer. Towards the ultimate conservative difference scheme. v. a second-order sequel to godunov's method. *J. Comp. Phys.*, 32(1), 1979. doi: 10.1016/0021-9991(79)90145-1.

C. Varela, F. Acín, J. De Haro, and I. Michel. The role of foot collateral vessels on angiosome-oriented revascularization. *Annals of translational medicine*, 5(21):431, 2017. doi: https://doi.org/10.21037/atm.2017.08.41.

M. Venermo and N. Settembre. Perfusion increase in foot angiosomes: Comparison between direct and indirect revascularization of crural arteries. *Scandinavian Journal of Surgery*, 113(2):174–181, 2024. doi: https://doi.org/10.1177/14574969241242205.

D. Wallace, M. Allison, and M. Stone. Inferior vena cava percentage collapse during respiration is affected by the sampling location: An ultrasound study in healthy volunteers. *Academic Emergency Medicine*, 17(1):96–99, 2010. doi: 10.1111/j.1553-2712.2009.00627.x.

J. Wan, B. Steele, S. A. Spicer, S. Strohband, G. R. Feijo´ o, T. J. Hughes, and C. A. Taylor. A one-dimensional finite element method for simulation-based medical planning for cardiovascular disease. *Computer Methods in Biomechanics & Biomedical Engineering*, 5(3):195–206, 2002.

J. Wang and K. Parker. Wave propagation in a model of the arterial circulation. *Journal of biomechanics*, 37(4):457–470, 2004.

M. Weininger, J. M. Barraza, C. A. Kemper, J. F. Kalafut, P. Costello, and U. J. Schoepf. Cardiothoracic ct angiography: current contrast medium delivery strategies. *American Journal of Roentgenology*, 196(3):W260–W272, 2011.

K. Wesseling and J. Settels. Circulatory model of baro-and cardio-pulmonary reflexes. In *Blood pressure and heart rate variability*, pages 56–67. IOS Press, 1993.

N. Westerhof and B. E. Westerhof. A review of methods to determine the functional arterial parameters stiffness and resistance. *Journal of hypertension*, 31(9):1769–1775, 2013.

N. Westerhof, F. Bosman, C. J. De Vries, and A. Noordergraaf. Analog studies of the human systemic arterial tree. *Journal of biomechanics*, 2(2):121–143, 1969.

N. Westerhof, P. Sipkema, G. V. D. Bos, and G. Elzinga. Forward and backward waves in the arterial system. *Cardiovascular research*, 6(6):648–656, 1972.

L. Wexler, D. Bergel, I. Gabe, G. Makin, and C. Mills. Velocity of blood flow in normal human venae cavae. *Circulation Research*, 23, 1968. doi: 10.1161/01.res.23.3.349.

T. H. Williamson and A. Harris. Ocular blood flow measurement. *The British journal of ophthalmology*, 78(12):939, 1994.

R. T. Woodall, S. L. Barnes, D. A. Hormuth, A. G. Sorace, C. C. Quarles, and T. E. Yankeelov. The effects of intravoxel contrast agent diffusion on the analysis of dce-mri data in realistic tissue domains. *Magnetic resonance in medicine*, 80(1):330–340, 2018.

W.-C. Wu, E. Mohler, S. J. Ratcliffe, F. W. Wehrli, J. A. Detre, and T. F. Floyd. Skeletal muscle microvascular flow in progressive peripheral artery disease: assessment with continuous arterial spin-labeling perfusion magnetic resonance imaging. *Journal of the American College of Cardiology*, 53(25):2372–2377, 2009.

N. Xiao, J. Alastruey, and C. Alberto Figueroa. A systematic comparison between 1-d and 3-d hemodynamics in compliant arterial models. *International journal for numerical methods in biomedical engineering*, 30(2):204–231, 2014.

M.-J. Yoon, E. Kim, S.-J. Lee, Y.-M. Bae, S. Kim, and S.-H. Park. Pulpal blood flow measurement with ultrasound doppler imaging. *Journal of endodontics*, 36(3):419–422, 2010.

M. Zaid, L. Sala, L. Despins, D. Heise, M. Popescu, M. Skubic, S. Ahmad, C. Emter, V. Huxley, and G. Guidoboni. Cardiovascular sex-differences: insights via physiology-based modeling and potential for noninvasive sensing via ballistocardiography. *Front. Cardiovasc. Med.*, 10, 2023. doi: 10.3389/fcvm.2023.1215958.

B. S. Zemel. Body composition during growth and development. *Human growth and development*, pages 517–545, 2022.

C. Zervides, A. J. Narracott, P. V. Lawford, and D. R. Hose. The role of venous valves in pressure shielding. *Biomedical engineering online*, 7(1):8, 2008.

X. Zhang, S. Noda, R. Himeno, and H. Liu. Gravitational effects on global hemodynamics in different postures: A closed-loop multiscale mathematical analysis. *Acta Mechanica Sinica*, 33(3):595–618, 2017.